

Multi-Cation Perovskite Semiconductors for All-Perovskite Tandem Solar Cells

Zur Erlangung des akademischen Grades einer

**DOKTORIN DER INGENIEURWISSENSCHAFTEN
(Dr.-Ing.)**

von der KIT-Fakultät für
Elektrotechnik und Informationstechnik des
Karlsruher Instituts für Technologie (KIT)

angenommene

Dissertation

von

M. Sc. Somayeh Moghadamzadeh
geb. im Iran

Tag der mündlichen Prüfung: 19.02.2021

Hauptreferent: Prof. Dr. Uli Lemmer

Korreferent: Prof. Dr. Jan Philipp Hofmann



This document is licensed under a Creative Commons
Attribution-ShareAlike 4.0 International License (CC BY-SA 4.0):
<https://creativecommons.org/licenses/by-sa/4.0/deed.en>

Kurzfassung

Der steigende Energiebedarf sowie der damit verbundene rasante Anstieg der Treibhausgasemissionen verursacht durch fossile Brennstoffe erfordern einen Übergang hin zu alternativen, sauberen Energiequellen. Dabei spielt die Photovoltaik als reichlich verfügbare und vielseitige Energiequelle eine entscheidende Rolle bei der Umsetzung dieses Übergangs. Perowskit-Solarzellen mit elektrischen Wandlungswirkungsgraden von über 25% gehören zu den vielversprechendsten Kandidaten neuer Photovoltaiktechnologien. Es wird erwartet, dass sie nicht nur aufgrund ihrer bemerkenswerten Entwicklungen in Bezug auf Leistungssteigerung, sondern auch auf Kostensenkung eine Schlüsselrolle in der Zukunft der Photovoltaik-Technologie spielen werden.

Über ein Jahrzehnt an Optimierungen der Bauteilarchitektur und dem Erlangen neuer Erkenntnisse zu den Materialeigenschaften haben zur Verbesserung der Wirkungsgrade der Perowskit-Solarzellen und so zu deren stetigen Weiterentwicklung geführt. Dennoch sind diverse Fragen zum Verständnis der Eigenschaften dieser Materialklasse weiterhin ungeklärt. Ein häufig beobachtetes Phänomen ist die spontane Erhöhung des Wirkungsgrades frisch hergestellter Perowskit-Solarzellen, die über eine Zeitskala von einigen Tagen bis Wochen bei Lagerung bei Raumtemperatur auftritt. Der Ursprung dieses umstrittenen Phänomens ist eine Fragestellung, der im ersten Teil dieser Arbeit nachgegangen werden soll. Eine detaillierte Untersuchung zeigt, dass die spontane Erhöhung des Wirkungsgrades für eine Vielzahl von Multikationhalogenid Perowskit-Solarzellen mit unterschiedlichen Absorberzusammensetzungen und Bauteilarchitekturen auftritt.

Trotz ihrer rasanten Entwicklung ist der Wirkungsgrad von einfachen Perowskit-Solarzellen nach oben theoretisch begrenzt (<30%). Tandemtechnologien zeigen jedoch einen Weg auf, dieses fundamentale Limit zu überwinden (>35%). Kürzlich haben vollständig Perowskit-basierte Tandemsolarzellen, bestehend aus einer oberen Perowskit-Solarzelle mit hoher Bandlücke und einer unteren Perowskit-Solarzelle mit geringerer Bandlücke, eine neue Möglichkeit hin zu hocheffizienten aber gleichzeitig kostengünstigen Solarzellen eröffnet. In dieser Arbeit werden die Herausforderungen der Perowskit-Solarzellen mit geringer Bandlücke im Hinblick auf der Erzielung hocheffizienter Solarzellen diskutiert und Strategien zu deren Überwindung entwickelt.

Zu Beginn dieser Arbeit wird durch Optimierung der Absorberzusammensetzung eine deutliche Verbesserung der Photostabilität in diesen Solarzellen erzielt. Dies ermöglicht die Herstellung stabiler Perowskit-Absorber mit Bandlücken von 1,26 eV, was einem breiten Photonenabsorptionsbereich entspricht, der sich bis zu ca. 1000 nm erstreckt. Eine generelle Einschränkung bei der effizienten Nutzung des Potenzials dieser Absorber sind die optischen Verluste durch alle vor dem Absorber mit geringer Bandlücke befindlichen Schichten in der Tandemkonfiguration.

Diese Arbeit stellt sich der Herausforderung, die optischen Verluste auf zwei Arten zu reduzieren: (i) Ersatz der kommerziellen transparenten Frontelektrode durch eine gesputterte

hochtransparente Elektrode mit deutlich geringerer parasitärer Absorption im nahen infraroten Bereich (<2%) und (ii) Beseitigung der lochselektiven Transportschicht der Solarzelle mit geringer Bandlücke welche die optischen Verluste im kurzwelligen Bereich begrenzt. Als Ergebnis können stabile und effiziente vollständig Perowskit-basierte Tandemsolarzellen mit Wirkungsgraden von bis zu 24,8% demonstriert werden, was zu den höchsten bisher berichteten Werten für dieses Bauteilkonzept gehört.

Abstract

Rising energy demand as well as a rapid increase in greenhouse gas emission emanating from fossil fuels call for a transition to alternative clean energy resources (renewables). Photovoltaics as an abundantly available and versatile source of energy plays a prominent role in maximizing the forward momentum of this transition. Perovskite solar cells with power conversion efficiencies exceeding 25% are among the most promising candidates for the new photovoltaics technologies. They are expected to play a key role in the future of photovoltaic technology not only due to their remarkable developments in terms of performance enhancement but also cost reduction.

Over a decade, countless investigations into improving the performance of perovskite solar cells through optimizing device architecture and understanding the material properties have resulted in the constant development of perovskite solar cells. Nevertheless, a few effects still shadow our comprehension of the properties of this class of material. A common phenomenon is the *spontaneous enhancement* of power conversion efficiency of pristine perovskite solar cells that occurs over a timescale of a few days to weeks storage at room temperature. The genesis of this phenomenon, which has been under debate, is a question the first part of this thesis sets out to explore. A detailed investigation reveals that spontaneous enhancement of power conversion efficiency occurs for a variety of multi-cation-halide perovskite solar cells with different perovskite compositions and device architectures. The structural analysis uncovered that a reduction in stain-induced trap states within the lattice structure of perovskite thin films is the origin of this phenomenon.

Despite their rapid growth, the power conversion efficiency of single-junction perovskite solar cells is fundamentally limited (<30%). Fortunately, tandem technologies reveal a path to surpass this limitation (>35%). Recently, all-perovskite tandem solar cell configurations, consisting of a wide-bandgap top and a narrow-bandgap bottom perovskite solar cell, have opened a window into highly efficient yet cost-effective solar cells. In this thesis, the challenges of narrow-bandgap perovskite solar cells with respect to improving photostability and achieving high efficiency solar cells are discussed and strategies to overcome them are developed.

From the outset, composition engineering exhibits a pronounced improvement in the photostability of narrow-bandgap perovskite solar cells. This allows for the development of a stable narrow-bandgap perovskite thin film, whose bandgap of 1.26 eV corresponds to a broad photon absorption range extending up to ≈ 1000 nm. One limitation in the way of exploiting the potential of this absorber is the optical losses in electrodes and top layers of a tandem configuration. This thesis meets the challenge of reducing the optical losses in two ways: (i) replacing the commonly used transparent electrodes with a sputtered highly transparent electrode with significantly low parasitic near-infrared absorption (<2%) and (ii) removing the hole transport layer of the narrow-bandgap bottom perovskite solar cells that limits the optical losses in the short wavelength region. As a result, stable and highly efficient four-terminal all-perovskite tandem solar cell attain power conversion efficiencies

as high as 24.8%, which is amongst the highest values reported for all-perovskite tandem solar cells to date.

Abbreviations and Acronyms

2T	two-terminal
4T	four-terminal
4- <i>t</i> BP	4-tert-Butylpyridine
Ag	silver
AM0	solar spectrum outside the atmosphere
AM1.5G	air-mass 1.5 global
AFM	atomic force microscopy
All-PTSC	all-perovskite tandem solar cell
Au	gold
BCP	bathocuproine
c-Si	crystalline silicone
C ₆₀	buckminsterfullerene
CB	chlorobenzene
CL	cathodoluminescence
Cs	cesium
CsI	cesium iodide
Cu	copper
DCB	di-chlorobenzene
DMF	N,N-dimethylformamide
DMSO	dimethyl sulfoxide
ETL	electron transport layer
EQE	external quantum efficiency
FA	formamidinium; HC(NH ₂) ₂
FAI	formamidinium iodide; HC(NH ₂) ₂ I
FF	fill factor
FTO	fluorine-doped tin oxide; SnO ₂ :F
GaAs	gallium arsenide
GBL	γ-butyrolactone
Ge	germanium
GuaSCN	guanidinium thiocyanate
HI	Hysteresis Index
HTL	hole transport layer
IO:H	hydrogen-doped indium oxide; In ₂ O ₃ :H
ITO	indium tin oxide; In ₂ O ₅ Sn
IZO	indium zin oxide; InZnO
<i>J</i> - <i>V</i>	current-density–voltage
Li-TFSI	lithium bis(trifluoromethyl sulfonyl)imide
MgF ₂	magnesium fluoride
MA	methylammonium; CH ₃ NH ₃
MAI	methylammonium iodide; CH ₃ NH ₃ I

Abbreviations and Acronyms

MABr	methylammonium bromide; CH ₃ NH ₃ Br
MoO _x	molybdenum oxide
MPP	maximum power point
NIR	near-infrared
np-SnO ₂	nanoparticles of SnO ₂
np-TiO ₂	nanoparticles of TiO ₂
Pb	lead
PbI ₂	lead iodide
PbBr ₂	lead bromide
Pb(SCN) ₂	lead thiocyanate
PCBM	[6,6]-Phenyl-C ₆₁ -butyric acid methyl ester
PCE	power conversion efficiency
PL	photoluminescence
PTAA	poly[bis(4-phenyl)(2,4,6-trimethylphenyl)amine]
PSC	perovskite solar cell
PV	photovoltaics
PVD	physical vapor deposition
SCD	spin coating deposition
SEM	scanning electron microscopy
SRH	Shockley-Read-Hall
Sn	tin
SnBr ₂	tin bromide
SnCl ₂	tin chloride
SnF ₂	tin fluoride
SnI ₂	tin iodide
SPCE	stabilized power conversion efficiency
Spiro-MeOTAD	2,2',7,7'-Tetrakis[N,N-di(4-methoxyphenyl)amino]-9,9'-spirobifluorene
SQ	Shockley-Queisser
STC	standard test condition; 100 mW/cm ² , 25 °C
TCO	transparent conductive oxide
TSC	thermally evaporated current
UV	ultraviolet
UV-vis	ultraviolet-visible
VAGC	vacuum-assisted growth control
XPS	X-ray photoelectron spectroscopy
XRD	X-ray diffraction

Table of Contents

Kurzfassung	i
Abstract	iii
Abbreviations and Acronyms	v
1. Introduction	1
2. Theoretical Background	5
2.1. Hybrid organic-inorganic perovskite semiconductors	5
2.1.1. Structural properties of ABX ₃ halides	5
2.1.2. Structural stability of metal-halide perovskites	6
2.1.3. Optoelectronic properties of metal-halide perovskites	8
2.2. Application of metal-halide perovskites in solar cells	13
2.2.1. Working principles of perovskite solar cells	13
2.2.2. Photovoltaic characteristics of a solar cell	16
2.2.3. Theoretical efficiency limit of a single-junction solar cell	21
2.3. Tandem solar cells	22
2.3.1. All-perovskite tandem solar cells	23
3. Materials and Characterization Methods	25
3.1. Materials and deposition methods	25
3.1.1. Solution preparation	25
3.1.2. Deposition of perovskite solar cells	28
3.2. Characterization techniques	31
3.2.1. Characterization of thin films	31
3.2.2. Characterization of perovskite solar cells	40
4. Spontaneous Enhancement of Power Conversion Efficiency	43
4.1. Motivation	43
4.2. Investigation of perovskite composition	44
4.3. Investigation of charge transport layers	48
4.4. Suppression of strain-induced trap states	53
4.5. Investigation of charge recombination mechanisms	56
4.6. Reduction of electronic trap states in the perovskite bulk	61
4.7. Summary	63
5. Narrow-bandgap Multi-Cation Mixed Tin/Lead Perovskite Solar Cells	65
5.1. Motivation	65

5.2.	Improved photo-stability of narrow-bandgap perovskite solar cells	67
5.3.	Morphology and surface characterizations	69
5.4.	Reduction of residual $\text{Sn}_y\text{Pb}_{(1-y)}\text{I}_2$	71
5.5.	Investigation of $\text{Sn}_y\text{Pb}_{(1-y)}\text{I}_2$ excess in perovskite thin films.....	74
5.6.	Four-terminal all-perovskite tandem solar cells	77
5.7.	Summary.....	81
6.	Hole-Transport-Layer-Free Tin/Lead Perovskite for Four-Terminal All-Perovskite Tandem Solar Cells	83
6.1.	Motivation	83
6.2.	Hole-transport-layer-free narrow-bandgap perovskite solar cells	85
6.3.	Highly transparent conductive oxide as a front electrode	85
6.4.	Narrow-bandgap perovskite solar cells with alternative front electrodes	92
6.5.	Four-terminal all-perovskite tandem solar cells with alternative front electrodes	95
6.6.	Summary.....	99
7.	Conclusion and Outlook	103
Appendix	107	
A.	Appendix of Chapter 4	107
B.	Appendix of Chapter 5.....	108
References	111	
List of Publications and Conference Contributions.....	127	
Acknowledgements.....	131	

1. Introduction

Global demand for energy (electricity and heat) is expected to grow by 20-30% or more through 2040 and beyond.¹ This growth is driven by population and economic development in developing countries, as energy consumption in developed countries is anticipated to remain constant.¹ Fossil fuels (coal, oil, and natural gas) are the current dominant energy resources and provide 80% of humanity's needs today.¹ However, they are not suitable for addressing future energy demands. On the one hand, continued use will inevitably deplete them,² and on the other hand, they have exacted a heavy price on our planet, from air and water pollution to climate change. They produce large quantities of greenhouse gases when burned, which trap heat in the atmosphere and lead to global warming.³

Since pre-industrial times, the planet has warmed about 1 °C at a substantially faster rate than it warmed over the previous 7000 years.⁴ Without ambitious climate policies, adopted at an international scale to slow down the current rate of heating, global warming will be on track to increase the earth's temperature by 3-5 °C by the end of this century.⁴ For the current global warming trend, all other natural explanations have been eliminated using direct observations.⁵ Instead rising concentrations of greenhouse gases, led by growing fossil fuel consumption, is the definitive main cause.⁵ The Paris Agreement united all nations in an ambitious undertaking to limit the rise in global temperatures to 2 °C in order to avert increases in extreme weather, rising sea levels, and the extinction of plant and animal species.⁶ To accomplish this, a determined focus on bringing down fossil fuel consumption is urgently needed. This calls for alternative clean energy resources (renewables), not only to sustain the future of the planet but also to reliably fulfill rising energy demands.⁷

Renewable energies are expected to overtake coal and gas in power generation in the mid-2030s and become the dominant source of electricity generation by 2040 (Figure 1.1a). Among the renewables, *solar power* is a versatile source of energy and abundantly available. Although solar power currently contributes to <20% of the total electricity generation from renewables, it will dominate electricity generation by 2050 with a share of 40% (Figure 1.1b).⁸

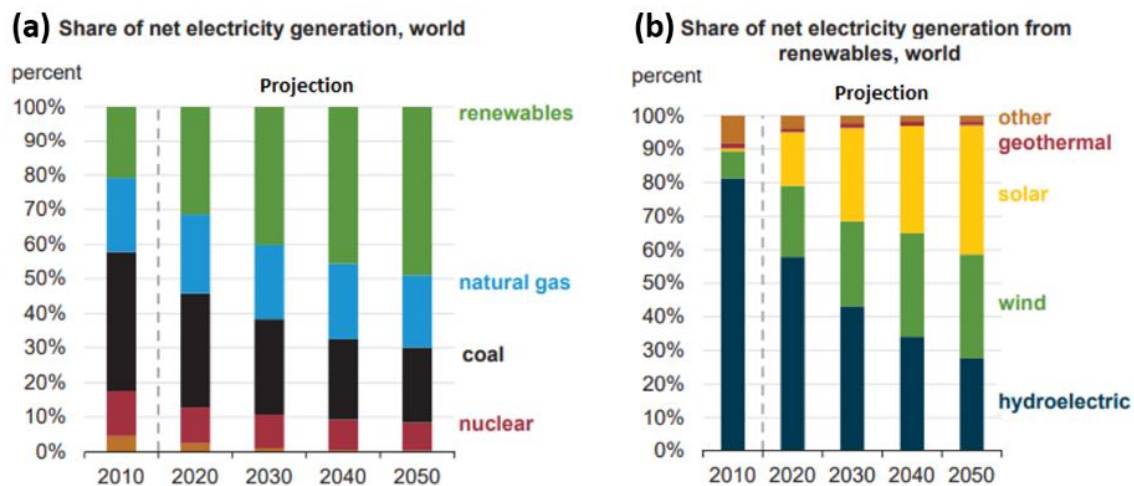


Figure 1.1. (a) growth in electricity generation by renewables. (b) share of solar energy in electricity generation from renewables. Based on the International Energy Outlook 2019 with projections to 2050.⁸ (www.eia.gov/outlooks/ieo/pdf/ieo2019.pdf. All rights reserved.)

Between 1980 and 2019, economies of scale and technological improvements meant each doubling of the accumulated photovoltaic (PV) module output (in GW_p), which was associated with a 25% relative reduction in price for commercially available solar PV technologies.⁹ In Germany, for example, prices for a typical PV rooftop-system decreased in average from 14,000 €/kW_p in 1990 to 1,050 €/kW_p in 2019, which is a net price regression of 92% over a 29-year period.⁹ Cost reduction is key to further development of PV across all markets and improving power conversion efficiency (PCE) of solar cells/modules is key to decrease costs. The PCE of the market-dominant silicon-based PV has nearly reached its theoretical limit in laboratory conditions,¹⁰ therefore, the industry is urged to continue working on alternative PV technologies to currently established crystalline silicon (c-Si) in order to continue obtaining gains. Tandem PV has been developed as a pathway to surpassing the theoretical limits for single-junction devices. It utilizes a combination of absorbers with different optical bandgaps that enables efficient harvesting of different shares of the Sun spectrum, outperforming the PCE of single-junction PV. Hence, tandem technologies are expected to maximize the forward momentum of the PV technology as it transitions into the leading source of electricity generation in the future.¹¹ Perovskite solar cells (PSCs) with a tunable bandgap are the most promising film-based tandem partners for silicon.¹¹ PSCs have been successfully partnered with c-Si solar cells in tandem configurations, with a current PCE record of 29.1% exceeding the PCE record of single-junction c-Si (27.6%) and perovskite (25.5%) solar cells.¹²

PSCs are expected to play a key role in the future of PV solar energy system due to the impressive developments in terms of performance enhancement and cost reduction. The PCE of single-junction PSCs has rapidly raised from only 3.8% in 2009¹³ to its current record of 25.5%¹² over a decade of intense research. PSCs are becoming more pronounced because aside from their rapid growth of efficiency, they are highly cost-effective and therefore a possible alternative for silicon-based PV (with a market dominance of 95%). Perovskites can be processed from inexpensive precursor materials using a variety of low-temperature and

scalable fabrication methods ranging from solution- to vacuum-based.^{14–17} Moreover, thanks to their tunable bandgap,^{18–23} they are also ideal candidates to replace the c-Si bottom cell in a tandem configuration. Consequently, all-perovskite tandem solar cells (all-PTSCs), composed of semi-transparent top and narrow-bandgap bottom PSCs, have been promoted as possible strategies to surpass the theoretical limits of single-junction PSCs while benefiting from low-temperature and low-cost fabrication methods.

Despite recent advances, all-PTSCs with a current PCE record of 25%,²¹ lag behind their Si-based tandem counterparts, and therefore further intensive research efforts and new strategies are still needed to exploit the potential of this new technology. So far most studies have been focused on developing and optimizing wide-bandgap PSCs and their applications as the top cell in perovskite/Si tandem solar cells.^{24–28} Meanwhile the PCE of the single-junction narrow-bandgap PSC, which is used as the bottom cell in all-PTSC configurations, has recently reached 20%.^{21–23,29,30} Aside from the comparatively lower efficiency of narrow-bandgap PSCs, their stability is another key challenge in the way of all-PTSCs to commercialization. The crystal structure of perovskite semiconductors strongly affects the stability of perovskite thin films and compositional engineering is an established strategy to adapt the crystal structure of perovskite materials to improve the stability of the respective PSCs.³¹ In this thesis, *the possible effects of Cs incorporation on improving the efficiency and operational photo-stability of narrow-bandgap perovskite solar cells* is one of the research questions set to be investigated.

Followed by the application of the highly stable and efficient narrow-bandgap PSCs as bottom cells in four-terminal (4T) all-PTSCs, we explored the possible pathways in improving the PCE of the all-PTSCs. Although the top and bottom solar cells in a 4T tandem device can work independently, they are optically interlinked such that the optical losses in the layer stack of the top cell can directly influence the performance of the bottom cell and consequently the overall performance of the tandem solar cell. The primary factors increasing the optical losses in all-PTSCs are parasitic absorption (caused primarily by the front and rear transparent conductive oxide (TCO) electrodes)^{32–36} and unfavorable reflection (partly caused by TCO electrodes and partly by various interfaces within the tandem stack structure).^{37,38} These losses diminish the transmission of the semi-transparent top PSC, consequently reducing the share of the solar spectrum reached by the bottom PSC and therefore its PCE. This work aims to reduce the optical losses caused by TCO front electrodes in both top and bottom solar cells of all-PTSC devices by utilizing a TCO with high transmittance and low parasitic absorption.^{33,36} Furthermore, removing the hole transport layer (HTL) in the narrow-bandgap bottom PSC is determined as a method to further reduce the absorption loss at this layer without compromising other PV characteristics. In this context, this thesis investigates the second research question, i.e., *what are the possible pathways to decrease optical losses introduced by transparent conductive oxide electrodes and the layer stack in a four-terminal all-perovskite tandem solar cell?*

The constant development in efficiency, stability, and scalability of PSCs over a decade is a consequence of countless investigations into improving perovskite material compositions,

morphology, interfaces, and device architecture; as well as understanding material properties and device-relevant effects such as degradation mechanisms associated with various factors (e.g., light, heat, bias, moisture, oxygen, or their combinations). Nevertheless, there are still some effects that shadow our comprehension of perovskite material properties. One of these effects is a very common observation whereupon the PCE of pristine PSCs tends to spontaneously enhance and reach its highest value a few days after device fabrication.³⁹⁻⁴⁴ Despite several efforts, a systematic study on the genesis of this phenomenon is still missing. We refer to this phenomenon as *spontaneous enhancement* within this thesis and aim at providing a systematic study that can shed light on the underlying mechanisms of this phenomenon by applying a combination of characterizations. This leads us to the next research question of this thesis: *What are the underlying mechanisms initiating spontaneous enhancement of the power conversion efficiency of pristine multi-cation perovskite solar cells?*

The scope of this thesis is outlined as follows:

Chapter 2: This chapter starts with a detailed discussion on structural, optical, and electronic properties of metal-halide perovskite materials, followed by a fundamental review of the working principle of single-junction and tandem solar cell configurations.

Chapter 3: This chapter introduces the material, fabrication methods, and the characterization tools implemented in this thesis.

Chapter 4: The scope of this chapter is an evaluation of underlying mechanisms initiating spontaneous enhancement of the power conversion efficiency of multi-cation perovskite solar cells.

Chapter 5: This chapter deals with optimizing narrow-bandgap perovskite solar cells with improved stability as well as its application in an all-perovskite tandem solar cells configuration, providing respectable power conversion efficiency compared to recent reports.

Chapter 6: This chapter presents further research in improving the performance of all-perovskite tandem solar cells with a focus on reducing parasitic absorption losses from the top and bottom perovskite solar cells. The first part of this chapter is an experimental investigation of hole-transport-layer-free narrow-bandgap perovskite solar cells, followed by characterizations on this class of perovskite solar cells fabricated on different transparent conductive oxide in the absence of a hole transport layer. The second part explores alternative transparent conductive oxide electrodes for the top cell and their influence on the overall performance of all-perovskite tandem solar cells.

Chapter 7: This chapter outlines the key findings of this study and provides an outlook for the discussed topics.

2. Theoretical Background

A photovoltaic solar cell is an electrical device that generates electricity when exposed to electromagnetic solar radiation (photons). In general, a thin slice of a semiconductor material, which is connected to an external circuit through two contacts, generates free charge carriers upon interaction with incident radiation. The effectiveness of a solar cell highly depends on the choice of the light-absorbing semiconductor material and the way whereby the semiconductor is connected to the external circuit.

Metal-halide perovskite semiconductors, which are the focus of this thesis, are proved to be promising light-absorbing semiconductor candidates for solar cell photovoltaics due to their excellent optical and electronic properties, such as tunable bandgap,^{45,46} high absorption coefficient,⁴⁷ low exciton binding energy,^{48,49} long diffusion length,⁵⁰ high charge carrier mobilities,^{51,52} and low non-radiative recombination rates,^{51,52} which are essential for photovoltaic applications.⁵³ This chapter begins with an overview of the structural properties of this class of material, followed by a detailed discussion on their superior photovoltaic properties and their application in single-junction and all-perovskite tandem solar cell devices.

2.1. Hybrid organic-inorganic perovskite semiconductors

A family of compounds with a general formula of ABX_3 are called *perovskites*, named after the mineralogist Count Lev Aleksevich Perovski. A and B are cations (usually large- and middle-sized, respectively) and X is an anion. Perovskites are realized to possess very useful physical and chemical properties that, more importantly, can be modified in a controlled way by replacement of any of the A, B, and X ions. A complex composition of this family is called organic-inorganic metal-halide perovskites. This section summarizes the most important properties of these materials.

2.1.1. Structural properties of ABX_3 halides

The crystal structure of ABX_3 is generally described as an arrangement of the A-site located in the center of a cuboctahedral with corner-sharing BX_6 octahedra (Figure 2.1, left). From a crystallographic perspective, an idealized perovskite structure is a cubic structure

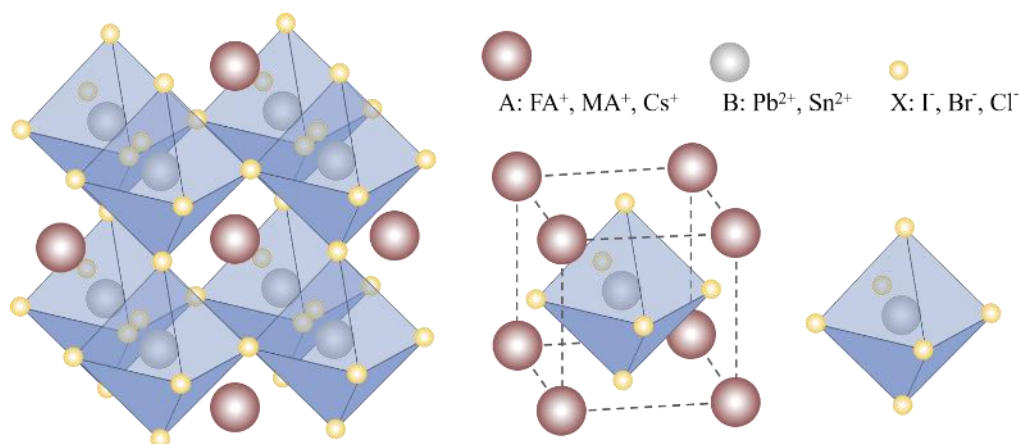


Figure 2.1. Idealized cubic structure of ABX_3 perovskite (left panel), unit cell with A at the corner of the cubic cage, B at the body-center, and X at the face-center positions (center panel), and BX_6 octahedra (right panel).

(Figure 2.1). The size and interaction of the A-site and BX_6 octahedra determine the structure of an ABX_3 compound.⁵⁴ The Goldschmidt tolerance factor (t) and octahedral factor (μ), which is a measure of octahedral stability, are suggested to predict whether a combination of A, B, and X forms a stable perovskite structure.⁵⁴ These factors are defined as follows:

$$t = \frac{r_A + r_X}{\sqrt{2}(r_B + r_X)} \quad , \quad \mu = \frac{r_B}{r_X} \quad 2.1$$

where r_A , r_B , and r_X are the ionic radii of the respective atoms. A t - μ structure map, which is a plot of t vs. μ can be used to assess whether an ABX_3 is a perovskite structure. Figure 2.2 shows such a t - μ structure map which was established on a study in which 96% of 186 different compounds were correctly classified.⁵⁴ According to this map, a stable ABX_3 halide perovskite structure with ($X = F, Cl, Br, \text{ and } I$) forms if $0.87 < t < 1.1$ and $\mu > 0.44$, approximately. When $t = 1$, the perovskite structure is adopted to an ideal cubic structure. In the lower range ($t \approx 0.87$) the cubic structure might be distorted due to tilting of the BX_6 octahedra and leading to less symmetric tetragonal and orthorhombic structures. If $t > 1$, the A-site is too large, and if $t < 0.8$, the A-site is too small, which leads to a formation of non-perovskite structures.⁵³ For perovskite materials with more complex compositions, the concept of t and μ can be extended. For example, for a mixed-cation perovskite with a composition $A_yA'_{1-y}BX_3$, the tolerance factor can be determined as $t = \frac{y r_A + (1-y) r_{A'} + r_X}{\sqrt{2}(r_B + r_X)}$.⁵⁵

Furthermore, the ABX_3 perovskite structures are temperature- and pressure-sensitive, which will be briefly discussed in the next section. Detailed studies about the phases of a perovskite structure and its correlation with ambient temperature and pressure conditions are beyond the scope of this thesis and can be found in references [55] and [56].

2.1.2. Structural stability of metal-halide perovskites

Metal-halide perovskite semiconductors possess a chemical structure of ABX_3 with an idealized cubic crystal structure shown in Figure 2.1. The A-site is large enough to

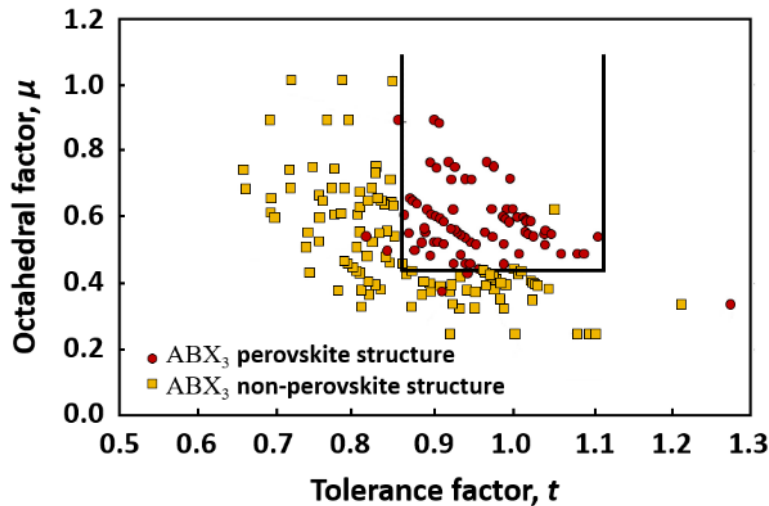


Figure 2.2. The t - μ structure map; tolerance factor (t) vs. octahedral factor (μ) for ABX_3 halides. Reproduced from [54].

accommodate complex organic ions like formamidinium ($\text{NH}_2=\text{CHNH}_2$)⁺, written as FA^+ , and methylammonium (CH_3NH_3)⁺, written as MA^+ , as well as inorganic ions like cesium (Cs^+). B-site is occupied with a divalent metal from elements of group 14 germanium (Ge^{2+}), tin (Sn^{2+}), and/or lead (Pb^{2+}). X-site is filled with halogen chloride (Cl^-), bromide (Br^-), and/or iodide (I^-). The combination of these ions in the A-, B-, and X-sites not only determines the structural phase and stability of ABX_3 metal-halide perovskites but also determines whether the properties of the resulting structure are suitable for photovoltaic applications.

In general, organic-inorganic metal-halide perovskites are realized to have three perovskite (black) phases with cubic (denoted as α -phase), tetragonal (denoted as β -phase), and orthorhombic (denoted as γ -phase) structures as well as non-perovskite (yellow) phases with hexagonal (denoted as δ_{H} -phase) and orthorhombic (denoted as δ_{O} -phase) structures.^{31,53} Different compositions may stabilize in one of these phases at different temperatures. The archetypal MAPbI_3 composition (referred to as MAPI) shows phase transitions at 165 and 327 K. It has a non-perovskite (orthorhombic) δ_{O} -phase for $T < 165$ K, a perovskite (tetragonal) β -phase between $165 < T < 327$ and a perovskite (cubic) α -phase for $T > 327$ K.⁵⁷ FAPbI_3 composition is an example of a non-perovskite structure at room temperature. This composition is only stable in a perovskite (cubic) α -phase at a high temperature of 423 K, while the large ionic radius of FA^+ ($r_{\text{A}} = 2.53 \text{ \AA}$) causes a transition to a non-perovskite (hexagonal) δ_{H} -phase at room temperature. CsPbI_3 , on the other hand, has a too-small tolerance factor (t) due to the relatively small ionic radius of Cs^+ ($r_{\text{A}} = 1.74 \text{ \AA}$) and at room temperature stabilizes in a non-perovskite orthorhombic (δ_{O} -phase), while its perovskite (cubic) α -phase is only attainable at a temperature higher than 573 K.⁵⁸

Compositional substitution, as a well-established approach, enables us to tune the tolerance (t) and octahedra (μ) factors in the relevant ranges to form a stable perovskite structure at a

finite temperature with desired properties. For example, the unwanted phase transition of FAPbI₃ at room temperature, from cubic (α -phase) to hexagonal (δ_{H} -phase), can be prevented by partial substitution of FA⁺ with Cs⁺ with a relatively smaller ionic radius.⁵⁹ Incorporation of Cs⁺ results in a contraction of cuboctahedral volume which consequently enhances the interaction between FA⁺ and I⁻ and leads to a better photo- and moisture-stability.⁵⁹ In general, using mixed cations has been realized as a convenient strategy to create stable perovskite structures. In particular, using a triple-cation mixture (CsFAMA) with a perovskite (cubic) α -phase at room temperature, was introduced as a novel strategy to effectively suppressing yellow phase impurities and facilitating a pure defect-free perovskite thin film.⁶⁰

2.1.3. Optoelectronic properties of metal-halide perovskites

Bandgap tunability

While the organic and/or inorganic components (A-site) mainly determine the structural phase stability of an ABX₃ composition, the divalent metal cation (B-site) and halogen anion (X-site) and their interaction determine whether the electronic properties (e.g., electronic bandgap) of the resulting perovskite would be advantageous for photovoltaic applications. Theoretical investigations, particularly based on the density functional theory (DFT) method revealed that (i) organic/inorganic metal-halide perovskites (ABX₃) are semiconductors with direct bandgaps for which (ii) the valence band maximum forms by an antibonding combination of s-orbitals of the metal and p-orbitals of the halide, whereas (iii) the conduction band minimum is a combination of less antibonding and more nonbonding p-orbitals of the metal and halide.⁶¹ Therefore, a compositional substitution that leads to alteration in the B–X overlap changes the bandgap of the resulting perovskite. If the alteration (substitution or phase transition) reduces the distance between metal (B-site) and halogen (X-site), the energy of the valence band maximum increases more than the energy of the conduction band minimum.^{45,62} Therefore, a larger B–X overlap results in a smaller bandgap and a decreased B–X overlap increases the bandgap.⁴⁵

Bandgap alteration upon phase transition is reported, as would be expected. For example, at a phase transition from tetragonal (at room temperature) to orthorhombic (at low temperature), the bandgap of MAPI increases by ~100 meV.⁶³ In contrast, band-edge states of MASnI₃ do not change at its phase transitions from cubic (at room temperature) to tetragonal to orthorhombic (at low temperature).⁶⁴ However, compositional engineering, which is a way to control perovskite structure, can also tune its bandgap conveniently in a controlled way. Experimental work has shown that a wide range of bandgaps between 1.10–1.55 eV (by tuning the ratios of Sn:Pb)^{45,65,66} and 1.5–2.3 eV (by tuning the ratios of I:Br)^{27,46,67} is attainable. Increasing Br content results in a larger bandgap. Substitution of Pb with Sn (partial or total) can decrease the bandgap to very low values, although reduced stability due to the formation of Sn⁴⁺ (an oxidation product of Sn²⁺) is an issue. Bandgap tunability is an advantage for metal-halide perovskite semiconductors making them suitable candidates for photovoltaic applications such as solar cells.

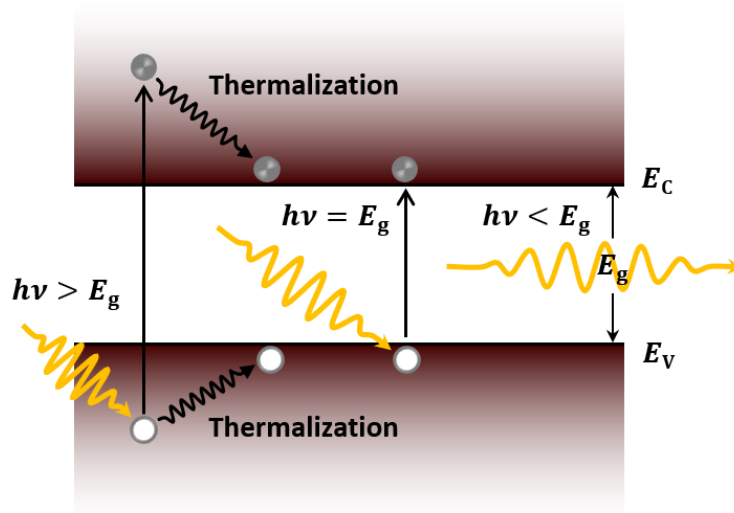


Figure 2.3. Absorption of photons with different wavelengths in a semiconductor. If the energy of the photon ($h\nu$) is much higher than the bandgap (E_g), the excited electron is thermalized to the conduction band minimum. E_V and E_C represent the valence band maximum and conduction band minimum, respectively.

High absorption coefficient

Whereupon interaction of a semiconductor with incident photons (i) all photons with energy equal to or greater than the bandgap of the semiconductor ($h\nu \geq E_g$) can be absorbed and (ii) all photons with energy less than the bandgap of the semiconductor ($h\nu < E_g$) are transmitted. Absorbed photons generate excitons (electron-hole pairs) by exciting electrons from the valence band to the conduction band of the semiconductor. If the photon energy is much larger than the bandgap, the excited electron or generated hole releases the excess energy ($h\nu - E_g$) to reach thermal equilibrium (conduction band minimum (E_C) for electrons or valence band maximum (E_V) for holes) and the released energy transforms into lattice vibration and creates heat. This process is called thermalization. Figure 2.3 illustrates these processes schematically.

If I_0 is the intensity of the incident light at the top surface (neglecting reflection at the interface) of a semiconductor with an absorption coefficient of α (in cm^{-1}), the intensity of light at a distance in the material (x) can be calculated according to Beer-Lambert law:

$$I(x) = I_0 e^{-\alpha x} \quad 2.2$$

This equation shows that the light intensity decreases exponentially within a semiconductor and drops to $1/e$ of its initial value at $x = 1/\alpha$. This distance is called absorption depth at which 63% of the incident light is absorbed through the material. As schematically shown in Figure 2.3, photons with much larger energies (shorter wavelength) are absorbed within a short distance inside the semiconductor, while photons with lower energies (longer wavelength) penetrate deeper into the material. Therefore, the semiconductor is required to be sufficiently thick ($d > 1/\alpha$) to absorb most of the incident light.

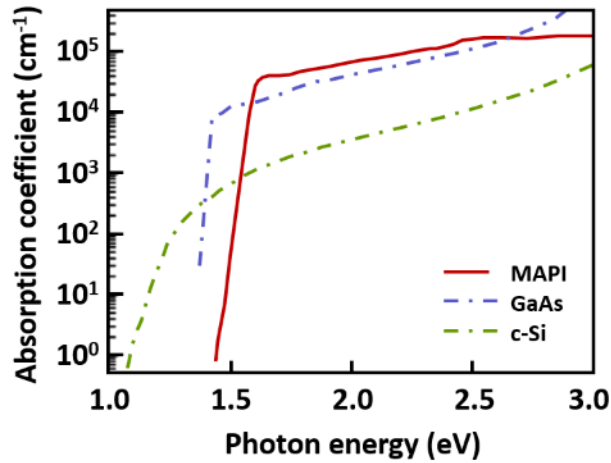


Figure 2.4. Absorption coefficient of a 200-nm perovskite thin film (MAPI) compared with other common photovoltaic materials such as gallium arsenide (GaAs) and crystalline Silicon (c-Si), all measured at room temperature. Reproduced from [47].

Conclusively, semiconductors with very high absorption coefficient are not required to be too thick to absorb most of the incident light. Thinner thickness means shorter paths for charge transport in the material, and therefore a reduction in the possibilities of recombination. Very thin metal-halide perovskite semiconductors with higher absorption coefficient, compared to other semiconductors such as GaAs (direct bandgap) and c-Si (indirect bandgap), are excellent choices to be used as the absorber layers in solar cells. The absorption coefficient of a MAPI film with only 220 nm was shown to be $>10^4 \text{ cm}^{-1}$ for wavelength below 700 nm (Figure 2.4).⁴⁷ This guarantees high absorption particularly in the visible light range, which is critical for high efficiency solar cell devices. Furthermore, the absorption onset occurs at higher absorption coefficients than all the other most comparable semiconductors explaining why even a very thin perovskite film is sufficient for solar cell applications. The most efficient perovskite solar cells (PSCs) with high efficiencies have employed perovskite thin films in the range between 300-600 nm which is almost three orders of magnitude thinner than silicon solar cells.

Exciton generation

Equation 2.2 can be used to calculate the number of photogenerated electron-hole pairs. Assuming that the absorption of photons directly generates electron-hole pairs, then the generation rate (G) in a thin slice of material (dx) is determined by finding the change in light intensity across this slice (dI). Therefore, the generation rate at any point in the device (x) can be calculated as follows:

$$G(x) = \alpha N_0 e^{-\alpha x} \quad 2.3$$

where N_0 is photon flux at the surface and α is the absorption coefficient. The above equation shows that at the surface of the material ($x = 0$), the generation rate is maximum, while further into the solar cell the generation rate becomes nearly constant. Since the incident light consists of a combination of many different wavelengths, the generation rate at each

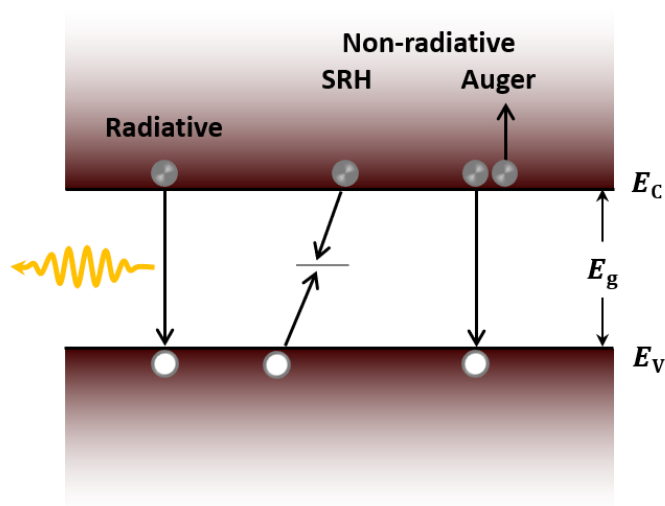


Figure 2.5. Schematic of, from left to right, radiative band-to-band, trap-assisted nonradiative Shockley-Read-Hall (SRH), and non-radiative Auger recombination.

wavelength is different, and therefore the net generation is the sum of the generation for each wavelength.

Low exciton binding energy

Exciton binding energy determines whether the primary charges are free carriers or bound as excitons (electron-hole pairs). Due to their high dielectric constant,⁶⁸ organic-inorganic metal-halide perovskites have low exciton binding energy, which results in an ultra-fast and spontaneous exciton dissociation upon light absorption and consequently a balanced high population of free charge carriers (both electrons and holes).^{48,49}

Using a high magnetic field, the exciton binding energy of MAPI was measured to be only 16 ± 2 meV at low temperature and even smaller (a few millielectronvolts) at room temperature.^{48,49} Additionally, femtosecond pumped transient THz spectroscopy revealed that free charge carriers in MAPI thin films are generated within 2 ps, indicative that the absorption essentially generates free carriers.⁶⁹

Low charge recombination rate

After being generated, a free charge carrier can recombine with another charge carrier of the opposite type. There are three kinds of recombination in the bulk of a semiconductor: radiative band-to-band, non-radiative Shockley-Read-Hall (SRH), and non-radiative Auger recombination (Figure 2.5). Upon band-to-band recombination, an electron from the conduction band recombines with a hole in the valence band and releases a photon with an energy equal to the bandgap. Therefore, it is radiative and dominates in semiconductors with direct bandgaps. Band-to-band recombination, which involves two particles, is bimolecular.

SRH occurs through defects in the crystal lattice of the material. An electron (hole), which is trapped by a defect-induced energy state located in the bandgap (energetically), can non-radiatively recombine with a trapped hole (electron) at the same energy state. SRH

recombination is monomolecular recombination and dominates at low charge carrier densities. Those traps which are located near any either of two band edges (conduction band minimum and valence band maximum) are called shallow traps and are less likely to cause SRH recombination because the trapped electron (hole) is more likely to be re-emitted to the conduction (valence) band. By contrast, near mid-gap (deep) traps are very effective for SRH recombination. Upon Auger recombination, the energy of electron-hole recombination is given to another electron (hole) in the conduction (valence) band rather than emitting a photon. This electron (hole) thermalizes back to the conduction (valence) band edge. Auger recombination, which involves three particles, is trimolecular and dominates at high charge carrier densities.

Perovskite semiconductors have shown all three recombination pathways.⁷⁰ However, the charge recombination rates are surprisingly low in these materials. An excellent experimental work revealed that the monomolecular recombination rate ranges between 5 and 15 μs^{-1} for metal-halide perovskites, which is indicative of low trap- or impurity-assisted recombination in contrast with other commonly used materials such as GaAs.^{52,71}

Long charge carrier diffusion length

Low non-radiative recombination rates of metal-halide perovskites are associated with long lifetimes and are consistent with long electron-hole diffusion lengths. Diffusion length (L_D) is a distance that a free photogenerated charge carrier (electron or hole) travels inside a semiconductor before recombining. Mobility (μ) and lifetime (τ) of a free charge carrier are the main factors in determining the diffusion length, such that:

$$L_D = \sqrt{\frac{\mu k_B T}{q}} \cdot \tau \quad 2.4$$

where k_B is the Boltzmann constant, q is the electron charge, and T is the sample temperature. As discussed earlier, the absorption coefficient (α) is a factor to determine the required minimum thickness of the absorber layer of a solar cell device. The diffusion length of the free charge carriers, on the other hand, sets an upper limit to the thickness such that, $1/\alpha < d < L_D$.

The charge carrier diffusion length of metal-halide perovskite semiconductors is estimated (experimentally and theoretically) to be of the order of microns, while their absorption coefficient requires their minimum thickness to be only several hundreds of nanometers.^{50,52,72} More importantly, the diffusion length for electrons and holes is well-balanced, which is essential for extracting both carriers efficiently in thin film solar cell configurations.⁷³ Therefore, from this perspective, perovskite semiconductors are excellent absorbers for solar cell applications. Experimental results, validated with density functional theory (DFT) calculation, show that the charge carrier diffusion length exceeds 10 μm with an associated lifetime of $\sim 1 \mu\text{s}$.^{21,72} Related to the carrier diffusion lengths is the charge carrier mobility. Although theoretical calculations estimate high values for mobilities of charge carriers in perovskite, comparable to those of crystalline inorganic semiconductors,

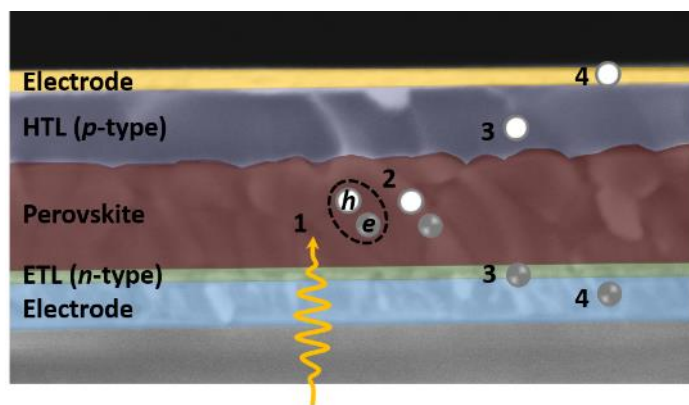


Figure 2.6. Schematic of the physical processes in a $p-i-n$ perovskite solar cell: (1) absorption of photons, (2) generation of free charge carriers, (3) selective extraction of charges, and (4) collection of charges by the contacts.

experimental values derived from different characterization methods, such as Hall effect,⁵¹ field-effect transistors,⁷⁴ and time of flight,⁷⁵ are not always coherent.

The unbalanced transport of free carrier in most semiconductors is due to different effective masses of electrons and holes (m_e^* and m_h^*). Startlingly, free electrons and holes in metal-halide perovskite semiconductors are evidenced to have similar effective masses ($m_e^* = 0.23 m_0$ and $m_h^* = 0.29 m_0$) that leads to their balanced transport.⁷⁶ These values, which are estimated for MAPI including spin-orbit coupling effects, are slightly greater than the theoretical values ($m_e^* = 0.12 m_0$ and $m_h^* = 0.15 m_0$).⁷⁷ The slightly larger hole's effective mass compared to electron, leads to its slightly shorter diffusion length (lower mobility).

2.2. Application of metal-halide perovskites in solar cells

Tunable bandgap, high absorption coefficient, low exciton binding energy, low non-radiative recombination rates, high charge carrier mobilities, and long diffusion length are all superior optoelectronic properties making organic-inorganic metal-halide perovskites excellent candidates as the absorber layer in solar cell configurations, which is the focus of the following section.

2.2.1. Working principles of perovskite solar cells

A PSC is a $p-i-n$ (or $n-i-p$) junction consisting of a metal-halide perovskite as the intrinsic (i) semiconductor sandwiched between two doped selective layers: a p -type and an n -type semiconductor. As illustrated in Figure 2.6, the operational principle of a PSC includes four basic attributes: (i) photon absorption by perovskite absorber layer, (ii) ultra-fast spontaneous exciton dissociation into free charge carriers (electrons and holes), (iii) charge extraction through selective layers (p and n layers), and (iv) charge collection at respective electrodes.

Charge Extraction

As discussed earlier, photon absorption in perovskite semiconductors leads to generation of free carriers. Therefore, in contrast to organic and dye-sensitized solar cells, PSCs do not

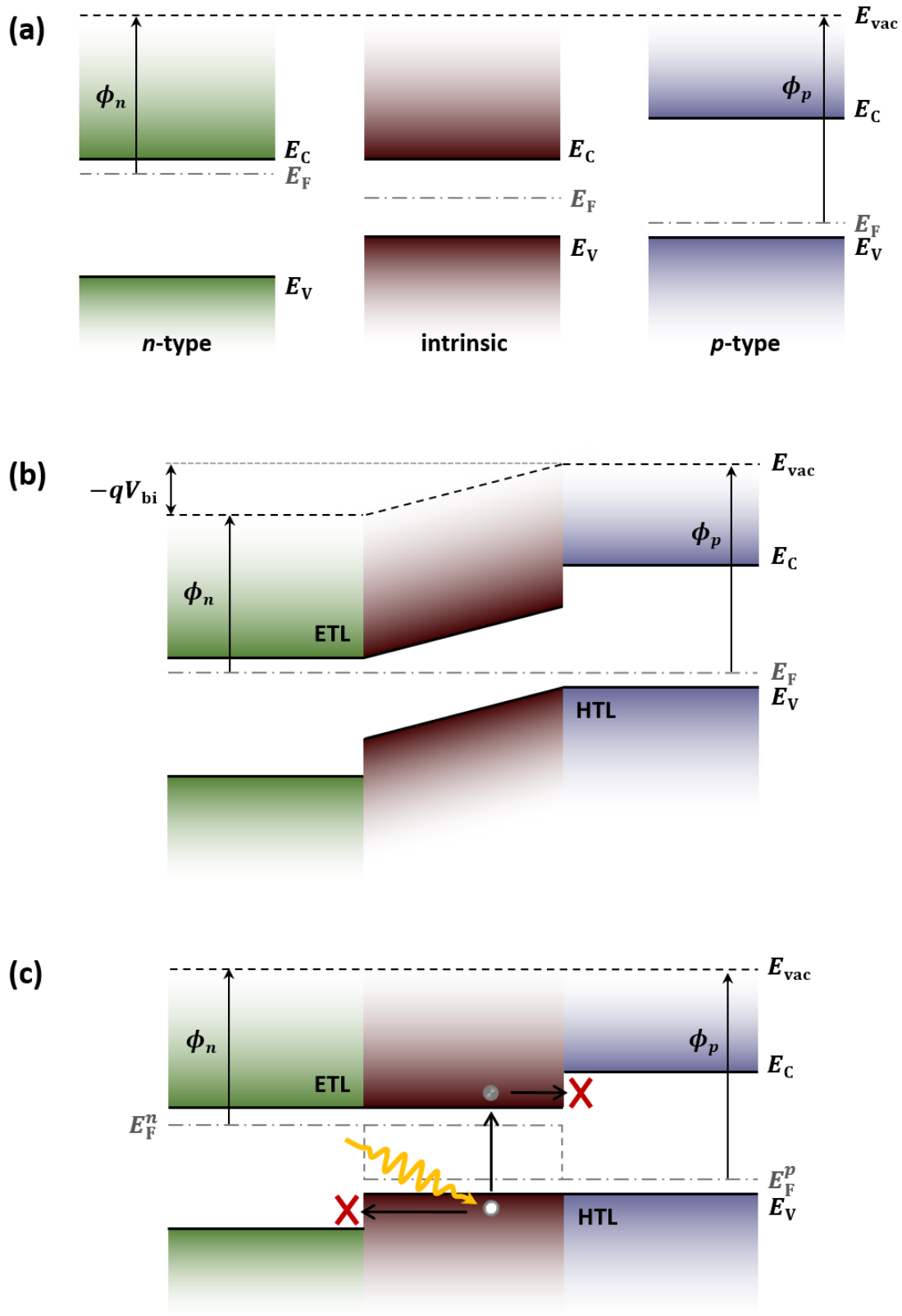


Figure 2.7. Schematic model of energy levels of an *n*-type (with a low work function ϕ_n), an intrinsic, and a *p*-type (with a high work function ϕ_p) semiconductor in (a) isolation and when connected as a *p-i-n* heterojunction (b) in equilibrium (in the absence of light and bias voltage), (c) upon illumination at open circuit condition.

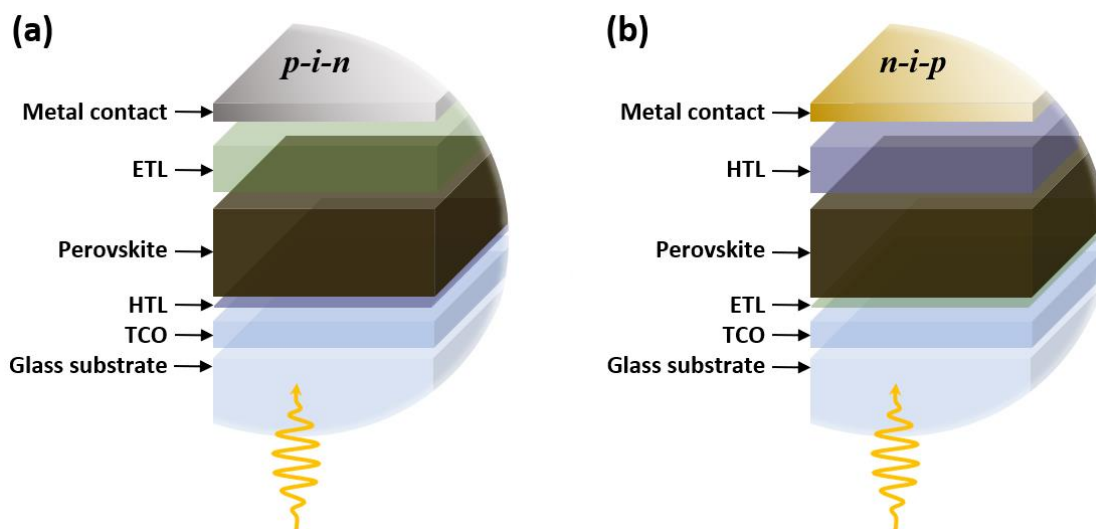


Figure 2.8. Schematic illustration of single-junction perovskite solar cells with typical (a) $p-i-n$ and (b) $n-i-p$ structures.

require heterojunction interfaces to dissociate the electron-hole pair. However, the n -type and p -type selective layers in Figure 2.6, which are often termed as electron transport layer (ETL) and hole transport layer (HTL), respectively, act to modify the electrodes' work functions and assist in efficient extraction of free charge carriers by reducing the electrode-junction potential barriers. Figure 2.7a illustrates the energy levels of an n -type, an intrinsic (perovskite), and a p -type semiconductor in isolation. When connected as a $p-i-n$ solar cell in equilibrium (in the absence of light and biased voltage), Fermi levels of n and p layers align across each other at the same height. The difference in the work functions of the n and p selective layers (ETL and HTL) build a built-in field (qV_{bi}) across the active layer (perovskite) which acts as a driving force for charge carrier extraction (Figure 2.7b).

However, upon illumination (Figure 2.7c) electrons in the perovskite layer are promoted from E_V to E_C . The light causes the Fermi level to split into two separate Fermi levels, so-called quasi-Fermi levels for the electrons (E_F^n) and holes (E_F^p). This light-induced quasi-Fermi level separation creates a photovoltage, which is equal to the difference between the two quasi-Fermi levels. At open-circuit condition (not connected to an external load) this photovoltage defines the maximum voltage of a photovoltaic device (V_{OC}). At the open-circuit condition, the conduction and valence bands of the semiconductor shift and create an equilibrium (flat bands). When connected to an external circuit, separated electrons and holes are selectively extracted from perovskite by ETL and HTL, respectively, and finally collected at the electrodes.

Band-alignment engineering at the ETL/perovskite and perovskite/HTL plays a prominent role in efficient charge extraction (or charge blocking) and affects the performance of the resulting PSC.^{78,79} An ETL with a shallower conduction band (HTL with deeper valence band) than that of the perovskite semiconductor acts as a potential barrier, and therefore hampers electron (hole) extraction at the ETL/perovskite (HTL/perovskite) interface. While electrons (holes) will be extracted effortlessly if the conduction band (valence band) of ETL

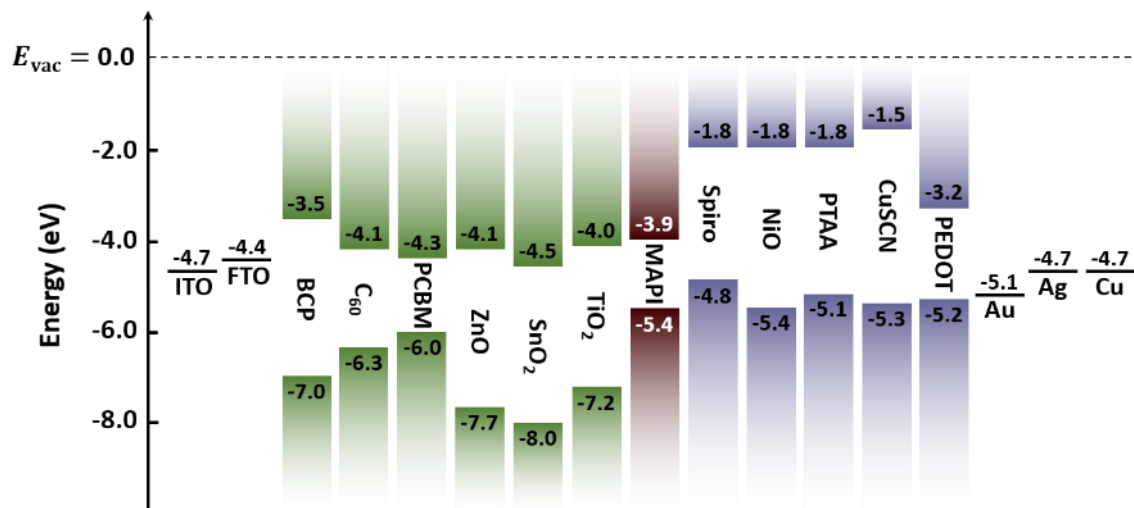


Figure 2.9. The band diagrams of the most common ETLs (green bars) and HTLs (blue bars) as well as transparent front (ITO, FTO) and metal back (Au, Ag, Cu) electrodes, compared to the archetypal MAPI perovskite.

is deeper (shallower) than that of the perovskite semiconductor. Additionally, ETLs and HTLs also play the role of blocking charges of the opposite types. As illustrated in Figure 2.7c, an ETL with a deeper valence band (an HTL with shallower conduction band) than that of the perovskite semiconductor acts as a potential barrier and effectively blocks holes (electrons) preventing them from recombination at the ETL/perovskite (HTL/perovskite) interface. Therefore, from an energetic perspective, ideal ETLs (HTLs) are those with deeper (shallower) conduction and valence bands.^{78,79} Here, shallower and deeper bands are compared to the vacuum energy level (E_{vac}).

***P-i-n* and *n-i-p* single-junction perovskite solar cells**

Depending on the order of the stacked layers, a typical single-junction PSC has two common structures (Figure 2.8): *n-i-p* (standard) and *p-i-n* (inverted). A transparent conductive oxide (TCO) is typically used as the front electrode, while a metal electrode (gold (Au), silver (Ag), or copper (Cu)) is used as the back contact. The most common TCOs, ETLs, HTLs, and metal contacts as well as their band diagrams are illustrated in Figure 2.9. As shown in this figure, SnO₂ and TiO₂, which are the most common ETLs in *n-i-p* structures, have significantly deeper valence band maximums than the archetypal MAPI, which means they are very good hole blockers. On the other side, the most common HTLs like spiro, NiO, and PTAA with remarkably shallower conduction band minimums are very good electron blockers. C₆₀ is the most common ETL in a *p-i-n* structure that is usually coated with a thin layer (~3 nm) of BCP atop as a hole blocker at the ETL/metal contact interface and avert recombination at this interface.

2.2.2. Photovoltaic characteristics of a solar cell

Current-density–voltage characteristics

In its simplest way, a solar cell is modeled by an electrically equivalent circuit composed of a single-diode in parallel with a current source, which is the photogenerated current under

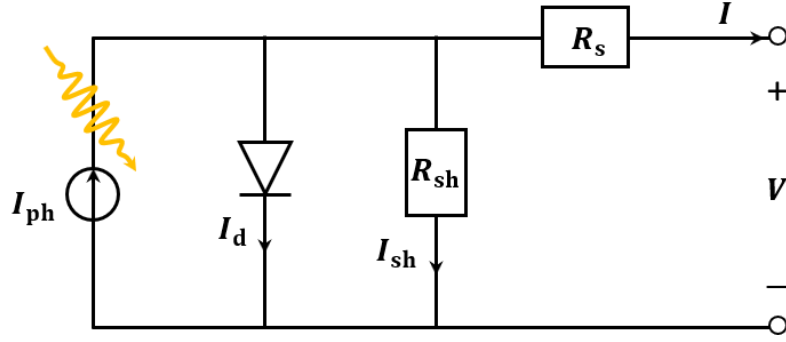


Figure 2.10. An equivalent scheme of a solar cell based on a single-diode model.

sunlight illumination (Figure 2.10).⁸⁰ Furthermore, a shunt (R_{sh}) and a series (R_s) resistance are added to represent any leakage current path due to imperfections and electrical resistance of the solar cell, respectively. The current produced by this circuit (equivalent to the current produced by the solar cell) is equal to photogenerated current (I_{ph}) and dark current of a diode (I_d) determined by the Shockley diode equation and shunt current (I_{sh}) determined by Ohm's law:

$$I = I_{ph} - I_d - I_{sh} \quad 2.5$$

Minus in Equation 2.5 shows that I_d and I_{sh} are in the opposite direction. Considering the active area of the solar cell (A), the output current density ($J = I/A$) of this circuit is then given by:

$$J = J_{ph} - J_d - J_{sh} \quad 2.6$$

$$J(V) = J_{ph} - J_0 \left[\exp\left(\frac{q(V + J(V) A R_s)}{n k_B T}\right) - 1 \right] - \frac{V + J(V) A R_s}{R_{sh}} \quad 2.7$$

where J_0 is the dark saturation current density, n is the ideality factor of the diode, q is the electron charge, k_B is the Boltzmann constant and T is temperature. The current-density–voltage (J – V) characteristics of an ideal solar cell are approximated assuming that the effects of parasitic resistances are neglected ($R_s = 0$ and $R_{sh} \rightarrow \infty$). Hence, Equation 2.7 is simplified to:

$$J(V) \approx J_{ph} - J_0 \left[\exp\left(\frac{q V}{n k_B T}\right) - 1 \right] \quad 2.8$$

If the applied voltage is zero ($V = 0$), the current flowing through the solar cell (so-called short-circuit current (J_{sc})) is $J(0) = J_{sc} \approx J_{ph}$. This is the maximum current a solar cell can produce. At open-circuit condition ($V = V_{oc}$) no current is flowing through the solar cell ($J = 0$) and therefore:

$$J(V_{oc}) \approx J_{ph} - J_0 \left[\exp\left(\frac{q V_{oc}}{n k_B T}\right) - 1 \right] = 0 \quad 2.9$$

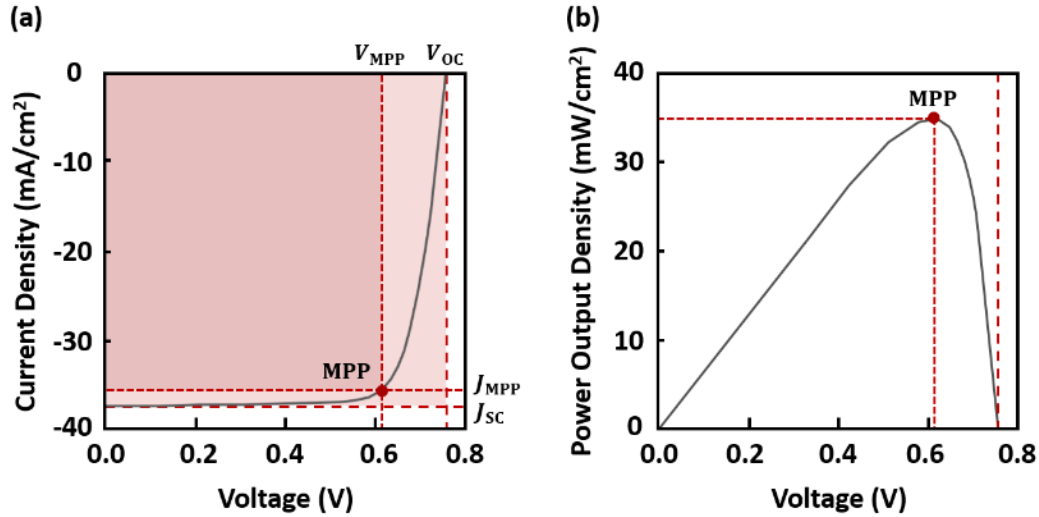


Figure 2.11. (a) typical current-density–voltage (J – V) characteristics. (b) Corresponding power output density of a solar cell under illumination. Denoted are the short-circuit current (J_{SC}), the open-circuit voltage (V_{OC}), as well as current-density (J_{MPP}) and voltage (V_{MPP}) at maximum power point (MPP).

Hence, open-circuit voltage (V_{OC}) can be approximated by:

$$V_{OC} \approx \frac{n k_B T}{q} \ln \left(\frac{J_{ph}}{J_0} + 1 \right) \quad 2.10$$

here the (+1) term can be neglected because the V_{OC} of PSCs is typically large (in the range of several hundreds of microvolts).

The J – V characteristics determine the performance of a solar cell. Figure 2.11 shows typical J – V characteristics and the corresponding generated power output density of a solar cell. The generated power density of a solar cell is given by $P = JV$. It is apparent that at short-circuit ($V = 0$) and open-circuit ($J = 0$) conditions no power is extracted from a solar cell. However, power output density reaches its maximum at an operating optimum point referred to as maximum power point (MPP), where the product of the current and voltage is maximum, therefore:

$$P_{MPP} = J_{MPP} V_{MPP} \quad 2.11$$

Fill factor (FF) is defined as a proportionality constant describing the ratio between $V_{MPP} J_{MPP}$ and $V_{OC} J_{SC}$:

$$FF = \frac{J_{MPP} V_{MPP}}{J_{SC} V_{OC}} < 1 \quad 2.12$$

This equation determines the squareness of the J – V characteristics (the ratio of the dark red and the light red rectangles in Figure 2.11a). The influence of R_s and R_{sh} on the J – V characteristics is shown in Figure 2.12. It is apparent that these resistances influence FF significantly. Therefore, FF can be a measure of imperfections in a solar cell, such that a solar cell with lower FF suffers from high R_s and low R_{sh} .

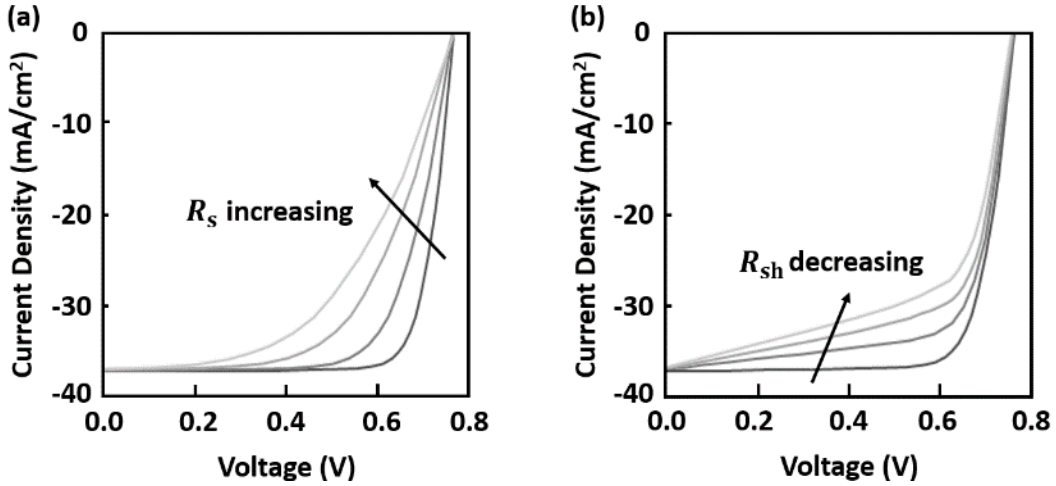


Figure 2.12. Effect of series and shunt resistances on the J - V characteristics of a solar cell. For the dark gray curves $R_s = 0$ (a) and $R_{sh} \rightarrow \infty$ (b).

The power conversion efficiency (PCE), which is the most important characteristic of a solar cell, is the power density at MPP as a fraction of the incident light power density:

$$\text{PCE} = \frac{P_{\text{MPP}}}{P_{\text{incident}}} \quad 2.13$$

Based on this equation, the PCE of a solar cell depends on the power and the spectrum of the incident light. Therefore, to facilitate an accurate comparison between efficiencies of different solar cells a well-defined standard test condition (STC) is required for measuring the J - V characteristics (see Section 3.2.2).

The J - V characteristics (Figure 2.11 a) is determined by sweeping an applied bias across the terminals of a solar cell over a predetermined voltage range and measuring the current flowing through the external circuit, while the solar cell is exposed to an ‘AM1.5G’ spectrum at 25 °C. The ‘AM1.5G’ spectrum with an integrated power density of 1000 W/m² is the standard spectrum, which simulates the sun’s radiation at the earth’s surface (Figure 2.13a). G stands for global and AM1.5 stands for air mass, which quantifies the reduction in the power of the sunlight as traveling through the atmosphere before reaching the earth’s surface at an angle of 48.2° (Figure 2.13b). Therefore, the PCE is commonly expressed as a percentage of the total incident light power density:

$$\text{PCE} = \frac{P_{\text{MPP}}}{P_{\text{incident}}} = \frac{\text{FF} V_{\text{OC}} J_{\text{SC}}}{100 \text{ mW/cm}^2} \quad 2.14$$

Hysteresis in the J - V characteristics of perovskite solar cells

The J - V characteristics of a PSC exhibit different responses depending on the scan direction, forward scan (from the short-circuit to open-circuit condition), and backward scan (from open-circuit to short-circuit condition). The difference is mainly observed in FF and sometimes V_{OC} that manifest as *hysteresis* in the J - V characteristics (Figure 2.14a).

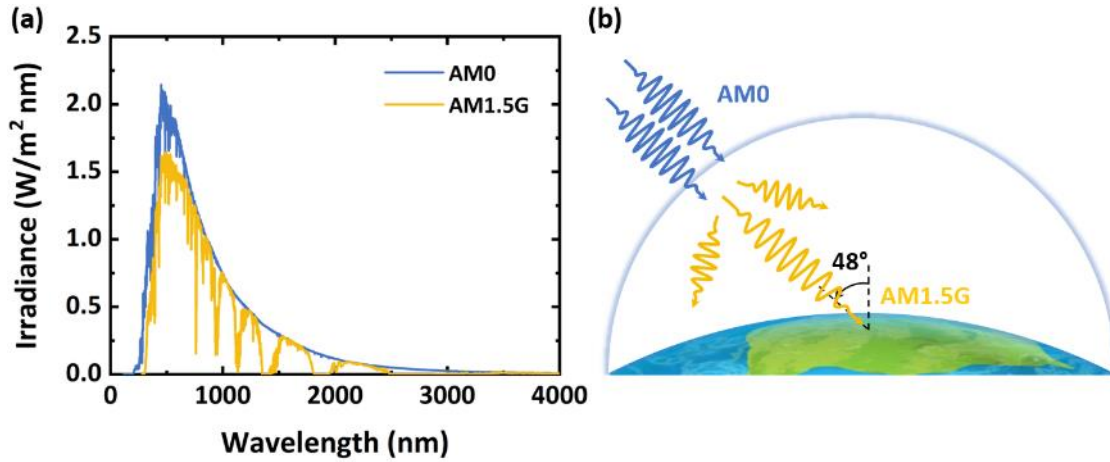


Figure 2.13. (a) Radiation of air-mass (AM) spectra. (Excel data from Wikipedia. Accessed on 2020.12.15) (b) An illustration of the definition of air-mass AM spectra. AM0 spectrum with an integrated power density of 1353 W/m² is measured outside the earth's atmosphere, while AM1.5G with an integrated power density of 1000 W/m² is measured at the earth's surface.

Therefore, determining the MPP and consequently the PCE of a solar cell from the J - V characteristics is problematic in the presence of hysteresis. In this case, deriving a stabilized power output from an MPP tracking measurement (Figure 2.14b) together with the J - V characteristics provides a more reliable understanding of the performance of a PSC. To quantify hysteresis, determining the hysteresis factor ($F_{\text{Hys}} = \frac{PCE_{\text{BW}} - PCE_{\text{FW}}}{PCE_{\text{BW}}}$) or hysteresis index ($HI = \frac{A_{\text{FW}}}{A_{\text{BW}}}$), are common. PCE_{FW} , PCE_{BW} , A_{FW} , and A_{BW} are the PCEs extracted from forward and backward scans and the area under each, respectively.

Hysteresis is known to be a property of perovskite absorbers.⁸¹ There is a growing consensus that this phenomenon is governed by ion migration in the perovskite absorber layer, although an experimental direct proof is still missing.⁸² Ion migration cause accumulation of ions at the interfaces of perovskite and the charge transport layers (ETL and HTL). Accumulation of the ions can introduce trap states at these interfaces and accordingly hamper the charge extraction and reduce the FF of a PSC. Furthermore, the charge transport layers which are not selective efficiently (extracting *and* blocking), can cause surface recombination and therefore hysteresis can also affect V_{OC} .⁸³ This highlights the importance of the energy band alignment of perovskite and the charge transport layers, as well as quality of the interfaces.⁸⁴

External quantum efficiency

The external quantum efficiency (EQE), or incident photon-to-electron conversion efficiency (IPCE), is the ratio of the photogenerated electrons in a solar cell (at short-circuit condition) to the number of incident photons at a specific wavelength. Therefore, the integration of EQE is used to calculate the maximum current available by a solar cell (J_{SC}):

$$J_{\text{SC}} = q \int_{\lambda_1}^{\lambda_2} \text{EQE}(\lambda) \phi_{\text{AM1.5G}}(\lambda) d\lambda \quad 2.15$$

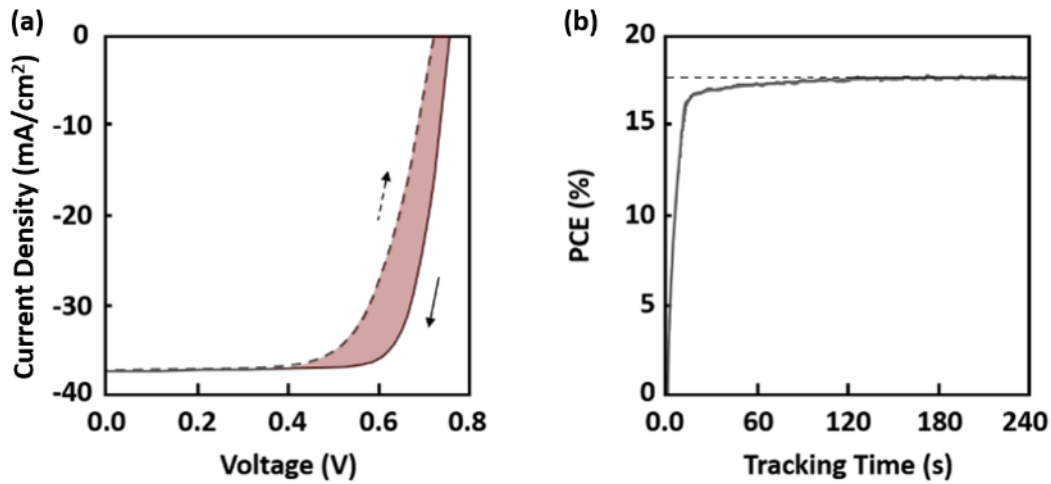


Figure 2.14. For a perovskite solar cell, (a) typical J - V characteristics measured from short-circuit to open-circuit (forward scan) and from open-circuit to short-circuit (backward scan) with a pronounced hysteresis. The colored area in (a) represents the discrepancy between forward and backward scans. (b) a typical power conversion efficiency as a function of time.

where q is the electron charge, $\phi_{\text{AM1.5G}}$ is the wavelength-dependent photon flux of the solar spectrum (AM1.5G) per unit area at wavelength (λ). A typical EQE spectrum is shown in Figure 2.15. Analyzing this spectrum over different wavelength regions provides us with information about optical (parasitic absorption) and electronic (recombination) losses.

Limited EQE in shorter wavelengths indicates that only small fractions of the photons with shorter wavelengths are absorbed by the absorber layer and converted into excitons (electron-hole pairs), which could be due to reflection losses at the interfaces and/or parasitic absorption by the layer stack prior to the absorber layer, such as the TCO front electrode, the ETL (in n - i - p structures), and/or the HTL (in p - i - n structures). Reduced EQE in longer wavelengths indicates incomplete absorption that occurs when the absorption depth ($1/\alpha$) exceeds the optical thickness of the absorber layer, and therefore photons with longer wavelength leave the absorber before they can be absorbed (see Section 2.1.3). In addition to the optical loss mechanisms, short carrier diffusion length compared to the absorber thickness and/or surface recombination will limit the EQE spectrum to lower values.

2.2.3. Theoretical efficiency limit of a single-junction solar cell

Shockley and Queisser calculated an energy conversion efficiency limit (termed SQ limit) for a single-junction solar cell as a function of the bandgap of the absorber layer (Figure 2.16), assuming:

- (i) 100% absorption of all the photons with $h\nu \geq E_g$
- (ii) 0% absorption of all the photons with $h\nu < E_g$
- (iii) 100% electron/hole generation upon absorption
- (iv) 100% collection of all the photogenerated electrons and holes
- (v) Only radiative recombination

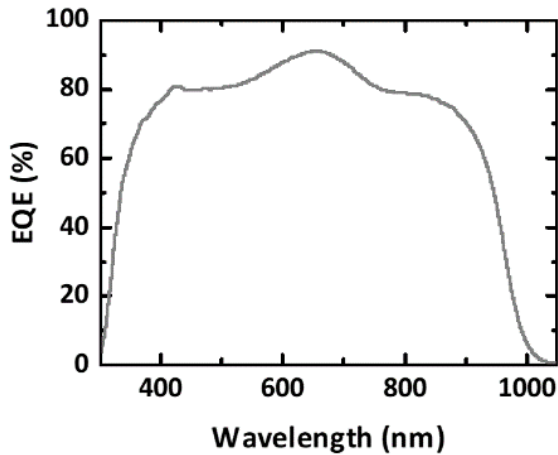


Figure 2.15. External quantum efficiency spectrum of a typical perovskite solar cell with a narrow-bandgap of 1.26 eV.

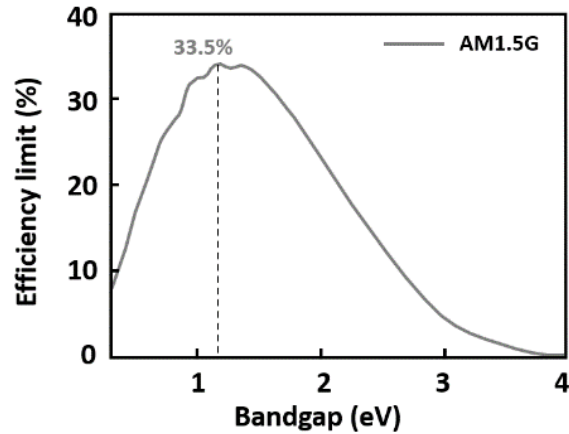


Figure 2.16. Shockley-Queisser limit for conversion efficiency of a single-junction solar cell under AM1.5G spectrum.

This model is known as the detailed balance limit model, which was first proposed by Shockley and Queisser in 1961.⁸⁵ According to this model, if radiative recombination is *only a fraction* of all the recombination, the efficiency is reduced below the SQ limit. In addition to radiative recombination losses, the model also considers the thermalization losses (which occur for the photons with energies larger than the bandgap) and the optical losses (occurring for the photons with energies smaller than the bandgap).⁸⁶ Figure 2.16 depicts the SQ efficiency limits as a function of bandgap, which reaches a maximum value of 33.5% (at ~ 1.1 eV).

Although a PCE of 25.2% is certified for PSCs to date,⁸⁷ it is still lower than the SQ limit. The foremost reason for the efficiency distance for a given bandgap is losses in V_{OC} and FF, which is mainly caused by defect-induced non-radiative SRH recombination in the bulk of the perovskite (see Section 2.1.3) and interface non-radiative recombination losses emanating from all of the interfaces involved in the PSC.⁷⁰ Based on the detailed balance model, any non-radiative recombination will reduce the efficiency below the SQ limit. Therefore, strategies to suppress the non-radiative recombination channels are of most interest in the field. The list of all the proposed strategies so far is too long and beyond the scope of this thesis. Reference [70] is a very detailed review that provides comprehensive discussions in this matter for interested readers.

2.3. Tandem solar cells

Based on the SQ model, if the absorber's bandgap of a single-junction solar cell is too wide, the optical losses will increase, and if it is too narrow the thermalization losses will dominate. Utilizing two absorber layers with different optical bandgaps in a tandem configuration provides a route to minimize these losses and accordingly surpass the SQ limit. As schematically illustrated in Figure 2.17a, if a tandem configuration is exposed to the light, first, the top absorber with a wide-bandgap (E_g^W) absorbs all the photons with $h\nu \geq E_g^W$, while transmitting all the other photons with $h\nu < E_g^W$. Then, the bottom absorber with a narrow-

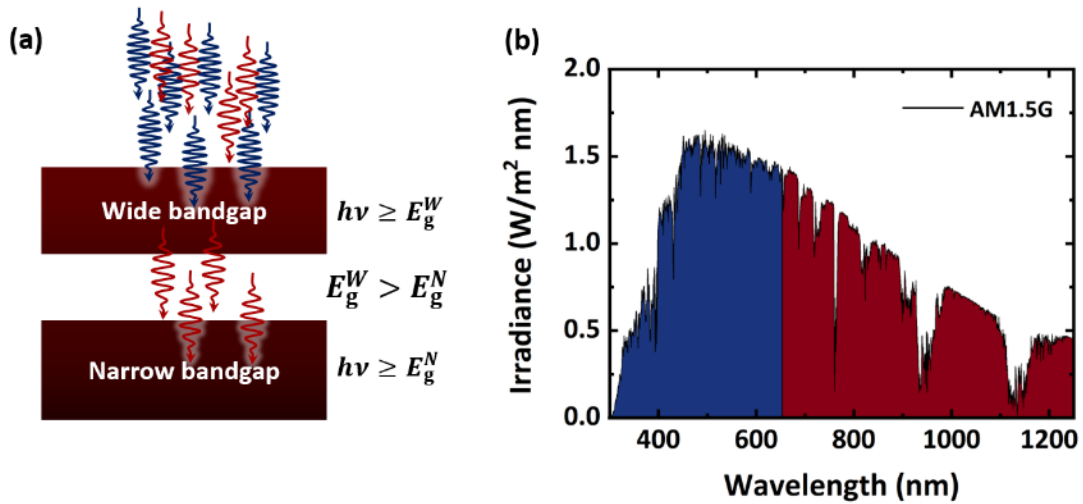


Figure 2.17. (a) Schematic illustration of a tandem configuration composed of two absorbers with wide and narrow-bandgaps ($E_g^W > E_g^N$). (b) AM 1.5G spectrum, and the corresponding absorption fraction absorbed by the wide-bandgap (blue) and the narrow-bandgap (red) absorber layers of a typical tandem configuration.

bandgap ($E_g^N < E_g^W$) absorbs all the transmitted photons with ($h\nu \geq E_g^N$). Therefore, a wide-bandgap absorber reduces the thermalization losses while the narrow-bandgap absorber improves the utilization of the solar spectrum. This very simple but smart idea can improve the SQ limit, such that the calculated maximum efficiency of a tandem solar cell with $E_g^W = 1.9 \text{ eV}$ and $E_g^N = 1.0 \text{ eV}$ under AM1.5G is 42.3%. For such a tandem solar cell the spectrum will be absorbed up to $\sim 1240 \text{ nm}$ (Figure 2.17b) with minimum thermalization loss.⁸⁸

Four-terminal (4T) and two-terminal (2T) tandem solar cells (Figure 2.18) are the most common tandem configurations, while each has advantages and disadvantages. Sub solar cells of a 4T configuration are fabricated separately and then stacked mechanically, while the top solar cell of a 2T configuration is fabricated atop the bottom solar cell. Therefore, the maximum achievable PCE of a 2T tandem solar cell highly depends on the current matching between the two solar cells which are connected in series. That limits the range of the bandgap selection for each sub solar cell. In contrast, current matching is not an issue for a 4T configuration, and therefore they are less restricted to the bandgap selection and deliver relatively higher efficiencies compared to their 2T counterparts.²⁰ Although the top and bottom solar cells in a 4T tandem configuration work independently, they are optically interlinked such that the optical losses (particularly in longer wavelength) in the layer stack of the top solar cell can directly influence the performance of the bottom solar cell and accordingly the total performance of the tandem solar cell. Thus, to minimize the optical losses in a 4T configuration implementing TCOs with nearly zero parasitic absorption and an intermediate light coupling layer between the two sub solar cells are required.

2.3.1. All-perovskite tandem solar cells

As discussed in Section 2.1, the bandgap of metal-halide perovskite semiconductors is tunable. Hence, they are excellent choices for both top and bottom absorbers of a tandem solar cell. Since replacing Pb with Sn in the B-site can reduce the bandgap down to very low

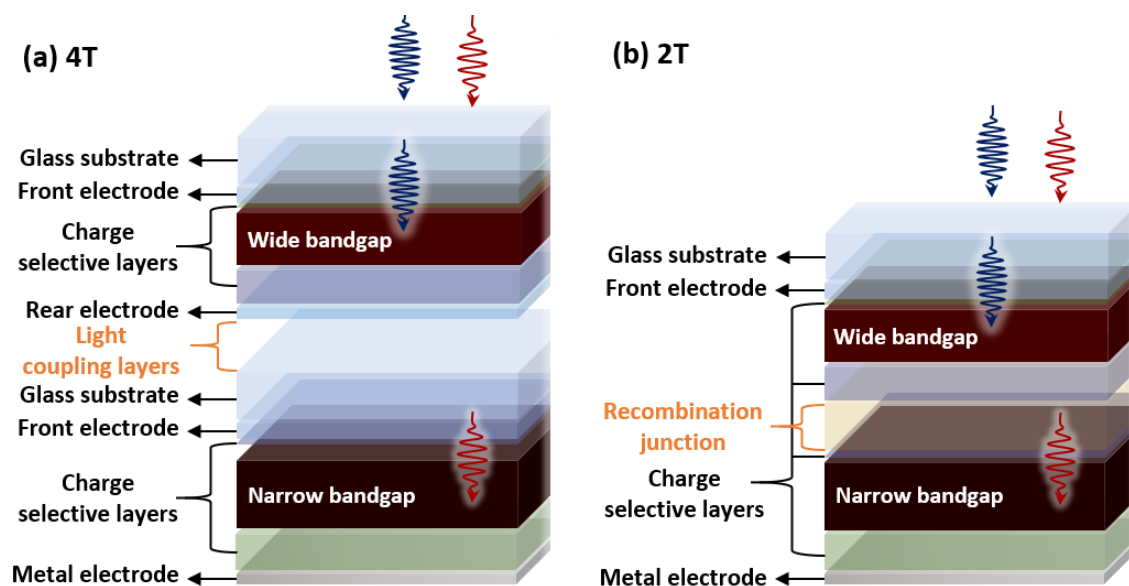


Figure 2.18. Schematic illustrations of tandem solar cell with a (a) 4T and (b) 2T structure.

values (1.10-1.5) and substituting I with Br in the X-site of a Pb-based perovskite semiconductor can increase the bandgap (1.5-2.3 eV), an all-perovskite tandem solar cell (all-PTSC) is composed of a pure-Pb mixed halide perovskite and a mixed Sn/Pb halide perovskite as the absorber layers of the top and bottom solar cells, respectively.

Although utilizing a tandem configuration provides a path to further exploiting the potential of perovskites, all-PTSCs experience a set of challenges compared to a single-junction PSC. On the one hand, Sn, which is used to achieve narrow-bandgap perovskites is prone to oxidation (from Sn^{2+} to Sn^{4+}). This results in a degradation of optoelectronic performance of the narrow-bandgap perovskite and hinders both efficiency and stability of the narrow-bandgap PSCs. On the other hand, wide-bandgap perovskites tend to form a high density of deep traps and therefore suffer from voltage losses. Moreover, a high ratio of Br in wide-bandgap perovskites causes poor photo-stability due to halide segregation. Despite all these challenges, with recent advances, all-PTSCs have attained high certified PCEs of 25% and 23.1% for 4T and 2T configuration, respectively.²¹

3. Materials and Characterization Methods

This chapter includes two sections. First section presents the materials and deposition methods (spin-coating, thermal evaporation, and sputtering) we used for fabricating the perovskite solar cells and thin films. Second section describes the experimental methods we applied for characterizing the perovskite solar cells and thin films, including ellipsometry, spectrophotometry, photoluminescence spectroscopy, X-ray diffraction, X-ray photoelectron spectroscopy, scanning electron microscopy, cathodoluminescence, atomic force microscopy, profilometer measurement, four-point probe measurement, and Hall-effect measurement (for thin films) as well as current-density–voltage characteristics, maximum power point tracking measurement, external quantum efficiency, ideality factor, and thermally stimulated current (for perovskite solar cell devices).

3.1. Materials and deposition methods

This section addresses the material and deposition techniques used for preparing the perovskite solar cells (PSCs) and thin films in this thesis. Figure 3.1 illustrates the deposition sequence of the PSCs with (i) *n-i-p* structures with pure-Pb perovskite absorber layers, which are prepared with two different back contacts including metal back electrodes (Figure 3.1a) and in-house sputtered transparent conductive oxide (TCO) rear electrodes, denoted as semi-transparent PSCs (Figure 3.1b) as well as (ii) *p-i-n* structures (Figure 3.1c) with mixed Sn/Pb absorber layers, denoted as narrow-bandgap PSCs. The semi-transparent Pb-based PSCs and narrow-bandgap Sn/Pb-based PSCs are used as the top and bottom PSCs in four-terminal all-perovskite tandem solar cell (4T all-PTSC) configurations in Chapters 5 and 6. In the following, we explain the preparation of the solutions for the charge transport and perovskite absorber layers.

3.1.1. Solution preparation

Preparation of electron transport solutions

Nanoparticles of TiO₂ (np-TiO₂) solution were prepared through a chemical synthesis from the following recipe. In a glovebox, add 4.5 mmol of titanium (IV) chloride (TiCl₄; Acros Organics) dropwise to 2 ml of anhydrous ethanol (EtOH; Acros Organics) solution. Stir the

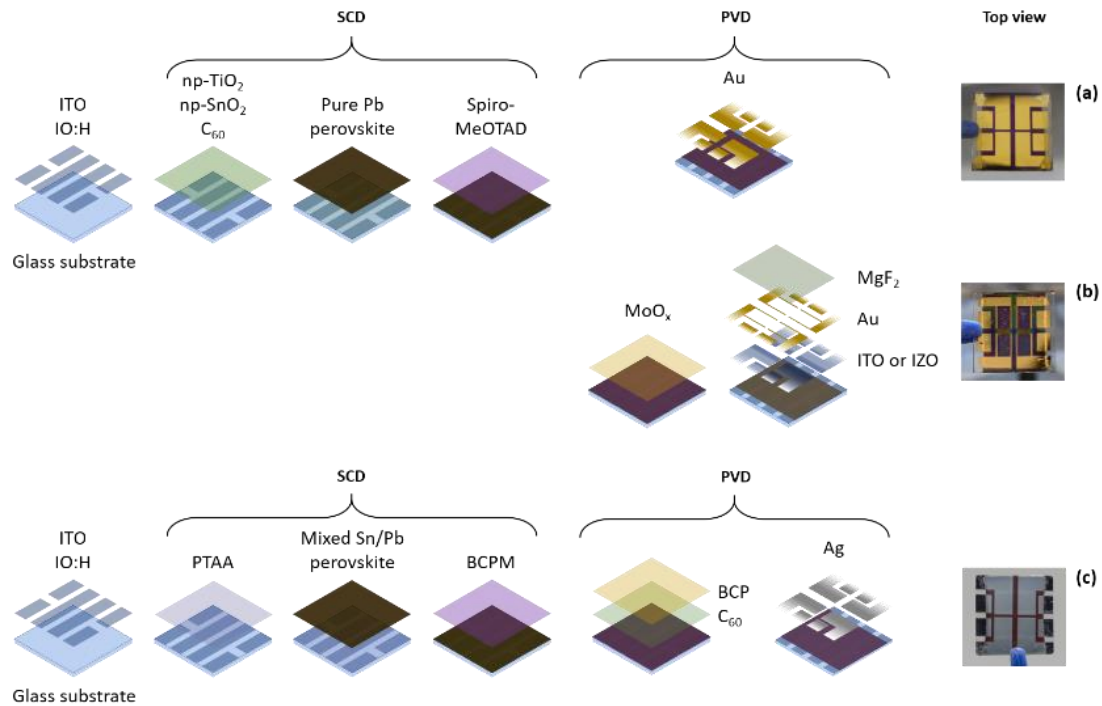


Figure 3.1. Preparation sequence and deposition methods for fabrication of PSCs and their top views with three different structures: (a) *n-i-p* PSC, (b) *n-i-p* semi-transparent PSCs, and (c) *p-i-n* narrow-bandgap PSCs. SCD and PVD stand for spin-coating deposition and physical vapor deposition, respectively.

resulting mixture continuously, afterward add 10 mL of benzyl alcohol (BnOH; Acros Organics) to the solution. Upon continuous heating at ~ 70 °C for 16 h, a slightly hazy solution is obtained. After cooling down, transfer 4 mL of the solution to a 50 mL centrifuge tube. Add 10 ml of diethyl ether (Et₂O; Honeywell) to the tube for precipitation of np-TiO₂ and centrifuge at 8000 rpm for 3 min. Wash the np-TiO₂ with 10 ml of EtOH while stirring the centrifuge tube to disperse the np-TiO₂ in EtOH. Repeat the last step (Et₂H and EtOH) two more times. In the last cycle, add EtOH and 12 ml of 1-butanol (Sigma Aldrich) to disperse the np-TiO₂. Finally, add 180 μ l of titanium diisopropoxide bis(acetylacetonate) (Ti(O-*i*Pr)₂(acac)₂; Sigma Aldrich) in order to prevent the np-TiO₂ from agglomeration. Stir at room temperature for 1 h to obtain a greenish semi-transparent solution.

Nanoparticles of SnO₂ (np-SnO₂) solution were prepared by diluting 15% aqueous colloids of SnO₂ nanoparticles (Alfa Aesar) with distilled water to a concentration of 2.04%.

Buckminsterfullerene (C₆₀) solution was prepared by dissolving 10 mg/ml of C₆₀ (Sigma Aldrich) in 1,2-dichlorobenzene (DCB; Sigma Aldrich, anhydrous) and filtered using a 0.45 μ m PVDF filter.

[6,6]-Phenyl-C61-butyric acid methyl ester (PCBM) solution was prepared by dissolving 5 mg PCBM (Sigma Aldrich) in 1 ml DCB and filtered using a 0.45 μ m PVDF filter.

Preparation of hole transport solutions

2,2',7,7'-tetrakis[N,N-di(4-methoxyphenyl)amino]-9,9'-spirobifluorene (Spiro-MeOTAD) solution was prepared by dissolving 80 mg spiro-MeOTAD (Luminescence Technology) dissolved in 1 ml chlorobenzene (CB, Sigma Aldrich) with the additives 4-*tert*-butylpyridine (4-*t*BP) (28.5 μ l per 1 ml CB) and lithium bis(trifluoromethanesulfonyl)imide (Li-TFSI) (17.5 μ l per 1 ml CB from a 520 mg/ml acetonitrile stock solution).

Poly[bis(4-phenyl)(2,4,6-trimethylphenyl)amine] (PTAA) solution was prepared by dissolving 1.5 mg of PTAA ($M_w = 17,800$ g/mol, EM INDEX) in 1 ml toluene.

Preparation of perovskite solutions

In this thesis, we used perovskite thin films with different compositions, all prepared with following precursors:

Formamidinium iodide (FAI; Dyesol)
Methylammonium bromide (MABr; Dyesol)
Methylammonium iodide (MAI; Dyesol)
Lead iodide (PbI₂; TCI)
Lead bromide (PbBr₂; TCI)
Lead thiocyanate (Pb(SCN)₂, Sigma Aldrich)
Tin iodide (SnI₂; Alfa Aesar)
Tin fluoride (SnF₂, Sigma Aldrich)
Cesium iodide (CsI; Alpha Aesar)
Dimethylformamide (DMF; Sigma Aldrich, anhydrous)
Dimethyl sulfoxide (DMSO; Sigma Aldrich, anhydrous)

In the following, the recipes we used to prepare the perovskite solutions with different compositions are explained.

Cs_x(FA_{0.83}MA_{0.17})_(1-x)Pb(I_{0.83}Br_{0.17})₃

First, by dissolving 1 M FAI, 0.2 M MABr, 1.1 M PbI₂, and 0.2 M PbBr₂ in a 4:1 (v:v) mixture of DMF:DMSO, we prepared a double-cation precursor solution with a stoichiometric formula of FA_{0.83}MA_{0.17}Pb(I_{0.83}Br_{0.17})₃. By adding 42.1 μ l, 88.9 μ l, and 141.2 μ l from a 1.5 M CsI stock solution (in DMSO) into 1 ml of the double-cation FA_{0.83}MA_{0.17}Pb(I_{0.83}Br_{0.17})₃ solution, we achieved the final triple-cation perovskite solution of Cs_x(FA_{0.83}MA_{0.17})_(1-x)Pb(I_{0.83}Br_{0.17})₃ for $x = 0.05$, 0.1 , and 0.15 , respectively. The resulting perovskite thin films were used as absorber layers for the PSCs (Figure 3.1a) in Chapter 4. Perovskite thin films with Cs_{0.1}(FA_{0.83}MA_{0.17})_{0.9}Pb(I_{0.83}Br_{0.17})₃ with a bandgap of 1.62 eV were used as the absorber layer for the semi-transparent PSCs (Figure 3.1b) in tandem configuration in Chapter 6.

Cs_{0.1}(FA_{0.83}MA_{0.17})_{0.9}Pb(I_{0.67}Br_{0.33})₃

First, we diluted FAPbI₂Br (0.87 M FAI, 0.43 M FABr, 0.957 M PbI₂, 0.43 M PbBr₂) and MAPbI₂Br (0.87 M MAI, 0.43 M MABr, 0.957 M PbI₂, 0.43 M PbBr₂) in 4:1 (v:v) mixture of DMF:DMSO, while CsPbI₂Br (0.87 M CsI, 0.43 M CsBr, 0.957 M PbI₂, 0.43 M PbBr₂) was diluted in pure DMSO. Next, by mixing FAPbI₂Br, MAPbI₂Br, and CsPbI₂Br stock solutions with ratios of 0.75%, 15% and 10%, respectively, we formed the final perovskite solution. Perovskite thin films with the composition Cs_{0.1}(FA_{0.83}MA_{0.17})_{0.9}Pb(I_{0.67}Br_{0.33})₃ have a wide-bandgap of 1.73 eV and were used for the PSCs (Figure 3.1a) in Chapter 4.

Cs_{0.17}FA_{0.83}(I_(1-y)Br_y)₃

By dissolving 0.83 M FAI, 0.17 M CsI, and 1.49 M PbI₂ and 0.51 M (for y = 0.17) or 0.64 M PbI₂ and 0.36 M PbBr₂ (for y = 0.24) in a 4:1 (v:v) mixture of DMF:DMSO, we prepared double-cation perovskite solutions with the stoichiometric formulas of Cs_{0.17}FA_{0.83}(I_{0.83}Br_{0.17})₃ or Cs_{0.17}FA_{0.83}(I_{0.76}Br_{0.24})₃, respectively. Perovskite thin films with the compositions Cs_{0.17}FA_{0.83}(I_{0.83}Br_{0.17})₃ and Cs_{0.17}FA_{0.83}(I_{0.76}Br_{0.24})₃ have bandgaps of 1.63 and 1.65 eV and were used as absorber layers for the PSCs (Figure 3.1a) in Chapter 4 and semi-transparent PSCs (Figure 3.1b) in tandem configuration in Chapter 5, respectively.

Cs_x(FA_{0.8}MA_{0.2})_(1-x)Pb_{0.5}Sn_{0.5}I₃

First, we prepared the double-cation FA_{0.8}MA_{0.2}Sn_{0.5}Pb_{0.5}I₃ perovskite precursor solution by dissolving 1.1 M FAI, 0.3 M MAI, 0.7 M SnI₂, 0.7 M PbI₂, 0.008 M Pb(SCN)₂, and 0.045 M SnF₂ in a 9:1 (v:v) mixture of DMF:DMSO. Next, we prepared CsI stock solution by dissolving 1.5 M CsI in DMSO. By adding 8.8, 21.8, 42.4, and 80.4 μl from the CsI stock solution into 1 ml of the double-cation FA_{0.8}MA_{0.2}Sn_{0.5}Pb_{0.5}I₃ solution, we prepared the final triple-cation Cs_x(FA_{0.8}MA_{0.2})_(1-x)Sn_{0.5}Pb_{0.5}I₃ perovskite solution for x = 0.01, 0.025, 0.05, and 0.1, respectively. We stored the solution in a nitrogen-filled glovebox (with O₂ < 0.2 ppm and H₂O < 0.4 ppm) for 1 hour before fabrication. The resulting triple-cation has a bandgap of 1.26 eV and was used as the absorber layer for the narrow-bandgap PSCs (Figure 3.1c) in the tandem configuration in Chapters 5 and 6.

For the Cs_x(FA_{0.8}MA_{0.2})_(1-x)Sn_{0.5}Pb_{0.5}I₃ perovskite thin films with Sn and Pb excess, which were investigated in Chapter 5, we added additional PbI₂ and SnI₂ to FA_{0.8}MA_{0.2}Sn_{0.5}Pb_{0.5}I₃ in order to achieve the required 7.5% excess Sn_{0.5}Pb_{0.5}I₂, followed by adding Cs from a 1.5 M stock solution to reach 3%, 7.5%, and 12.5% Cs concentrations.

3.1.2. Deposition of perovskite solar cells

Preparation of the transparent conductive oxides

In this thesis, we used three different TCOs as front electrodes including pre-patterned indium tin oxide (ITO; Luminescence Technology), fluorine-doped tin oxide (FTO; Sigma Aldrich), hydrogen-doped indium oxide (IO:H; sputtered by a collaboration partner (ZSW)) (see Table 3.1). We patterned FTO and IO:H substrates by laser scribing using a pulsed laser ablation for the defined cell area. For all the PSCs, we prepared 16 × 16 mm² glass substrates

coated with pre-structured TCOs (ITO, FTO, or IO:H) in an ultrasonic bath with acetone and isopropanol for 10-15 min each, followed by oxygen plasma treatment at 100 W power for 3 min before deposition of the ETL (HTL) for the PSCs with *n-i-p* (*p-i-n*) structures.

Fabrication of perovskite solar cells with *n-i-p* structures

For the PSCs with *n-i-p* structure (Figure 3.1a and b), we spin-coated np-TiO₂ ETLs on the IO:H (only for semi-transparent PSCs) and ITO substrates at a speed of 7000 rpm for 30 s followed by 100 °C annealing step for 30 min in ambient atmosphere with a relative humidity of 45% at room temperature. We set the rpm and annealing temperature to 4000 rpm and 200 °C in case of using np-SnO₂ ETLs and to improve their wettability used oxygen plasma treatment (at 30 W for 1 min) shortly before deposition of perovskite. We processed C₆₀ ETLs by spin-coating the solution at a rate of 1500 rpm for 1 min followed by an annealing step at 75 °C for 2 min in an inert atmosphere, subsequently.

For all pure-Pb perovskite thin films, we spin-coated the solution by a two-step process on top of the ETL: (1) 1000 rpm for 10 s, (2) 6000 rpm for 20 s. We poured 100 µl of CB on the spinning substrate 10 s prior to the end of the second step followed by an annealing process at 100 °C for 60 min in an inert atmosphere. Next, we deposited the spiro-MeOTAD HTL using a spin-coating process (4000 rpm for 30 s), followed by overnight oxygen doping in a box with a relative humidity of <25%.

For the PSCs with metal back electrodes, we swiped the edges using γ -butyrolactone (GBL; Merck) to allow the back electrode to connect the front electrode while depositing. Next, we used a Vactec Coat 360 evaporator to evaporate 70 nm gold (Au) layer through shadow masks to complete the fabrication of the PSCs with an active area of 10.5 mm² and a layer stack of glass / ITO / np-TiO₂ or np-SnO₂ or C₆₀ / perovskite / spiro-MeOTAD / Au, for which perovskite varies in composition: Cs_x(FA_{0.83}MA_{0.17})_(1-x)Pb(I_{0.83}Br_{0.17})₃ (with x = 0, 0.05, 0.1, and 0.15), Cs_{0.1}(FA_{0.83}MA_{0.17})_{0.9}Pb(I_{0.67}Br_{0.33})₃, or Cs_{0.17}FA_{0.83}(I_{0.83}Br_{0.17})₃.

Table 3.1. Sputtering parameters of the IO:H front as well as ITO and IZO rear electrodes.

* DC: direct-current, RF: radiofrequency

Sputtering parameters	IO:H (front)	ITO (rear)	IZO (rear)
Deposition system	Von Ardenne CS 370 S	Kurt J. Lesker PVD-75	Kurt J. Lesker PVD-75
Sputtering type	DC*	DC	RF*
Power (W)	600	50	100
Pressure (mTorr)	7.5	0.8	1.5
Temperature (°C)	25	25	25
Sputtering gas	Ar	Ar	Ar
Reactive gas	O ₂ (1.7%), H ₂ (3.4%)	O ₂ (2.5%)	O ₂ (1%)
Deposition time (s)	210	2300	2550
Post conditioning	Vacuum annealing at 200°C for 75 min	—	—
Layer thickness (nm)	230	150	165

For the semi-transparent PSCs, we continued the layer sequence with thermal evaporation (see Figure 3.1) of 10 nm molybdenum oxide (MoO_x ; Sigma Aldrich) at a rate of 0.8 Å/s using a Lesker Spectros system at 6×10^{-6} mbar pressure. MoO_x is used as a buffer layer to protect the spiro-MeOTAD while sputtering the rear electrodes in the next step. Before sputtering the ITO (for PSCs in Chapter 5) or IZO (for PSCs in Chapter 6) rear electrodes we swiped the edges using GBL to allow the rear and front electrode to connect. Table 3.1 summarizes all the sputtering parameters we used. To increase the conductivity of the rear electrode, we thermal-evaporated ~ 75 -nm Au fingers at a rate of 2 Å/s using a shadow mask. Finally, we completed the stack by depositing ~ 165 nm magnesium fluoride (MgF_2 ; Sigma Aldrich) thermally using Lesker Spectros PVD system at a rate of 3–4 Å/s at 6×10^{-6} mbar pressure. MgF_2 plays the role of an anti-reflection layer on top of the rear electrode.²⁷ As a result, we achieved semi-transparent PSC with an active area of 10.5 mm² and a layer stack of glass / ITO / np-SnO₂ / perovskite / spiro-MeOTAD / MoO_x / ITO / MgF_2 , for which perovskite is $\text{Cs}_{0.17}\text{FA}_{0.83}\text{Pb}(\text{I}_{0.76}\text{Br}_{0.24})_3$ (Chapter 5) or $\text{Cs}_{0.1}(\text{FA}_{0.83}\text{MA}_{0.17})_{0.9}\text{Pb}(\text{I}_{0.83}\text{Br}_{0.17})_3$ (Chapter 6). For the PSCs with the composition $\text{Cs}_{0.17}\text{FA}_{0.83}\text{Pb}(\text{I}_{0.76}\text{Br}_{0.24})_3$ (Chapter 5), we spin-coated 100 µl n-butylammonium bromide (BABr, Dysol) dissolved in isopropanol (2 mg/ml) at 5000 rpm for 30 s on top of the perovskite thin film after annealing step to obtain a 2D/3D perovskite heterostructure.

Fabrication of perovskite solar cells with *p-i-n* structures

For the PSCs with *p-i-n* structure (Figure 3.1c), we spin-coated PTAA HTLs on the TCO substrates (ITO, FTO, or IO:H) at 4000 rpm for 30 s followed by annealing at 100 °C for 30 min. Next, we spin-coated the narrow-bandgap $\text{Cs}_x(\text{FA}_{0.8}\text{MA}_{0.2})_{(1-x)}\text{Sn}_{0.5}\text{Pb}_{0.5}\text{I}_3$ perovskite thin film on PTAA at 5000 rpm for 10 s. We immediately vacuum-exposed the layers for 10 s in a vacuum chamber (≈ 10 Pa) with a 150 ml volume size. We, sequentially, annealed the perovskite thin films at 100 °C for 7 min. Next, we spin-coated 5 nm PCBM at 4000 rpm for 60 s on the perovskite. PCBM, which we used in the narrow-bandgap mixed Sn/Pb PSCs (Figure 3.1c) is meant to prevent electron-hole recombination at the perovskite/ C_{60} interface.⁸⁹

In sequence, we used a Lesker PVD system to thermally evaporate ≈ 20 nm of C_{60} and ≈ 5 nm of bathocuproine (BCP; Luminescence Technology) as the electron transport material, in 6×10^{-6} mbar pressure and at a rate of 0.1-0.2 and 0.2-0.3 Å/s, respectively. After swiping the edges with GBL, we completed the PSC stack by evaporating a back contact of Ag (≈ 100 nm) through shadow masks using a Vactec Coat 360 evaporator. As a result, we achieved PSCs with active area of 10.5 mm² and a layer stack of glass / ITO or FTO or IO:H / perovskite / PCBM / C_{60} / BCP / Ag.

For HTL-free narrow-bandgap PSCs (Chapter 6), we spin-coated the perovskite thin film with the composition $\text{Cs}_{0.025}(\text{FA}_{0.8}\text{MA}_{0.2})_{0.975}\text{Sn}_{0.5}\text{Pb}_{0.5}\text{I}_3$ directly on the TCO substrates (ITO, FTO, and IO:H), in the absence of any HTL.

3.2. Characterization techniques

This section describes experimental techniques we used for characterizing thin films and PSCs in this thesis.

3.2.1. Characterization of thin films

Ellipsometry

Ellipsometry measures the alteration in the reflected polarization of an incident light upon reflection or transmission at an interface. In an ellipsometry measurement, a defined polarization (produced by a polarizer) is reflected or transmitted from the sample and the output elliptical polarization is measured (Figure 3.2). The polarization of the incident light may have two components, perpendicular and parallel to the plane of incidence. The ellipsometry measures the change in the phase difference (Δ) between these two components, which is introduced by the reflection, and the change of their amplitude ratio (Ψ). Thus, the complex reflectance ratio (ρ), which is the ratio of the parallel and perpendicular reflection coefficients (r_{\parallel} and r_{\perp}) is given by:

$$\rho = \frac{r_{\parallel}}{r_{\perp}} = \tan \Psi \cdot e^{i\Delta} \quad 3.1$$

The measured parameters (Δ and Ψ) cannot be directly used to determine the optical constants of a material. Using an appropriate model based on Maxwell's equations is needed to calculate the parameters of interest and determine the dielectric properties, i.e., complex refractive index ($\tilde{n} = n + ik$) and complex dielectric function ($\tilde{\epsilon} = \tilde{n}^2$) of a thin film.

In this thesis, we determined the refractive index (n) and extinction coefficient (k) of TCO thin films (ITO, FTO, and IO:H) by implementing a Woolam Variable Angle Spectroscopic Ellipsometer (WVASE). We used the software provided by the manufacturer to analyze the data.

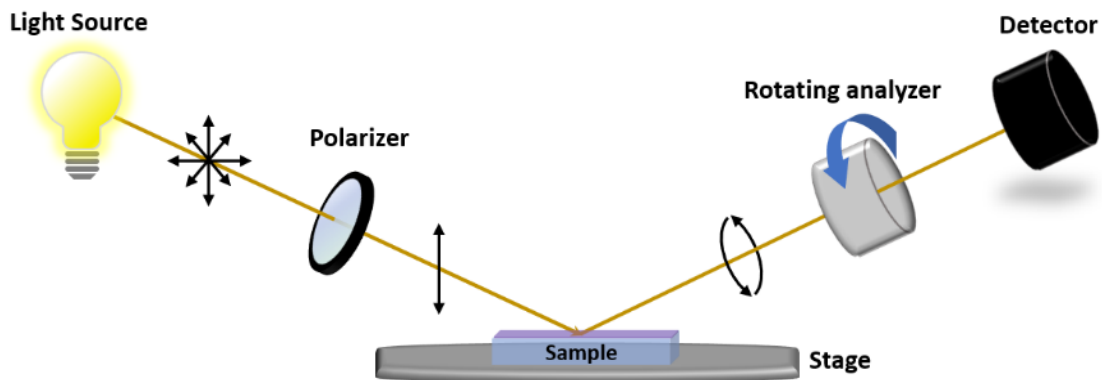


Figure 3.2. Schematic illustration of a typical ellipsometry setup.

Spectrophotometry

Spectrophotometry is widely used to analyze the optical properties of thin films in terms of transmittance and reflectance. Most commonly ultraviolet, visible, and infrared radiation (300-1200 nm) passes through a monochromator, whereupon the adjusted wavelength is sent to the sample (Figure 3.3). The transmitted and reflected lights are then detected. The transmittance is determined as $T = I/I_0$, where I_0 and I are the intensity of the light before and after passing through the sample, respectively. The intensity of the light after being reflected from a sample (I) is compared to the intensity of light after being reflected from a reference material (I_0) such as a silicon solar cell, and the reflectance is determined as $R = I/I_0$. The transmittance and reflectance are commonly expressed as a percentage. The absorbance is calculated as $A = 1 - T - R$. Moreover, the absorption coefficient of a thin film with a thickness of d can be calculated from:

$$\alpha = \frac{1}{d} \ln \frac{(1 - R)^2}{T} \quad 3.2$$

By using α and $h\nu$ as the photon energy, the optical bandgap (E_g) of the thin film can be extracted from a plot of $(\alpha h\nu)^{1/n}$ vs. $(h\nu)$, which is known as Tauc plot. n denotes the nature of transition and equals 1/2 for thin films with direct bandgap. Therefore, using the Tauc relation:

$$(\alpha h\nu)^2 = C (h\nu - E_g) \quad 3.3$$

the bandgap (E_g) can be estimated as the intercept of $(\alpha h\nu)^2 = 0$.

In this thesis, we used a Bentham PVE300 photovoltaic characterization system (located in a nitrogen-filled glovebox) to measure the transmittance and reflectance spectra of the perovskite and TCO thin films upon illumination with modulated monochromatic light source.

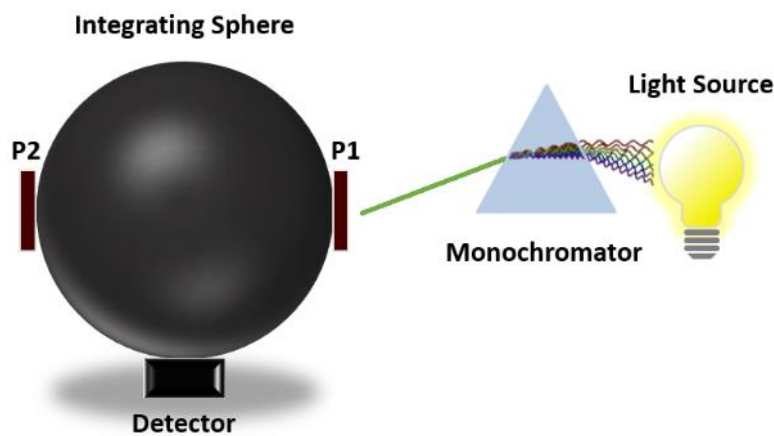


Figure 3.3. Schematic illustration of a typical spectrophotometry setup.

Photoluminescence spectroscopy

Photoluminescence (PL) spectroscopy is a non-destructive technique, commonly used for characterizing the optical and electronic properties of a semiconductor. A sample is illuminated with a laser beam, whereupon photons with energies higher than the bandgap of the examined material are absorbed and electrons are excited to conduction bands. After being thermally relaxed, these electrons radiatively recombine with holes in the valence band and emit light with an energy in the range of bandgap. The light signal is then dispersed by a monochromator and the spectrum is detected by a camera (Figure 3.4).

In general, a PL spectroscopy characterization is performed as steady-state (SSPL) and time-resolved (TRPL). SSPL spectroscopy explores the average emission from the sample upon excitation with a detection window in the range of micro- to milli-second. TRPL spectroscopy measures the decay in the PL spectra with respect to time while reducing the detection window to pico-seconds. SSPL and TRPL are widely used to provide insights into dominant recombination processes and determine the carriers' lifetime. When the material is photoexcited, the excited charges either relax through band-to-band radiative recombination or fill the defect-induced traps (see Section 2.1.3). The latter results in trap-assisted non-radiative recombination that reduce the intensity of a SSPL signal, and therefore can be indicative of defect density in the material.

In this thesis, we recorded the PL kinetics by a Hamamatsu Universal Streak Camera C10910 operated in single sweep mode and coupled to an Acton SpectraPro SP2300 spectrometer. We used two different time windows (200 ns and 1 μ s) respectively. Excitation with a pulse width of 140 fs was done by a mode-locked Ti:sapphire laser (Coherent, Chameleon Ultra). Its output of 960 nm was frequency doubled by a second harmonic generator (Coherent, Chameleon Compact OPO-Vis) and the repetition rate of 80 MHz reduced to 2 MHz for the 200 ns and 2/3 MHz for the 1 μ s time window using a pulse picker (APE, pulseSelect). We recorded the SSPL spectra by a fiber-coupled UV-vis spectrometer (Avantes, AvaSpec-2048L). We measured all SSPL and TRPL spectra with a pump fluence of 30 nJ/cm². The samples were under dynamic vacuum at pressures of $\sim 10^{-5}$ hPa during each measurement.

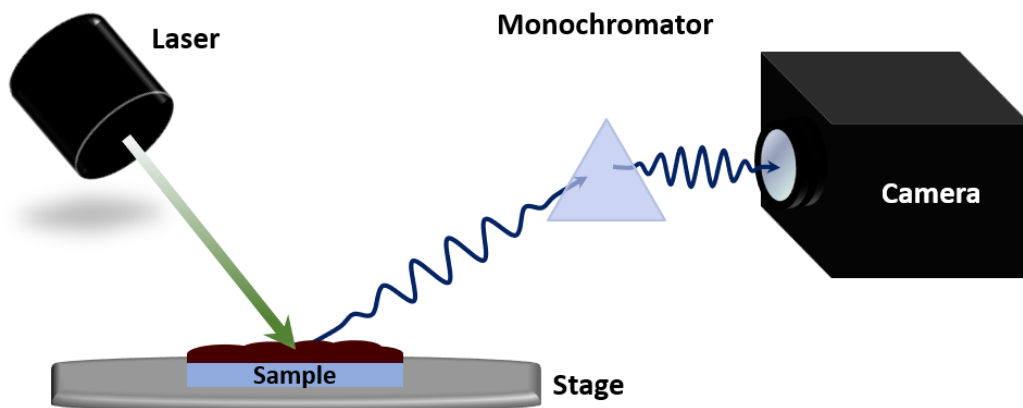


Figure 3.4. Schematic illustration of a typical photoluminescence spectroscopy setup.

X-ray diffraction

X-ray diffraction (XRD) is a non-destructive analytical technique which is widely used to determine the crystal structure of a thin film by providing information about intensity, position, and width of diffraction peaks. Peak intensity indicates the total scattering from each crystal planes and therefore determines the preferential crystal orientation of the material in interest. The peak position reveals the crystal structure (lattice parameters) and the contributing phases. Moreover, a shift in the peak position demonstrates a change in the interplanar d -spacing. Therefore any macrostrains (also termed as homogenous strain) can be determined by analyzing shift of the peak positions.⁹⁰ A peak shift to smaller angles reflects a tensile crystallite, while a shift to larger angles indicates a compressive crystallite (Figure 3.5). Therefore, homogenous strain can be simply determined as follows:

$$\epsilon = \Delta d/d \quad 3.4$$

Peak width is associated with crystallite size and inhomogeneous strain (also termed as microstrain). The broadening of a peak can be identified by its full width at half maximum (FWHM). Williamson-Hall equation relates the peak broadening to crystallite size and microstrain as follows:

$$\text{FWHM} = \frac{K \lambda}{D \cos \theta} + C \epsilon \tan \theta \quad 3.5$$

where K is the scale factor depending on the shape of the grains (typically 0.9), λ is the X-ray wavelength, D is the crystallite size, θ is the Bragg angle of the detected peak, C is a constant (≈ 4 or 5), and ϵ is the microstrain. The first and second terms of Equation 3.5 are correlated with size- and strain-induced broadening, respectively. Therefore, for a crystal structure in the absence of inhomogeneous strain the first term, which is known as Scherrer equation, determines the crystallite size. By multiplying Equation 3.5 by $\cos \theta$, and denoting FWHM as β (in radians) we rewrite it as follows:

$$\beta \cos \theta = C \epsilon \sin \theta + \frac{K \lambda}{D} \quad 3.6$$

Therefore, by plotting $\beta \cos \theta$ vs. $\sin \theta$ we can determine the strain component ($C\epsilon$) from the slope and the size component ($K\lambda/D$) from the intercept. Such a plot is known as a Williamson-Hall plot.⁹⁰

In this thesis, we utilized a Bruker D2Phaser system with Cu-K α radiation ($\lambda = 1.5405 \text{ \AA}$) to determine the crystallite structure, composition, and strain of perovskite thin films (Chapters 4, 5, and 6), as well as TCO thin films (Chapter 6). For PbI₂, SnI₂, and Sn_{0.5}Pb_{0.5}I₂ thin films (Chapter 5), we use a nitrogen-filled sealed holder to prevent the samples from degradation in ambient air while being measured.

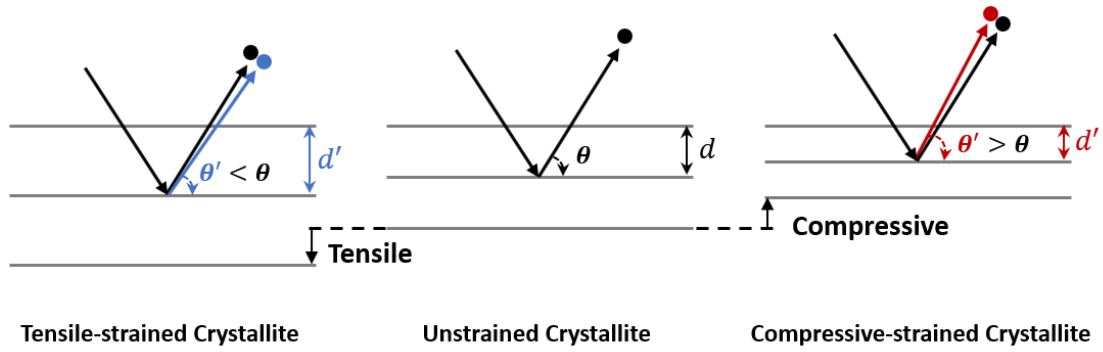


Figure 3.5. A peak shift from its original position (middle panel) to smaller (left panel) and larger (right panel) reflection angles (θ) indicative of a tensile- and compressive-strained crystallite.

X-ray photoelectron spectroscopy

X-ray photoelectron spectroscopy (XPS) is one of the most common surface characterizations in material science, which is used to determine the atomic composition of a sample's surface non-destructively. It also provides information about binding energies and oxidation states by subjecting a sample to a high-energy X-ray irradiation that penetrates through the sample for 2 to 10 nm. As illustrated by Figure 3.6a, a high-energy X-ray photon excites an electron from a core level into the vacuum. The energy conservation for the photoelectric effect dictates that:

$$E_b = h\nu - (E_K + \phi) \quad 3.7$$

where E_b is the binding energy of the excited electron (photoelectron), $h\nu$ is the energy of the X-ray photon (~ 1.49 keV for Al K_α X-ray and 1.25 keV for Mg K_α X-ray), E_K is the kinetic energy of the photoelectron measured by the instrument, and $\phi = E_{\text{vac}} - E_F$ is the work function of the sample (see Figure 3.6a). The energies relative to the Fermi level are achieved by grounding the sample to the detector. The binding energy of the detected photoelectrons serves as a *fingerprint* for the chemical composition of the sample's surface.

An XPS spectrum (known as survey spectrum) is usually plotted as intensity (in count) vs. binding energy (in eV) of the detected photoelectrons (Figure 3.7). Each element produces a set of XPS peaks corresponding to the electron's configuration, e.g., 1s, 2s, 2p, etc. The background beneath the peaks in the spectrum is due to electrons that are inelastically scattered before leaving the sample's surface. Such inelastic scatterings, which reduce the kinetic energy of the photoelectron, are mainly originated from interaction of the photoelectron with another electron, a photon, and/or composition impurity.⁹¹ The distance an excited electron can travel within a material while keeping its kinetic energy is called inelastic mean free path, which determines surface sensitivity and can be roughly determined by a universal curve.⁹²

In this thesis, we used XPS measurements to determine composition and oxidation states of mixed Sn/Pb metal-halide perovskite and TCO thin films. We utilized an Omicron Argus CU electron analyzer, a non-monochromatized DAR 450 twin anode X-ray source providing

Mg K_{α} and Al K_{α} X-rays, and a SIGMA Surface Science MECS X-ray source providing monochromatized Al K_{α} X-rays. The samples were transported and transferred without any air exposure into the ultra-high-vacuum (UHV) surface analysis system. The base pressure of the analysis chamber was $\approx 7 \times 10^{-11}$ mbar. The Fermi levels of sputter-cleaned Au, Ag, and Cu foils were used to calibrate the energy axis.⁹³ For all measurements, no charging was observed. The emission angle of the photoelectrons was perpendicular to the surface leading to a characteristic attenuation length (λ) of 1-3 nm.⁹⁴ To prevent an influence of beam-induced changes from the X-rays on the spectra, the measurement times did not exceed 10 min (for the non-monochromatized x-ray source) and 40 min (for the monochromatized X-ray source, due to lower photon flux).

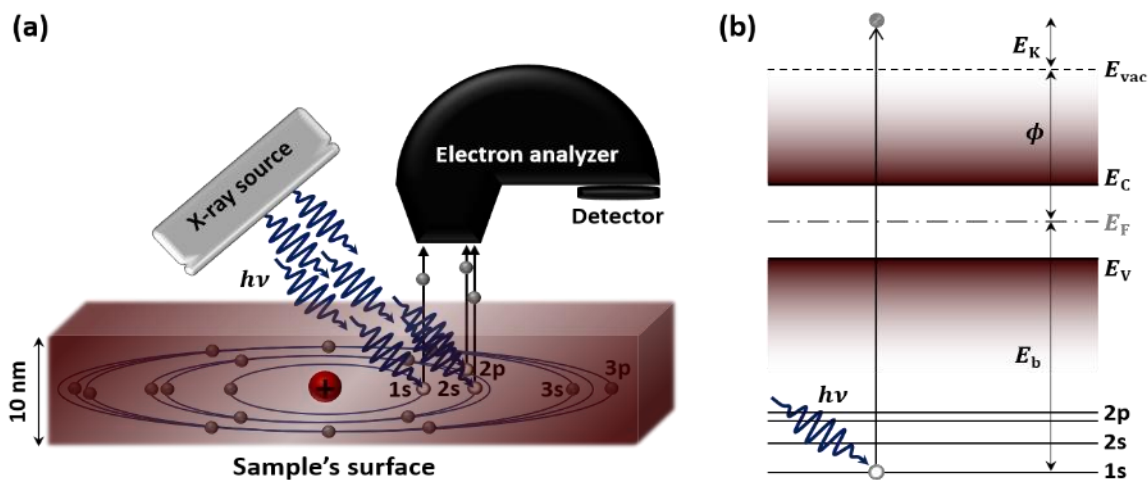


Figure 3.6. (a) Schematic illustration of the photoelectric effect in an X-ray photoelectron spectroscopy measurement. (b) Illustration of the X-ray-matter interaction in a semiconductor.

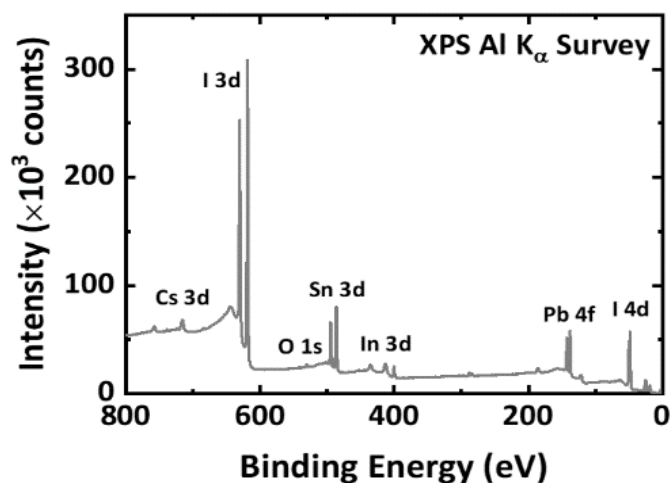


Figure 3.7. A typical x-ray photoelectron microscopy (XPS) pattern of a mixed Sn/Pb narrow-bandgap perovskite thin film.

Scanning electron microscopy and cathodoluminescence

As schematically illustrated in Figure 3.8a, in a typical scanning electron microscope a thermionically emitted and accelerated electron beam passes through pairs of condenser lenses and is focused over a sample. The beam has a typical energy in the range of 0.2 to 40 keV and can be focused to a spot about 0.4 to 5 nm. Finally, the beam is deflected to raster-scan over a rectangular area of the sample's surface. Upon interaction of the primary electron beam with atoms at different depth within a sample, the primary electrons undergo random scattering and absorption and lose their energy. As a result, different types of signals (Figure 3.8b) such as reflection of elastically back-scattered electrons, emission of inelastic-scattered secondary electrons and Auger electrons, as well as emission of electromagnetic radiation (X-rays and light) are generated, and each detected by a dedicated detector. The detection of the secondary electrons (with low energies in the range of 50 eV), which reveal the topographical information, is used to project a scanning electron microscopy (SEM) image with a resolution of below 1 nm. Moreover, the back-scattered electron images provide information about atomic number and phase differences in a sample.

Typically, the energy of the primary electrons in this technique is far too high to directly excite an electron from valence band to conduction band. However, the secondary electrons with energies higher (about three times) than the bandgap of the examined material can excite electrons from valence band to conduction band. After thermalization, the electrons radiatively recombine with holes in the valence band and emit light. This phenomenon is known as cathodoluminescence (CL). A CL detector captures the emitted light and characterizes the aspects of the light signal such as intensity, wavelength (CL spectrum), color, etc. CL is a powerful technique in detecting phases and tracing impurities and defect distribution in semiconductors.

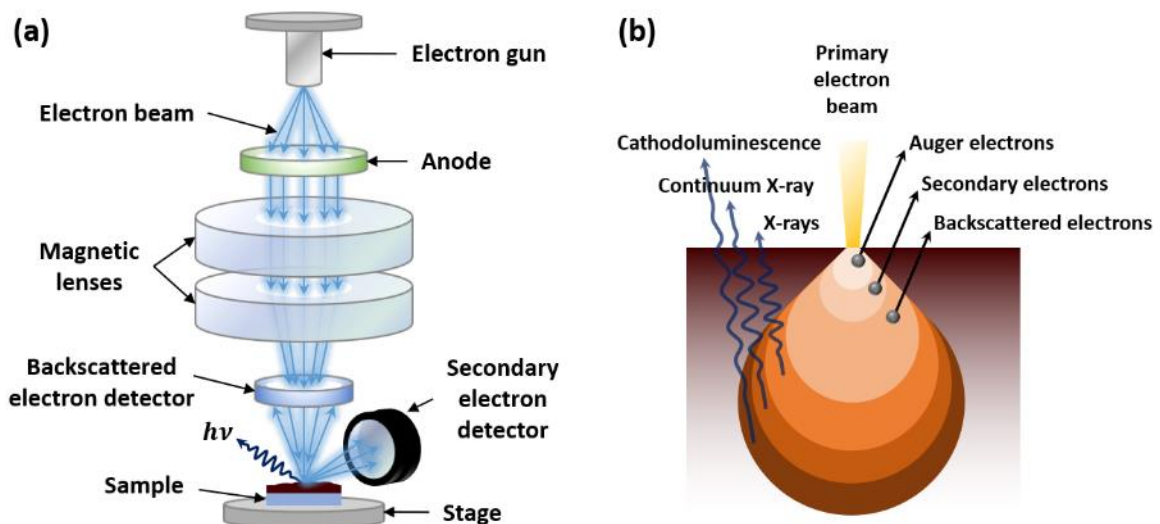


Figure 3.8. (a) Schematic illustration of a scanning electron microscope setup. (b) Illustration of electron-matter interaction volume and types of signal generated.

In this thesis, we used two different scanning electron microscopes (Zeiss LEO1530 and Zeiss Supra60 VP) with an in-lens detector and an aperture size of 20 μm for the SEM images captured with a 3-kV acceleration voltage. For CL characterizations, we used an FEI Verios scanning electron microscope equipped with a Gatan MonoCL4 Elite CL system. The CL spectrum was obtained at a constant accelerating voltage of 5 kV with a beam current of 22 pA. Although CL is a powerful technique to study the electronic properties of perovskite materials, to avoid any beam-induced damage the irradiation conditions should be thoroughly controlled.

Atomic force microscopy

Atomic force microscopy (AFM) is a technique to identify the topography of a sample's surface in the range of a few nanometers. As illustrated in Figure 3.9, an AFM set-up is consisting of a laser beam focused on the tip of a cantilever, which raster scans over the surface and probes its topography. A standard AFM can be operated in different modes (static contact and dynamic contact) depending on the operation of the tip motion. A tapping mode is a dynamic contact mode that enables us to probe the surface of the perovskite thin films non-destructively. It was particularly important in this thesis (Chapter 4), where we aimed at tracking morphology alterations of perovskite thin films on different days after storage. In a tapping mode the cantilever is oscillating up and down at its resonance frequency. When the tip comes close to a surface the interaction of the tip with the surface in the form of van der Waals forces, electrostatic forces, dipole-dipole interaction, etc. changes the amplitude of the cantilever's oscillation. A raster scan is then produced by imaging the force that is needed to adjust the cantilever's oscillation amplitude to the set value as the cantilever is probing over the sample's surface.

In this thesis, we used an AFM (Bruker Dimension Icon) in peak force tapping mode and a PDNISP diamond tip nano-indenter with a spring constant of 236 N/m, resonance frequency of $f_0 \sim 67$ kHz and a calibrated effective tip radius of $r_c \sim 57$ nm at a calibrated indentation depth of $\delta_c \sim 5$ nm. The AFM was operated by a Nanoscope 5 Controller and Nanoscope 8.15 SR8 software.

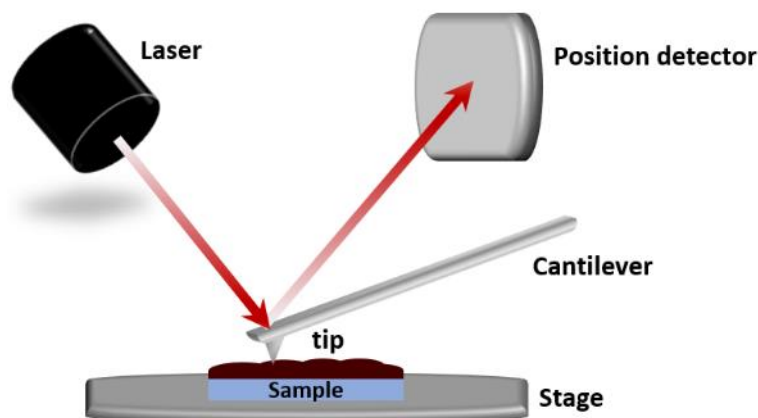


Figure 3.9. Schematic illustration of a typical atomic force microscopy setup.

Profilometer measurement

A profilometer is an instrument to determine the surface profile and thickness of a thin film. A diamond stylus probes the surface of the sample while moving in contact with the surface and the changes in the vertical position of the stylus is recorded by the instrument. In this thesis, we used a Bruker Dektak XT profilometer to measure the thickness of perovskite and TCO thin films.

Four-point probe measurement

A four-point probe is composed of four equally spaced probes (Figure 3.10) which are used to measure sheet resistance of thin layers or substrates. While a current (I) is forced through the outer probes, the voltage (V) across the inner probes is measured. In case the thickness of the film (d) is ideally smaller than the distance between the probes ($d \ll s$) and the lateral dimensions of the sample is about 40 times larger than s , the sheet resistance (R_{sq}) in units of ohm per square (Ω/sq) can be calculated using the following equation:

$$R_{sq} = \frac{\pi V}{\ln 2 I} \quad 3.8$$

In this thesis, we utilized a custom-made four-point setup to measure sheet resistances of TCO thin films. The setup includes a S-302 four-point probe mounting stand and a Picotest M3500A multimeter.

Hall-effect measurement

To characterize the electrical properties of TCO thin films, we employed Hall measurement based on a deflection of charge carriers in a direction perpendicular to an applied magnetic field, which generates a measurable voltage (Hall voltage) across the sample. Using the Hall voltage, we calculated the resistivity and Hall coefficient of the samples, and accordingly determined the concentration and mobility of the charge carriers for different TCO thin films. The samples were cut in $10 \times 10 \text{ mm}^2$ and contacted at the corners in a custom-made system in van der Pauw configuration with a magnetic field of 0.6 T and currents of tens of milliamps.

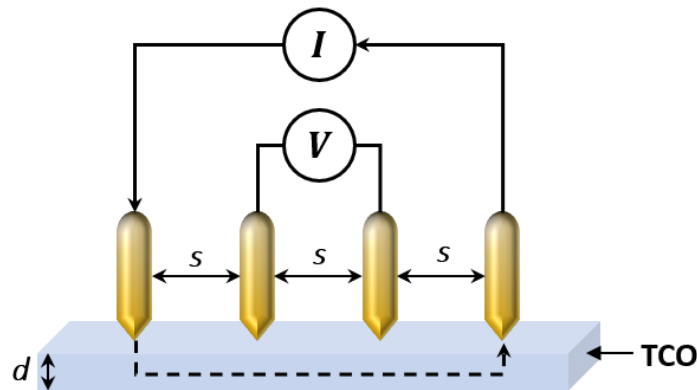


Figure 3.10. Schematic illustration of a four-point probe setup used for measuring the sheet resistance of transparent conductive oxide (TCO) electrodes.

3.2.2. Characterization of perovskite solar cells

Current-density–voltage characteristics

As discussed in section 2.2.2, the current-density–voltage (J – V) characteristics has to be performed in a standard test condition (STC), i.e., constant illumination under air-mass 1.5 global (AM1.5G) (100 mW/cm^2) at $25 \text{ }^\circ\text{C}$. We performed this measurement by applying xenon-lamp solar simulator (Newport Oriel Sol3A) that provides an AM1.5G spectra (100 mW/cm^2) at a temperature set to $25 \text{ }^\circ\text{C}$ using a Peltier element connected to a microcontroller while performing the J – V analysis. In all the measurements we set the scan rate at 0.6 V/s from open-circuit to short-circuit (backward scan direction) and from short-circuit to open-circuit (forward scan direction) using a Keithley 2400 source-meter. We calibrated the irradiation intensity using a certified silicon reference solar cell (a KG5 for the pure Pb PSCs and a KG0 for the narrow-bandgap mixed Sn/Pb PSCs).

By calculating the power conversion efficiency (PCE) from the J – V , we determined the performance of the PSCs. To determine the PCE of a 4T all-PTSCs we added the PCEs of the respective semi-transparent top PSC and bottom PSC (under semi-transparent perovskite filters with a larger area ($16 \times 16 \text{ mm}^2$) with the same layer stack and optical properties as the semi-transparent top PSC). We did not use any spacers (light coupling layers) between the bottom PSC and the filter. We add the PCE of the semi-transparent top and the narrow-bandgap bottom PSCs to determine the final PCE of the 4T all-PTSCs.

Maximum power point tracking measurement

In Section 2.2.2, we explained that deriving a stabilized power output from a maximum power point (MPP) tracking measurement together with the J – V characteristics provides a more reliable understanding of the performance of a PSC. Using the same set-up as for the J – V characteristics, we determined the stable power conversion efficiency of the PSCs by measuring the photocurrent at a constant voltage close to the MPP (Chapter 4) and at the MPP (Chapters 5 and 6). The MPP tracking measurements were performed under STC.

External quantum efficiency

As discussed in section 2.2.2, the external quantum efficiency (EQE) measurement enables us to determine the spectral response of a PSC. In this thesis, we performed the EQE measurement using a Bentham system with a halogen and xenon lamp while applying a chopping frequency of $\sim 930 \text{ Hz}$ with an integration time of 500 ms . The devices were not subjected to any preconditioning. We noticed that varying the frequency between 200 Hz to 950 Hz did not significantly affect the results. For measuring the bottom solar cell with a top perovskite filter, we used a large illumination spot to average over possible variations in the EQE spectrum. The possible variations could be induced by inhomogeneous scattering and transmission properties due to typical thickness variations of the perovskite thin film used for the filter.

Ideality factor

Ideality factor is a parameter used for interpreting the dominant recombination mechanism in a solar cell. Typically an ideality factor close or equal to 1 indicates that band-to-band radiative and/or non-radiative surface recombination are the dominant recombination mechanisms, while an ideality factor close or equal to 2 suggests that non-radiative trap-assisted SRH bulk recombination is dominant.⁹⁵ These values are subjected to vary for PSCs with complex multilayers.^{95,96} Identifying ideality factor from light-intensity dependent V_{OC} analysis is more reliable, since at open-circuit condition the series resistance loss can be avoided. In this method ideality factor can be determined from the slope of a logarithmic fit of a V_{OC} vs. light intensity plot, using the following equation (which is derived from Equation 2.10):

$$n_{id}(I) = \frac{q}{k_B T} \frac{dV_{OC}}{\text{dln} \frac{I}{1 \text{ mW/cm}^2}} \quad 3.9$$

where q is the electron charge, k_B is the Boltzmann constant, T is temperature, and I is the irradiation intensity.⁹⁵

In this thesis, we extracted the ideality factor of PSCs (Chapter 4) from a light-intensity dependent V_{OC} , which were measured using an all-in-one measurement system Paios (Fluxim AG). We used a white LED (Cree XP-G) for the illumination in all experiments.

Thermally stimulated current

Thermally stimulated current (TSC) technique is a powerful method to reveal information about the properties of shallow and/or deep traps of a solar cell. In this method, the device is illuminated for a limited time at a very low initial temperature (here 15 K). The photogenerated charge carriers fill the trap states. Upon heating the device with a low constant rate (here 7 K/min) to room temperature (300 K), the trapped carriers are thermally excited and released from the trap states. The released charge carriers are collected through the respective electrodes. The transient current originating from the released charge carriers is measured as a function of temperature. The resulting plot is called TSC curve consisting of peak(s) associated with the trap states (like Figure 4.17). Analyzing the peak(s) provides information about the trap states such as activation energy and concentration of carriers in the trap centers. Since the examined PSC has an identical configuration, possible changes in the current are ascribed to an alteration in the trap density.

In this thesis, TSC measurements were performed in a closed cycle He cryostat under helium gas atmosphere which also acts as heat transfer medium. We illuminated the PSCs with a white LED array for 5 min to fill the traps. During device heating, TSC signal was monitored using a sub-femtoamp source meter (Keithley-6430) under built-in field without external bias.

4. Spontaneous Enhancement of Power Conversion Efficiency

In this chapter, we study the origin of *spontaneous enhancement* of power conversion efficiency of perovskite solar cells that occurs after a few days of sample preparation. We observe spontaneous enhancement for a variety of multi-cation-halide perovskite solar cells with different perovskite compositions and architectures. The primary contributor to the improved efficiency is an increased open-circuit voltage. We employ various characterization methods to better understand the intrinsic causes of this effect. The generality of spontaneous enhancement for different compositions of multi-cation-halide perovskite solar cells highlights the importance of determining the absolute power conversion efficiency increase over time initiated by this phenomenon.

This chapter is based on our publication in the *Journal of Materials Chemistry A* [97] with the title “Spontaneous enhancement of the stable power conversion efficiency in perovskite solar cells”. Most of the graphs in this chapter are adapted or reproduced with permission of The Royal Society of Chemistry.

4.1. Motivation

It is a common observation that in most cases the power conversion efficiency (PCE) of multi-cation perovskite solar cells (PSCs) tends to reach its highest value after a few days of storage in the dark after device fabrication. Several studies reported the phenomenon for PSCs with various perovskite absorber compositions, such as MAPbI₃,^{42–44} multi-cation-halide,^{39–44} Pb-free,⁹⁸ and mixed Sn/Pb perovskite (see Chapter 5) thin films. Various hypotheses were presented in the literature to explain this phenomenon.^{41–44} One early study related the spontaneous enhancement of PCE to a coalescence of smaller crystallites during storage.⁴¹ As a result, a reduction in non-radiative recombination at the grain boundaries was suggested to lead to a better performance of the respective PSCs.⁴¹ Another study suggested an improved crystallinity in addition to released residual stress and lattice distortion to be the origin of the spontaneous enhancement over long-term storage.⁴² A gradual diffusion of sodium (Na⁺) ions from the ITO-coated glass substrate into the perovskite thin film was

presented as another possible explanation.⁴⁴ Passivation at the grain boundaries initiated by Na^+ was suggested to result in a reduction in density of trap states during the storage time improving the photovoltaic performance of the PSCs.⁴⁴ Despite all of the above-mentioned studies and investigations, yet no consensus was reached on the genesis of the spontaneous enhancement and a systematic study was still missing.

In this chapter, we provide a systematic experimental comparison of different architectures and perovskite compositions to ascertain the generality of the spontaneous enhancement and its causes. In Section 4.2, we introduce the spontaneous enhancement for a case study using a triple-cation composition as the reference perovskite thin film. Afterwards, we investigate a variety of perovskite thin films with different compositions, including double-cation MA-free $[\text{CsFAPb}(\text{IBr})_3]$ and Cs-free $[\text{FAMAPb}(\text{IBr})_3]$ as well as triple-cation $[\text{CsFAMAPb}(\text{IBr})_3]$ perovskite thin films with different Cs concentrations. In Section 4.3, we study the role of charge transport layers by using different electron transport layers (ETLs) like nanoparticles of TiO_2 (np- TiO_2), buckminsterfullerene (C_{60}) (deposited on top of the np- TiO_2 layer), and nanoparticles of SnO_2 (np- SnO_2) as well as varying the point in time of the hole transport layer (HTL) deposition.

In Section 4.4, we analyze the X-ray diffraction (XRD) patterns of pristine and stored perovskite thin films, which are suggestive of a reduction in the strain in the perovskite thin films after storage. The reduced strain can result in diminished trap-state density discussed in Sections 4.5 and 4.6. In Section 4.5, we discuss that the improved open-circuit voltage (V_{OC}) of the PSCs upon storage is due to a reduction in non-radiative Shockley-Read-Hall (SRH) recombination, which is revealed by a decreased ideality factor as well as enhanced charge carrier lifetimes. Moreover, photoluminescence (PL) measurements reveal the existence of lower-energy states with 80 meV difference to the bulk bandgap phase that disappear after a few days of storage with only the peak of the bulk bandgap phase remaining. Lastly, in Section 5.6, we discuss the results provided by thermally stimulated current (TSC) measurements applied on complete PSC devices. TSC discloses that the density of trap states close to the bandgap is drastically reduced after storage, which can be due to strain relaxation over a few days of storage, and thereby results in the spontaneous enhancement in the PCE of PSCs.

4.2. Investigation of perovskite composition

Using perovskite thin films in the composition $\text{Cs}_{0.1}(\text{FA}_{0.83}\text{MA}_{0.17})_{0.9}\text{Pb}(\text{I}_{0.83}\text{Br}_{0.17})_3$, referred to as Cs_1FM_9 hereafter, we fabricated reference PSCs with a layer stack of glass / ITO / np- TiO_2 / Cs_1FM_9 / spiro-MeOTAD / Au (Figure 4.1a). We measured the reference PSCs on the day of sample preparation (day 1) and tracked their performance after having them stored for several days at room temperature in the dark in an inert atmosphere (nitrogen-filled glovebox).

The PCE of a Cs_1FM_9 PSC with a very low initial value ($\approx 13.0\%$) did not stabilize over 5 min when measured at a constant voltage close to the maximum power point (MPP) voltage (Figure 4.1b). Interestingly, after storage, the PCE gradually increased and stabilized at

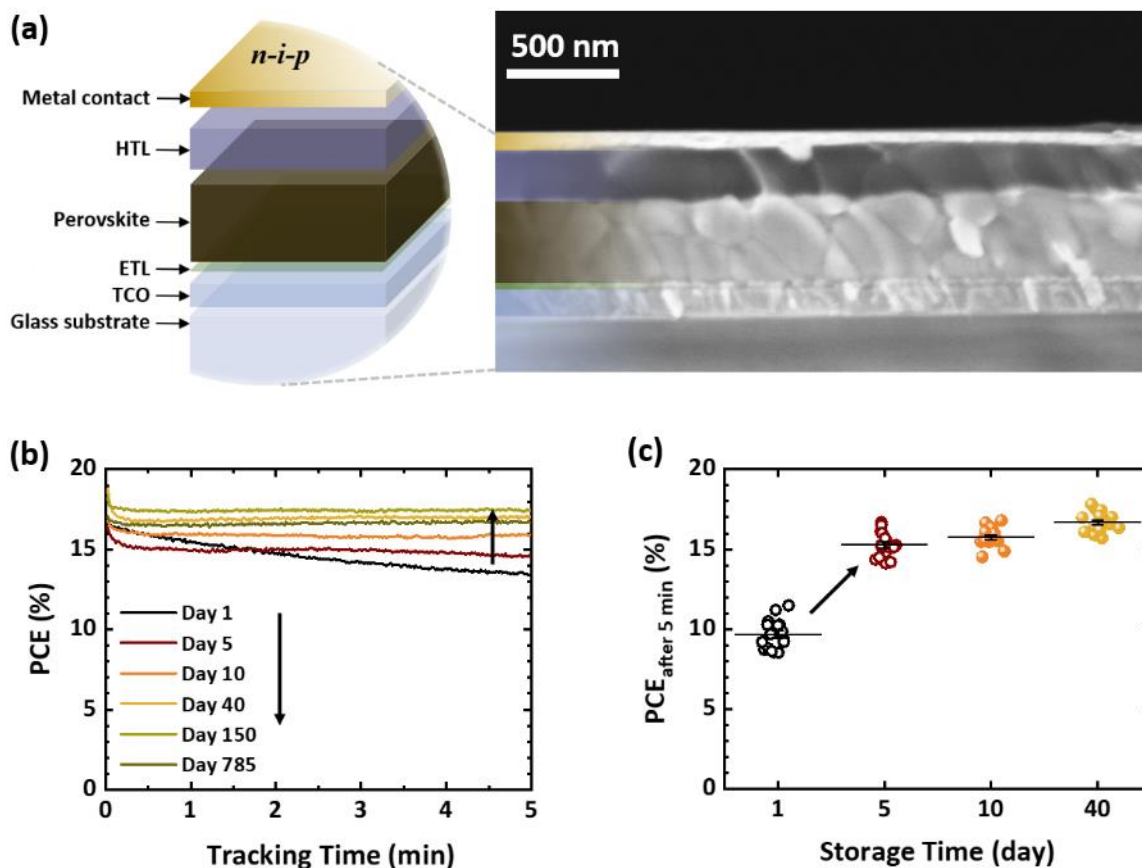


Figure 4.1. (a) A schematic layer stack and a cross-sectional scanning electron microscopy (SEM) image of a reference Cs_1FM_9 PSC. (b) Power conversion efficiency (PCE) at a constant voltage close to the maximum power point (MPP) measured on the day of sample preparation (day 1) and after storage (days 5, 10, and 40) and (c) statistical distribution of the same values after 5 min ($\text{PCE}_{\text{after 5 min}}$) for 16 identically prepared reference Cs_1FM_9 PSCs. Open symbols indicate that, on days 1 and 5, the power output does not stabilize over 5 min. SEM measurement was performed by Dr. Bahram Abdollahi Nejang. Adapted from [97] with permission of The Royal Society of Chemistry.

16.0% on day 10 and further increased to 17.0% on day 40. The improvement in PCE continued to 17.5% up to day 150, while on day 785 the PCE dropped only by $\approx 1\%$ absolute to 16.6% possibly due to material degradation starting to appear after such long-term storage. In order to corroborate the reproducibility of the results, we tracked the performance of 16 identically prepared Cs_1FM_9 PSCs. Interestingly, the averaged PCE improved significantly from $\approx 10.0\%$ on day 1 to $\approx 17.0\%$ on day 40, following the same trend shown in Figure 4.1b for the reference PSC. The statistical distribution of the PCEs of these devices after 5 min ($\text{PCE}_{\text{after 5 min}}$) are shown in Figure 4.1c, confirming the improved performance on different days of storage.

Notably, as Figure 4.2a depicts open-circuit voltage (V_{OC}) was the main photovoltaic characteristic that improved during the storage, which increased from 1.13 V on day 1 (with a PCE of 16.7%) to 1.19 V on day 40 (with a PCE of 18.0%) in the backward scan direction (solid lines). A V_{OC} of 1.19 V is a remarkable value for a single-junction PSC with a bandgap (E_g) of 1.62 eV, relating to a low voltage deficit of only ≈ 0.43 V (calculated by subtracting the V_{OC} from E_g).⁹⁹ It is also apparent that the hysteresis in the current-density–voltage (J –

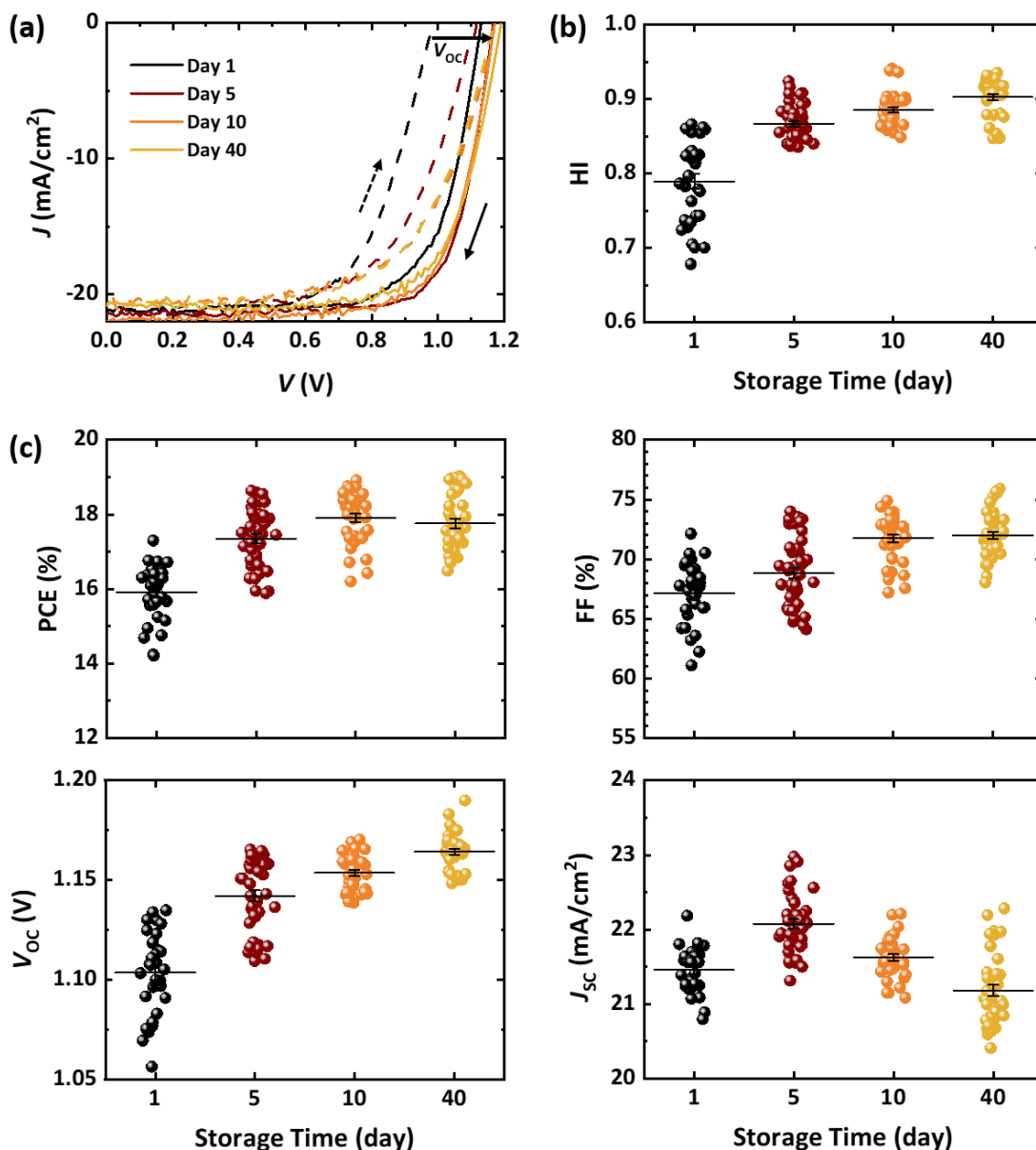


Figure 4.2. (a) Current-density–voltage (J – V) characteristics of a reference Cs_1FM_9 PSC in backward (solid lines) and forward (dash lines) scan directions, measured on day 1 and several days after storage. (b) Calculated hysteresis index (HI) and (c) statistical distribution of power conversion efficiency (PCE), fill factor (FF), open-circuit voltage (V_{oc}), and short-circuit current (J_{sc}), for 40 identically prepared reference Cs_1FM_9 PSCs. Adapted from [97] with permission of The Royal Society of Chemistry.

V) characteristics of the PSC decreased over time, which agrees with the quicker stabilization of the power output in the MPP measurements shown in Figure 4.1b.¹⁰⁰ Comparing the J – V characteristics of 40 identically prepared PSCs measured on different days confirmed the observed trend in hysteresis. We calculated the hysteresis index (HI) of the PSCs (see Section 2.2.2) as $\text{HI} = A_{FW}/A_{BW}$, where A_{FW} and A_{BW} are the areas under forward and backward scans in the J – V characteristics, respectively. A HI of 1 represents a PSC without hysteresis. As shown in Figure 4.2b, a pronounced hysteresis (low HI) for pristine Cs_1FM_9 PSCs on day 1 gradually reduced over time (HI approached 1). Photovoltaic characteristics of these PSCs (Figure 4.2c) show that the V_{oc} and fill factor (FF) are the main contributors

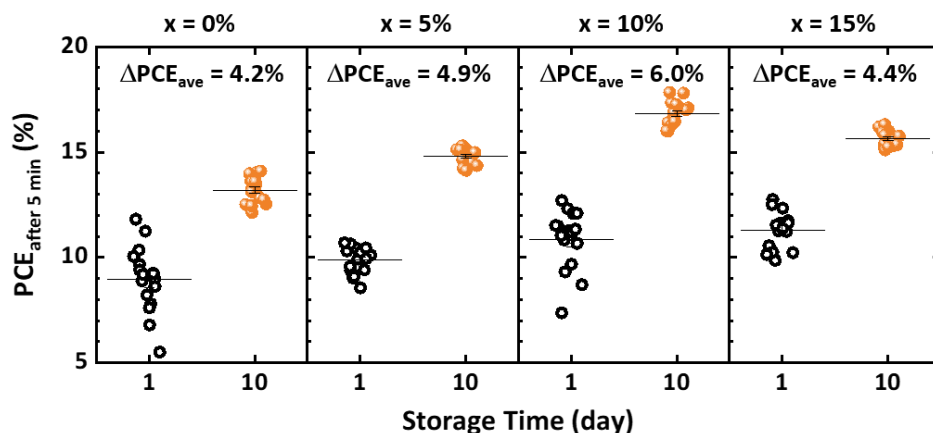


Figure 4.3. Statistical distribution of power conversion efficiency at a constant voltage close to the maximum power point after 5 min ($PCE_{after\ 5\ min}$) for 16 identically prepared $Cs_x(FA_{0.83}MA_{0.17})_{(1-x)}Pb(I_{0.83}Br_{0.17})_3$ PSCs, where x is the concentration of Cs. Open symbols indicate that the power output does not stabilize over 5 min on day 1. ΔPCE_{ave} corresponds to the average enhancement of the PCE of the PSCs compared to day 1. All the PSCs were processed on np-TiO₂ ETL under identical conditions. Reproduced from [97] with permission of The Royal Society of Chemistry.

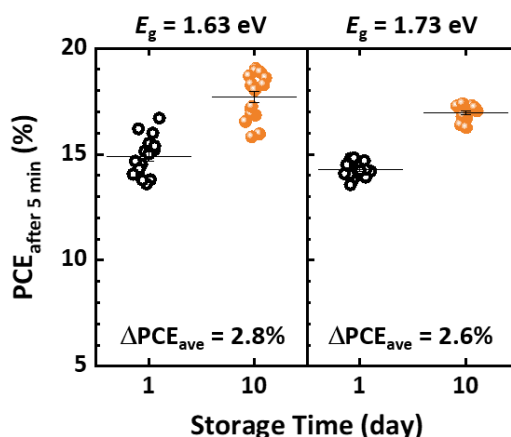


Figure 4.4. Statistical distribution of power conversion efficiency at a constant voltage close to the maximum power point after 5 min ($PCE_{after\ 5\ min}$) for double-cation $FA_{0.83}Cs_{0.17}Pb(I_{0.83}Br_{0.17})_3$ and triple-cation $Cs_{0.1}(FA_{0.83}MA_{0.17})_{0.9}Pb(I_{0.67}Br_{0.33})_3$ PSCs (16 identically prepared samples of each) with bandgap (E_g) of 1.63 and 1.73 eV, respectively. ΔPCE_{ave} corresponds to the average enhancement of the PCE of the PSCs compared to day 1. All the PSCs were processed on np-SnO₂ ETL under identical conditions. Reproduced from [97] with permission of The Royal Society of Chemistry.

to the enhanced PCE. By contrast, the short-circuit current (J_{SC}) is initially improved on day 5 and started to drop afterwards on days 10 and 40.

The incorporation of different cations into the metal-halide perovskite structure is known to impact the optoelectronic properties and stability of the respective PSCs.^{60,101–103} The incorporation of Cs, for example, decreases the non-radiative recombination rate due to a reduction in trap density in the bulk and/or at the grain boundaries of perovskite materials.^{60,101} We investigated a possible effect of Cs in the spontaneous enhancement of the PCE by incorporating Cs into double-cation $FA_{0.83}MA_{0.17}Pb(I_{0.83}Br_{0.17})_3$. Interestingly,

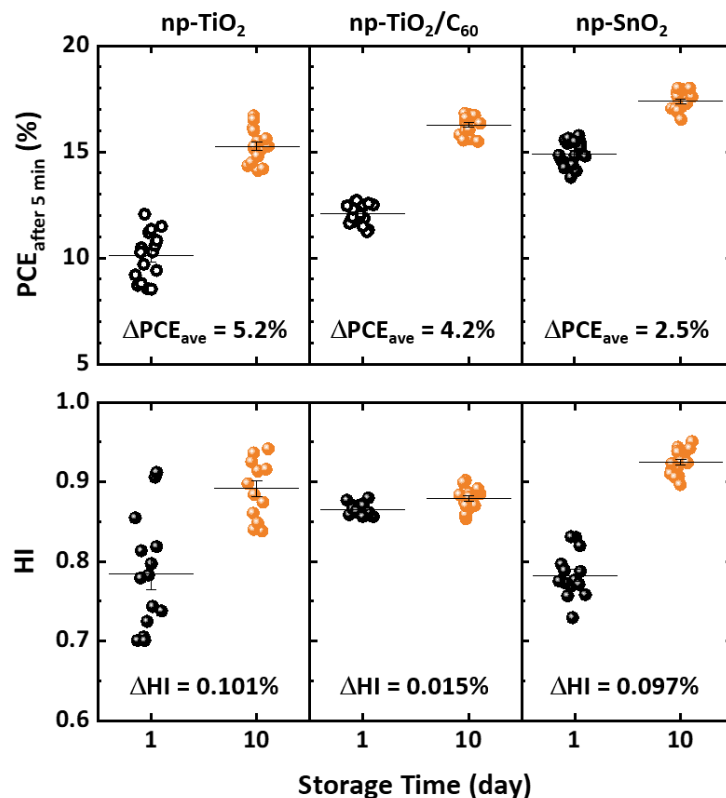


Figure 4.5. (a) Statistical distribution of power conversion efficiency at a constant voltage close to the maximum power point after 5 min ($PCE_{\text{after 5 min}}$) and (b) calculated hysteresis index (HI) of 16 Cs₁FM₉ PSCs with various electron transport layers. Open symbols in the top panel indicate that the power output of the np-TiO₂- and np-TiO₂/C₆₀-based PSCs does not stabilize over 5 min. ΔPCE_{ave} and ΔHI corresponds to the average enhancement of the PCE and HI of the PSCs compared to day 1, respectively. Reproduced from [97] with permission of The Royal Society of Chemistry.

as depicted in Figure 4.3, the average PCE of PSCs with and without Cs enhanced in the range between 4.2% and 6.0% (absolute) over 10-day storage. In order to explore the effect of the perovskite composition, we prepared PSCs with wide-bandgap triple-cation Cs_{0.1}(FA_{0.83}MA_{0.17})_{0.9}Pb(I_{0.67}Br_{0.33})₃ and MA-free double-cation FA_{0.83}Cs_{0.17}Pb(I_{0.83}Br_{0.17})₃ perovskite thin films. As presented in Figure 4.4, our observations revealed that regardless of the composition of multi-cation-halide perovskites, the spontaneous enhancement is a common effect for PSCs with different compositions. The literature supports this conclusion, as it has been previously reported for multi-cation-halide,^{39–44} MAPbI₃,^{42–44} and Pb-free⁹⁸ PSCs. Moreover, in Chapter 5, we show that this phenomenon occurs for mixed Sn/Pb PSCs as well.

4.3. Investigation of charge transport layers

Charge transport layers play a prominent role in the performance of PSCs. In particular, the ETL defines the morphology of perovskite thin films in PSCs with *n-i-p* structures. As discussed in details in section 2.2.1, the type of ETL is also important for the energy level alignment, which is critical for extracting electrons and blocking holes at the ETL/perovskite junction.^{104–107} Therefore, in order to examine the possible effect of ETLs on the spontaneous

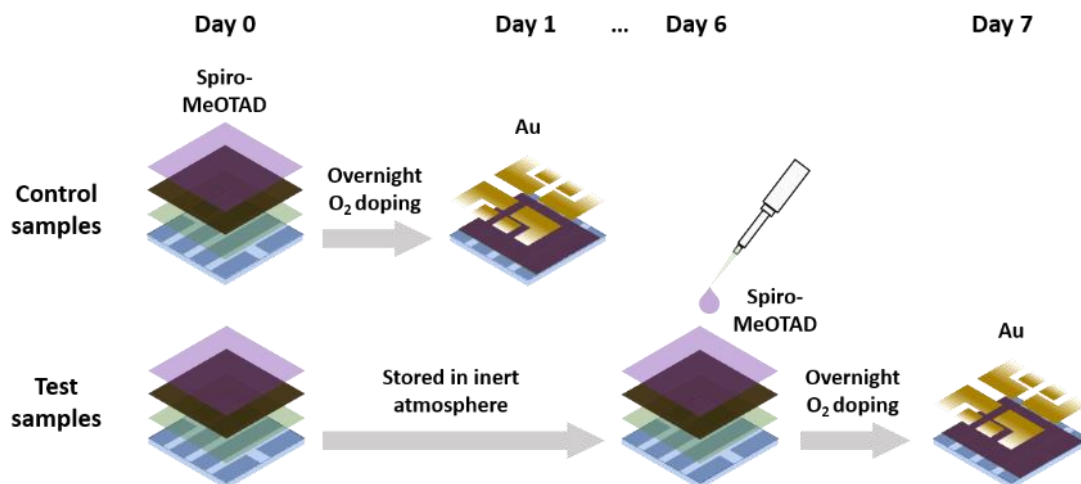


Figure 4.7. A schematic illustration of fabrication in terms of the point in time of the hole transport layer (spiro-MeOTAD) deposition. Top row (fabrication of control samples with immediate spiro-MeOTAD) and bottom row (fabrication of test samples with delayed spiro-MeOTAD). Reproduced from [97] with permission of The Royal Society of Chemistry.

enhancement of the PCE, we prepared PSCs with three different ETLs: np-TiO₂, C₆₀ (deposited on top of np-TiO₂), and np-SnO₂. TiO₂ is one of the most widely used ETLs for PSCs with high PCEs due to its efficient electron extraction and hole blocking abilities.^{108–111} According to the literature, PSCs including C₆₀ or its derivatives at the ETL side show less hysteresis in the J - V characteristics since they are less influenced by ion migration and trap-assisted recombination at the ETL/perovskite interface.^{112–114} More recently, SnO₂ ETLs are widely used due to their high electron mobility,¹¹⁵ enhanced electron extraction,¹¹⁶ as well as their relatively high stability under ultraviolet (UV) illumination.^{117,118} Our findings showed that the average value of the PCE of PSCs with different ETLs improved similarly by at least 2.5% absolute on day 10 (Figure 4.5). However, we note that the magnitude of enhancement varies for devices with different ETLs, which might be related to the different morphology of perovskite thin film formed on different substrates,¹⁰⁴ which will be discussed in more details in the following sections.

We observed that incorporating C₆₀ onto the np-TiO₂ substrates decreased the hysteresis, and therefore the HI of the np-TiO₂/C₆₀-based Cs₁FM₉ PSCs on day 1 was closer to unity compared to that of the np-TiO₂-based Cs₁FM₉ PSCs (see Figure 4.5 for comparison). Nevertheless, the reduced hysteresis did not diminish the overall spontaneous enhancement of the np-TiO₂/C₆₀-based PSCs, indicating that the spontaneous enhancement does not only occur for PSCs with enormous initial hysteresis. Moreover, in contrast to the np-TiO₂- and np-TiO₂/C₆₀-based PSCs, the PCE of a pristine np-SnO₂-based Cs₁FM₉ PSC stabilized already on day 1 (Figure 4.6a). Based on the J - V characteristics the best-performing np-SnO₂-based PSC exhibited a PCE of 19.6% on day 50 (which is a respectable value for solvent-quenched triple-cation based PSCs)^{60,119} with a V_{OC} of ≈ 1.14 V, J_{SC} of ≈ 22.3 mA/cm², and FF of $\approx 77\%$. In general, evidenced by our observations, PSCs with high (low) initial PCEs showed a lower (more prominent) spontaneous enhancement, in line with a previous report.⁴¹

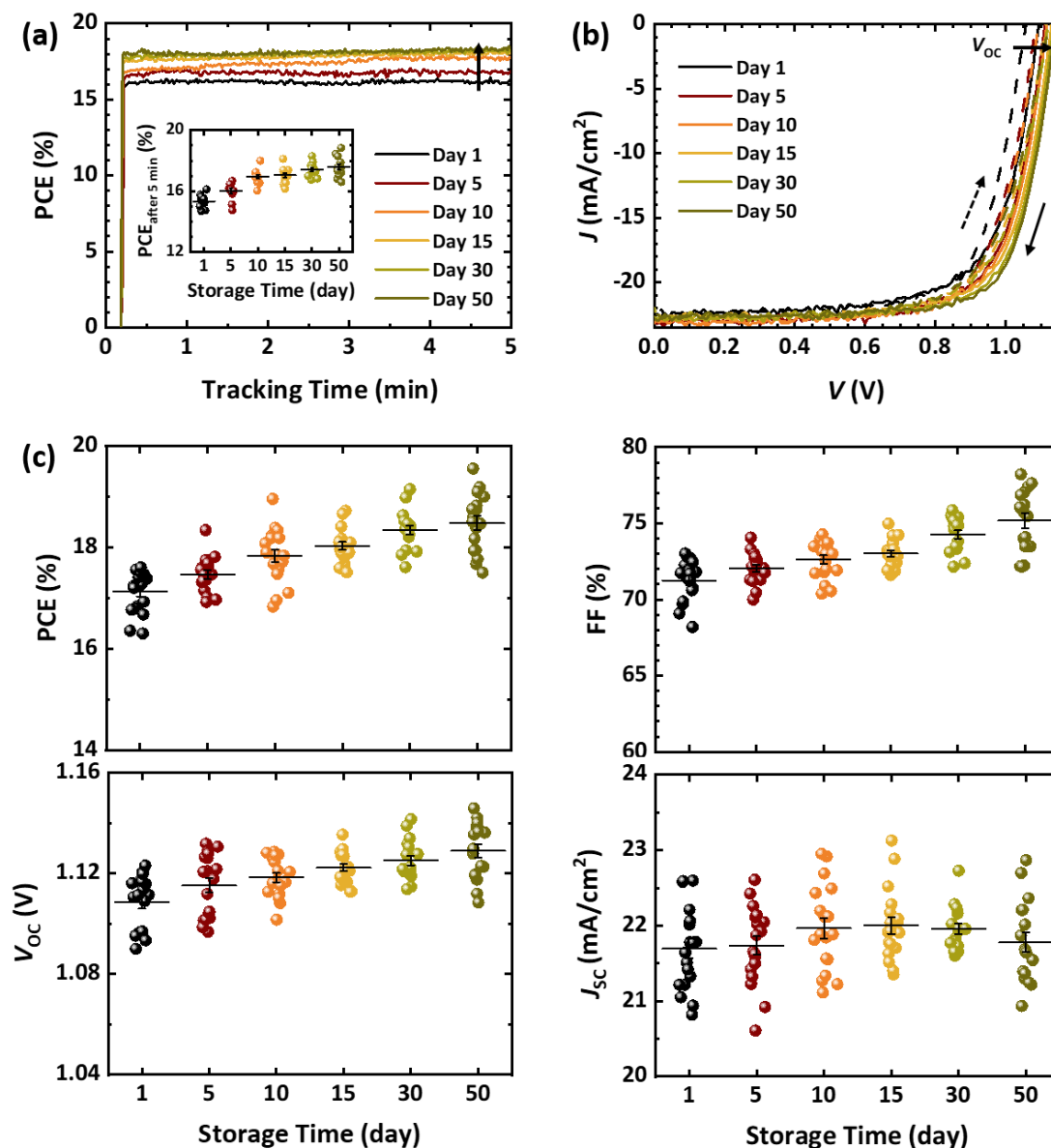


Figure 4.6. (a) Power conversion efficiency (PCE) at a constant voltage close to the maximum power point (inset represents the statistical distribution of the same value after 5 min for 16 identically prepared PSCs) and (b) current-density–voltage (J – V) characteristics in backward (solid lines) and forward (dash lines) scan directions of the best-performing Cs₁FM₉ PSC deposited on np-SnO₂. (c) Statistical distribution of power conversion efficiency (PCE), fill factor (FF), open-circuit voltage (V_{OC}), and short-circuit current (J_{SC}) for 40 identically prepared np-SnO₂-based Cs₁FM₉ PSCs, with a champion cell improving from PCE of 16.0% on day 1 to 19.6% after 50 days. Reproduced from [97] with permission of The Royal Society of Chemistry.

According to the literature, organic HTLs (the most employed spiro-MeOTAD) doped with lithium bis(trifluoromethanesulfonyl)imide (Li-TFSI) and 4-*tert*-butylpyridine (4-*t*BP) can negatively affect the stability of PSCs.^{120,121} This is due to the highly diffusive character of the additives (especially the Li-ions) that can affect the hysteresis and stability of PSCs under external factors like light, temperature, and/or an external bias voltage. We varied the time interval between the deposition of the perovskite thin films and the doped spiro-MeOTAD/Au layers to discriminate whether the spontaneous enhancement is dependent on

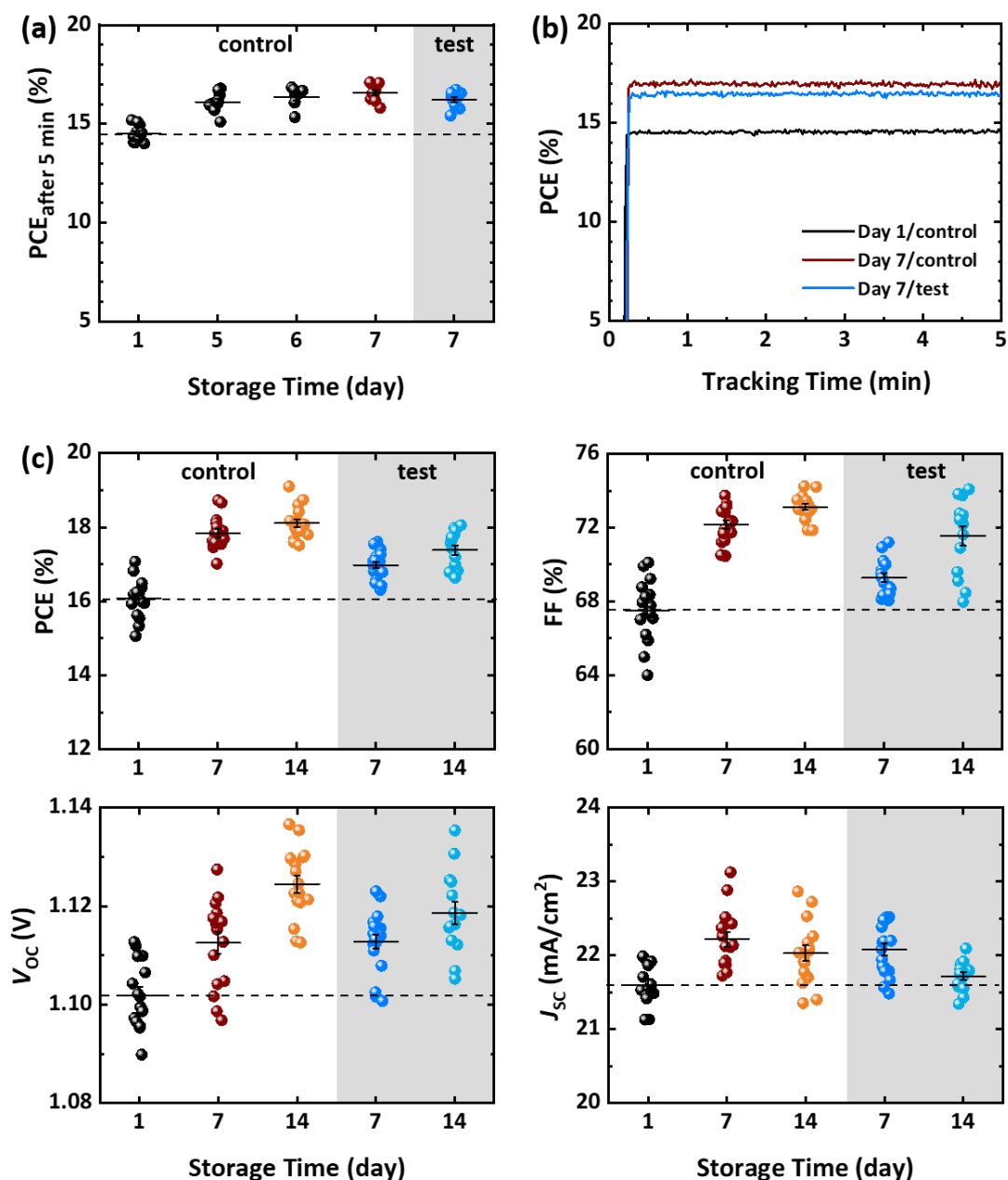


Figure 4.8. (a) Statistical distribution of power conversion efficiency after 5 min ($PCE_{\text{after 5 min}}$) at a constant voltage close to the maximum power point (MPP) for Cs_1FM_9 PSCs with immediate (control samples) and delayed (test samples) spiro-MeOTAD deposition. (b) PCE at a constant voltage close to the MPP for the best performing PSCs (control and test samples). (c) Statistical distribution of PCE, fill factor (FF), open-circuit voltage (V_{OC}), and short-circuit current (J_{SC}) for 16 identically prepared Cs_1FM_9 PSCs (control and test samples) measured on the day of preparation (day 1) and after storage (days 7 and 14). Reproduced from [97] with permission of The Royal Society of Chemistry.

the presence of spiro-MeOTAD on top of the perovskite thin films. Since the power output of devices with np-SnO₂ ETL stabilizes on day 1 and to avoid more complexity, we employed np-SnO₂ as the ETL for all PSCs in the following.

We fabricated (1) the *control* samples (as explained in Section 3.1.2) and (2) *test* samples without spiro-MeOTAD and Au, comprised of only ITO/np-SnO₂/Cs₁FM₉, and stored them in a nitrogen-filled glovebox (see Figure 4.7). By measuring the *control* samples every day

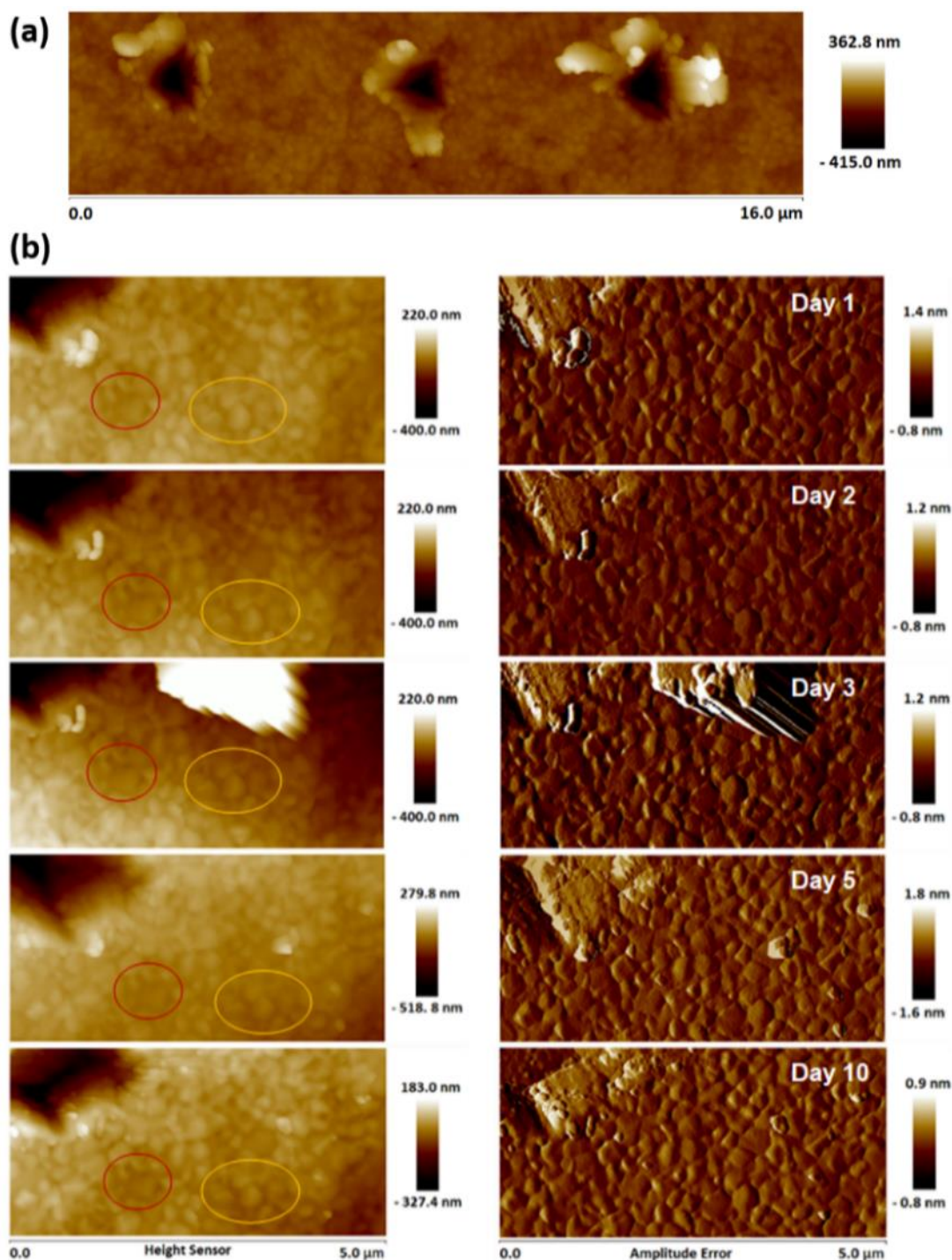


Figure 4.9. (a) Atomic force microscopy (AFM) of the exact same spot on the surface of a Cs_1FM_9 perovskite thin film using a diomand tip indentation. (b) Left column images manifest the data of the height sensor, containing information of the surface topography of the sample. Right column images exhibit the amplitude error, shown for a better illustration of the contrast. The roughness of the layer is ≈ 18.4 nm with no considerable changes on different days. Reproduced from [97] with permission of The Royal Society of Chemistry.

after preparation, we found a remarkable improvement of the PCE on day 5 by 1.5% absolute on average as exhibited in Figure 4.8a. Therefore, we completed the layer stack of the *test* samples with spiro-MeOTAD (deposited on day 6) and Au (deposited on day 7 after

overnight oxygen doping) and measured them. Interestingly, they immediately exhibited a stable power output comparable to that of the *control* samples (Figure 4.8a and b). After another week of storing the completed samples (day 14), all the J - V characteristics improved for both *control* and *test* samples (Figure 4.8c). It was noticeable that the V_{OC} and FF were the parameters dominating the PCE enhancement over time. This experiment leads to the conclusion that the spontaneous enhancement of the PCE during storage is not relying on the presence of an HTL and an electrode or the specific characteristics of doped spiro-MeOTAD. In the following sections, we systematically characterize the pristine and stored perovskite thin films to understand the causes. To begin with, in the next section, we apply atomic force microscopy (AFM) measurements and XRD analysis on pristine and stored perovskite thin films to impart further information about the surface and the crystallinity of the perovskite thin films before and after storage.

4.4. Suppression of strain-induced trap states

The spontaneous enhancement of the PCE of PSCs was attributed to the coalescence of small perovskite crystallites resulting in fewer grain boundaries.^{41,43} Although there is a long-term literature debate on whether grain boundaries are benign or detrimental to the performance of PSCs,^{122,123} based on some studies, grain boundaries account for trap-induced non-radiative SRH recombination in PSCs.¹²⁴⁻¹³⁰ They discuss that perovskite thin films with a fewer number of grain boundaries (larger grains)¹²⁴⁻¹²⁷ and/or passivated grain boundaries¹²⁸⁻¹³⁰ are less influenced by non-radiative SRH recombination and consequently the respective PSCs exhibits better performance.¹²⁵⁻¹³¹

We conducted a series of tapping-mode AFM images (see Section 3.2.1) of a perovskite thin film on day 1 and various days after storage. This experiment provided us with insights into the above-mentioned possibility of crystallites' coalescence as the genesis of the spontaneous enhancement. By performing an indentation with a diamond AFM tip on the surface of the perovskite thin film (Figure 4.9a), we could approach the indented sample spot (in a range of micrometers) and collect the scans from roughly the same spot of the perovskite thin film at different days. We did not observe any topographic alteration (i.e., coalescence or surface roughening) on the surface of the samples before and after storage. Figure 4.9b shows the AFM images on different days for an exemplary sample. This observation agrees with another study for which no coalescence was evidenced for perovskite thin films stored under ambient or inert conditions for two weeks.⁴⁴

The morphology and crystallinity of the perovskite thin films were particularly characterized after two weeks of interaction with air and nitrogen at room temperature in the dark.¹³² As evidenced, in the presence of moisture and oxygen at room temperature the perovskite grains grow larger spontaneously.¹³² By contrast, no considerable changes in the grains and crystallite sizes of the perovskite films that were stored in nitrogen for the same period were observed, which agrees with our findings from AFM. However, in those studies reporting on coalescence, the samples were stored in air.^{41,43} In conclusion, the spontaneous

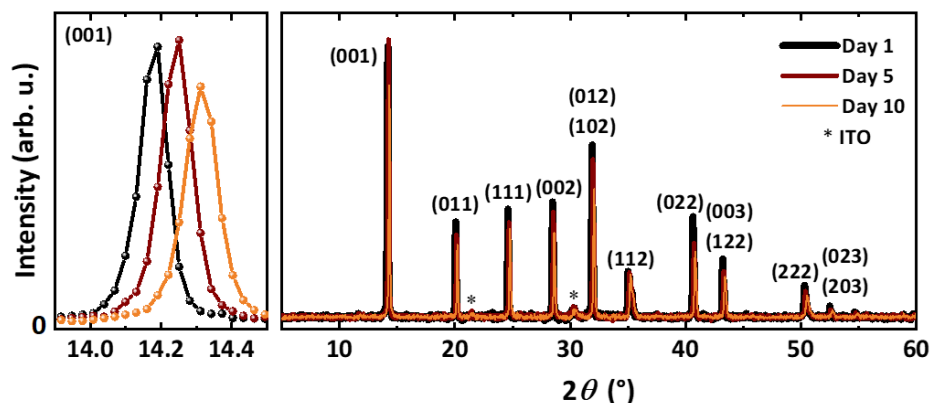


Figure 4.10. Right panel: X-ray diffraction (XRD) patterns of a Cs_1FM_9 perovskite thin film deposited on glass/ITO/np-SnO₂, collected on the day of sample preparation (day 1) and after storage (days 5 and 10). Left panel: shift of (001) perovskite peak from $2\theta = 14.16^\circ$ on day 1 to larger diffraction angles $2\theta = 14.23^\circ$ on day 5 and $2\theta = 14.30^\circ$ on day 10. Reproduced from [97] with permission of The Royal Society of Chemistry.

enhancement occurs regardless of storing the devices in ambient air (in the presence of oxygen) or inert atmosphere (e.g., nitrogen-filled glovebox).

To study the crystallinity properties for the perovskite thin films in more details, we performed XRD measurements on our perovskite thin films. Figure 4.10 compares the XRD patterns of a Cs_1FM_9 perovskite thin film on day 1 and after a few days of storage (on days 5 and 10). In accordance with the literature, all X-ray reflections are indexed in cubic space group $Pm-3m$.¹³³ Using the Scherrer equation (see Section 3.2.1), we measured the crystallite sizes on different days (Table 4.1). The crystallite size of the perovskite altered after storage because the width of the reflections, which among other effects is the main reminiscence of the crystal size, slightly changed. Moreover, the relative intensities of the perovskite diffraction peaks collected on different days remained consistent (Figure 4.10, right panel). Therefore, in line with the AFM results, the XRD characterizations revealed no signs of coalescence.

Nevertheless, we observed a prominent shift in the XRD reflection peaks of the perovskite thin film at different days. Using the X-ray reflections of the ITO substrates at $2\theta = 21.5^\circ$ and 30.4° as reference,^{134–136} we could exclude a sample height misalignment and detect a similar shift for all the perovskite peaks from day 1 to day 10. Figure 4.10, left panel, exhibits an exemplary of the shift in the (001) reflection from $2\theta = 14.2^\circ$ (on day 1) to larger diffraction angles $2\theta = 14.2^\circ$ (on day 5) and 14.3° (on day 10) (Figure 4.10, left panel). A shift to larger angles in the XRD patterns of a triple-cation perovskite thin film after storage was also reported elsewhere,⁴² and was taken as an indication of a plane shrinkage and more compact atomic packing. As discussed in Section 3.2.1, a shift to larger diffraction angles implies a smaller d -spacing, which could be associated with a homogenous strain release. Therefore, we hypothesized that a gradual release of initial strain in the perovskite thin film leads to the observed shift in the XRD pattern from day 1 to day 5 and day 10. We estimated the relative strain (listed in Table 4.1) according to the following expression:⁹⁰

$$\epsilon_r = \frac{\Delta d}{d} = \frac{d_{\text{strained}} - d_{\text{unstrained}}}{d_{\text{unstrained}}} \quad 4.1$$

where d_{strained} is the mean d -spacing of the (001) and (002) reflections ($= d(001) + d(002) / 2$) for the strained sample on day 1 or day 5 and $d_{\text{unstrained}}$ is the mean d -spacing of the (001) and (002) reflections for the unstrained sample on day 10. Thereby, ϵ_r was equal to 0.73% ($0.0073 \text{ \AA} = \text{\AA} 6.234 \text{ \AA} - 6.189 \text{ \AA} / 6.189 \text{ \AA}$) on day 1 and 0.39% ($0.0039 \text{ \AA} = 6.123 \text{ \AA} - 6.189 \text{ \AA} / 6.189 \text{ \AA}$) on day 5, compared to day 10.

Organic-inorganic perovskite thin films deposited by solution-based methods including antisolvent-quenching and annealing (for solvent removal) steps, which are required for high efficiency PSCs, are strained.¹³⁷ While antisolvent-quenching step leads to a fast nucleation and crystallization of the perovskite thin films and may leave residual strain in the film, annealing temperature and mismatch in thermal expansion coefficient between perovskite and substrates is the mainspring of the residual strain in the spin-coated perovskite thin films.^{138,139} The mismatched thermal expansion coefficient also explains the different magnitude of spontaneous enhancement observed for the PSCs with different ETLs (Figure 4.5) since the strain level is expected to depend on the substrate (here the ETLs).¹⁴⁰ A typical substrate like glass and ITO as well as ETLs such as SnO₂ and TiO₂ have smaller thermal expansion coefficient than metal-halide perovskite thin films.¹⁴⁰ Therefore, upon cooling down, the substrate (which was annealed) shrinks back faster than perovskite and restricts perovskite lattice from a full shrinkage to its origin size, which results in tensile strain in the film.¹³⁹ However, the strain in the lattice is gradually relaxed upon storage. The strain relaxation, which results in plane shrinkage, manifests itself in the peak positions shifted to the larger diffraction angles.

Table 4.1. Crystallographic parameters extracted from X-ray diffraction (XRD) patterns of a Cs₁FM₉ perovskite thin film on days 1, 5, and 10. Reproduced from [97] with permission of The Royal Society of Chemistry. The strain analysis was performed in collaboration with Amir. A. Haghighirad.

Storage Time	Day 1	Day 5	Day 10
FWHM	0.090193°	0.101353°	0.0886624°
Crystallite Size (D)	128 nm	103 nm	89 nm
Diffraction angle of (001)	14.165°	14.231°	14.301°
Diffraction angle of (002)	28.466°	28.529°	28.599°
d -spacing of (001)	6.247 Å	6.218 Å	6.188 Å
d -spacing of (002)	6.221 Å	6.206 Å	6.191 Å
Mean d -spacing: $d(001) + d(002)/2$	6.234 Å	6.213 Å	6.189 Å
Error: $ d(001) - d(002) $	0.026 Å	0.012 Å	0.0024 Å
Relative Strain ($\epsilon_r: \Delta d/d$)	0.73%	0.39%	0.00%

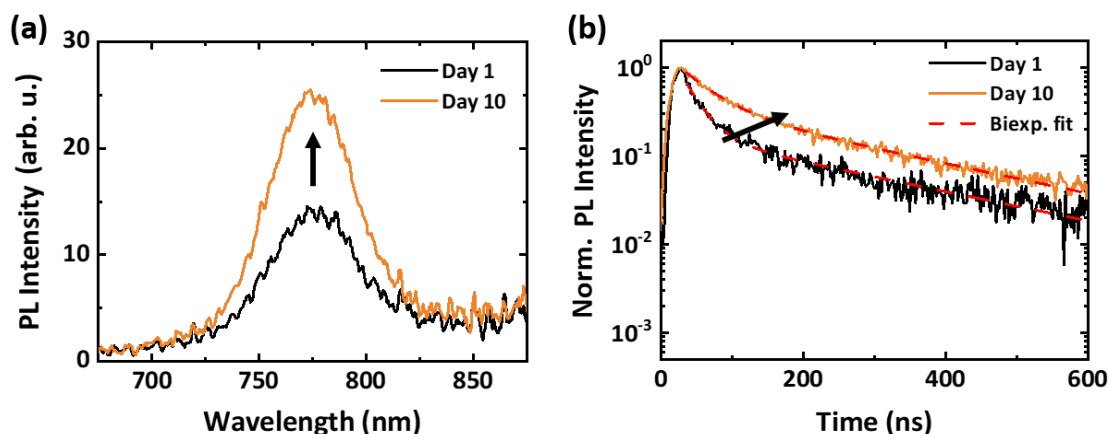


Figure 4.11. (a) Photoluminescence (PL) spectra and (b) normalized time-resolved PL kinetics of a Cs_1FM_9 perovskite thin film deposited on bare glass. The data were collected on the day of sample preparation (day 1) and a few days after storage. The measurements were performed by Dr. Diana Rueda-Delgado. Reproduced from [97] with permission of The Royal Society of Chemistry.

Lattice strain was reported to increase deep and shallow trap concentrations that cause non-radiative recombination. As reported, a local non-radiative decay revealed by time-resolved PL was associated with a reduction in strain-induced defects.¹⁴¹ Therefore, in the following, we used a variety of characterization methods including PL emission, ideality factor measurement, and TSC for identifying recombination mechanisms and calculating defect density in pristine and stored perovskite thin films and PSC devices. The results enabled us to reveal alteration in (strain-induced) trap density and recombination rates within the perovskite thin films upon storage.

4.5. Investigation of charge recombination mechanisms

As mentioned in Section 2.2.3, band-to-band radiative recombination, non-radiative SRH recombination in the bulk of perovskite thin films, as well as non-radiative recombination at grain boundaries and interfaces heavily impact the final device performance, especially the V_{OC} and FF of a PSC (see Section 2.2.3).^{70,142–144} We demonstrated that spontaneous enhancement of the PCE of PSCs is mainly governed by an improvement in the V_{OC} and FF (Sections 4.2 and 4.3). Therefore, having insights into recombination mechanisms may provide us with information about the origin of the spontaneous enhancement.

Steady-state and time-resolved PL characterizations conducted on perovskite thin films reveal valuable information about charge recombination properties of PSCs (see Section 3.2.1).^{70,145} Here, we used PL measurement to gain more insights into charge recombination properties of perovskite thin films regarding the spontaneous enhancement. As presented in Figure 4.11, we observed a two-fold stronger PL intensity and a remarkably enhanced charge carrier lifetime after 10-day storage for Cs_1FM_9 perovskite thin films deposited on bare glass, which implies a reduction in non-radiative SRH recombination.^{70,146} As mentioned earlier, the strain was reported to result in trap-induced non-radiative recombination.^{139,141,147,148} Therefore, the decreased PL intensity for the pristine sample can

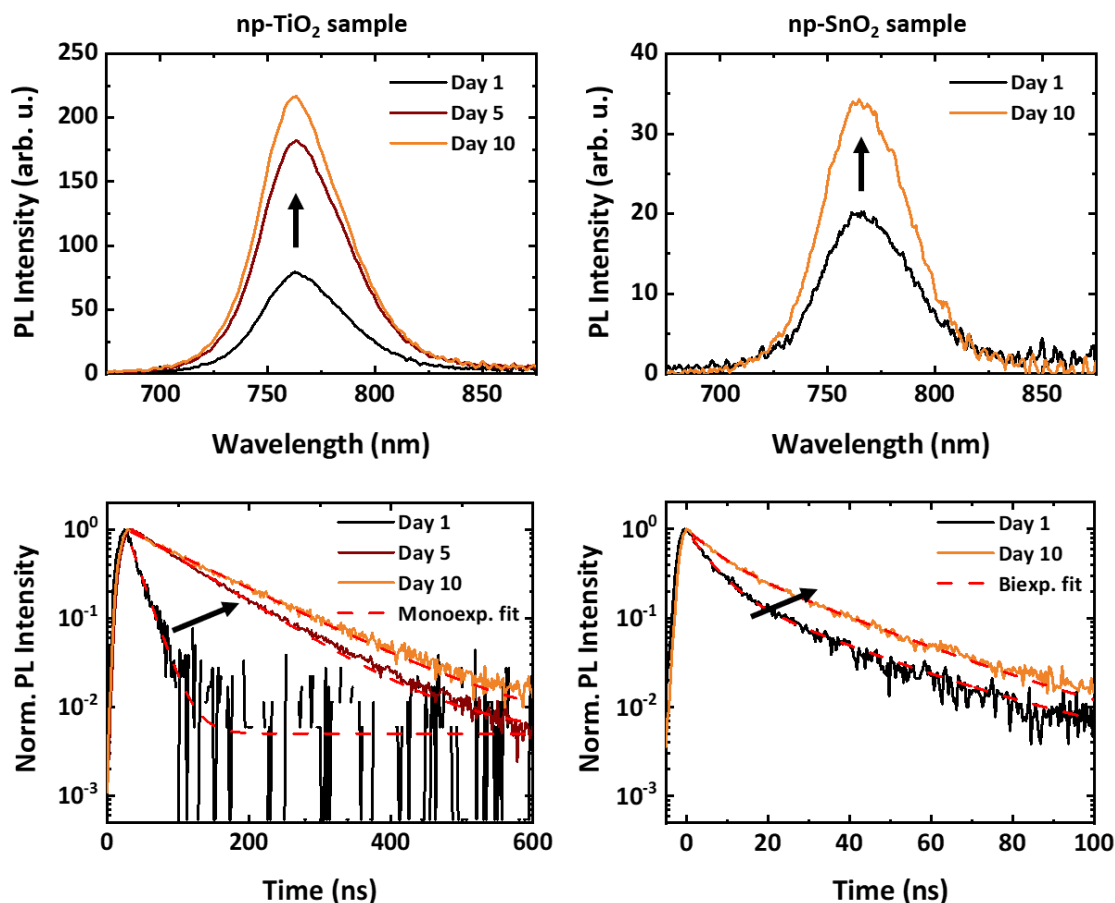


Figure 4.12. Photoluminescence (PL) spectra (top row) and normalized time-resolved PL kinetics (bottom row) of perovskite thin films deposited on ITO/np-TiO₂ (np-TiO₂ sample) and ITO/np-SnO₂ (np-SnO₂ sample). The data were collected on the day of samples preparation (day 1) and after storage (days 5 and 10). The measurements were performed by Dr. Diana Rueda-Delgado. Reproduced from [97] with permission of The Royal Society of Chemistry.

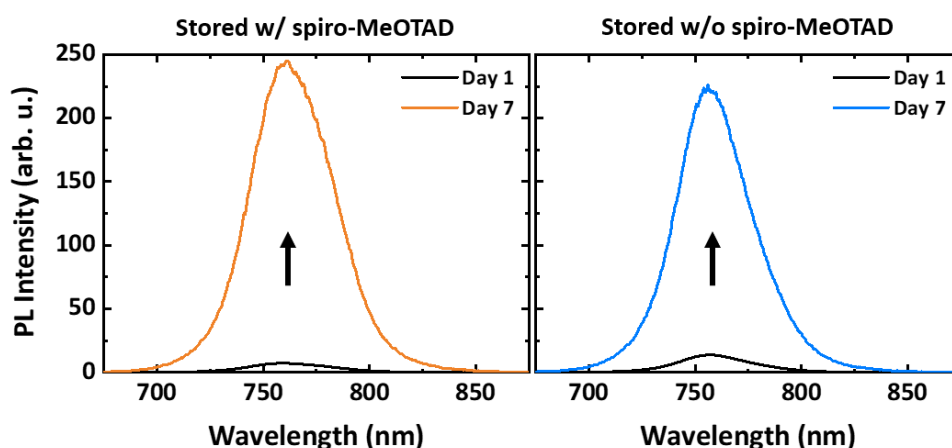


Figure 4.13. Photoluminescence (PL) spectra of Cs₁FM₉ perovskite thin films stored with (left panel) and without (right panel) spiro-MeOTAD measured on the day of samples preparation (day 1) and after storage (day 7). We use 0.15 ml chlorobenzene to wash the spiro-MeOTAD layer off the sample before measurement. The measurements were performed by Dr. Diana Rueda-Delgado. Adapted from [97] with permission of The Royal Society of Chemistry.

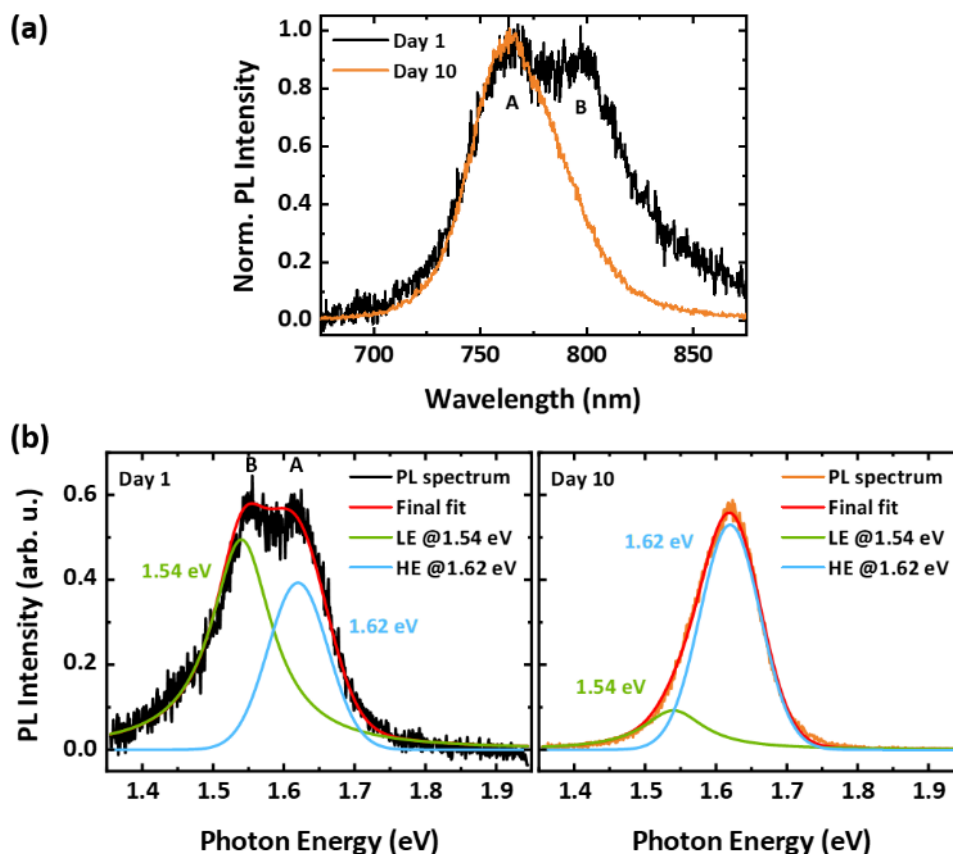


Figure 4.14. (a) Wavelength-scaled time-resolved photoluminescence (PL) spectra (normalized to peak A) integrated in a time delay between 100 to 600 ns after the excitation pulse for a Cs_1FM_9 perovskite thin film deposited on bare glass. The data were collected on the day of sample preparation (day 1) and after storage (day 10). (b) Energy-scaled PL spectra of day 1 (left panel) and day 10 (right panel) fitted with a two-peak pseudo-Voigt profile for the lower-energy (LE) and the higher energy (HE) peaks. The measurements were performed by Marius Jackoby. Reproduced from [97] with permission of The Royal Society of Chemistry.

be indicative of the existence of strain-induced (as revealed by XRD) trap states, which diminish upon strain relaxation resulting in intensified PL emission.

As mentioned in previous section, lattice strain is initiated by a mismatched thermal expansion between perovskite thin films and the substrates. Therefore, in order to determine if only a different amount of strain relaxation on the glass substrates could lead to the aforementioned observations, we conducted PL measurement on Cs_1FM_9 perovskite thin films deposited on glass substrates coated with $\text{ITO}/\text{np-TiO}_2$ and $\text{ITO}/\text{np-SnO}_2$. A similar trend (improved PL intensity and lifetime) ruled out this possibility. As shown in Figure 4.12, the PL intensity and lifetime enhanced more prominently for the np-TiO_2 samples as compared to the np-SnO_2 samples (Figure 4.12), which correlates with the different magnitude of spontaneous enhancement of the PCE in the PSCs with these ETLs (see Figure 4.5). Hence, in agreement with the literature,¹⁴⁰ we conclude that the choice of substrate can alter the level of strain initiated in the perovskite thin film and accordingly the magnitude of spontaneous enhancement of the PCE.

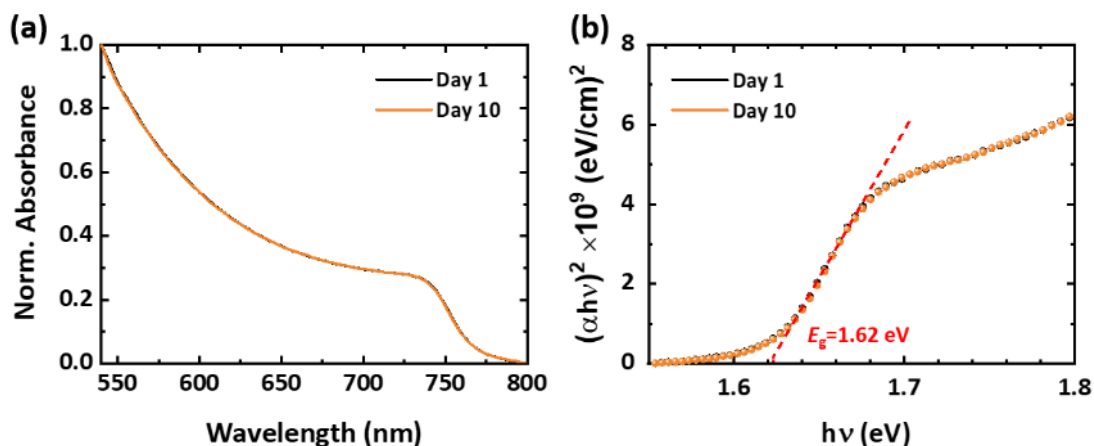


Figure 4.15. (a) Normalized absorbance of a Cs₁FM₉ perovskite thin film on the day of sample preparation (day 1) and after storage (day 10). (b) Direct optical bandgap (E_g) of the film determined by Tauc plot. Adapted from [97] with permission of The Royal Society of Chemistry.

Interestingly, as shown in Figure 4.13, the enhancement of the PL intensity of perovskite thin films was apparent for the samples stored both with and without a doped spiro-MeOTAD layer atop (the HTL of the sample with spiro-MeOTAD was washed away before the measurements). Therefore, enhancement of the PL intensity for the perovskite thin films after storage was independent of the presence of the spiro-MeOTAD HTL, which is strongly in line with the results presented in Section 4.2. PL results indicated that trap-assisted bulk recombination is dominating the total recombination in the PSCs, and its reduction explains the increased V_{OC} and FF of the respective PSCs.

To study the effect of the spontaneous enhancement on the PL spectra in more details, we performed a delayed emission spectrum, which was integrated from 100 to 600 ns after excitation, derived from a perovskite thin film before and after storage. The result revealed the coexistence of two distinct emission peaks (peak A at 763 nm and peak B at 804 nm) for the pristine perovskite thin film on day 1 (Figure 4.14a). Interestingly, after storage the same sample exhibited a remarkably intensified peak A, while peak B was completely diminished.

To identify the maximum of these peaks, at first, we converted the original wavelength-scaled PL spectra (Figure 4.14a) to energy-scale (Figure 4.14b) by applying a Jacobian transformation:¹⁴⁹

$$E = hc/\lambda, \quad f(E) \sim \lambda^2 f(\lambda) \quad 4.2$$

Additionally, to delineate a comprehensive picture, we applied a pseudo-Voigt profile (see Appendix A for more details) to fit the energy-scaled PL spectra (Figure 4.14b). Based on the findings, peaks A and B were positioned at 1.62 and 1.54 eV, respectively. Although it may not be directly correlated, the energy difference between these two peaks is comparable with the improvement in the average V_{OC} of the respective PSCs (from ~1.10 V on day 1 to ~1.17 V on day 10, see Figure 4.2c). The position of peak A at 1.62 eV correlates to the expected bandgap of the triple-cation Cs₁FM₉ perovskite thin film (as also revealed by Tauc

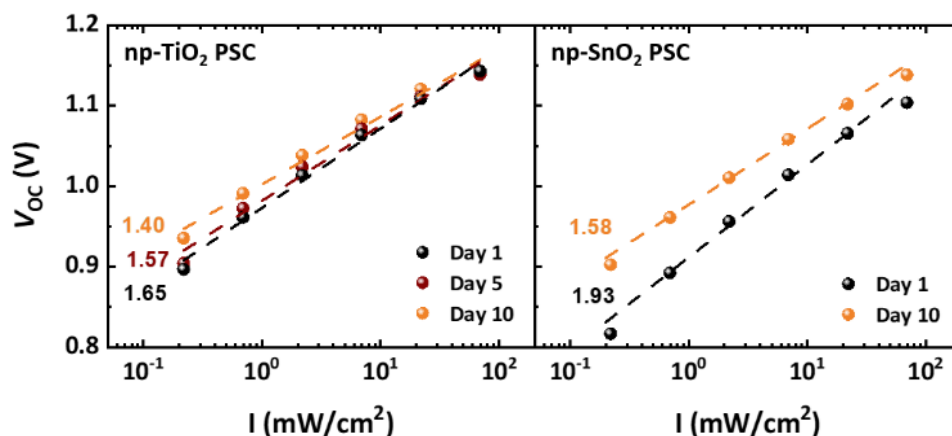


Figure 4.16. Open-circuit voltage (V_{OC}) vs. light intensity (I) measurements derived from Cs_1FM_9 PSCs with np-TiO₂ (left panel) and np-SnO₂ (right panel) electron transport layers, measured on the day of samples preparation (day 1) and after storage (days 5 and 10). Dashed lines manifest logarithmic fits and the numbers indicate the ideality factor (n_{id}) deduced from the slopes using Equation 4.3. Reproduced from [97] with permission of The Royal Society of Chemistry.

plot shown in Figure 4.15). The ratio of these peaks contributing to the total PL peak can be investigated by comparing the areas under the PL peaks (after their deconvolution) for different days. Peak analysis (see Appendix A) determined that on day 1, 66% of the PL emission comes from the lower-energy peak (peak B at 1.54 eV) and only 34% emanates from the bulk emission (peak A at 1.62 eV). While, on day 10, this ratio decreases to only 21% for Peak B and increases to 79% for the bulk emission associated to peak A.

It was recently revealed that local strain can result in phase segregation (separation of halide ions of different types).^{140,150} Therefore, the low-energy PL emission (peak B) might be associated with a lower-energy phase, which could be explained by strain-induced phase segregation for pristine samples right after film formation.¹⁵⁰ Therefore, a decrease in the intensity of peak B upon storage could be related to a volumetric reduction of the low-energy phase after strain relaxation that correlates well to the increased intensity of the bulk emission (peak A). However, even if such a lower-energy phase coexists on day 1, its volume fraction must be very low, because absorption measurements of the perovskite thin film revealed that the bandgap is equal to the bulk bandgap (~ 1.62 eV) on day 1 as well as day 10 (Figure 4.15). Thereby, even for a pristine sample the major fraction of the material must be in the bulk bandgap phase, although a small fraction of the lower-energy phase is sufficient to dominate the PL emission.

Identifying the ideality factor values of a complete solar cell is a common way to interpret the dominant recombination mechanisms.^{70,95,151,152} However, for devices with complex multilayers like PSCs, it is important to avoid misinterpreting this parameter.^{95,96} As discussed in the literature, if SRH bulk recombination is dominant, an ideality factor approaching 1 is indicative of less trap-assisted non-radiative SRH recombination and therefore desirable for PSCs.⁹⁶ As explained in Section 3.2.2, the ideality factor values can be derived from the slope of a logarithmic fit of a plot based on V_{OC} vs. light intensity (I). Figure 4.16 shows the V_{OC} of the Cs_1FM_9 PSCs (with different ETLs) as a function of light

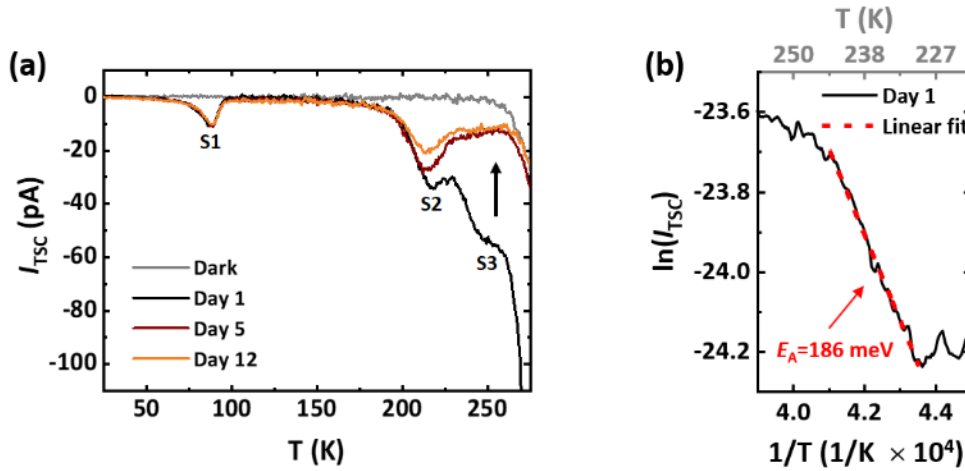


Figure 4.17. (a) Thermally stimulated current (TSC) spectra of a Cs_1FM_9 PSC measured directly after device preparation (day 1) and after storage (days 5 and 12). (b) Arrhenius plot of the respective TSC spectrum showing the activation energy (E_t) of the Cs_1FM_9 PSC measured on day 1. The red line represents the data range used for fitting initial rise associated with signal T3. The measurement were performed by Dr. Motiur Rahman Khan. Reproduced from [97] with permission of The Royal Society of Chemistry.

intensity for pristine devices (day 1) and after storage (days 5 and 10). Implementing the following expression:

$$n_{\text{id}} = \frac{qm}{k_{\text{B}}T} = 38.76 m \quad (4.3)$$

where m is the slope of the fits of the plots in Figure 4.16. We identified a gradual decrease in the ideality factor of the PSCs (independent of the ETLs) on different days of storage. As concluded from PL results, the bulk recombination is the dominant recombination mechanism in the perovskite thin films, therefore the gradual decrease of the ideality factor is indicative of a reduction in trap-assisted SRH recombination in the bulk of the perovskite thin films. Thereby, the voltage losses induced by the non-radiative SRH recombination are alleviated and can be correlated to the strain relaxation upon storage (revealed by XRD results) in the perovskite thin films deposited on different substrates. Following section will provide us with more insights into the matter.

4.6. Reduction of electronic trap states in the perovskite bulk

Thermally stimulated current (TSC) is a powerful method for characterizing complete solar cell devices to provide detailed information about electronic trap states and/or recombination centers (see Section 3.2.2).^{101,153,154} Here, we applied TSC characterization to track changes in the trap densities of the perovskite thin films of pristine and stored Cs_1FM_9 PSCs. Figure 4.17a shows the TSC responses of a PSC which was probed on day 1 (after device fabrication) and on days 5 and 12 (after the PSC demonstrated a spontaneous enhancement in its PCE) over a temperature range of 25 K to 270 K. On day 1, two distinct TSC signals were revealed at around 88 K (denoted as S1) and 215 K (denoted as S2) as well as a broad TSC signal at around 245 K (denoted as S3) that implies a broad distribution of trap states

in the pristine device. Same measurement on the same sample showed that S3 completely disappeared on days 5 and 12, while S1 did not alter and S2 reduced negligibly. Since we detected the first two signals (S1 and S2) for other PSCs with the same transport layer sequence but different perovskite absorber layers, we only considered S3 to originate from the Cs₁FM₉ perovskite thin film. Thereby, the current reduction associated with S3 is indicative of an overall suppression in trap density in the bulk and/or at the grain boundaries of the Cs₁FM₉ perovskite thin film over time.

We analyzed this signal by applying the initial rise method to estimate the activation energy of the corresponding trap states.^{153,154} Based on this method, the initial rise of the TSC signal is assumed to correspond to the moment when the trap states start to empty at a certain temperature (T) and the current (I_{TSC}) is determined as follows:

$$I_{TSC} \propto \exp(-E_t/k_B T) \quad (4.4)$$

where E_t is the activation energy of trap states and k_B is the Boltzmann constant.^{153,154} Therefore, the activation energy can be estimated from a natural logarithmic plot of the current associated with signal S3 ($\ln(I_{TSC})$) vs. reciprocal of the temperature ($1/T$), known as Arrhenius plot. As shown in Figure 4.17b, this plot gives a straight line in the beginning of the TSC peak with a slope value of $-E_t/k_B$. Using this method, we found a trap activation energy of $E_t \approx 186.0 \pm 2.2$ meV corresponding to the signal S3 for a pristine PSC on day 1.

The lower limit of the trap density (N_t) can be obtained by integrating the TSC spectrum over time for each peak according to the following expression:

$$\int_{t_0}^{t_{\text{final}}} I_{TSC} dt = bqN_t V \quad (4.5)$$

where t_0 is the time at which heating begins, b is the heating rate, and V is the volume of the sample (calculated by multiplying the device thickness by the active area).^{153,154} Here, we determined the lower limit of trap density (N_t) as 1.6×10^{16} cm⁻³ from the time integral of the TSC signal. The reduced trap signal is in line with the enhanced V_{OC} of the respective PSC upon storage. We emphasize that the trap concentration value was probably underestimated here due to the following limiting factors: (1) the peak profile was only partially observed within the measured temperature range and (2) the charge carriers might have recombined without contributing to the thermally stimulated current flow.¹⁵⁴

Overall, the TSC results revealed a reduced number of traps within the bulk at grain of the perovskite thin film after a few days of storage. Taken together with XRD analyses, we hypothesized that trap states in pristine PSCs were induced by initial strain in the lattice of the perovskite thin film directly after film fabrication. Strain relaxation over time explains the disappearance of the trap states detected by TSC characterization. The reduction in trap density comes along with a diminution of the lower-energy state detected by PL. Although no straightforward methods are providing direct proof that the observed lower-energy state

is due to the existence of strain, we hypothesize that the decrease in the low-energy PL peak is related to reduced strain in the bulk of the perovskite thin films upon storage.

4.7. Summary

In this chapter, spontaneous enhancement of PCE of PSCs with multi-cation-halide perovskite thin films is studied. We examined the spontaneous enhancement for different perovskite compositions as well as different ETLs. We also investigated whether the spontaneous enhancement is dependent on the existence of doped spiro-MeOTAD and Au. Our observations exhibited that the magnitude of spontaneous enhancement in PCE differs for PSCs with different perovskite compositions and different ETLs. We noted that devices with initially-poor PCEs tend to enhance further over time, such that the highest PCEs we observed in this study were 18.94% on day 40 (enhanced from 14.21% on day 1) and 19.60% on day 50 (enhanced from 16.30% on day 1) for PSCs with np-TiO₂ and np-SnO₂ ETLs, respectively. Moreover, by delaying the time of deposition, we ruled out effects of spiro-MeOTAD and Au on the spontaneous enhancement in PCE. Measuring $J-V$ characteristics determined that V_{OC} and FF are the main contributors to the enhanced PCE, correlating with a significant increase in the PL intensity and charge carrier lifetime of the perovskite thin films as well as a shift in the ideality factor towards radiative recombination. Moreover, as revealed by time-resolved PL spectra, initially-present low-energy state, which dominate the PL emission immediately after film formation, disappeared after a few days of storage.

Structural characterization deduced from XRD measurements disclosed a shift in the XRD patterns of a pristine perovskite thin film after storage to larger diffraction angles. Based on detailed XRD analysis, this shift is suggestive of a reduction in lattice strain in the perovskite thin films upon storage, which could be attributed to the mismatched thermal expansion between the perovskite thin films and the ETLs as the substrates. Therefore, the reduction of the low-energy state (revealed by PL measurement) could be attributed to a suppressed strain-induced phase segregation. TSC characterization supported the existence of strain-induced trap states in pristine PSC. However, strain relaxation over time (revealed by XRD analysis) leads to a reduction of these traps. From the aforementioned results, we proposed that the spontaneous enhancement of the PCE of multi-cation PSCs is attributed to a gradual reduction in strain in the bulk of perovskite thin film overtime during storage.

5. Narrow-bandgap Multi-Cation Mixed Tin/Lead Perovskite Solar Cells

In this chapter, we demonstrate that by incorporating minute quantities of Cs as a cation into $\text{FA}_{0.8}\text{MA}_{0.2}\text{Sn}_{0.5}\text{Pb}_{0.5}\text{I}_3$ perovskite absorber layer, the operational photo-stability of the respective narrow-bandgap perovskite solar cells significantly improves such that the power conversion efficiency maintains up to 99% of its initial value after 120 min constant illumination. A detailed study on the perovskite thin film suggests that the improved photo-stability correlates with a reduction in residual nanosized $\text{Sn}_y\text{Pb}_{(1-y)}\text{I}_2$ aggregates on the surface of the perovskite thin films due to reactions with Cs resulting in a volumetric growth of the perovskite thin films. Furthermore, a beneficial stoichiometric composition and better crystallinity of the perovskite absorber leads to improved photo-stability of the narrow-bandgap perovskite solar cells.

This chapter is based on our publication in the *Journal of Materials Chemistry A* [155] with the title “Triple-cation low-bandgap perovskite thin-films for high-efficiency four-terminal all-perovskite tandem solar cells”. Most of the graphs in this chapter are adapted or reproduced with permission of The Royal Society of Chemistry. The semi-transparent top perovskite solar cells employed in this chapter were developed by Saba Gharibzadeh and Ihteaz M. Hossain.

5.1. Motivation

Metal-halide perovskite semiconductors with a wide range of bandgaps (1.1-2.3)^{27,65–67,156} are suitable candidates for the top (with pure Pb mixed-halide perovskite) and the bottom (with mixed Sn/Pb perovskite) sub-cells in a tandem structure. So far, pure Pb-based perovskite solar cells (PSCs) and their applications as the top sub-cell in perovskite/Si and perovskite/CIGS tandem solar cells were the main focus of the most studies.^{24,26–28,157} However, recent advances have promoted mixed Sn/Pb narrow-bandgap PSCs with reasonable efficiencies (>20%),^{21–23,29,30} as the new candidates to replace Si and CIGS bottom sub-cells in tandem solar cell configurations benefiting from low-temperature and low-cost fabrication methods.

Despite the recent advances, the low operational stability of mixed Sn/Pb narrow-bandgap PSCs is still an obstacle for the alternative all-perovskite tandem solar cell (all-PTSC) configurations. Hence, strategies that address the poor stability of narrow-bandgap PSCs are essential. Although partial substitution of Sn^{2+} for Pb^{2+} lowers the bandgap of the perovskite absorber to the values suitable for the bottom sub-cell in all-PTSCs (1.1-1.3 eV),^{65,158–161} it results in poor stability because unlike Pb, Sn is prone to oxidation from Sn^{2+} to Sn^{4+} even in an inert atmosphere with a trace amount of oxygen.^{22,162,163} Apart from oxygen-induced degradation, light-induced degradation,^{164,165} thermal decompositions,^{164,166} and crystal-structure transition^{167,168} are the other degradation mechanisms less explored for mixed Sn/Pb PSCs. Applying 2D components as passivation layers,^{169–171} utilizing Sn-reduced precursor solutions,^{22,29} incorporating antioxidant additives such as SnF_2 ,^{163,172–175} SnBr_2 ,^{163,172,176} SnCl_2 ,^{172,177} GuaSCN,²¹ ascorbic acids,¹⁷⁸ and sulfonic acid group,¹⁷⁹ as well as compositional engineering¹⁸⁰ are established strategies to prevent oxidation.

The crystal structure of perovskite semiconductors (ABX_3) plays a prominent role in their thermal and phase-stability (see Section 2.1.2).³¹ Compositional engineering in the A-site is a proven method to tune the tolerance factor to have a stable structure. Incorporating Cs into crystalline lattice of double-cation $\text{FA}_x\text{MA}_{(1-x)}$, for example, improves the structural stability and the optoelectronic properties of pure Pb-based perovskite semiconductors.^{60,101} Integration of Cs into the lattice structure of the perovskite alters the structural properties beneficially and results in a reduction in trap density in the bulk and at the grain boundaries of the perovskite.^{60,101} Incorporating Cs into mixed Sn/Pb-based perovskite semiconductors is also beneficial for the photovoltaic performance of narrow-bandgap PSCs.^{30,161,180,181} For example, incorporating Cs into mono-cation mixed Sn/Pb-based perovskite reduces the crystallization rate that leads to an enhanced film formation and effectively restrains the Sn^{2+} oxidation even if exposed to the ambient environment.¹⁸⁰ Moreover, Cs incorporation was reported to improve the J_{SC} and V_{OC} of $\text{MASn}_{0.5}\text{Pb}_{0.5}\text{I}_3$ and $\text{FASn}_{0.5}\text{Pb}_{0.5}\text{I}_3$ PSCs remarkably.¹⁸⁰ In another study, replacing MA with Cs in $\text{FA}_{0.6}\text{MA}_{0.4}\text{Sn}_{0.6}\text{Pb}_{0.4}\text{I}_3$ was demonstrated to enhance the thermal and operational stability of the corresponding PSCs.¹⁸¹ A recent study investigated the role of Cs when integrated into a double-cation $\text{FA}_{0.5}\text{MA}_{0.5}\text{Sn}_{0.5}\text{Pb}_{0.5}\text{I}_3$ perovskite.³⁰ As proposed, Cs incorporation leads to a reduction in strain-induced trap densities and therefore improved performance of the PSCs.³⁰

In this chapter, we investigate the role of Cs in improved photo-stability when incorporated into a double-cation mixed Sn/Pb perovskite for the first time. In Section 5.2, we demonstrate that the photo-stability of $\text{Cs}_x(\text{FA}_{0.8}\text{MA}_{0.2})_{(1-x)}\text{Sn}_{0.5}\text{Pb}_{0.5}\text{I}_3$ narrow-bandgap PSCs remarkably improves upon introducing minute amounts of Cs, $x = 2.5\%$ and 5% , maintaining 92% and 99% of their initial power conversion efficiencies (PCEs), respectively. In Sections 5.3 and 5.4, we verify that the formation of nanosized $\text{Sn}_y\text{Pb}_{(1-y)}\text{I}_2$ aggregates is mitigated upon Cs incorporation based on scanning electron microscopy (SEM) and cathodoluminescence (CL) characterizations. The role of Cs in mitigation of $\text{Sn}_y\text{Pb}_{(1-y)}\text{I}_2$ aggregates (with $0 < y < 1$), is investigated by X-ray diffraction (XRD) characterizations in Section 5.5. In the last section of this chapter, Section 5.6, we combine the highest-performing triple-cation mixed Sn/Pb narrow-bandgap PSCs ($E_g \approx 1.26$ eV) with semi-transparent double-cation PSCs

($E_g \approx 1.65$ eV) and report on four-terminal (4T) all-PTSCs with PCEs as high as 23.6% (25.4% in case of using an anti-reflection coating at the front side of the top sub-cell).

5.2. Improved photo-stability of narrow-bandgap perovskite solar cells

Compared to the pure Pb-based perovskite thin films, the formation of high-quality solution-processed Sn-based perovskite thin films is more challenging to control.¹⁸² The antisolvent-quenching, which is the most common method used in spin-coating perovskite thin films, is not favorable for Sn-based perovskite thin films. Antisolvent-quenching initiates fast nucleation and crystallization and produces very small crystallites with increased grain boundaries which is not beneficial for Sn-based PSC in contrast to their Pb-based counterparts.^{158,183} Vacuum-assisted growth control (VAGC) is an efficient approach to processes uniform and pinhole-free Sn-based perovskite thin films even on extremely hydrophobic substrates such as PTAA (see Section 3.1.1).¹⁸⁴ Therefore, we used this method to prepare mixed Sn/Pb narrow-bandgap perovskite absorber layers in the composition $Cs_x(FA_{0.8}MA_{0.2})_{(1-x)}Sn_{0.5}Pb_{0.5}I_3$, hereafter denoted as Cs_x with $x = 0\%$, 1% , 2.5% , 5% , and 10% . Figure 5.1a exhibit a schematic illustration of the layer stack of a narrow-bandgap PSC consisting of glass / ITO / PTAA / perovskite / PCBM / C₆₀ / BCP / Ag and a cross-sectional SEM image of the same layer stack for $x = 2.5\%$ (denoted as Cs2.5%).

We compared the PCE of the best-performing narrow-bandgap PSCs prepared with different Cs concentrations (denoted as Cs0%, Cs1%, Cs2.5%, Cs5%, and Cs10%) (Figure 5.1b) from maximum power point (MPP) tracking measurement. Cs2.5% PSC provided the highest PCE of 17.5%, which is a respectable value for narrow-bandgap PSCs. Notably, as presented in Figure 5.1c, a clear trend in the operational photo-stability of these devices exhibited a significant improvement upon incorporation of Cs. The PSCs with Cs2.5% and Cs5% maintained 92% and 99% of their initial efficiencies after 120 min MPP tracking (in a nitrogen-filled glovebox with an oxygen level of ≈ 50 ppm). By contrast, a PSC without Cs (denoted as Cs0%) degraded to 61% of its initial value under the same measurement. We confirmed the reproducibility of the observed trend regarding the PCE with different Cs concentrations by measuring the efficiency of six identically prepared PSCs (for each Cs concentration) under MPP tracking conditions (see Figure B1 in Appendix B).

The current-density–voltage (J – V) characteristics (Figure 5.1d) revealed that the highest PCE ($\approx 18.2\%$) provided by a Cs2.5% PSC was enabled by a short-circuit current (J_{SC}) of 32.0 mA/cm². The integrated J_{SC} values calculated from the external quantum efficiency (EQE) responses of the PSCs with Cs0%, Cs1%, Cs2.5%, Cs5%, and Cs10% (Figure 5.1e) were 29.4 , 29.5 , 31.4 , 29.0 , 27.3 mA/cm², respectively, confirming the observed trend in the J_{SC} derived from the J – V characteristics. Moreover, statistical distribution of the J – V characteristics (Figure 5.2) from 30 identically prepared PSCs (for each Cs concentration) verified that the PCE of PSCs with Cs2.5% was the highest in average. The J – V characteristics of the champion PSCs and the average values of the PSCs from Figure 5.2 are also summarized in Table 5.1.

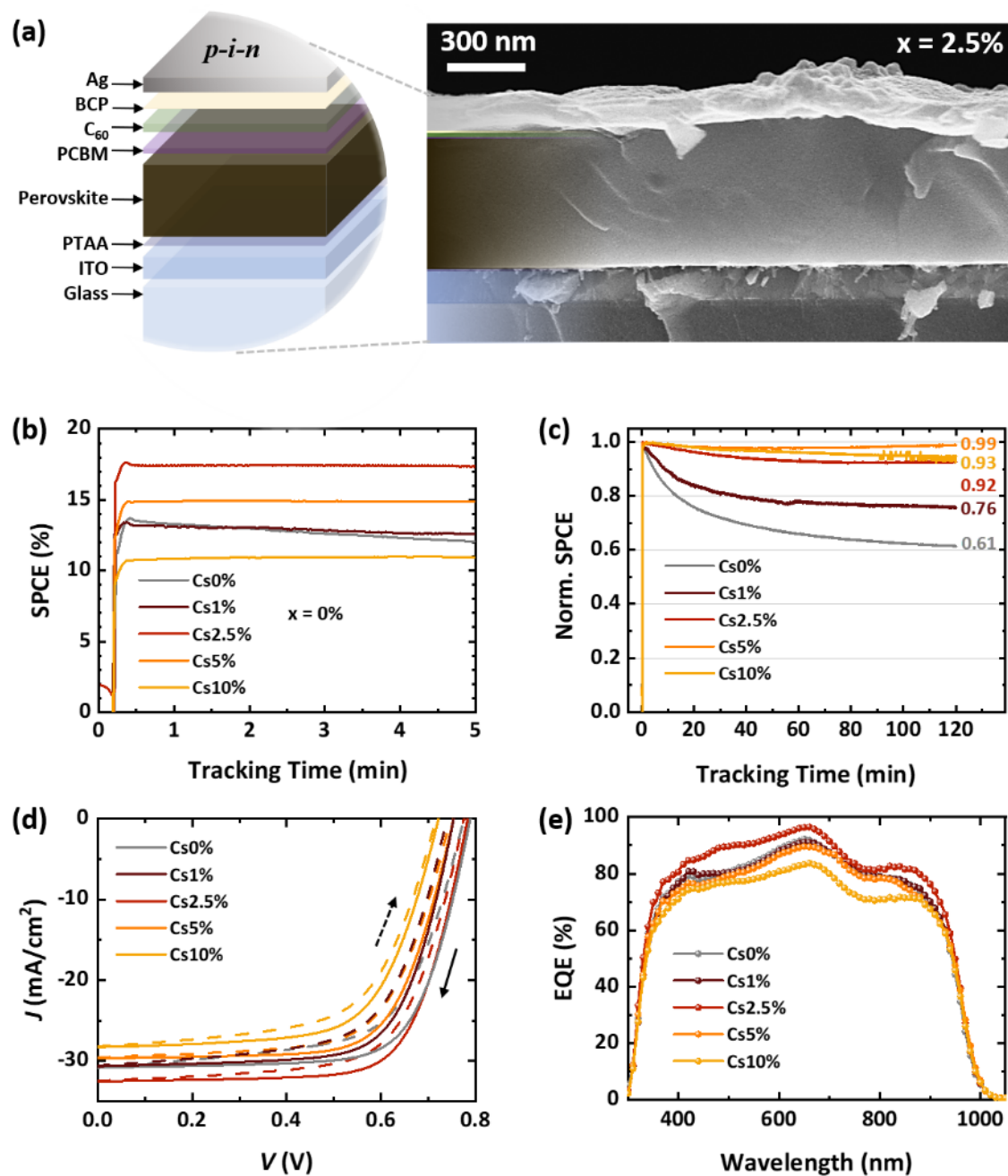


Figure 5.1. (a) A schematic illustration of the layer stack and a cross-sectional scanning electron microscopy (SEM) image of a narrow-bandgap PSC with 2.5% Cs concentration (denoted as Cs2.5%). (b) Power conversion efficiency (PCE) from maximum power point (MPP) tracking of the best performing narrow-bandgap PSCs with Cs_x(FA_{0.8}MA_{0.2})_(1-x)Sn_{0.5}Pb_{0.5}I₃ perovskite thin films prepared with different Cs concentrations varying from 0% to 1%, 2.5%, 5%, and 10% (denoted as Cs0%, Cs1%, Cs2.5%, Cs5% and Cs10%) at MPP tracking condition. (c) PCE from MPP tracking for 120 min of the same PSCs normalized to their initial values (when the light is switched on). (d) Current-density–voltage (*J*–*V*) characteristics and (e) external quantum efficiency (EQE) spectra of the same PSCs. The SEM measurement was performed by Dr. Tobias Abzieher. Reproduced from [155] with permission of The Royal Society of Chemistry.

To be mentioned, the PCE of the mixed Sn/Pb PSCs improved slightly after one night storage in a nitrogen-filled glovebox (with an oxygen level of ≈ 50 ppm). As shown in Figure B2 (Appendix B), the enhancement in PCE was driven by the slightly enhanced V_{OC} and FF.

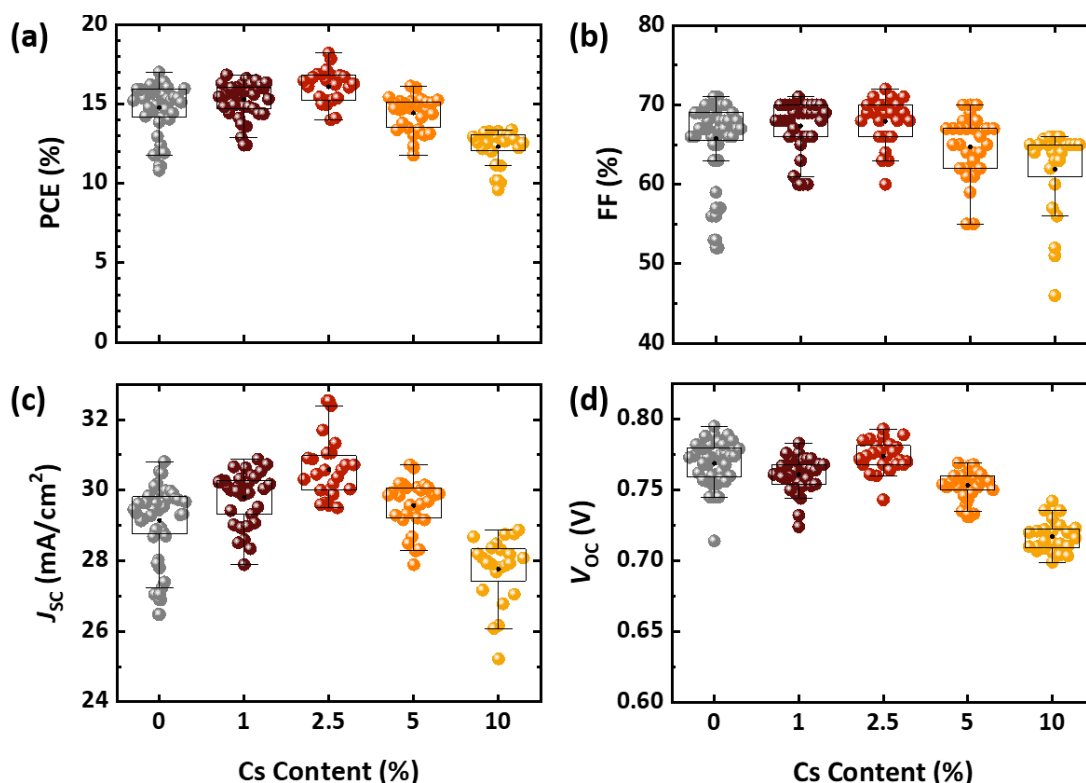


Figure 5.2. Statistical distribution of (a) power conversion efficiency (PCE), (b) fill factor (FF), (c) short-circuit current (J_{sc}), and (d) open-circuit voltage (V_{oc}) of $Cs_x(FA_{0.8}MA_{0.2})_{(1-x)}Sn_{0.5}Pb_{0.5}I_3$ narrow-bandgap PSCs with different Cs concentrations varying from 0% to 10%. The black dots show the average values of 30 PSCs that are identically prepared in 10 different batches. Reproduced from [155] with permission of The Royal Society of Chemistry.

Earlier in Chapter 4, we introduced this phenomenon as ‘spontaneous enhancement’. We showed that it is a common observation for multi-cation Pb-based PSCs with different perovskite compositions possibly attributed to gradual relaxation of lattice strain over time. However, the magnitude of the spontaneous enhancement of PCE was negligible for mixed Sn/Pb PSCs. We explain this by considering the different fabrication method we used for preparing the mixed Sn/Pb perovskite thin films. Strain arises during the annealing and cooling process, which was 1 hour at 100 °C for the perovskite thin films we investigated in Chapter 4. However, here, we used vacuum-assisted method followed by only 7 min at 100 °C annealing step, which could possibly lead to less amount of residual strain.

5.3. Morphology and surface characterizations

Studying the morphology of the perovskite thin films can reveal valuable information about the effect of Cs in the photovoltaic enhancement of the PSCs. Therefore, we compared the morphology of the surface of the perovskite thin films prepared with different Cs concentrations. SEM images (Figure 5.3a) revealed that the perovskite thin films with Cs0% to Cs5% were all compact and pinhole-free. By contrast, a perovskite thin film with Cs10% possessed a poor morphology with inhomogeneous coverage composed of pinholes and cracks between the grains. As evidenced by SEM images, the size of the perovskite grains gradually enlarged from 217 nm for Cs0% to 570 nm for Cs10%, upon increasing the

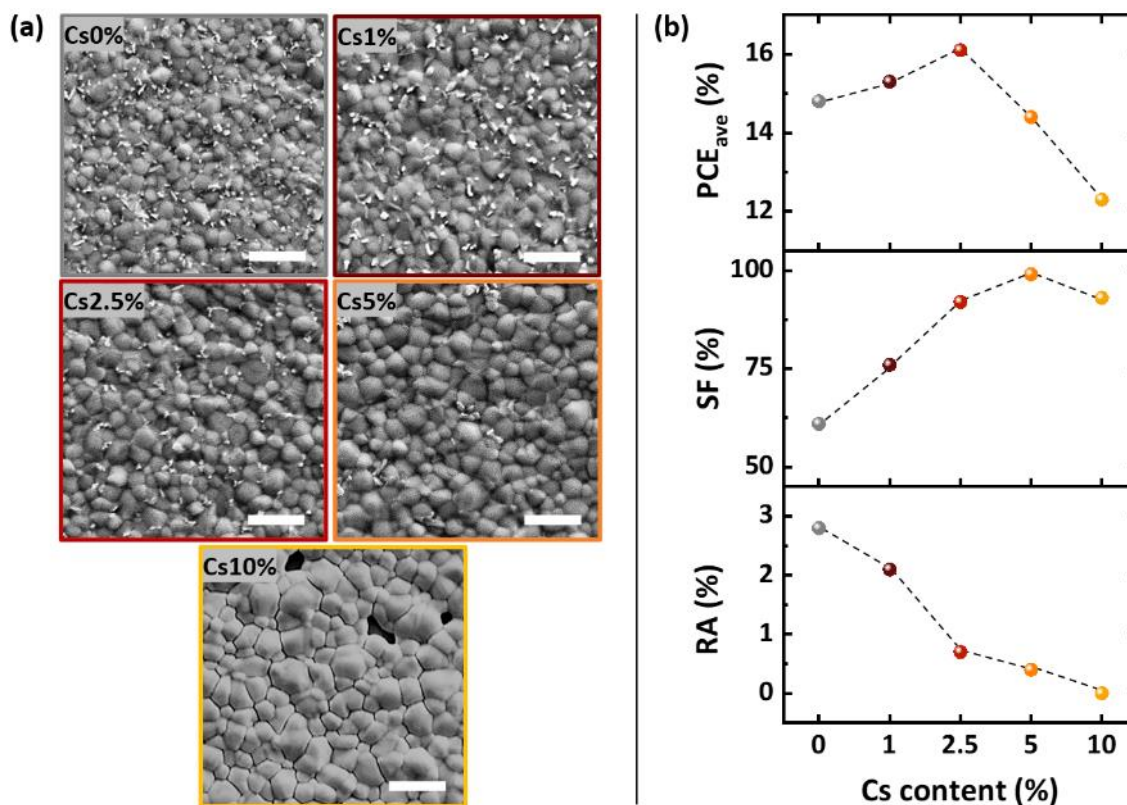


Figure 5.3. (a) Top-view scanning electron microscopy (SEM) images of $Cs_x(FA_{0.8}MA_{0.2})_{(1-x)}Sn_{0.5}Pb_{0.5}I_3$ narrow-bandgap perovskite thin films with Cs concentrations varying from $x = 0\%$, to 1%, 2.5%, 5%, and 10% (denoted as Cs0%, Cs1%, Cs2.5%, Cs5%, and Cs10%, respectively). The scalebar is indicative of 1 μm . (b) Comparison of the relative area (RA) of the bright nanosized aggregates (RA = area of the aggregates/area of the grains), the stability factor (SF = $SPCE_{final}/SPCE_{initial}$), and the average PCE (PCE_{ave}) of the PSCs as a function of Cs content. $SPCE_{final}$ and $SPCE_{initial}$ are the initial and final values of the stabilized PCE (SPCE) derived from maximum power point tracking for 120 min. SEM measurements were performed by Dr. Bahram Abdollahi Nejand. Reproduced from [155] with permission of The Royal Society of Chemistry.

amount of Cs concentration. Larger grains are indicative of fewer grain boundaries. As mentioned in Chapter 4, the role of grain boundaries on the performance and the stability of the PSCs is still under debate.^{122,123} In several studies, grain boundaries were reported to act as trap centers that cause recombination losses, and therefore decrease device stability under illumination.^{124,185,186} This is in line with our observations for narrow-bandgap PSCs with different Cs concentrations. For the investigated range, the perovskite thin films with higher Cs concentration (up to 5%) had larger grains (fewer grain boundaries) and the corresponding PSCs showed better photo-stability. PSCs with Cs10%, however, showed poor stability due to pin-holes and poor morphology of the perovskite thin films.

More importantly, SEM images revealed the existence of bright nanosized aggregates (<100 nm) on the perovskite thin films. These aggregates were reduced with increasing Cs and completely disappeared for perovskite thin films with Cs10%. By comparing the relative area (RA) of the bright aggregates (RA = area of the aggregates/area of the grains) with the stability factor (SF = $SPCE_{final}/SPCE_{initial}$; SPCE stands for stabilized PCE extracted from

MPP tracking measurement) and the average PCE (PCE_{ave} , from $J-V$ characteristics) of the narrow-bandgap PSCs for different Cs concentrations in the investigated range, we realized that an optimal amount of Cs (5%) is beneficial for device stability, while a lower amount of Cs (2.5%) is sufficient to attain the highest PCE.

Having verified that the reduction of these aggregates relates to the improvement in the operational photo-stability of the respective PSCs upon increasing Cs, one hypothesis for the origin of the bright aggregates would be residual PbI_2 . PbI_2 crystals were shown to suffer from an intrinsic photo-instability triggered by photo-decomposition under illumination.^{187–189} Residual PbI_2 in Pb-based perovskite thin films was reported to cause photo-induced degradation under illumination even in an inert atmosphere.^{187,188,190,191} Here, for the mixed Sn/Pb perovskite, the bright aggregates might be composed of residual PbI_2 , SnI_2 , or a mixture of both. This motivated us for further investigations to provide more insights into the origin of these aggregates, which will be discussed in the following sections.

5.4. Reduction of residual $Sn_yPb_{(1-y)}I_2$

Several studies have utilized cathodoluminescence (CL) characterization (see Section 3.2.1) as a suitable technique to detect phase segregations and residual materials such as PbI_2 in the perovskite thin films.^{192–194,195} Here, we collected the CL spectra of the mixed Sn/Pb perovskite thin films with different Cs concentrations within the spectral range from 400 to 900 nm (Figure 5.4a). An emission peak at around 600 nm implied the presence of a wide-bandgap phase or a material with a bandgap of about 2.1 eV, which is much higher than the bulk bandgap of the narrow-bandgap perovskite thin films (≈ 1.26 eV). Interestingly, this peak gradually diminished by increasing the Cs concentration from 0% to 10%.

To corroborate the above-mentioned hypothesis regarding the existence of PbI_2 , SnI_2 , or a mixture of both, we prepared $Sn_yPb_{(1-y)}I_2$ thin films with $y = 0, 0.5,$ and 1 for CL

Table 5.1. Current-density–voltage ($J-V$) characteristics of champion (Ch.) narrow-bandgap PSCs with different Cs concentrations varying from 0% to 10%. The average (Ave.) values are derived from 30 narrow-bandgap PSCs identically prepared in 10 different batches. Reproduced from [155] with permission of The Royal Society of Chemistry.

Cs Concentration	Scan Direction	V_{OC} (V)		J_{SC} (mA/cm ²)		FF (%)		PCE (%)	
		Ch.	Ave.	Ch.	Ave.	Ch.	Ave.	Ch.	Ave.
Cs0%	Backward	0.79	0.77	30.8	29.1	70.6	65.8	17.2	14.8
	Forward	0.77	0.76	30.9	28.9	63.3	60.5	15.2	13.2
Cs1%	Backward	0.75	0.76	30.7	29.8	69.2	67.3	16.0	15.3
	Forward	0.74	0.75	30.6	29.7	63.4	62.0	14.3	13.8
Cs2.5%	Backward	0.78	0.78	32.5	30.6	71.8	68	18.2	16.1
	Forward	0.77	0.77	32.5	30.4	66.5	63.7	16.7	14.8
Cs5%	Backward	0.75	0.75	29.7	29.6	68.9	64.7	15.4	14.4
	Forward	0.75	0.75	29.6	29.3	65.7	61.2	14.5	13.3
Cs10%	Backward	0.72	0.72	28.3	27.8	65.3	62.0	13.3	12.3
	Forward	0.72	0.73	28.3	26.5	61.4	61.1	12.4	11.9

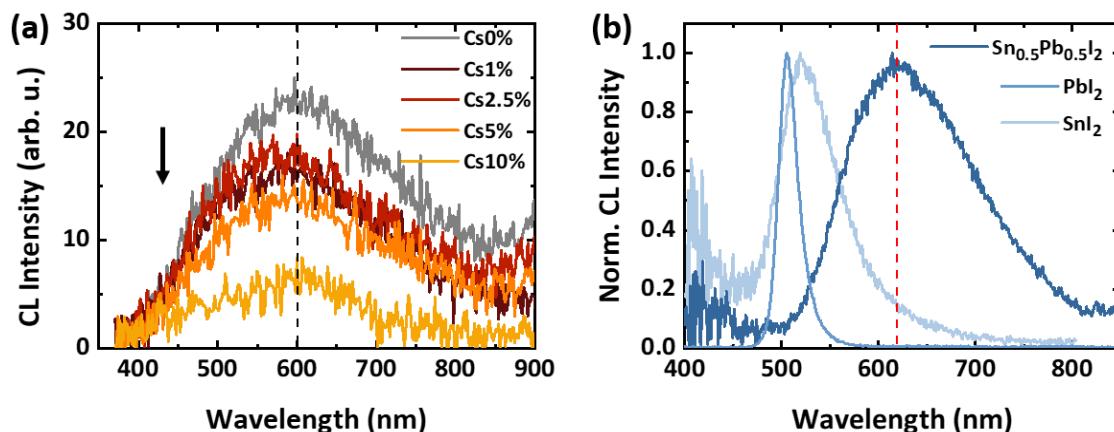


Figure 5.4. Cathodoluminescence (CL) spectrum obtained from (a) $\text{Cs}_x(\text{FA}_{0.8}\text{MA}_{0.2})_{(1-x)}\text{Sn}_{0.5}\text{Pb}_{0.5}\text{I}_3$ narrow-bandgap perovskite thin films prepared with different Cs concentrations varying from $x = 0\%$, to 1% , 2.5% , 5% , and 10% (denoted as Cs0%, Cs1%, Cs2.5%, Cs5%, and Cs10%, respectively) and (b) PbI_2 , SnI_2 , and $\text{Sn}_{0.5}\text{Pb}_{0.5}\text{I}_2$ thin films. The CL measurements were performed by Huyen Phan in collaboration with Dr. The Duong at Australian National University. Reproduced from [155] with permission of The Royal Society of Chemistry.

measurement. The results (Figure 5.4b) revealed narrow peaks at 505 nm (for PbI_2 ; $y = 0$) and 518 nm (for SnI_2 ; $y = 1$). Whereas the mixed $\text{Sn}_{0.5}\text{Pb}_{0.5}\text{I}_2$ ($y = 0.5$) displayed a broad CL peak positioned at around 600 nm that matches well with the CL emission peak (at 618 nm) associated to the narrow-bandgap perovskite thin films (Figure 5.4a). The anomalous trend that we observed in the bandgap of $\text{Sn}_y\text{Pb}_{(1-y)}\text{I}_2$ (2.46, 2.07, and 2.39 eV for $y = 0, 0.5$, and 1, respectively) does not fulfill Vegard's law.¹⁹⁶ The deviation from the linear behavior in the bandgap (with respect to y) is probably due to the 'band inversion' model.^{197,198} According to this model, a band inversion occurs with varying ' y ', which is correlated to the bandgap of SnI_2 being 'inverted' relative to the bandgap of PbI_2 . This occurs because the conduction band minimum in SnI_2 and the valence band maximum in PbI_2 has a similar orbital composition. A similar trend was also detected for $\text{MASn}_x\text{Pb}_{(1-x)}\text{I}_3$ perovskite thin films due to the same reason, where the bandgap was determined as 1.55, 1.17, and 1.30 eV for $x = 0, 0.5$, and 1, respectively.⁶⁵

To conclude, the CL results together with the SEM images suggested that the observed bright aggregates were mixed $\text{Sn}_y\text{Pb}_{(1-y)}\text{I}_2$ composite with $0 < y < 1$ that gradually decrease by adding more Cs. Being located atop perovskite thin film, the $\text{Sn}_y\text{Pb}_{(1-y)}\text{I}_2$ aggregates with a bandgap of about 2.1 eV (as detected by CL) can impede the extraction of electrons from perovskite into PCBM electron transport layer (ETL) and hinder the photo-stability of the PSCs. In the following, we investigate the possible mechanisms resulting in the appearance of the $\text{Sn}_y\text{Pb}_{(1-y)}\text{I}_2$ by studying the effect of Cs on the crystal structure of the mixed Sn/Pn narrow-bandgap perovskite thin films.

Regardless of the amount of Cs, XRD patterns of $\text{Cs}_x(\text{FA}_{0.8}\text{MA}_{0.2})_{(1-x)}\text{Sn}_{0.5}\text{Pb}_{0.5}\text{I}_3$ thin films (Figure 5.5a) exhibited two dominant perovskite peaks at 14.1° and 28.3° that were assigned to the (002)/(110) and (004)/(220) planes of the tetragonal perovskite crystal structure, respectively.¹⁹⁹ A gradual growth in the intensity of these two peaks upon increasing Cs is indicative of an improved crystallinity and/or a change in the preferential crystal orientation

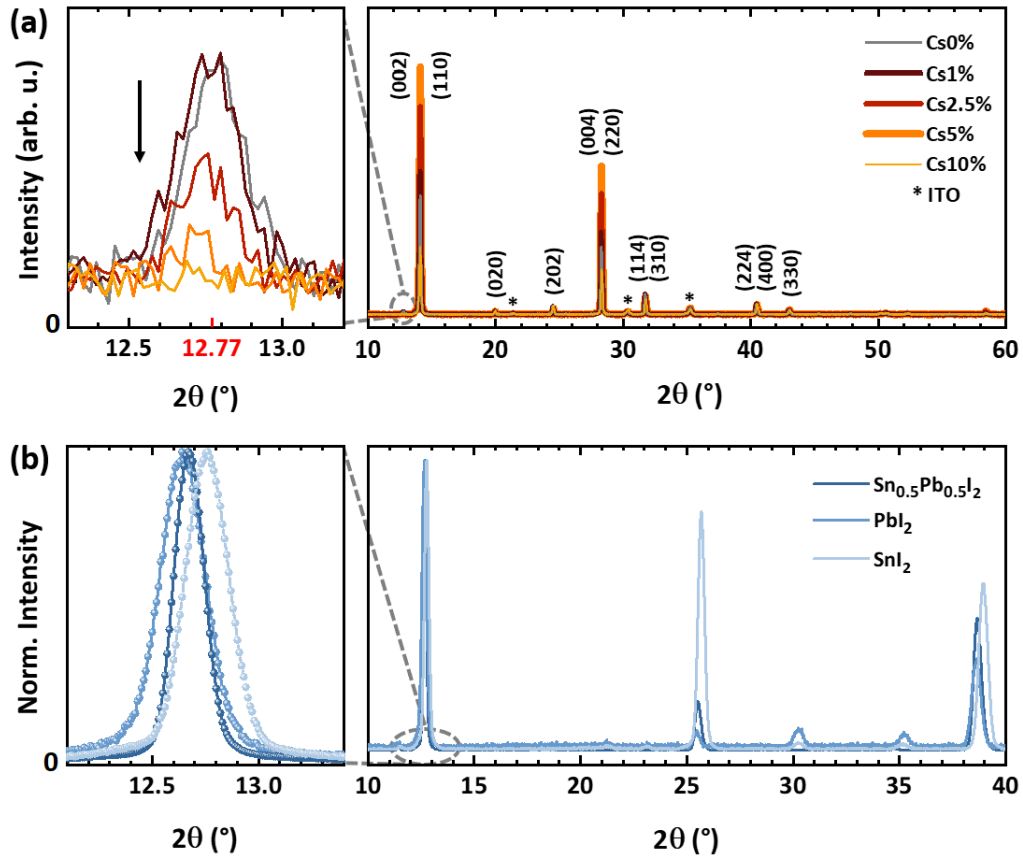


Figure 5.5. (a) X-ray diffraction (XRD) patterns of $\text{Cs}_x(\text{FA}_{0.8}\text{MA}_{0.2})_{(1-x)}\text{Sn}_{0.5}\text{Pb}_{0.5}\text{I}_3$ narrow-bandgap perovskite thin films with different Cs concentrations varying from $x = 0\%$, to 1% , 2.5% , 5% , and 10% (denoted as Cs0%, Cs1%, Cs2.5%, Cs5%, and Cs10%, respectively); left panel exhibits suppression of the XRD peak at 12.77° by increasing Cs content. (b) XRD patterns of $\text{Sn}_{0.5}\text{Pb}_{0.5}\text{I}_2$, PbI_2 , and mixed $\text{Sn}_{0.5}\text{Pb}_{0.5}\text{I}_2$; left panel compares the position of the first (main) XRD peak of each film. XRD measurement presented in figure b were performed by Dr. Tobias Abzieher. Reproduced from [155] with permission of The Royal Society of Chemistry.

of the perovskite thin film, which correlates with the observed increase in the grains' sizes for higher Cs concentrations (up to 5%). However, too high cation excess in the perovskite precursor solution^{189,191} and/or approaching the substitution limit (spinodal decomposition)^{60,200,201} are possible reasons for explaining the weak intensity of the XRD peaks detected for the perovskite thin films with Cs10%.

Most importantly, as shown in the left panel of Figure 5.5a, we realized that the intensity of a peak at 12.77° weakened as the concentration of Cs increased from 0% to 5% and disappeared for 10%. The XRD results derived from $\text{Sn}_y\text{Pb}_{(1-y)}\text{I}_2$ thin films with $y = 0, 0.5,$ and 1 (Figure 5.5b), which were deposited on ITO-coated glass substrates, revealed dominant peaks at $12.56^\circ, 12.76^\circ,$ and $12.67^\circ,$ respectively. The signal quality of the XRD data was not sufficient to discriminate between these materials. However, taken together with the CL results, we ascribed the peak at 12.77° detected in XRD patterns of the mixed Sn/Pb narrow-bandgap perovskite thin films to $\text{Sn}_y\text{Pb}_{(1-y)}\text{I}_2$ with ($0 < y < 1$) diminishing gradually upon adding Cs, in line with the number of bright aggregates detected in SEM images for higher Cs concentrations.

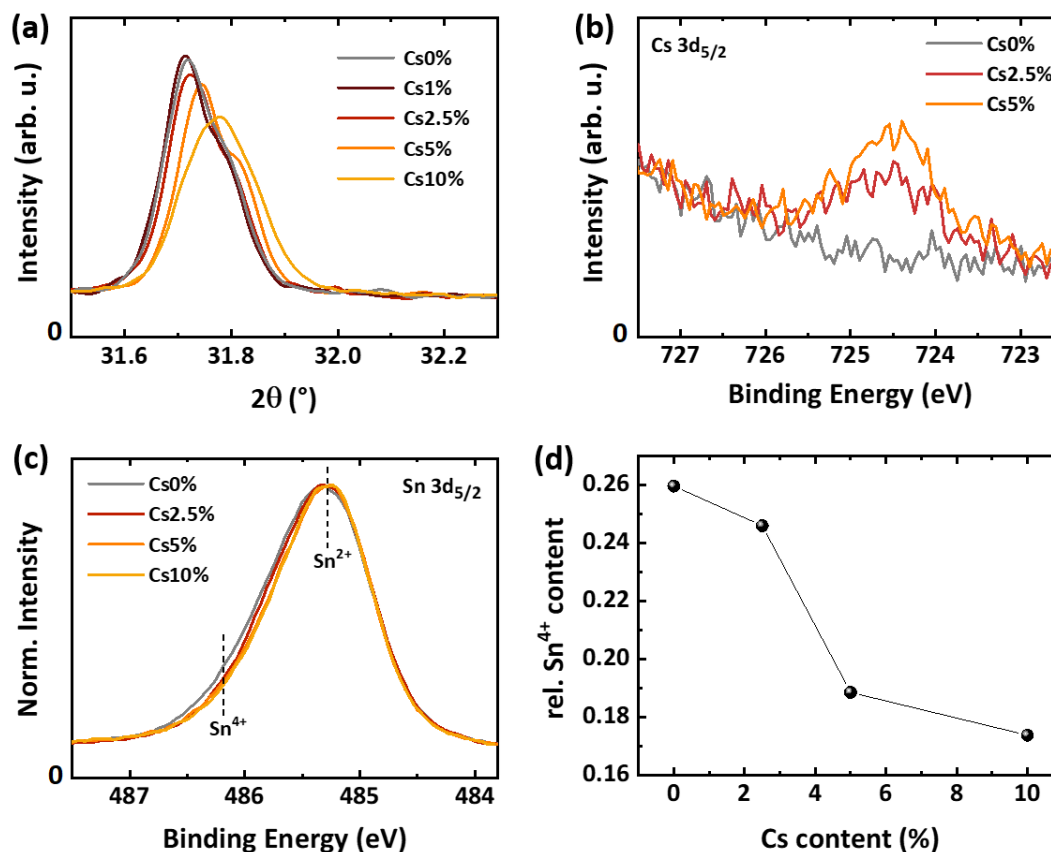


Figure 5.6. (a) X-ray diffraction (XRD) peaks assigned to (114)/(310) planes of the $\text{Cs}_x(\text{FA}_{0.8}\text{MA}_{0.2})_{(1-x)}\text{Sn}_{0.5}\text{Pb}_{0.5}\text{I}_3$ narrow-bandgap perovskite thin films shifting to larger diffraction angles by increasing Cs concentration. X-ray photoelectron spectroscopy (XPS) spectra of (b) the Cs 3d_{5/2} and (c) the Sn 3d_{5/2} core levels of the narrow-bandgap perovskite thin films with different Cs concentrations varying from 0% to 2.5%, 5%, and 10% (denoted as Cs0%, Cs2.5%, Cs5%, and Cs10%). (d) Relative change of Sn⁴⁺ as a function of Cs concentration. The XPS measurements were performed by Dr. Dirk Hauschild and Dr. Lothar Weinhardt. Figures a and b are reproduced from [155] with permission of The Royal Society of Chemistry.

A shift in the XRD peaks into the larger reflection angles (Figure 5.6a) is indicative of a lattice contraction upon the incorporation of Cs (with a much smaller ionic radius of 1.81 Å compared to FA⁺ and MA⁺ with ionic radii of 2.79 Å and 2.70 Å, respectively) into the lattice structure of the perovskite thin film.¹⁸⁰ The incorporation of Cs into the lattice, which was also confirmed by X-ray photoelectron microscopy (XPS) characterization (Figure 5.6b), was reported to reduce the crystallization rate and slow down the Sn²⁺ oxidation to Sn⁴⁺ due to a lattice contraction and a denser morphology of the perovskite thin films.¹⁸⁰ In agreement with the literature,¹⁸⁰ the Sn 3d_{5/2} core level XPS spectra of the $\text{Cs}_x(\text{FA}_{0.8}\text{MA}_{0.2})_{(1-x)}\text{Sn}_{0.5}\text{Pb}_{0.5}\text{I}_3$ narrow-bandgap perovskite thin films (Figure 5.6c) portrayed that Sn⁴⁺ was reduced by a factor of ≈ 2 by increasing Cs concentration from $x = 0\%$ to 10% (Figure 5.6d).

5.5. Investigation of Sn_yPb_(1-y)I₂ excess in perovskite thin films

In this section, we carried out further XRD analyses to understand the effectiveness of Cs incorporation in decreased residual Sn_yPb_(1-y)I₂. Figure 5.7 depicts XRD patterns of

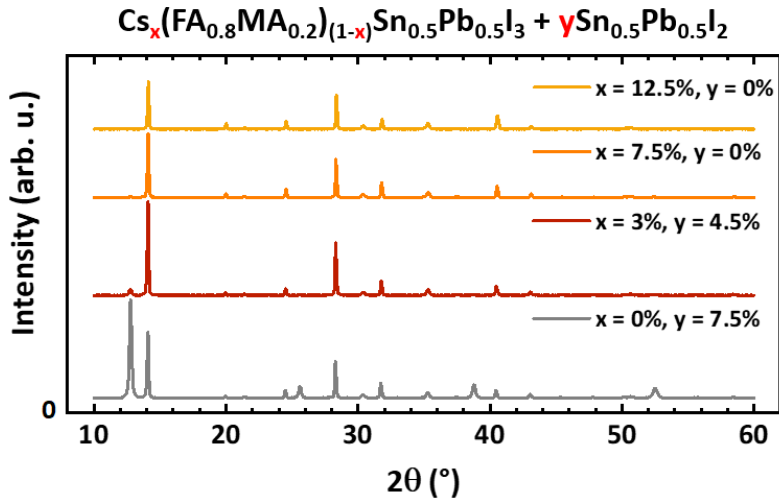


Figure 5.7. X-ray diffraction (XRD) patterns of $\text{Cs}_x(\text{FA}_{0.8}\text{MA}_{0.2})_{(1-x)}\text{Sn}_{0.5}\text{Pb}_{0.5}\text{I}_3$ prepared with a varying excess of Sn and Pb ($y\text{Sn}_{0.5}\text{Pb}_{0.5}\text{I}_2$) from $y = 7.5\%$, to 4.5% and 0% depending on the Cs concentrations, which varies from $x = 0\%$, to 3% , 7.5% , and 12.5% . Reproduced from [155] with permission of The Royal Society of Chemistry.

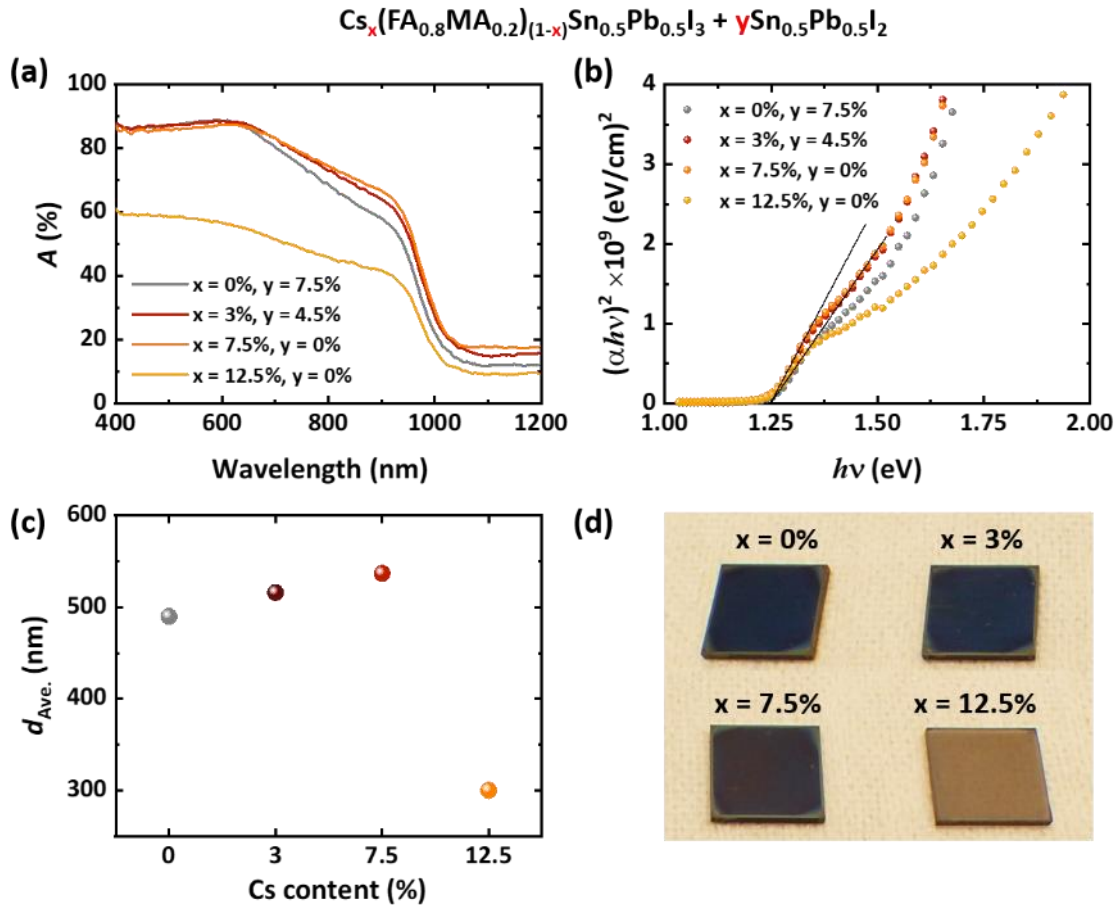


Figure 5.8. (a) Absorbance spectra (A), (b) Tauc plots, (c) the average thicknesses ($d_{\text{Ave.}}$), and (d) pictures of $\text{Cs}_x(\text{FA}_{0.8}\text{MA}_{0.2})_{(1-x)}\text{Sn}_{0.5}\text{Pb}_{0.5}\text{I}_3$ thin films prepared with excess Sn and Pb for different Cs concentrations of $x = 0\%$, 3% , 7.5% , and 12.5% . All the layers are deposited on glass substrates. The average thickness ($d_{\text{Ave.}}$) of each layer is an average of ten values obtained from two different samples on five different spots on each. Reproduced from [155] with permission of The Royal Society of Chemistry.

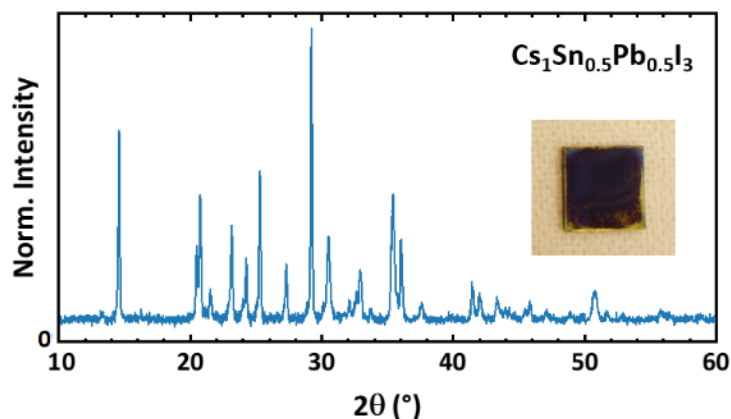


Figure 5.9. X-ray diffraction (XRD) pattern of a $\text{Cs}_1\text{Sn}_{0.5}\text{Pb}_{0.5}\text{I}_3$ thin film. Reproduced from [155] with permission of The Royal Society of Chemistry.

$\text{Cs}_x(\text{FA}_{0.8}\text{MA}_{0.2})_{(1-x)}\text{Sn}_{0.5}\text{Pb}_{0.5}\text{I}_3$ thin films that we intentionally prepared with pronounced amounts of Sn and Pb excess ($\approx 7.5\%$) while varying the Cs concentration from $x = 0\%$ to 3%, 7.5%, and 12.5%. A dominant peak at 12.77° and two small peaks at 25.5° and 38.5° appeared in the absence of Cs ($x = 0\%$), in accordance with the peaks detected for $\text{Sn}_{0.5}\text{Pb}_{0.5}\text{I}_2$ thin film (compare Figures 5.5b and 5.7), which is indicative of the existence of a considerable amount of $\text{Sn}_y\text{Pb}_{(1-y)}\text{I}_2$. More importantly, the dominant peak at 12.77° agrees with the small XRD peak detected for the narrow-bandgap perovskite thin films (compare Figures 5.5a and 5.7). By adding a minute amount of Cs, this peak that is ascribed to the existence of a large amount of residual $\text{Sn}_y\text{Pb}_{(1-y)}\text{I}_2$ subsided significantly, while the main perovskite peaks at 14.1° and 28.3° intensified remarkably. Increasing the amount of Cs to further values resulted in a further decrease (for $x = 7.5\%$) and a complete disappearance (for $x = 12.5\%$) of the $\text{Sn}_y\text{Pb}_{(1-y)}\text{I}_2$ XRD peak. The perovskite peaks also started to abate upon increasing Cs.

Ultraviolet-visible (UV-vis) measurements of the samples (Figure 5.8a) revealed an increase (for $x = 3\%$ and 7.5%) and a significant drop (for $x = 12.5\%$) in the absorption of the thin films, compared to that for a perovskite layer with no Cs ($x = 0\%$). This agrees with the average thickness of the perovskite thin films, i.e., 490, 516, 534, and 300 nm for $x = 0\%$, 3.5%, 7.5%, and 12.5%, respectively (Figures 5.8c and 5.8d). As mentioned earlier, the reduced absorption and the average thickness of the thin film with too large Cs concentration could be attributed to a too high cation excess in the precursor solution^{189,191} and/or substitution limit (spinodal decomposition)^{60,200,201}. Considering that the calculated bandgap of the thin films (according to Tauc plots) was independent of the Cs concentration (Figure 5.8b), we assumed that the increase in the absorption of the layers is indicative of a volumetric growth of the perovskite material in agreement with the intensified perovskite XRD peaks for $x = 3\%$ and 7.5% (Figure 5.7). These observations correlated well with the improved J_{SC} (Figure 5.2) of the PSCs with sufficient Cs concentrations and significantly diminished J_{SC} for too high Cs concentration (Cs10%).

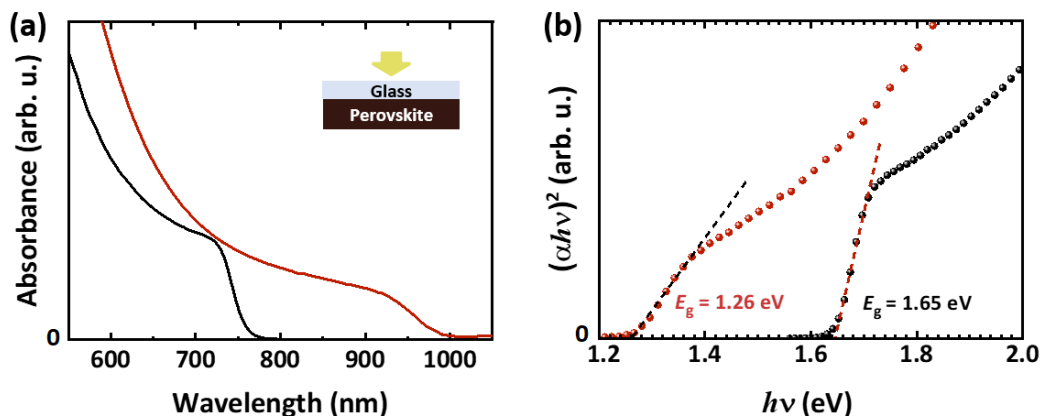


Figure 5.10. (a) Ultraviolet-visible (UV-vis) absorbance spectra and (b) Tauc plots of perovskite thin films (on glass) with double-cation $\text{Cs}_{0.17}\text{FA}_{0.83}\text{Pb}(\text{I}_{0.76}\text{Br}_{0.24})_3$ and a triple-cation $\text{Cs}_{0.025}(\text{FA}_{0.8}\text{MA}_{0.2})_{0.075}\text{Sn}_{0.5}\text{Pb}_{0.5}\text{I}_3$ compositions with bandgaps of $E_g \approx 1.65$ eV and $E_g \approx 1.26$ eV, respectively. Adapted from [155] with permission of The Royal Society of Chemistry.

A reaction between residual $\text{Sn}_y\text{Pb}_{(1-y)}\text{I}_2$ and CsI that could lead to formation of $\text{CsSn}_y\text{Pb}_{(1-y)}\text{I}_3$ impurity is an alternative explanation for the reduction of the nanosized aggregates. XRD measurement conducted on $\text{Cs}_1\text{Sn}_{0.5}\text{Pb}_{0.5}\text{I}_3$ thin film exhibited the typical perovskite peaks detected at 14.5° and 29.1° (Figure 5.9) attesting that incorporating Cs in $(\text{FA}_{0.8}\text{MA}_{0.2})\text{Sn}_{0.5}\text{Pb}_{0.5}\text{I}_3$ narrow-bandgap perovskite with residual $\text{Sn}_y\text{Pb}_{(1-y)}\text{I}_2$ in principle might also form a $\text{CsSn}_{0.5}\text{Pb}_{0.5}\text{I}_3$ perovskite. However, even if any $\text{CsSn}_{0.5}\text{Pb}_{0.5}\text{I}_3$ perovskite existed, its volume fraction must have been very low, and therefore hard to detect its peaks in the XRD patterns of the bulk narrow-bandgap perovskite thin films shown in Figure 5.5a.

In brief, our findings demonstrated that the introduction of small quantities of Cs into the $\text{FA}_{0.8}\text{MA}_{0.2}\text{Sn}_{0.5}\text{Pb}_{0.5}\text{I}_3$ narrow-bandgap perovskite thin films considerably reduced the formation of residual nanosized $\text{Sn}_y\text{Pb}_{(1-y)}\text{I}_2$ (with $0 < y < 1$) aggregates on the surface of the perovskite thin film. This reduction could be attributed to the reaction of Cs with the residual $\text{Sn}_y\text{Pb}_{(1-y)}\text{I}_2$ resulting in a volumetric growth of the narrow-bandgap perovskite thin films and an improved crystallinity. As a result, the respective PSCs exhibited improved photovoltaic performance and operational photo-stability.

5.6. Four-terminal all-perovskite tandem solar cells

Having verified that adding a sufficient amount of Cs into $\text{FA}_{0.8}\text{MA}_{0.2}\text{Sn}_{0.5}\text{Pb}_{0.5}\text{I}_3$ narrow-bandgap perovskite thin film resulted in the enhanced photovoltaic performance of the mixed Sn/Pb narrow-bandgap PSCs, we combined the best performing of these PSCs with Cs2.5% (with a PCE of 18.2%) as the bottom cell in a 4T all-PTSC. Figure 5.11a shows a schematic illustration of the 4T all-PTSC layer stack. We implemented a semi-transparent top cell composed of a 2D/3D perovskite heterostructure (see Section 3.1.2 for the details) with a layer stack of glass / ITO / np- SnO_2 / $\text{Cs}_{0.17}\text{FA}_{0.83}\text{Pb}(\text{I}_{0.76}\text{Br}_{0.24})_3$ / spiro-MeOTAD / MoO_x / ITO / MgF_2 as the top PSC.²⁷ As explained earlier in Section 3.2.1, MoO_x protected Spiro-MeOTAD from ion bombardment while sputtering the rear ITO and MgF_2 acted as an anti-reflection on the ITO increasing the optical transmittance of the top PSC.²⁰² As a result, a

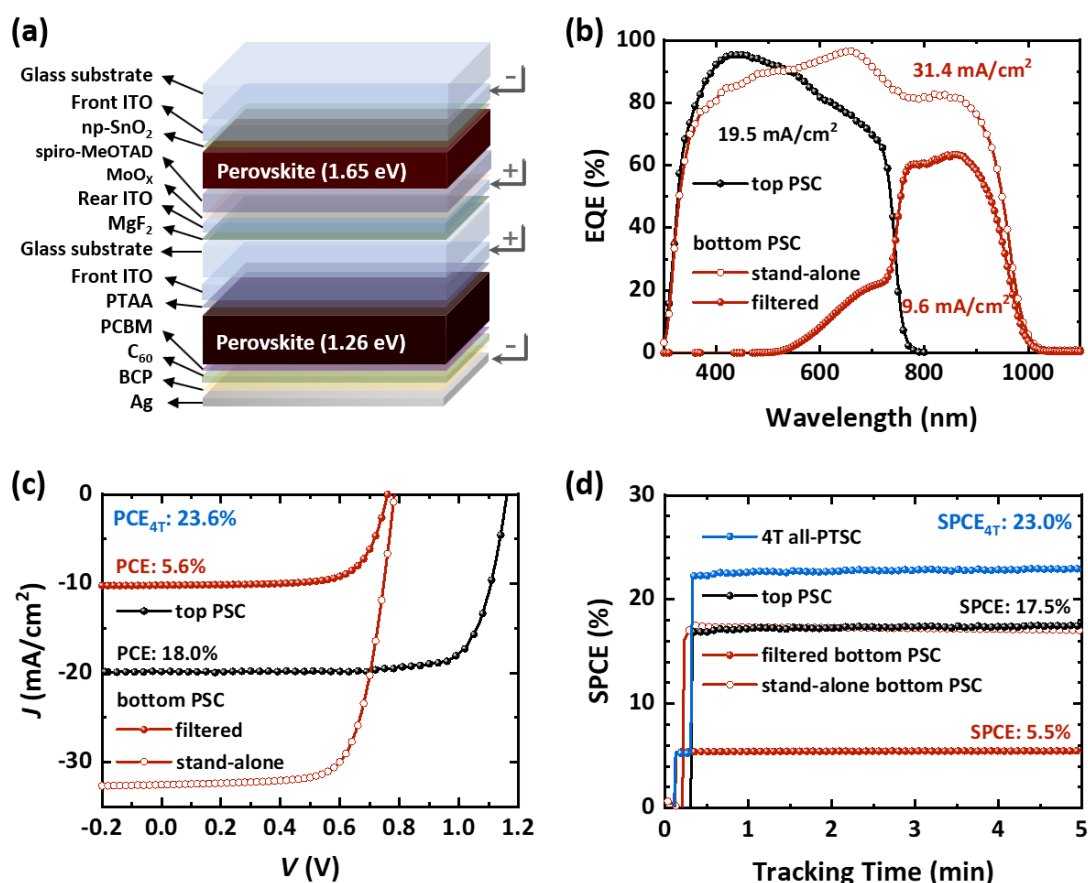


Figure 5.11. (a) A schematic illustration of the layer stack of a four-terminal all-perovskite tandem solar cell (4T all-PTSC) configuration with a semi-transparent top PSC ($E_g \approx 1.65 \text{ eV}$) and a narrow-bandgap bottom PSC (1.26 eV). (b) Current-density–voltage (J – V) characteristics in backward scan direction, (c) external quantum efficiency (EQE), and (d) power conversion efficiency (PCE) from maximum power point (MPP) tracking, for the semi-transparent top PSC and the narrow-bandgap bottom PSC (stand-alone and filtered). PCE_{4T} and SPCE_{4T} are the calculated PCE and stabilized PCE derived from the J – V characteristics and the MPP tracking measurements for the champion 4T all-PTSC, respectively. The calculated J_{SC} values from EQE responses for the semi-transparent top, stand-alone narrow-bandgap, and filtered narrow-bandgap bottom PSCs are 19.5, 31.4, and 9.6 mA/cm^2 , respectively. Reproduced from [155] with permission of The Royal Society of Chemistry.

semi-transparent PSC with a PCE of 18.0% was achievable. Figure 5.10 exhibits the absorbance spectra and Tauc plots of the perovskite absorber layers in the composition $\text{Cs}_{0.17}\text{FA}_{0.83}\text{Pb}(\text{I}_{0.76}\text{Br}_{0.24})_3$ (with $E_g \approx 1.26 \text{ eV}$ for the top cell) and $\text{Cs}_{0.025}(\text{FA}_{0.8}\text{MA}_{0.2})_{0.975}\text{Sn}_{0.5}\text{Pb}_{0.5}\text{I}_3$ (with $E_g \approx 1.65 \text{ eV}$ for the bottom cell).

To determine the PCE of the 4T all-PTSC, we measured the narrow-bandgap bottom PSC while applying a semi-transparent perovskite filter atop and achieved a PCE of 5.6%. The substrate area of the filter, which was fabricated under the same conditions with the same layer stack of the semi-transparent top PSC, was 225 mm^2 . UV-vis analyses of a semi-transparent filter and a semi-transparent PSC showed a negligible difference in their spectrophotometry parameters (see Figure B3 in Appendix B). The J_{SC} values integrated from the EQE responses (Figure 5.11b) of the semi-transparent top and narrow-bandgap

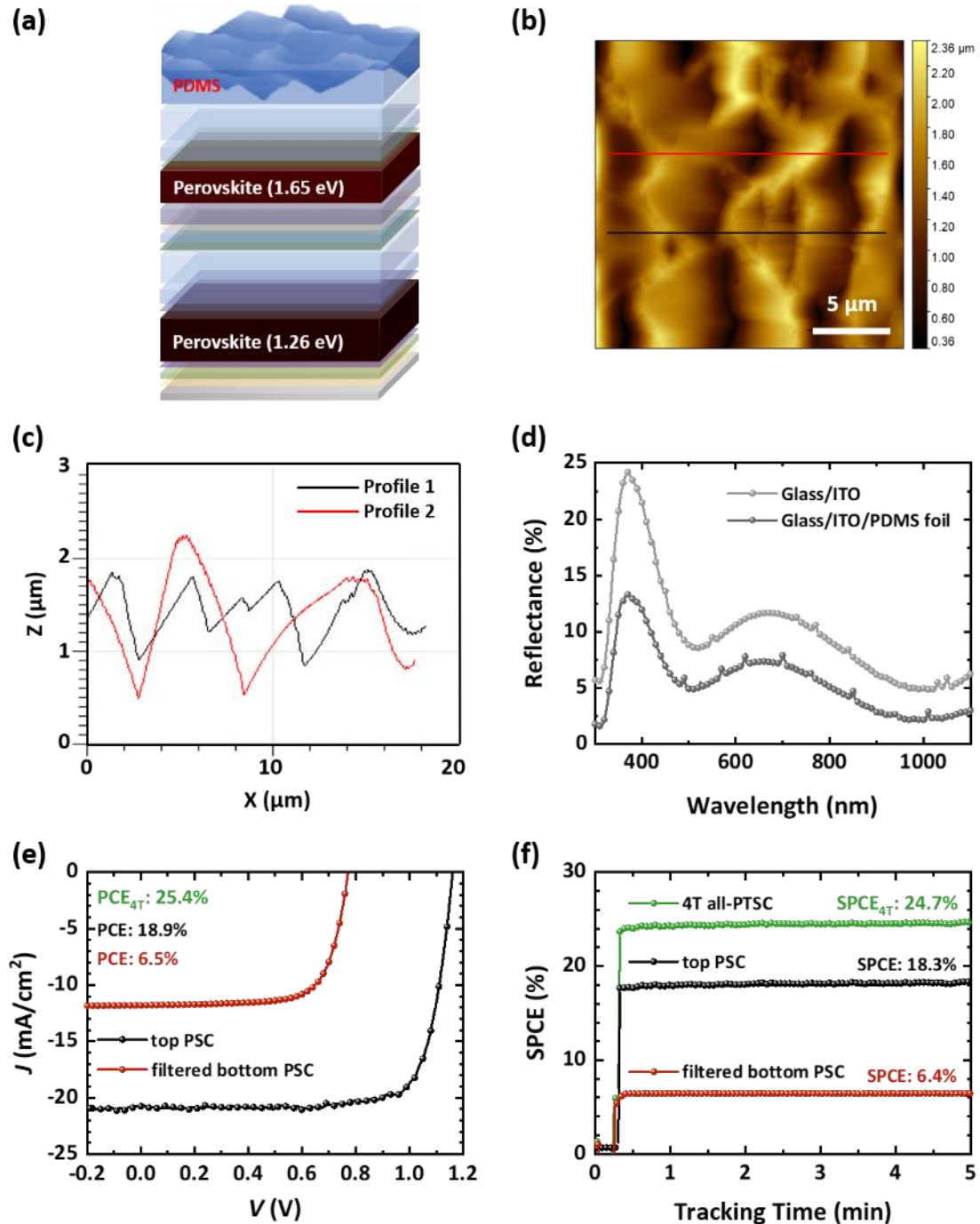


Figure 5.12. (a) A schematic illustration of the layer stack of a four-terminal all-perovskite tandem solar cell (4T all-PTSC) with a PDMS foil atop. (b) Atomic force microscopy (AFM) of the PDMS foil. (c) Depth profile of the AFM image (d) Reflectance spectra of an ITO-coated glass substrate with and without a textured PDMS foil implemented on the front-side of the ITO-coated glass substrate. (e) Current-density–voltage (J – V) characteristics and (f) power conversion efficiency from maximum power point (MPP) tracking, of a semi-transparent top PSC ($E_g \approx 1.65$ eV) and a filtered narrow-bandgap bottom PSC ($E_g \approx 1.26$ eV) while the PDMS foil was applied on the front electrode during the measurements. PCE_{4T} and $SPCE_{4T}$ are the calculated PCE and stabilized PCE derived from the J – V characteristics and MPP tracking measurements for the champion 4T all-PTSC, respectively. Figures d, e, and f are reproduced from [155] with permission of The Royal Society of Chemistry.

bottom PSCs were 19.5 mA/cm^2 and 31.4 mA/cm^2 (stand-alone) and 9.6 mA/cm^2 (filtered), respectively. By adding the PCE of the semi-transparent PSC (18.0%) with that of the filtered narrow-bandgap PSC (5.5%), we realized a 4T all-PTSC with a $\text{PCE}_{4\text{T}}$ of 23.6% (Figure 5.11c). The SPCEs from the MPP tracking measurement (Figure 5.11d) for the top and bottom cells were 17.5% and 5.5%, respectively. Therefore, the SPCE of the 4T all-PTSCs was equal to 23.0% (= 17.5% + 5.5%). Table 5.2 summarizes the J - V characteristics of the best performing semi-transparent top and the narrow-bandgap bottom sub-cells as well as calculated values for the 4T all-PTSC.

Mixed Sn/Pb narrow-bandgap perovskite thin film, as the light absorber layer of the bottom cell in a 4T all-PTSC possessed a bandgap as low as $\approx 1.26 \text{ eV}$ (Figure 5.1), which resulted in an absorption range up to around 1000 nm. To exploit this benefit, avoiding any absorption losses is essential. Polydimethylsiloxane (PDMS) anti-reflection foils can significantly reduce the reflection loss if applied on the front-side of the top electrode.^{203–206} Therefore, we repeated the photovoltaic characteristics of the 4T all-PTSCs, while applying a PDMS foil on the top of the layer stack (Figure 5.12a). The PDMS, we used here, is a silicon-based foil with a randomly-inverted pyramid texture. Figure 5.12b shows an atomic force microscopy (AFM) image ($20 \times 20 \mu\text{m}$) of the PDMS foil. Based on the depth profile of the AFM image (Figure 5.12c), which is taken at the position of the black and red lines in the AFM image, the depth of the pyramid texture is between 1 to $2 \mu\text{m}$. PDMS reduces the reflection loss from the ITO front electrode as shown in Figure 5.13d. As a result, a boost in the J_{SC} by 1 mA/cm^2 (for the semi-transparent top PSC) and 1.5 mA/cm^2 (for the filtered

Table 5.2. Photovoltaic parameters derived from current-density–voltage (J - V) scans measured at a fixed rate of 0.6 V/s from the open-circuit voltage (V_{OC}) to the short-circuit current (J_{SC}) (backward scan) and from J_{SC} to V_{OC} (forward scan) for champion semi-transparent top and narrow-bandgap (NBG) bottom (stand-alone and filtered) PSCs with and without implementing an anti-reflection PDMS foil in front side of the top sub-cell. The stabilized PCEs (SPCEs) of the top and filtered bottom PSCs and the corresponding calculated 4T all-perovskite tandem solar cell (all-PTSC) are given in bold. Reproduced from [155] with permission of The Royal Society of Chemistry.

PSC without PDMS	Scan	V_{OC} (V)	J_{SC} (mA/cm^2)	FF (%)	PCE (%)	SPCE (%)
	Direction					
Semi-transparent top	Backward	1.16	19.7	78.7	18.0	17.5
	Forward	1.13	20.0	74.8	16.9	
NBG bottom (stand-alone)	Backward	0.78	32.5	71.8	18.2	17.5
	Forward	0.77	32.5	66.5	16.7	
NBG bottom (filtered)	Backward	0.76	10.2	72.2	5.6	5.5
	Forward	0.75	10.2	68.4	5.2	
4T all-PTSC	Backward				23.6	23.0
	Forward				22.1	
PSC with PDMS	Scan	V_{OC} (V)	J_{SC} (mA/cm^2)	FF (%)	PCE (%)	SPCE (%)
	Direction					
Semi-transparent top	Backward	1.16	20.7	78.6	18.9	18.3
	Forward	1.13	21.0	74.4	17.7	
NBG bottom (filtered)	Backward	0.77	11.7	72.0	6.5	6.4
	Forward	0.76	11.7	67.5	6.0	
4T all-PTSC	Backward				25.4	24.7
	Forward				23.7	

narrow-bandgap bottom PSC) led to an improvement in the PCE from 18.0% and 5.6% to 18.9% and 6.5%, respectively (Figure 5.12c). Consequently, the PCE of the 4T all-PTSC was improved from 23.6% to 25.4% (= 18.9% + 6.5%) with an enhanced SPCE from 23.0% to 24.7% (Figure 5.12d). Table 5.2 summarizes the achieved photovoltaic characteristics with and without implementing a PDMS anti-reflection foil.

5.7. Summary

In this chapter, we investigated the effect of incorporating Cs into double-cation $\text{FA}_{0.8}\text{MA}_{0.2}\text{Sn}_{0.5}\text{Pb}_{0.5}\text{I}_3$ narrow-bandgap perovskite thin films and its role in improving the photovoltaic performance and the operational photo-stability of the respective PSCs with a layer stack of glass / ITO / PTAA / $\text{Cs}_x(\text{FA}_{0.8}\text{MA}_{0.2})_{(1-x)}\text{Sn}_{0.5}\text{Pb}_{0.5}\text{I}_3$ / PCBM / C_{60} / BCP / Ag, while varying Cs concentration from $x = 0\%$ to 1%, 2.5%, 5%, and 10%. We determined that a minute amount of Cs improves the photovoltaic performance and the operational photo-stability of the PSCs, such that the PSCs with 2.5% and 5% Cs concentrations maintained 92% and 99% of their initial values while measured under MPP tracking condition for 120 min. In contrast, the PCE of the PSCs without Cs concentration ($x = 0\%$) degraded to 61% of their initial values.

Top-view scanning electron microscopy (SEM) images of the narrow-bandgap perovskite thin films revealed a reduction in residual nanosized aggregates on the surface of the perovskite thin films upon increasing the concentration of Cs. CL characterizations conducted on narrow-bandgap perovskite thin films with different Cs concentrations as well as pure PbI_2 , pure SnI_2 , and mixed $\text{Sn}_{0.5}\text{Pb}_{0.5}\text{I}_2$ suggested that the aggregates observed in the SEM images were residual $\text{Sn}_y\text{Pb}_{(1-y)}\text{I}_2$ (with $0 < y < 1$) that reduced upon adding more Cs. In line with the CL results, XRD analyses confirmed the reduction of the residual $\text{Sn}_y\text{Pb}_{(1-y)}\text{I}_2$ upon adding more Cs suggesting a reaction between the incorporated Cs and the residual $\text{Sn}_y\text{Pb}_{(1-y)}\text{I}_2$.

To understand the effect of Cs in diminution of the SnPbI_2 aggregates and how it correlates to the enhanced performance and photo-stability of the respective PSCs, we prepared $\text{Cs}_x(\text{FA}_{0.8}\text{MA}_{0.2})_{(1-x)}\text{Sn}_{0.5}\text{Pb}_{0.5}\text{I}_3$ perovskite thin films with prominent Sn and Pb excess. UV-vis spectroscopy on these samples exhibited higher absorption for higher Cs concentrations suggestive of increased volumetric growth of the perovskite material. A reaction between the incorporated Cs and the residual $\text{Sn}_y\text{Pb}_{(1-y)}\text{I}_2$ could explain the volumetric growth. Nevertheless, too large amount of Cs resulted in a significantly reduced absorbance denoting that there is a substitution limit for the cation concentrations. Whereas, for an optimized amount of Cs in the investigated range, a beneficial stoichiometric composition and a perovskite thin film with a better crystallinity was achievable leading to PSCs with improved operational photo-stability as confirmed by MPP tracking measurements.

Briefly, we demonstrated the potential of triple-cation mixed Sn/Pb narrow-bandgap PSCs with improved photo-stability. By combining the best performing triple-cation narrow-bandgap PSCs with PCE of 18.2%, which were prepared with 2.5% Cs concentration, with

semi-transparent top PSCs with PCE of 18.0%, we achieved 4T all-PTSCs with PCEs as high as 23.6%, comparable to the highest PCE (25%) reported to date for 4T all-PTSCs.²¹

6. Hole-Transport-Layer-Free Tin/Lead Perovskite for Four-Terminal All-Perovskite Tandem Solar Cells

The focus of this chapter is on reducing the optical losses in the top and bottom sub-cells of a four-terminal all-perovskite tandem solar cell configuration. Using sub-layers with low parasitic near-infrared absorption is essential to exploit the performance potential of narrow-bandgap perovskite solar cells composed of mixed Sn/Pb perovskite thin films with a broad absorption range up to about 1033 nm. In this chapter, we approach this target by (i) applying a highly transparent conductive oxide front electrode in both semi-transparent top and narrow-bandgap bottom sub-cells; and (ii) removing hole transport layer in the narrow-bandgap bottom sub-cell. We demonstrate that (i) hydrogen-doped indium oxide with an ultra-low near-infrared optical loss and a high charge carrier mobility stands out as a suitable front contact in both sub-cells increasing the photocurrents; and (ii) removing hole transport layer reduces optical losses in the shorter wavelength without compromising the photovoltaic parameters of the narrow-bandgap perovskite solar cells.

This chapter is submitted and currently under review with the title “In₂O₃:H-based Hole-Transport-Layer-Free Tin/Lead Perovskite Solar Cells for Efficient Four-Terminal All-Perovskite Tandem Solar Cells”. Most of the graphs in this chapter are adapted or reproduced from the submitted paper. The In₂O₃:H front electrodes employed in this chapter were developed by Dr. Moritz Loy and Dr. Jan-Philipp Becker in collaboration with the group of Dr. Erik Ahlswede at ZSW.

6.1. Motivation

To date, single-junction mixed Sn/Pb narrow-bandgap perovskite solar cells (PSCs) have reached efficiencies slightly more than 20%.^{21–23,29,30} However, for attaining all-perovskite tandem solar cells (all-PTSCs) with efficiencies >30%, the single-junction mixed Sn/Pb narrow-bandgap PSCs have to provide efficiencies of at least 21% to 22%. Thus, research focus and strategies are required to further improve the performance of these solar cells. Mixed Sn/Pb perovskite thin films have a narrow-bandgap (≈ 1.2 eV) that corresponds to a favorable absorption up to 1033 nm and allows a larger fraction of the solar spectrum to be absorbed. However, high parasitic absorption losses by various layers inside the narrow-

bandgap PSC stack impedes the benefit of the narrow-bandgap PSCs in all-PTSCs. Therefore, implementing strategies to avoid parasitic absorption in the top layers (i.e., front electrode, electron transport layer (ETL) in *n-i-p*, and hole transport layer (HTL) in *p-i-n* structures) is essential and opens a pathway for designing narrow-bandgap PSCs with enhanced efficiencies.

The ideal choices for charge transport layers in the narrow-bandgap PSC structures are still under debate. Commonly used ETLs in *n-i-p* structures such as TiO₂ and SnO₂ presumably increase Sn oxidation due to the presence of oxygen in their stoichiometry.^{207,208} For the *p-i-n* structures, PSCs with inorganic NiO_x HTLs are reported to be very promising, however, they suffer from a lack of reproducibility because the oxidation state of the NiO_x depends on the exact conditions of processing.²⁰⁹ Alternative HTLs such as PEDOT:PSS and PTAA are becoming more common in mixed Sn/Pb narrow-bandgap PSCs.^{23,29,30,155,184} However, it was reported that thermal aging (at 85 °C) causes degradation at the interface between PEDOT:PSS as an HTL and mixed Sn/Pb perovskite absorber leading to device instabilities and poor charge extraction.²¹⁰ Replacing PEDOT:PSS with PTAA as an HTL was shown to boost the open-circuit voltage (V_{OC}) and improve the thermal stability of the respective PSCs (by retaining 80% of their initial power conversion efficiency (PCE) after 4000 h at 85 °C).²¹¹ Unfortunately, the extreme hydrophobicity of PTAA is a big challenge that causes unsatisfactory perovskite growth and inhibits device reproducibility.^{212,213} Additionally, prolonged ultraviolet (UV) light exposure was reported to degrade PTAA, which hampers charge carrier extraction.²¹⁴ Furthermore, in terms of optics, unwanted parasitic absorption losses that PTAA and PEDOT:PSS introduce in shorter and longer wavelength, respectively, results in a limited photocurrent of the PSCs.²¹⁵

Recently, HTL-free PSCs (without a dedicated HTL) with mixed Sn/Pb perovskite absorbers deposited directly onto ITO were reported to attain a respectable PCE of 16.4% (with only 0.2% drop in the absolute efficiency compared to their counterparts including PEDOT:PS as HTL).²¹⁰ In this chapter, we expand this investigation by employing a highly transparent hydrogen-doped indium oxide (In₂O₃:H), denoted as IO:H, as a front electrode in an HTL-free narrow-bandgap PSC for the first time and compare the performances with HTL-free PSCs deposited onto commonly used commercial ITO and FTO front electrodes. IO:H electrode, with excellent thermal and chemical stability,²¹⁶ has high carrier mobility and nearly zero near-infrared (NIR) absorption. Therefore, it is an ideal candidate for solar cells,^{217,218} as it has been successfully used as the front electrode in Si solar cells,^{219,220} CIGS solar cells,^{216,221} and in the top sub-cells in perovskite/Si and perovskite/CIGS tandem configurations.^{33,222,223}

In Section 6.1, we first compare the optical properties of an ITO substrate with an ITO substrate coated with PTAA. We investigate the photovoltaic performances of a PTAA-based narrow-bandgap PSC compared to an HTL-free narrow-bandgap PSC in the absence of PTAA. In the following section, Section 6.2, we study the optical properties of three different TCOs, commercial ITO, commercial FTO, and sputtered IO:H. We realize that IO:H substrates with ultra-low parasitic NIR absorption and high charge carrier mobility are

favorable candidates to be used as the front contact in PSC devices. In Section 6.4 and 6.5, we demonstrate the photovoltaic performances of HTL-free narrow-bandgap and semi-transparent PSCs applying different TCO electrodes. Combining these sub-cells, in Section 6.6, we compare photovoltaic performances of an IO:H-based 4T all-PTSC (composed of an IO:H-based HTL-free bottom PSC with an IO:H-based semi-transparent top PSC) with an ITO-based 4T all-PTSC and determine that replacing the ITO front contacts with IO:H results in a boost in the photocurrent of PSCs and consequently their overall efficiencies.

6.2. Hole-transport-layer-free narrow-bandgap perovskite solar cells

In this section, we introduced HTL-free PSCs with a layout illustrated in Figure 6.1a composed of a triple-cation narrow-bandgap ($E_g \approx 1.26$ eV) perovskite thin film with the composition $\text{Cs}_{0.025}(\text{FA}_{0.8}\text{MA}_{0.2})_{0.975}\text{Sn}_{0.5}\text{Pb}_{0.5}\text{I}_3$, which we investigated in Chapter 5. It is apparent that the current-density–voltage (J – V) of the stack with and without PTAA are comparable (Figure 6.1b). Interestingly, despite the lack of an HTL, we demonstrated a slightly improved fill factor (FF) and a comparable V_{OC} close to 0.8 V, which can be explained by the reported upward band-bending at the ITO/perovskite interface.²¹⁰ More notably, short-circuit current (J_{SC}) improved from 27.9 mA/cm² for the PSC with PTAA to 28.3 mA/cm² for the HTL-free PSC. Overall an improvement in the PCE from 15.7% (with PTAA) to 16.6% (without PTAA) was attainable.

Removing the PTAA layer, we observed an enhancement in the external quantum efficiency (EQE) responses (Figure 6.1c) for shorter wavelengths (300–500 nm), resulting in an increase in the integrated J_{SC} (by ≈ 0.5 mA/cm²). Both devices showed similar EQE responses above 500 nm. This suggests that removing PTAA is not detrimental for the quality of the mixed Sn/Pb perovskite thin film when deposited directly on bare ITO. In agreement with the literature,²¹⁵ we observed that PTAA introduces unwanted parasitic absorption in the shorter wavelength region when used as an HTL in *p-i-n* structures, and therefore led to a reduction in the EQE of the respective PSCs. Figure 6.1d depicts absorptance and transmittance of glass/ITO/PTAA stack (in red) compared to that of a glass/ITO stack (in dark gray). Coating ITO substrates with PTAA thin film (6 nm) increased the parasitic absorption loss (in line with reduced transmittance) mainly between 350 nm and 500 nm (Figure 6.1d). Therefore, the lower parasitic absorption in the absence of PTAA can explain the enhancement in the photocurrent and the EQE of the HTL-free PSC compared to that of a PSC with PTAA HTL.

6.3. Highly transparent conductive oxide as a front electrode

In the previous section, we showed that removing PTAA decreases unwanted parasitic absorption in the short wavelength and therefore improves the photo-current, without compromising any other photovoltaic parameters of the HTL-free PSCs. In this section, we investigated the parasitic NIR absorption for the commonly used TCOs: ITO (Luminescence

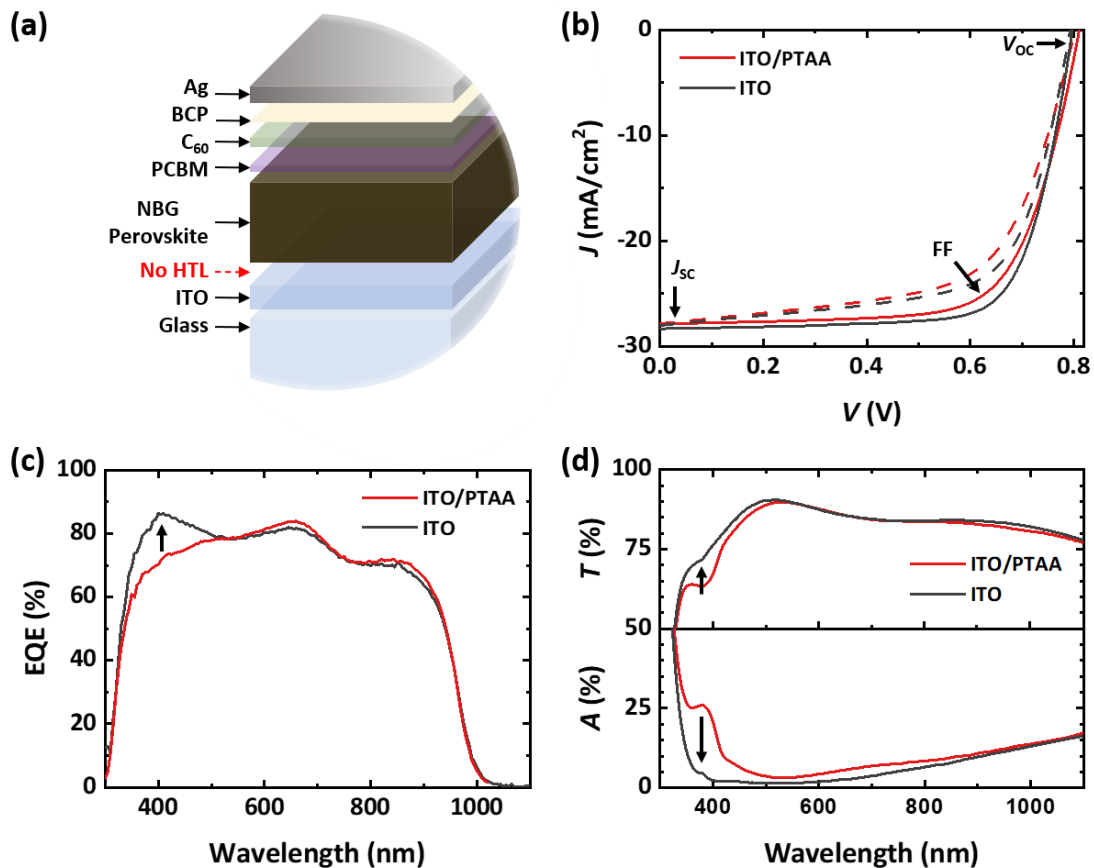


Figure 6.1. (a) A schematic illustration of a layer stack of an HTL-free PSC. (b) Current-density–voltage (J – V) characteristics and (c) external quantum efficiency (EQE) spectra of identically prepared narrow-bandgap PSCs with and without PTAA as an HTL. (d) Transmittance (T) and absorbance (A) of glass/ITO substrates coated with and without PTAA (performed in the air).

Technology), FTO (Sigma Aldrich), and sputtered IO:H (see Section 3.1.2 for details of sputtering the IO:H front electrodes).

Spectrophotometric measurements of glass/TCO stack, for which TCO differs from ITO to FTO and IO:H, are given in Figures 6.2a to 6.2c. High reflectance for IO:H is due to its higher refractive index (n) compared to ITO and FTO (Figure 6.2d). Thus, due to the higher refractive index of IO:H, a small refractive index contrast between the IO:H and the perovskite absorber layer (typically in the range 2.5) exists,^{48,157,224,225} which in principle ensures a reduced reflection loss as the light is coupled into the perovskite layer. More importantly, IO:H with an improved transmittance in the NIR region (700–1100 nm) demonstrates the lowest (<2%) absorbance, since its extinction coefficient (k) in the NIR wavelength is extremely low compared to ITO and FTO electrodes (Figure 6.2e).³³ The optical and electrical properties of TCOs are fundamentally interlinked. The lower extinction coefficient (k) or in other words the lower parasitic NIR absorption of IO:H is associated with its reduced number of charge carriers (see Table 6.1) because most of the free charge carriers absorb the incident photons in NIR wavelengths (lower energies). Therefore, in comparison to ITO and FTO, the charge carrier concentration (n_c) of IO:H is lowered by 1 order of magnitude. The low charge carrier concentration, however, comes at the expense of

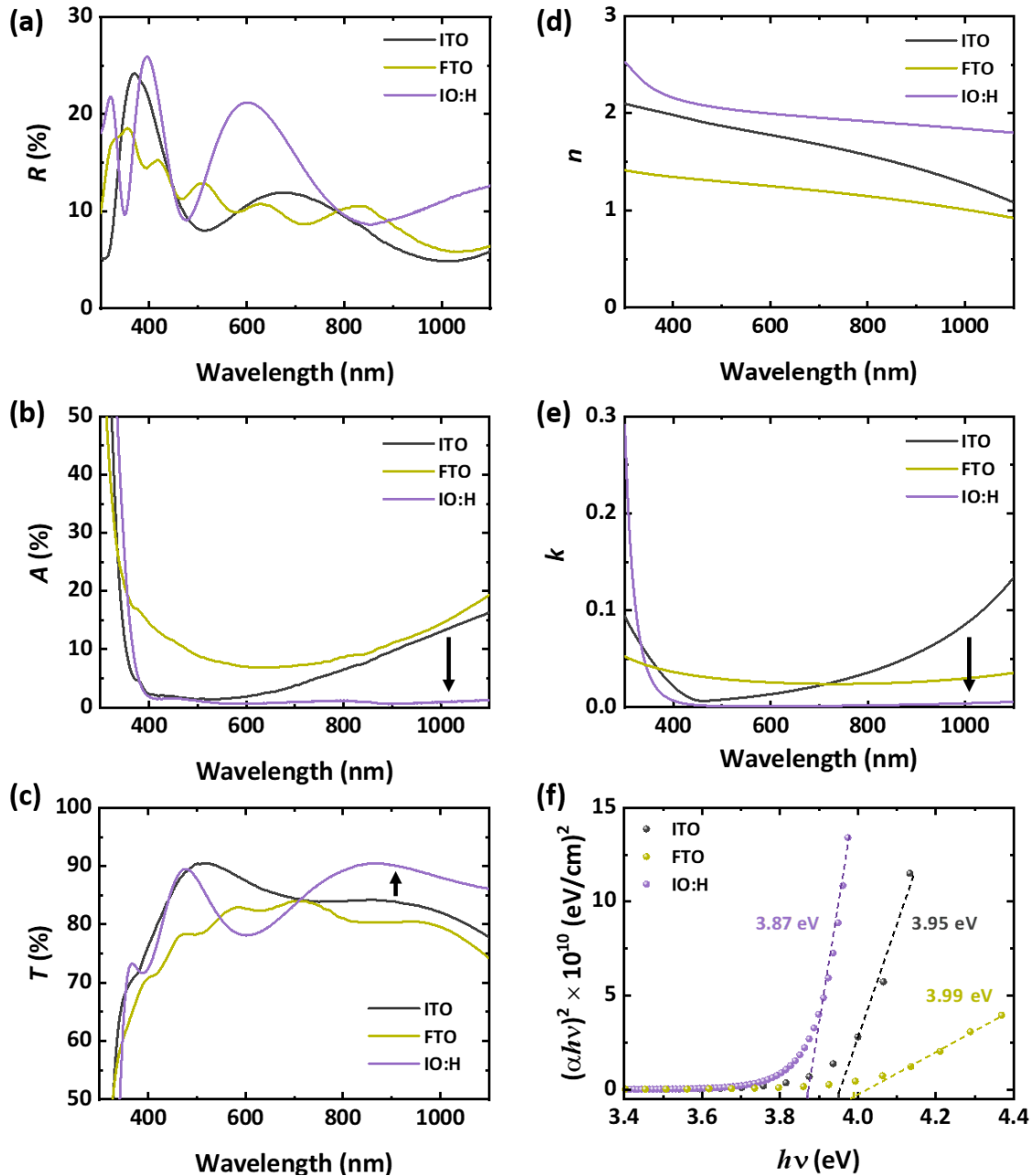


Figure 6.2. (a) Reflectance (R), (b) absorptance (A), (c) transmittance (T), (d) refractive index (n), (e) extinction coefficient (k), and (f) Tauc plots of glass substrates coated with ITO (140 nm), FTO (550 nm), and IO:H (230 nm) thin films. The ellipsometry measurements were performed by Dr. Adrian Mertens. All the characterizations were performed in the air.

higher resistivity. Though, higher mobility (μ) of IO:H can compensate partially for the low charge carrier concentration. In addition, the thickness of the layer must also be increased to reduce the overall sheet resistance (R_{sh}). Therefore, a significantly thicker IO:H layer was used and as a result an IO:H with only a slightly higher sheet resistance was obtained. The thickness difference of the TCOs is manifested as a shift in the interferences of the reflectance and transmittance spectra of the TCOs (Figure 6.2a and c). Evident from the Tauc plots (Figure 6.2f), the bandgap (E_g) of IO:H thin film was found to be only slightly lower (≈ 0.1 eV) than that of ITO and FTO (Figure 6.2f and Table 6.1).

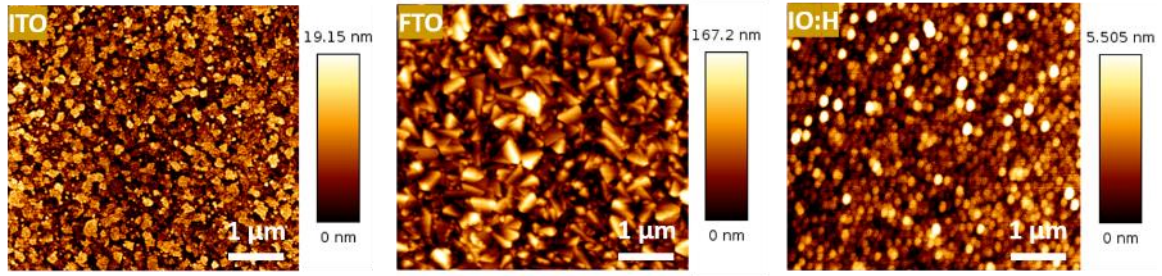


Figure 6.3. Atomic force microscopy (AFM) of commercial ITO, commercial FTO, and sputtered IO:H electrodes, with surface roughness (S_{rms}) of 3 ± 1 , 15 ± 5 , and < 1 nm, respectively. The AFM measurements were performed by Yidenekachew Donie.

According to atomic force microscopy (AFM) measurements, IO:H substrates used here had the lowest surface roughness (< 1 nm) compared to that of ITO ($\approx 3-4$ nm) and FTO (15 ± 5 nm), which makes IO:H a more suitable substrate for better nucleation of perovskite thin films. X-ray diffraction (XRD) measurement on the TCOs (Figure 6.4a) exhibited that all three TCOs were crystalline with preferential orientation along (222) planes (for ITO and IO:H) and (110) plane (for FTO). We calculated the crystallite size (D) for each TCO using the Scherrer equation (see Section 3.2.1 for the details). Table 6.2 summarizes the related parameters. IO:H with the lowest FWHM ($\approx 0.172^\circ$) had the most intensified reflection peaks and therefore better crystallinity compared to commercial ITO and FTO. This high crystallinity of the IO:H thin film was associated with the post-deposition annealing treatment of the IO:H substrates as discussed in reference [33]. The better crystallinity (lower FWHM) is indicative of larger crystallites of IO:H ($D = 48$ nm) compared to ITO ($D = 18.8$ nm) and FTO ($D = 37.3$ nm), which is beneficial for an improved interface and accordingly a better charge transport at the TCO/perovskite interface in the HTL-free PSCs. In general, a substrate has a prominent effect on the quality of the perovskite thin film and the substrate/perovskite interface.²²⁶ We characterized the TCO/perovskite interface as well as the crystallinity and the morphology of the $Cs_{0.025}(FA_{0.8}MA_{0.2})_{0.975}Sn_{0.5}Pb_{0.5}I_3$ perovskite thin films when directly deposited on ITO, FTO, and IO:H, to understand the working principles of the HTL-free PSCs with different TCO front electrodes, which will be discussed in the next section.

Table 6.1. Layer thickness (d), bandgap (E_g), charge carrier concentration (n_c), sheet resistance (R_{sh}), charge carrier mobility (μ), and surface roughness (S_{rms}) of the front transparent conductive oxide (TCO) electrodes.

TCO	ITO	FTO	IO:H
d (nm)	140	550	230
E_g (eV)	3.95	3.99	3.87
n_c ($1/cm^3$)	10.5×10^{20}	10.5×10^{20}	1.7×10^{20}
R_{sh} (Ω/sq)	15	7	23
μ (cm^2/Vs)	35.1 ± 3.9	34.4 ± 9.6	85.8 ± 1.2
S_{rms} (nm)	3 ± 1	15 ± 5	< 1

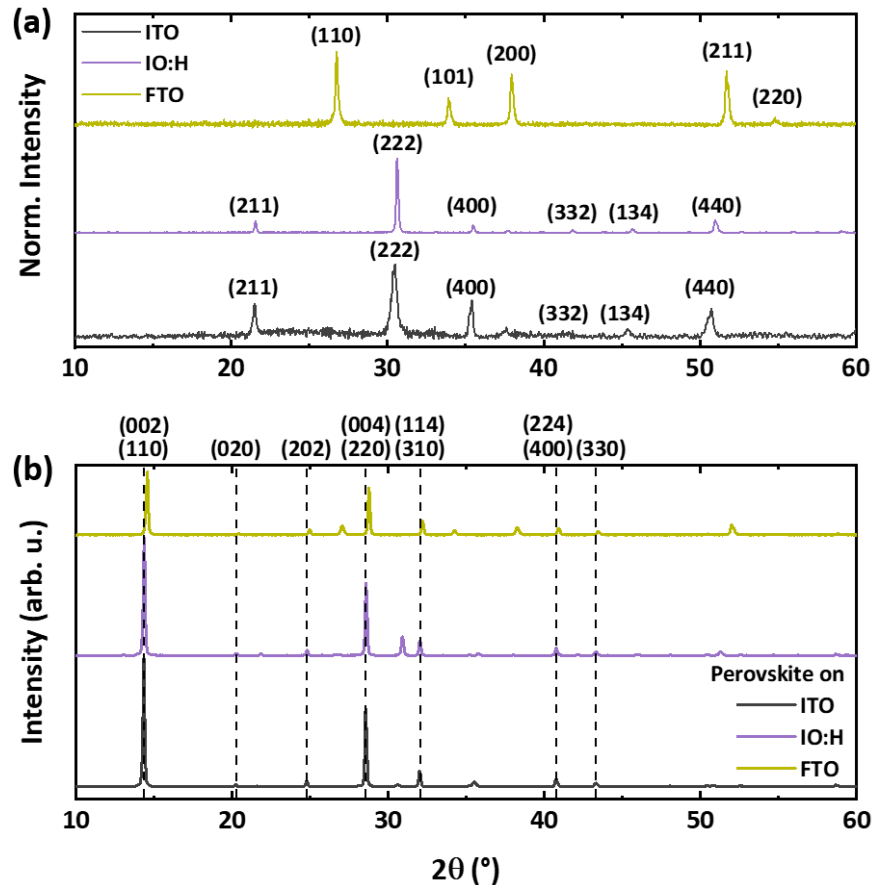


Figure 6.4. X-ray diffraction (XRD) patterns of (a) commercial ITO, commercial FTO, and sputtered IO:H electrodes, and (b) $\text{Cs}_{0.025}(\text{FA}_{0.8}\text{MA}_{0.2})_{0.975}\text{Sn}_{0.5}\text{Pb}_{0.5}\text{I}_3$ narrow-bandgap perovskite thin films deposited directly on the commercial ITO, commercial FTO, and sputtered IO:H electrodes. ITO-, FTO-, and IO:H-related peaks are detected in the XRD pattern of the perovskite film (compare a and b).

Regardless of the TCO substrates, XRD measurements of the $\text{Cs}_{0.025}(\text{FA}_{0.8}\text{MA}_{0.2})_{0.975}\text{Sn}_{0.5}\text{Pb}_{0.5}\text{I}_3$ perovskite thin film (Figure 6.4b) revealed two dominant reflection peaks at 14.1° and 28.3° . In agreement with the literature,¹⁹⁹ we assigned these two peaks to the (002)/(110) and (004)/(220) planes of the tetragonal perovskite crystal-structure, respectively, as also seen in Chapter 5. Although these two peaks existed for all three TCOs, they differed in intensity associated to different crystal orientations. In particular, the perovskite films deposited on IO:H and ITO showed more intensified reflection peaks, which correlates with larger grains as evidenced by scanning electron microscopy (SEM) images given in Figure 6.5. Therefore, IO:H and ITO with improved crystallinity (compared to FTO) are potentially better substrates for perovskite thin films. SEM images showed that perovskite thin films grow slightly larger grains on IO:H and ITO (implying fewer grain boundaries), which based on some studies could lead to fewer trap states at the grain boundaries, and therefore limited non-radiative recombination.^{124–127}

Besides the quality of the perovskite thin film itself, the TCO/perovskite interface plays a prominent role in the photovoltaic performance of the HTL-free PSCs as well, and therefore must be investigated.^{227–232} X-ray photoelectron microscopy (XPS) measurements can provide us with some insights into the TCO/perovskite interface (see Section 3.21). We

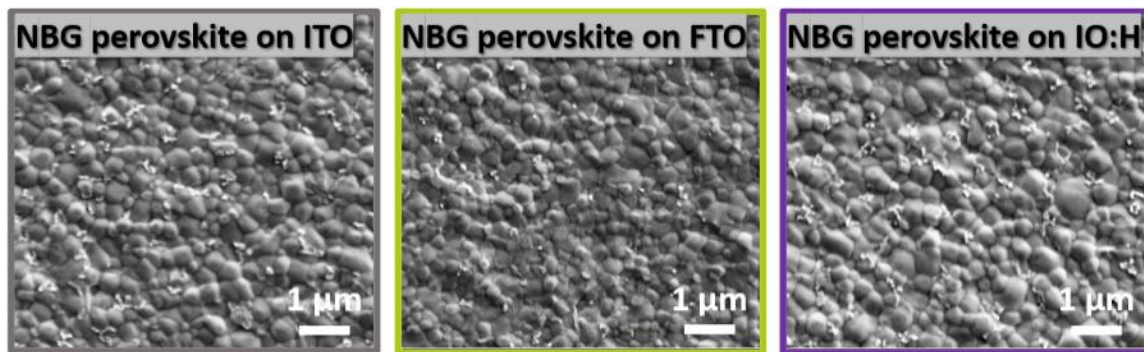


Figure 6.5. Scanning electron microscopy (SEM) images of narrow-bandgap (NBG) perovskite thin films with composition $\text{Cs}_{0.025}(\text{FA}_{0.8}\text{MA}_{0.2})_{0.975}\text{Sn}_{0.5}\text{Pb}_{0.5}\text{I}_3$ deposited directly on commercial ITO, commercial FTO, and sputtered IO:H electrodes. The SEM measurements were performed by Dr. Bahram Abdollahi Nejang.

characterized three different sets of samples: (1) TCO substrates, (2) TCO substrates coated with thin (≈ 3 nm) mixed Sn/Pb perovskite films, and (3) TCO substrates coated with thick (≈ 600 nm, i.e., same as the perovskite films used for the respective PSCs) mixed Sn/Pb perovskite films, with TCO varying from ITO to FTO and IO:H.

We noticed that all the TCO-related signals were present in the XPS survey derived from all the samples (Figure 6.6), while abating with increasing the thickness of the perovskite films. All the perovskite-related signals in the XPS spectra of the thick samples were similar, indicating that the TCO substrates had a negligible effect on the chemical structure of the bulk perovskite films. For having insights into the start point of the perovskite growth on the TCO substrates, we analyzed the XPS spectra of the thin samples. Assuming that the ‘thin’ perovskite has homogeneous thicknesses over a TCO substrate, we used the following equation to estimate the thickness of the ‘thin’ perovskite films,

$$I = I_0 \exp\left(-\frac{d}{\lambda \sin\varphi}\right) \quad 6.1$$

where I is the intensity of In 3d and/or O 1s core-level spectra derived from the TCO/thin perovskite samples, I_0 is the intensity of In 3d and/or O 1s core-level spectra for bare TCO, d is the thickness of the perovskite film, φ is the XPS take-off angle (90° in our measurements), and λ is the inelastic mean free path (Figure 6.7). We determined λ by using the ‘QUASES-IMFP-TPP2M’ software.²³³ We found the thickness of the ‘thin’ perovskite

Table 6.2. The full width at half maxima (FWHM) and the crystallite size (D) of the transparent conductive oxide (TCO) electrodes. The XRD analysis is done for the main peak assigned to the (222) plains for ITO and IO:H, and the (110) plain for FTO.

TCO	Plane (hkl)	2θ ($^\circ$)	FWHM ($^\circ$)	Crystallite size, D (nm)
ITO	222	30.4	0.439	18.75
IO:H	222	30.6	0.172	47.88
FTO	110	26.8	0.219	37.30

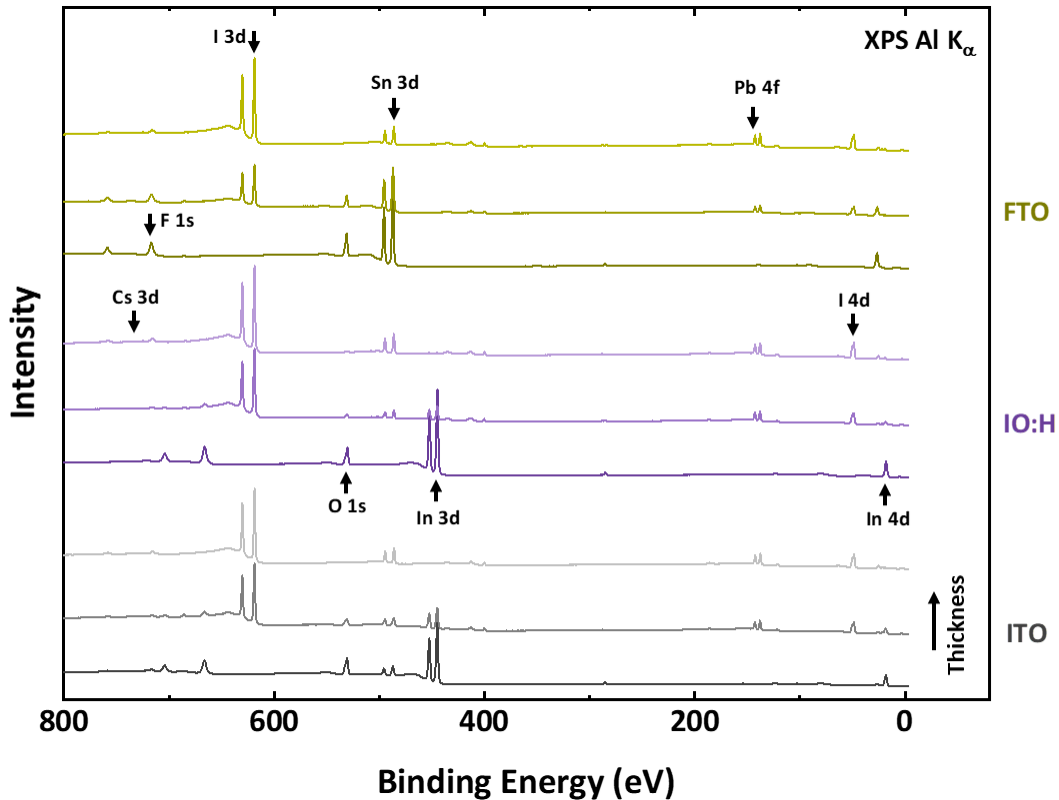


Figure 6.6. Al K_{α} X-ray photoelectron spectroscopy (XPS) survey spectra conducted on three sets of samples including bare TCO, TCO/thin perovskite (≈ 3 nm), and TCO/thick perovskite (600 nm) (bottom to top in a respective colored group): ITO (gray), IO:H (purple), and FTO (green). The perovskite films have a nominal composition of $\text{Cs}_{0.025}(\text{FA}_{0.8}\text{MA}_{0.2})_{0.975}\text{Sn}_{0.5}\text{Pb}_{0.5}\text{I}_3$. The XPS measurements were performed by Dr. Dirk Hauschild and Dr. Lothar Weinhardt.

on IO:H (5 ± 2 nm) to be twice as large as that on ITO or FTO (2 ± 1 nm). This is indicative of a more homogenous and faster growth of the perovskite on IO:H substrates, which agrees with the AFM results given in Figure 6.3.

Analyzing the most prominent XPS core levels of the narrow-bandgap perovskite films (i.e., Sn $3d_{5/2}$, Cs 3d, I 3d, N 1s, C 1s, and Pb 4f), gave us information about the impact of the TCOs on (1) the band-bending induced by the TCO/perovskite interface (indicated by peak shifts in the XPS survey of the thin and thick perovskite samples) and (2) the chemical species present at this interface (by comparing the spectral shapes of the XPS spectra of the thin and thick perovskite samples). Figure 6.8 shows that there are small peak shifts comparing the XPS spectra of the thin and thick perovskite samples, with an exception in the C 1s spectra. The strong spectral shift observed for the C 1s core level in the lower binding energy region (282-290 eV) could be due to different C species. Excluding this region, all the XPS core levels revealed a shift of $+0.06 \pm 0.04$ eV (for ITO), $+0.01 \pm 0.03$ eV (for IO:H), and -0.04 ± 0.04 eV (for FTO) in average, going from thin to thick perovskite films. This suggests that the type of the TCO impacts the band bending at the TCO/perovskite interface only slightly.

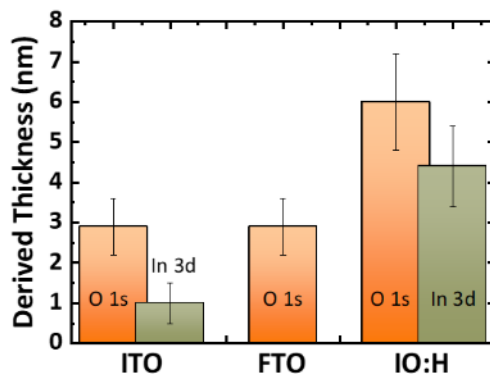


Figure 6.7. Derived thicknesses of the ‘thin’ perovskite films deposited on bare ITO, FTO, and IO:H transparent conductive oxide (TCO) electrodes.

Looking at the spectral shapes of the XPS peaks, we found a slight asymmetry for the Sn 3d_{5/2} of all three thick perovskite samples (orange lines in Figure 6.9), which could be associated with a small contribution from Sn⁴⁺.¹⁸⁴ In contrast to ITO and FTO substrate samples that showed Sn 3d_{5/2} peak (blue lines in Figure 6.9) at binding energies of 486.7 and 487.0 eV, respectively, no Sn-related peak was observed for the IO:H substrate sample. We tried to reproduce the Sn 3d_{5/2} signals of the thin perovskite samples (open circles in Figure 6.9) by a weighted sum of the XPS spectra of the TCO substrate samples and the respective thick perovskite samples, which allowed us to analyze the Sn-related signal of the thin perovskite. Interestingly, the Sn 3d_{5/2} spectra of the thin perovskite samples were reproduced for the ITO and FTO substrate samples, as shown in Figure 6.9 (overlap of the red fit lines and the open circles). Whereas, using this method for the IO:H substrate sample did not reproduce the Sn 3d_{5/2} signal of the thin perovskite sample because it only consisted of one spectral component indicative for Sn²⁺, while the IO:H substrate had no Sn signal and the thick perovskite exhibited Sn²⁺ and some Sn⁴⁺. This result suggests that the mixed Sn/Pb narrow-bandgap perovskite on Sn(-O) free substrate benefits from less oxidation, due to reduced Sn⁴⁺ formation at the IO:H/perovskite interface during the growth’s start. The reduced amount of Sn⁴⁺ at this interface could possibly be beneficial for the charge carrier transport and in general for the stability of the mixed Sn/Pb narrow-bandgap PSCs.^{22,234}

6.4. Narrow-bandgap perovskite solar cells with alternative front electrodes

At the beginning of the previous section, we showed that IO:H possess significantly improved optical properties compared to the commonly used ITO and FTO. In this section, we determine how the improved optical performance correlates to the photovoltaic performance of the respective PSCs. We fabricated three different sets of HTL-free narrow-bandgap PSCs with the following layer stack (see Section 3.1.2 for details): glass / TCO (ITO, FTO, or IO:H) / Cs_{0.025}(FA_{0.8}MA_{0.2})_{0.975}Sn_{0.5}Pb_{0.5}I₃ / PCBM / C₆₀ / BCP / Ag. The perovskite composition used here has a bandgap of ≈1.26 eV, as shown earlier in Chapter 5, (see Figure 5.10).

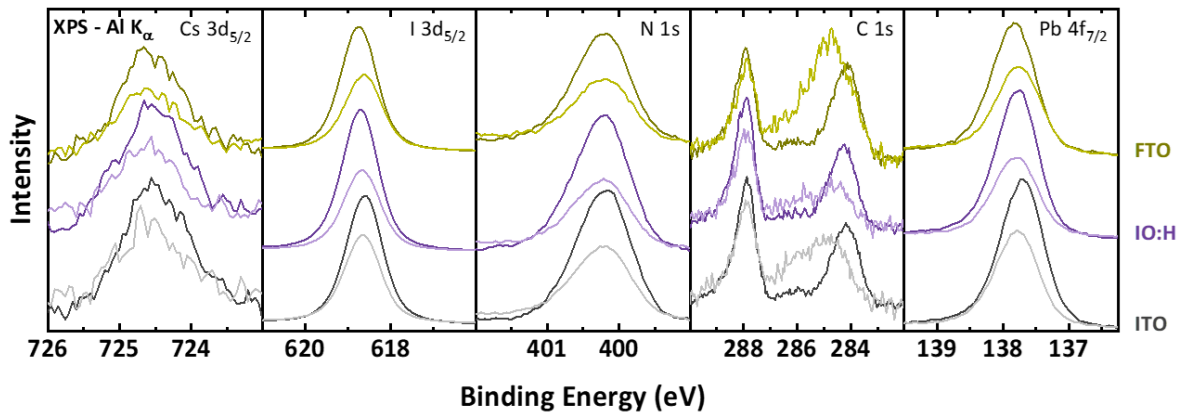


Figure 6.8. Monochromatized Al K α XPS spectra of perovskite-related core levels of thin (light colors) and thick (dark colors) narrow-bandgap Cs_{0.025}(FA_{0.8}MA_{0.2})_{0.975}Sn_{0.5}Pb_{0.5}I₃ perovskite films fabricated on different TCOs (ITO, IO:H, and FTO from bottom to top, respectively). The XPS measurements were performed by Dr. Dirk Hauschild and Dr. Lothar Weinhardt.

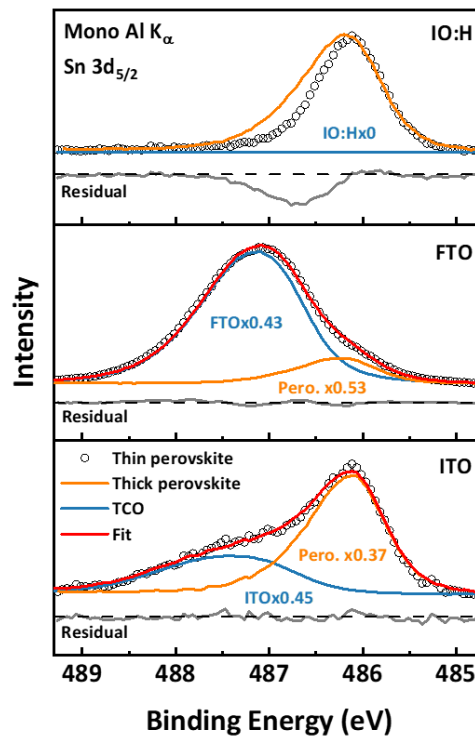


Figure 6.9. Monochromatized Al K α XPS spectra (open circles) of the Sn 3d_{5/2} region of the ‘thin’ perovskite for (from bottom to top) ITO, FTO, and IO:H substrate. Fits (red) are shown describing the spectra as a weighted sum of the substrate (blue) and thick perovskite (orange) spectra. Underneath each spectrum, the residuum is shown in gray. The XPS measurements were performed by Dr. Dirk Hauschild and Dr. Lothar Weinhardt.

The EQE spectrum of the IO:H-based PSC exhibited a broadband enhancement from 520 to 950 nm compared to the EQE spectra of the ITO- and FTO-based PSCs (Figure 6.10b). As discussed in the previous section, this enhancement in the EQE of the IO:H-based PSCs mainly arises from the reduced reflection (see Figure 6.10b) originating from the increased refractive index of the IO:H front electrode and lower parasitic NIR absorptions. As a

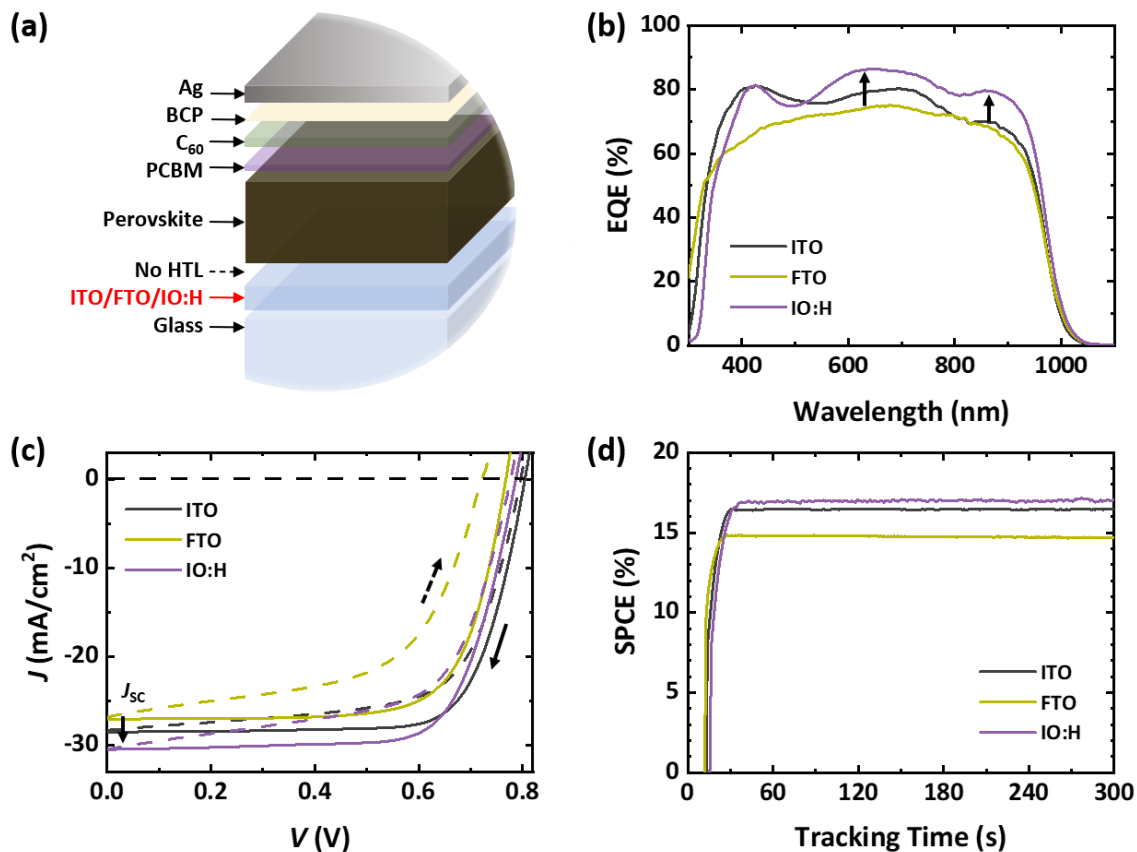


Figure 6.10. (a) A schematic illustration of the layer stack of an HTL-free PSC. (b) External quantum efficiency (EQE) spectra, (c) current-density–voltage (J – V) characteristics, and (d) stabilized power conversion efficiency (SPCE) from maximum power point (MPP) tracking measurements of the HTL-free narrow-bandgap PCSs with $\text{Cs}_{0.025}(\text{FA}_{0.8}\text{MA}_{0.2})_{0.975}\text{Sn}_{0.5}\text{Pb}_{0.5}\text{I}_3$ perovskite absorber layers deposited directly on commercial ITO, commercial FTO, and sputtered IO:H front electrodes.

consequence, the integrated J_{SC} from the EQE spectra revealed an improvement in the photocurrent when replacing the ITO (from 27.5 mA/cm²) or FTO (from 26.0 mA/cm²) front electrodes with a highly transparent IO:H (to 29.4 mA/cm²). This improvement in the photocurrent was also confirmed by the J_{SC} values derived from the J – V characteristics of the respective PSCs (Figure 6.10c).

Figure 6.11 depicts the J – V characteristics derived from 40 identically prepared PSCs of each TCO. It is apparent that the PCE of the IO:H-based HTL-free PSCs was slightly higher than the PCE of the ITO-based PSCs. We noticed that although the J_{SC} of the IO:H-based PSCs was higher than that of the ITO-based PSCs, by ≈ 2 mA/cm² on average, the higher FF of the ITO devices compensated for their lower J_{SC} . As discussed earlier in this chapter, this could be explained by the slightly higher sheet resistance of the IO:H compared to ITO and FTO substrates (see Table 6.1). Higher sheet resistance correlates with lower FF, which consequently affects the overall performance of the IO:H-based PSCs despite their remarkably higher J_{SC} .

Furthermore, we noticed that despite the lack of an HTL, the generated V_{OC} by all three TCOs were reasonable, as previously compared for an ITO-based device with and without

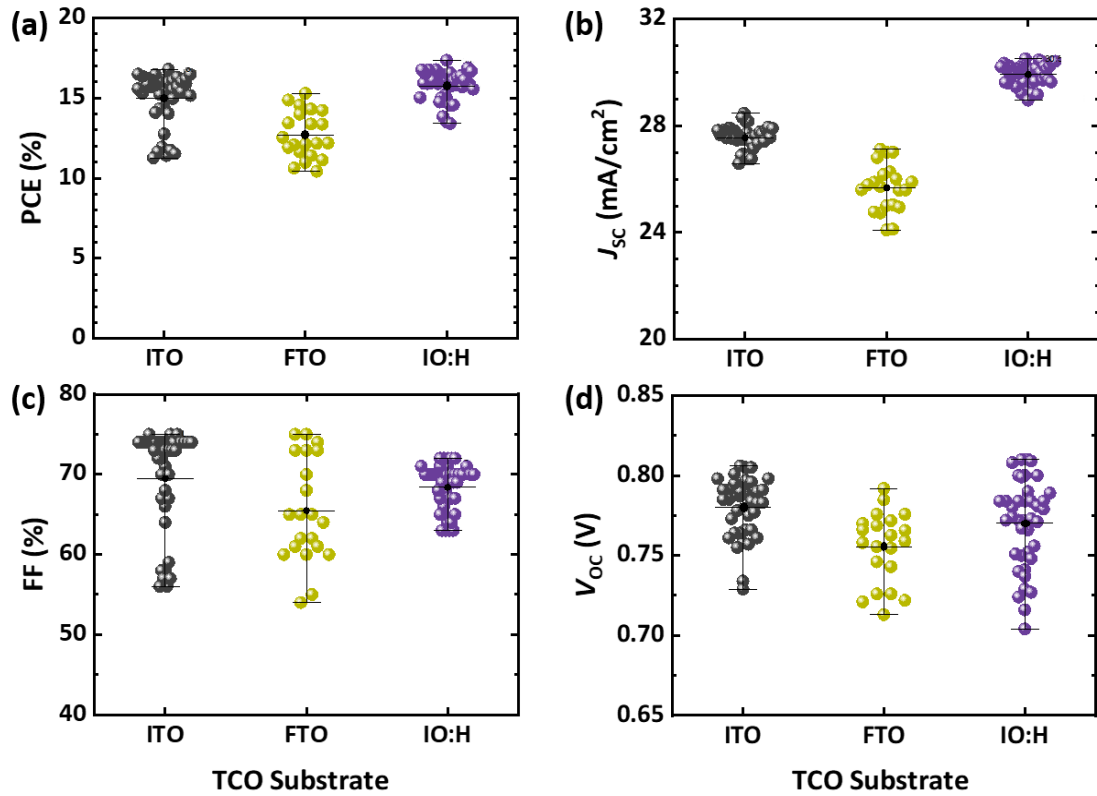


Figure 6.11. (a) Power conversion efficiency (PCE), (b) short-circuit current (J_{sc}), (c) fill factor (FF), and (d) open-circuit voltage (V_{oc}) of 40 identically prepared HTL-free narrow-bandgap PSCs deposited directly on different TCO front electrodes: commercial ITO, commercial FTO, and sputtered IO:H. The middle lines show the average values.

PTAA as an HTL (see Section 6.2). This indicates that the missing HTL is not affecting the band alignment at the TCO/perovskite interface significantly, which is in line with the XPS results. Compared to ITO or IO:H, the hysteresis was more pronounced in the FTO-based PSCs. This severe hysteresis of the FTO-based PSCs could be introduced by ion migration at the FTO/perovskite interface.²³⁵ Interestingly, removing HTL was not detrimental to the stabilized PCE (SPCE) of these PSC devices as shown in Figure 6.10d.

6.5. Four-terminal all-perovskite tandem solar cells with alternative front electrodes

Although the top and bottom cells of a 4T tandem solar cell work individually, the performance of the bottom sub-cell and consequently the overall performance of the tandem solar cell is correlated to the choice of the front and rear TCO electrodes of the top cell. The front and rear electrodes of the semi-transparent top cell introduce parasitic absorption and unfavorable reflection, which diminish the transmission of the top cell and reduce the share of the solar spectrum reached by the bottom cell.^{32–38} Therefore, reducing these optical losses can effectively improve the overall efficiency of the tandem solar cell.

To prove the point, we compared the performance of ITO- and IO:H-based 4T all-PTSCs, for which the front electrodes of both sub-cells are ITO and IO:H, respectively. At the outset,

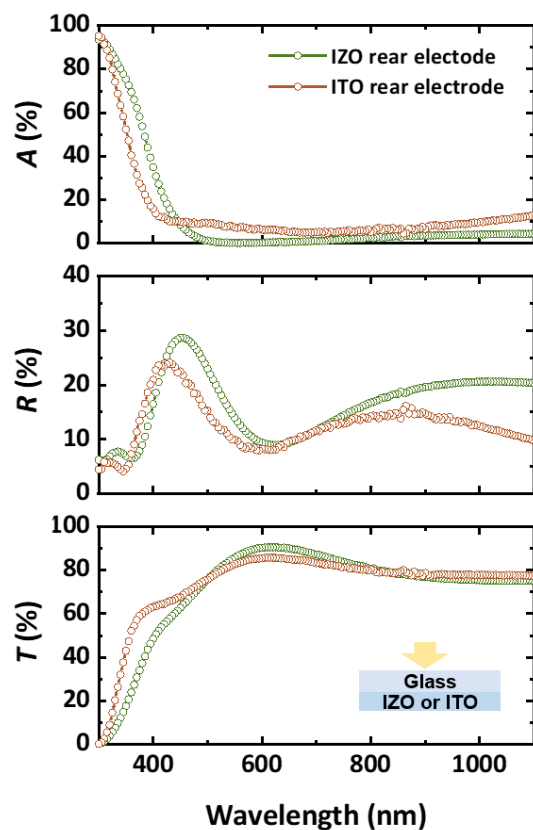


Figure 6.12. From bottom to top, transmittance (T), reflectance (R), and absorbance (A) of an ITO and IZO rear electrode sputtered on bare glass. The characterizations were performed in air. The ITO and IZO rear electrodes were prepared by Ihteaz M. Hossain.

the ITO- and IO:H-based (HTL-free) narrow-bandgap PSCs were partnered with semi-transparent PSCs consisting of a layer stack as follows: glass / TCO (**ITO** or **IO:H**) / np-SnO_2 / $\text{Cs}_{0.1}(\text{FA}_{0.83}\text{MA}_{0.17})_{0.9}\text{Pb}(\text{I}_{0.83}\text{Br}_{0.17})_3$ / spiro-MeOTAD / MoO_x / **IZO** / MgF_2 . The perovskite absorber layer used for the top cell was previously introduced in Chapter 4. As shown earlier in Chapter 4 (Figure 4.15), this perovskite composition ($\text{Cs}_{0.1}(\text{FA}_{0.83}\text{MA}_{0.17})_{0.9}\text{Pb}(\text{I}_{0.83}\text{Br}_{0.17})_3$) has a bandgap of 1.62 eV. An in-house sputtered IZO layer played the role of the rear electrode for both ITO- and IO:H-based semi-transparent top PSCs (see Table 3.1 in Section 3.1.1 for the deposition parameters). Spectrophotometric measurements (see Figure 6.12) conducted on glass/IZO revealed that the NIR absorbance is significantly low (<5%), which is the reason we substituted it for the in-house sputtered ITO rear electrode previously used for the 4T all-PTSC in Chapter 5. We used a 10-nm thick layer of MoO_x , which has a good band-alignment with spiro-MeOTAD, to protect the spiro-MeOTAD layer during IZO sputtering process.²³⁶ Moreover, a 165-nm thick layer of MgF_2 was used acting as an anti-reflection coating to enhance the transmittance of the photons with energies below the bandgap of the top perovskite absorber layer.²⁷

As expected, replacing the ITO front electrode with IO:H substrates in the semi-transparent top PSCs led to an enhanced PCE driven by a remarkable increase in the J_{SC} from 19.7 to 20.8 mA/cm^2 and a slight improvement in the V_{OC} from 1.11 to 1.15 V on average (for 25 identically prepared PSCs), while the averaged values of the FF remained comparable

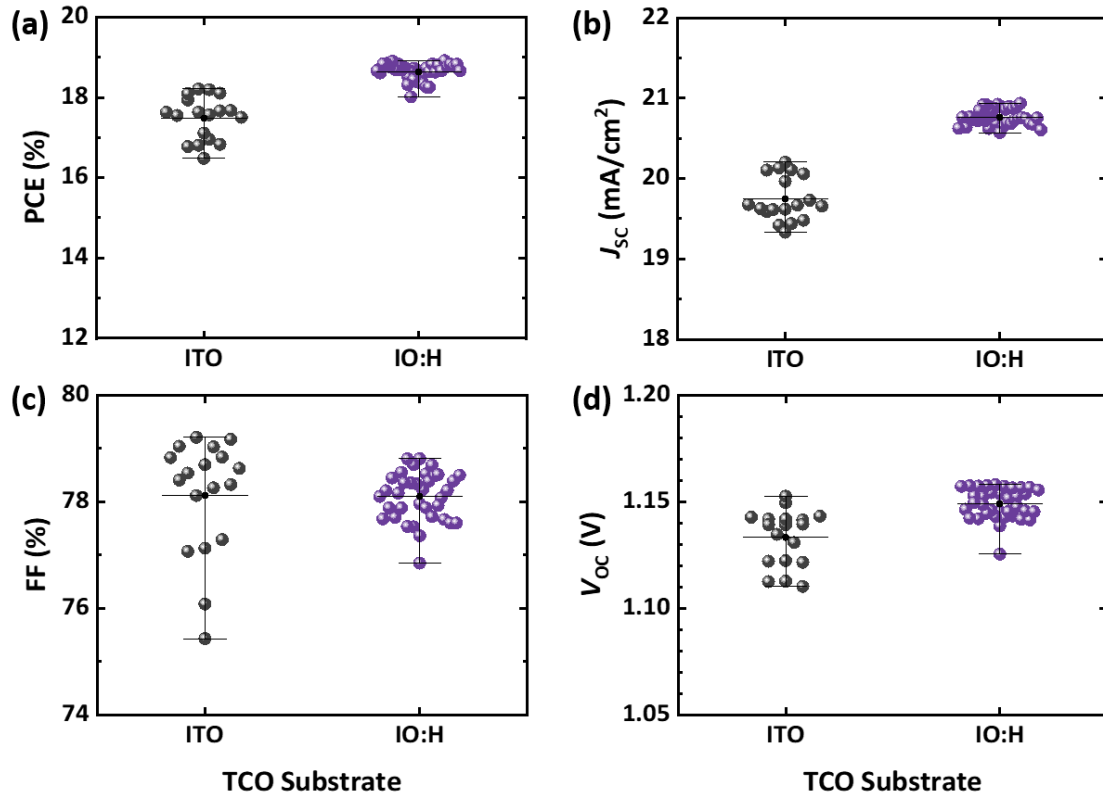


Figure 6.13. (a) Power conversion efficiency (PCE), (b) short-circuit current (J_{SC}), (c) fill factor (FF), and (d) open-circuit voltage (V_{OC}) of 25 identically prepared semi-transparent PSCs with two different TCO front electrodes: commercial ITO and sputtered IO:H. The middle lines show the average values.

(Figure 6.13). For the best performing semi-transparent top PSC, enhanced J_{SC} (from 20.2 to 20.9 mA/cm²) enabled the IO:H-based PSC to maintain a PCE of 19.0% compared to the best performing of an ITO-based counterpart PSC with a PCE of 18.2%. To evaluate the performance of the 4T all-PTSC, we used a triple-cation semi-transparent PSC filter ($E_g \approx 1.62$ eV) atop the triple-cation HTL-free narrow-bandgap PSC ($E_g \approx 1.26$ eV) (see Figures 6.14a). We fabricated two semi-transparent PSC filters (with substrate areas of 256 mm²) under identical conditions and layer stacks as the semi-transparent PSCs (with both ITO and IO:H front electrodes). Applying the filters, we determined the PCE of the narrow-bandgap PSCs as follows: 5.8% (for an IO:H-based narrow-bandgap PSC) under an IO:H-based filter) and 5.1% (for an ITO-based narrow-bandgap PSC under an ITO-based filter). This improvement from ITO-based to IO:H-based PSCs is a consequence of an enhanced J_{SC} from 8.5 mA/cm² (for an ITO-based narrow-bandgap PSC) to 10.5 mA/cm² (for an IO:H-based narrow-bandgap PSC), when measured under an ITO- and an IO:H-based semi-transparent PSC filters, respectively (Figures 6.14b and c).

Finally, by adding PCEs of the best performing semi-transparent top PSCs with that of the best performing filtered bottom PSCs, we determined a significant improvement in the PCE from 23.3% (= 18.2% + 5.1%) for an ITO-based 4T all-PTSC to 24.8% (= 19.0% + 5.8%) for an IO:H-based 4T all-PTSC. Table 6.3 summarizes all the photovoltaic parameters of the top and bottom sub-cells and their respective 4T all-PTSCs. Moreover, we calculated the SPCEs of the 4T all-PTSCs as the sum of the SPCEs of the semi-transparent top and the

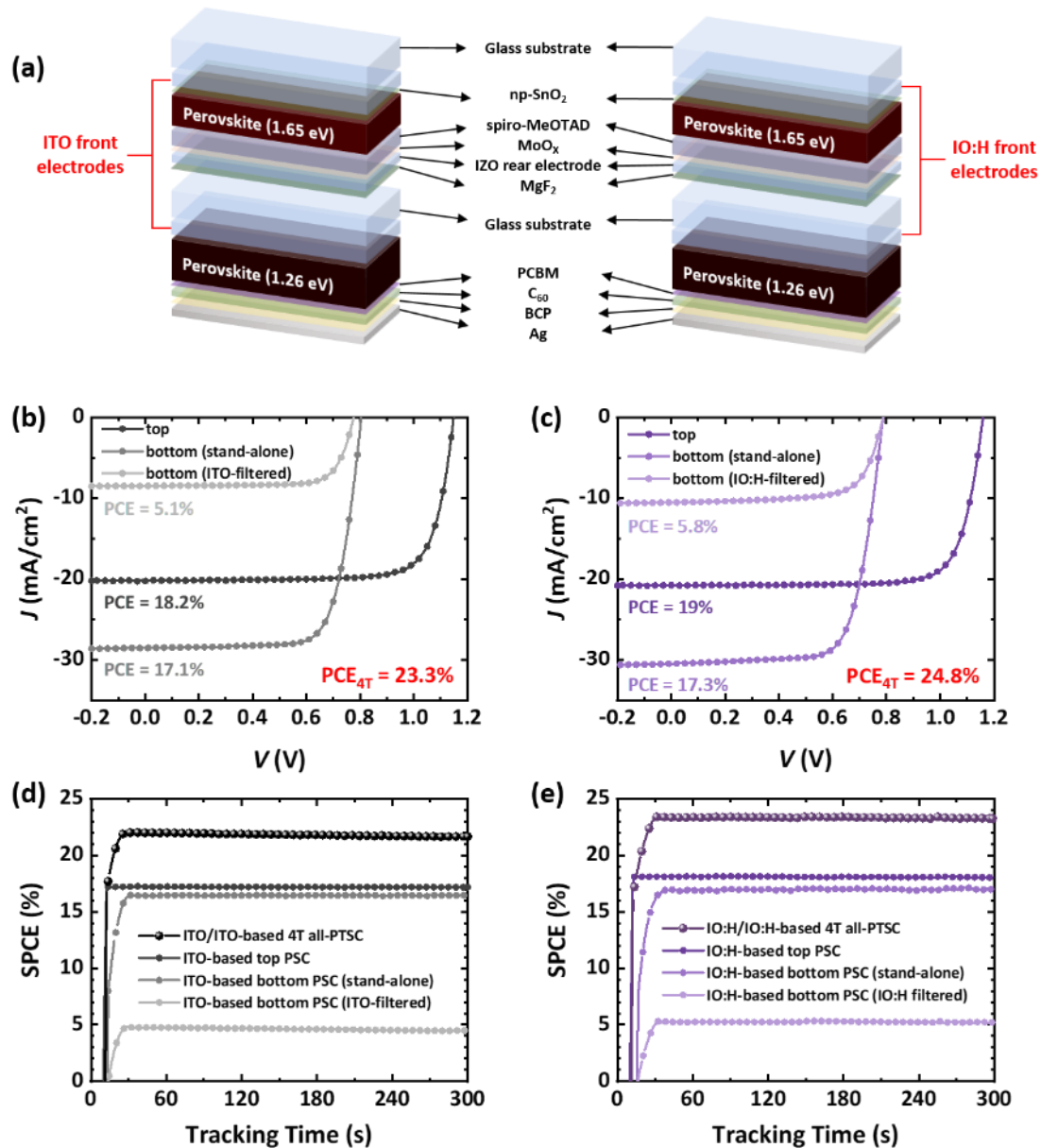


Figure 6.14. (a) Schematic cross-sectional images of an ITO- and IO:H-based 4T all-PTSCs. (b and c) Current-density–voltage (J – V) characteristics and (d and e) stabilized power conversion efficiency (SPCE) from MPP tracking measurements of the best performing ITO- and IO:H-based single-junctions and the resulting 4T all-PTSCs.

filtered narrow-bandgap PSCs from maximum power point (MPP) tracking measurements over 300 s (Figure 6.14d and e). An IO:H-based 4T all-PTSC attained a PCE of 23.3% outperforming that of an ITO-based 4T all-PTSC with a PCE of 21.9%.

To justify the improved PCEs of the IO:H-based 4T all-PTSC, we carried out spectrophotometric measurements on the semi-transparent perovskite filters with both ITO and IO:H filters. Similar to the narrow-bandgap bottom PSCs, substituting the ITO front electrode with IO:H resulted in an overall enhancement in the EQE spectra of the semi-transparent top PSCs (Figure 6.15a) from 500 nm to 760 nm (above the bandgap - 1.62 eV - of the triple-cation Cs_{0.1}(FA_{0.83}MA_{0.17})_{0.9}Pb(I_{0.83}Br_{0.17})₃ perovskite). This increase, as shown

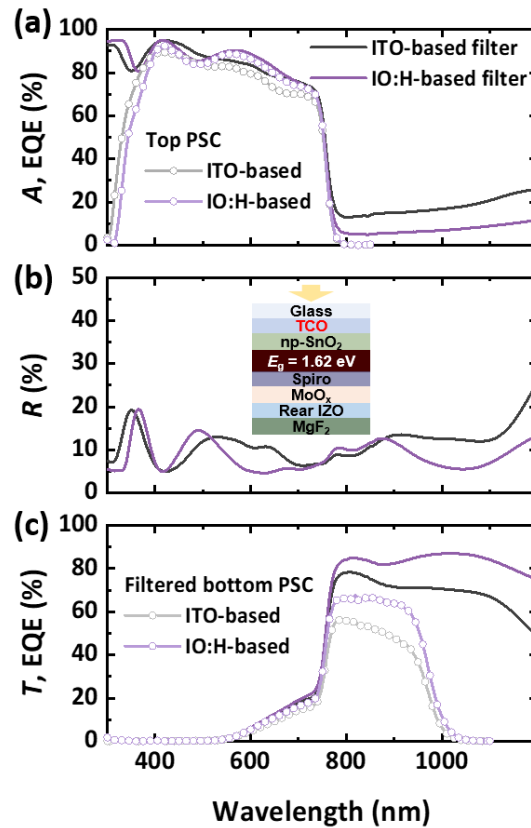


Figure 6.15. (a) Absorbance (A), (b) reflectance (R), and (c) transmittance (T) spectra of the semi-transparent perovskite filters with ITO and IO:H front electrodes. External quantum efficiency (EQE) spectra of the (ITO- and IO:H-based) top PSCs and filtered bottom PSCs are given in figures a and c, respectively.

in Figure 6.15b, is correlated with the reduced reflections of the IO:H-based top PSC compared to the ITO-based top PSC. The reduced reflection led to an improved absorbance up to the bandgap of the perovskite (<760 nm) for the IO:H-based top PSC (Figure 6.15a).

Comparing the EQE spectra of the ITO- and IO:H-based *filtered* bottom PSCs (Figure 6.15c), we realized that the EQE of the ITO-based *filtered* bottom PSCs are suppressed in longer wavelength (≈ 870 nm) when filtered by an ITO-based filter (Figure 6.14c), due to (1) reduced NIR transmittance of the semi-transparent top filter with an ITO front electrode (Figure 6.14c) as well as (2) reduced EQE of the ITO-based bottom PSC itself due to low transmittance of its ITO front electrode compared to an IO:H-based narrow-bandgap bottom PSC (Figure 6.10b).

These results highlight IO:H (with very low NIR parasitic absorption) as a beneficial front electrode for both top and bottom PSCs in a tandem configuration resulting in a boost in the photocurrent of the sub-cells and consequently the overall performance of the 4T all-PTSCs.

6.6. Summary

In the first part of this chapter, we introduced HTL-free narrow-bandgap PSCs in the absence of a dedicated HTL. By comparing the performance of an HTL-free PSC with a narrow-

bandgap PSC based on a PTAA HTL (both solar cells deposited on ITO), we showed that removing PTAA HTL does not hamper the photovoltaic characteristics of the respective PSCs.

Next, we investigated the optical and electrical properties of commonly used commercial TCOs (ITO and FTO) and compared them with sputtered IO:H substrates. We determined that IO:H has significantly higher transmittance especially in the NIR wavelengths, which is maintained by lower charge carrier concentration since most of the free charge carriers absorb photons in lower energies. Furthermore, we found that compared to ITO/perovskite and FTO/perovskite interfaces, IO:H/perovskite is a better interface particularly for HTL-free PSCs with mixed Sn/Pb perovskite because XPS exhibited that a lower amount of Sn⁴⁺ was formed at this interface during the growth of the perovskite. This reduced the oxidation of the mixed Sn/Pb perovskite thin film at the interface. Moreover, in line with AFM images, XPS results identified IO:H as a better substrate for a more homogenous growth of perovskite.

Having demonstrated that IO:H is a better electrode for mixed Sn/Pb perovskite thin film and has the highest transmittance compared to traditional ITO and FTO, we investigated the effects of these TCOs as the front electrodes on the performance of the HTL-free PSCs. Firstly, we realized that despite a lack of an HTL at the TCO/perovskite interface, all three

Table 6.3. Photovoltaic parameters of champion ITO- and IO:H-based semi-transparent top and HTL-free bottom perovskite solar cells (stand-alone and filtered by ITO and IO:H) derived from $J-V$ characteristics (backward scan: top row, forward scan: bottom row). The SPCE of the top and bottom (standalone and filtered) PSCs and the respective calculated 4T all-PTSC are in bold.

ITO-based Perovskite Solar Cell	J_{sc} (mA/cm ²)	V_{oc} (mV)	FF (%)	PCE (%)	SPCE (%)
Semi-transparent top	20.2	1.15	78.2	18.2	17.3
	20.1	1.11	70.1	15.6	
HTL-free bottom (stand-alone)	28.5	0.80	74.6	17.1	16.5
	28.3	0.79	66.3	14.9	
HTL-free bottom (filtered by ITO)	8.5	0.78	76.6	5.1	4.6
	8.4	0.77	68.8	4.4	
4T all-PTSC				23.3	21.9
				20.0	
IO:H-based Perovskite Solar Cell	J_{sc} (mA/cm ²)	V_{oc} (mV)	FF (%)	PCE (%)	SPCE (%)
Semi-transparent top	20.8	1.16	78.7	19.0	18.1
	20.7	1.13	73.9	17.4	
HTL-free bottom (stand-alone)	30.5	0.79	72.1	17.3	17.0
	30.4	0.78	61.7	14.6	
HTL-free bottom (filtered by IO:H)	10.5	0.79	70.2	5.8	5.2
	10.4	0.78	62.9	5.1	
4T all-PTSC				24.8	23.3
				22.5	

configurations with different TCOs work properly. However, the IO:H-based HTL-free PSCs showed better performances with improved photocurrent due to low NIR absorbance losses, as expected.

Finally, to maximize the PCE of a 4T all-PTSC, we replaced the commonly used ITO front electrodes in both sub-cells with highly transparent IO:H. This is the first study on the performance of 4T all-PTSCs, for which both sub-cells have IO:H front electrodes. Here, an IO:H-based HTL-free PSC with triple-cation mixed Sn/Pb narrow-bandgap perovskite thin film (with a bandgap of 1.26 eV) played the role of a tandem partner for an IO:H-based semi-transparent PSC with triple-cation pure Pb perovskite thin film (with a bandgap of 1.62 eV). The use of IO:H instead of ITO enabled us to improve the photocurrent in both sub-cells, and accordingly the PCE from 23.3% (for an ITO-based 4T all-PTSC) to 24.8% (for an IO:H-based 4T-all PTSC).

7. Conclusion and Outlook

Thin-film photovoltaics (PV) has drawn enormous attention as a sustainable and versatile source of electricity and will supposedly remain a focus of future research in the field. Perovskite thin films, in particular, interest the researchers most not only due to their rapid development in the power conversion efficiency (PCE) but also being highly cost-effective compared to their counterparts. Nevertheless, commercialization of this new technology relies on improving the efficiency and stability of perovskite solar cells (PSCs), which is feasible through having a deeper comprehension of the properties of perovskite materials and optimizing device architecture in the form of a single-junction as well as tandem configurations.

The contribution of this work is to (i) provide a better understanding of the most commonly used multi-cation perovskite materials by exploring a common phenomenon whereupon the PCE of pristine PSCs improves simply by storing the devices for a few days after fabrication, (ii) investigate the effects of Cs incorporation on improving the efficiency and photo-stability of narrow-bandgap PSCs, and (iii) determine pathways to reduce optical losses in four-terminal all-perovskite tandem solar cells (4T all-PTSCs).

Spontaneous enhancement of power conversion efficiency

PCE is the key characteristic of a solar cell commonly used to compare the performance of one solar cell to another. Therefore, it is of significant importance to thoroughly investigate any phenomena influencing this characteristic. A commonly observed phenomenon has been reported in the literature whereupon the PCE of PSCs enhances spontaneously only by storing the pristine devices for several days to weeks at room temperature, yet a comprehensive study on this phenomenon is still missing.

Based on the findings in this thesis (Chapter 4), the *spontaneous enhancement* of PCE is not restricted to specific PSC structures or perovskite compositions. Nevertheless, the magnitude of spontaneous enhancement in PCE differs for PSCs with various perovskite compositions and electron transport layers (ETLs). The enhancement of PCE is mainly driven by open-circuit voltage (V_{OC}) and fill factor (FF), which is in line with a remarkable enhancement in photoluminescence (PL) intensity and charge carrier lifetime. These observations

demonstrate that spontaneous enhancement is accompanied by a reduction in non-radiative recombination in the bulk of the perovskite.

Morphological and structural analyses provide evidence that no pronounced changes occur in perovskite grain size upon storage. Thus, we rule out spontaneous coalescence of the perovskite crystallites as a possible reason for spontaneous enhancement, as was proposed in the literature by a few studies. Though, we observe a shift of the perovskite reflection peaks to the larger diffraction angles in the X-ray diffraction (XRD) pattern of the perovskite thin film before and after storage. Performing strain analysis, we attribute this shift to a reduction in lattice strain in the perovskite thin films upon storage. Lattice strains generally emerge during film formation due to a mismatched thermal expansion between the perovskite thin films and the substrates. Strain induces defect concentration and trap states causing non-radiative recombination. Thermally stimulated current (TSC) results confirm the existence of trap states in pristine PSCs and their disappearance after storage, which could be due to strain relaxation in the perovskite material.

Moreover, according to the literature, strain can lead to a phase segregation in mixed halide perovskite thin films. Therefore, the observed low-energy state in the PL emission of the pristine perovskite thin films can be attributed to phase segregation induced by initially-present strain in the pristine perovskite thin films. However, strain relaxation upon storage lead to a volumetric reduction of the low-energy phase and accordingly disappearance of the low-energy state in the PL emission. In brief, the characterizations provided in this thesis demonstrate that the spontaneous enhancement of PCE is due to a gradual strain-relaxation in the bulk of the perovskite leading to a reduction in strain-induced trap density and/or suppression of strain-induced phase segregation.

The generality and magnitude of spontaneous enhancement for different compositions of multi-cation-halide perovskite and device structures of PSCs, which is realized in this thesis, highlights the importance of specifying the absolute PCE increase initiated by spontaneous enhancement when reporting the efficiency of a solar cell in the literature. Moreover, future studies on developing strategies that could accelerate this phenomenon are highly encouraged. Strategies for quickly inducing morphological changes that could accelerate strain relaxation and accordingly accelerate *spontaneous enhancement* might be of significant interest in such a context.

Stability improvement of narrow-bandgap perovskite solar cells

The second part of this thesis (Chapters 5) is focused on improving the stability of narrow-bandgap PSCs. At the outset, we realize that incorporating minute quantities of Cs into a double-cation $\text{FA}_{0.8}\text{MA}_{0.2}\text{Sn}_{0.5}\text{Pb}_{0.5}\text{I}_3$ perovskite significantly improves the operational photo-stability of narrow-bandgap PSCs. Through a comparative study on the optimum Cs concentration, we establish that narrow-bandgap PSCs with triple-cation $\text{Cs}_{0.025}(\text{FA}_{0.8}\text{MA}_{0.2})_{0.975}\text{Sn}_{0.5}\text{Pb}_{0.5}\text{I}_3$ perovskite absorbers can achieve PCEs as high as 18.2% while maintaining 92% of their initial efficiencies after 120 min of maximum power point (MPP) tracking, whereas the PCEs of double-cation $\text{FA}_{0.8}\text{MA}_{0.2}\text{Sn}_{0.5}\text{Pb}_{0.5}\text{I}_3$ narrow-bandgap

PSCs (in the absence of Cs) degrade to 61% of their initial values after 120 min MPP tracking.

While investigating the role of Cs in improved performance of narrow-bandgap PSCs, scanning electron microscopy (SEM) images reveal the existence of bright aggregates atop perovskite thin film in the absence of Cs that disappear by increasing Cs concentration. Evidenced by XRD and cathodoluminescence (CL), these aggregates are identified as residual $\text{Sn}_y\text{Pb}_{(1-y)}\text{I}_2$ (with $0 < y < 1$) with a bandgap of ≈ 2.1 eV, which can hamper charge extraction at the perovskite/PCBM interface and therefore hinder the stability of PSCs. A detailed study on perovskite thin films with pronounced amount of Sn and Pb excess reveal that reactions between Cs and residual $\text{Sn}_y\text{Pb}_{(1-y)}\text{I}_2$ results in increased volumetric growth of the perovskite material with a beneficial composition leading to an improved photo-current that increases the PCE of the PSCs with sufficient amount of Cs accordingly.

Using the triple-cation mixed Sn/Pb narrow-bandgap PSC (with a bandgap of 1.26 eV and a PCE of 18.2%) as a tandem partner with a semi-transparent PSC (with a bandgap of 1.65 eV and a PCE of 18.0%), we realize a 4T all-PTSC with a respectable PCE of 23.6%, which is comparable with the highest PCE (25.0%) ever reported for a 4T all-PTSC in the literature.

Briefly, we demonstrate the potential of triple-cation mixed Sn/Pb narrow-bandgap PSCs with improved photo-stability. It should be noted that compared to the recently published high-efficiency narrow-bandgap PSCs (with PCEs > 20%),^{21-23,29} our results have been attained in the absence of any additives such as GuaSCN,²¹ ascorbic acid,¹⁷⁸ sulfonic acid group,¹⁷⁹ and cadmium ions (Cd^{2+}).²³ Therefore, future studies to potentially improve the efficiency and stability of the triple-cation narrow-bandgap PSCs through establishing strategies such as incorporating antioxidant additives, Sn-reduced precursor solutions,^{22,29} and/or applying 2D components as passivation layers are suggested as future projects.

Mitigation of optical losses in all-perovskite tandem solar cells

On the path to further improve the performance of the 4T all-PTSCs established in Chapter 5, we effectively increase the PCE to 24.8% through (i) removing the hole transport layer (HTL) from the narrow-bandgap bottom PSC and (ii) reducing the optical losses introduced by the front and rear electrodes of the semi-transparent top PSC (Chapter 6).

To begin, we fabricate HTL-free narrow-bandgap PSCs by removing the PTAA layer, which we used as an HTL in the bottom cell of the 4T all-PTSC in Chapter 5. In line with the literature, we realize that PTAA introduces unwanted parasitic absorption in the shorter wavelengths (350-500 nm), which results in a decrease in the external quantum efficiency (EQE) responses of the narrow-bandgap PSCs. Removing PTAA improves short-circuit current (J_{SC}) integrated from the EQE spectra (by ≈ 0.5 mA/cm²) without hampering other photovoltaic characteristics (V_{OC} and FF), leading to an improvement (by $\approx 1\%$) in absolute PCE.

To reduce optical losses induced with the commonly used ITO front electrode, we replace it with a sputtered IO:H front electrode as an alternative with remarkably high transmittance

(>85%) and nearly zero parasitic absorption (<2%) in the near-infrared (NIR) wavelengths, maintained by a lower charge carrier concentration. Replacing the ITO front electrode with IO:H for HTL-free and semi-transparent PSCs enhances the averaged J_{SC} by ≈ 2 and 1 mA/cm^2 , respectively. The higher transmittance of IO:H comes with a higher sheet resistance that lowers the FF. However, the very high current enhancement compensates for the low FF of the IO:H-based HTL-free narrow-bandgap PSCs. Finding strategies to improve the FF of the IO:H-based narrow-bandgap PSCs can be the focus of future studies in this matter.

Having realized that IO:H-based PSCs perform better than ITO-based PSCs, we compare the performance of an ITO-based 4T all-PTSC (with ITO-based top and bottom PSCs) with an IO:H-based 4T all-PTSC (with IO:H-based top and bottom PSCs). As a result, the PCE of the tandem solar cell significantly enhances from 23.3% (for an ITO-based 4T all-PTSC) to 24.8% (for an IO:H-based 4T-all PTSC). This PCE is one of the highest PCEs ever reported for a 4T all-PTSC, and this is the first study on a 4T all-PTSC with only IO:H front electrodes (in the top and bottom PSCs). Furthermore, we replace the in-house sputtered ITO rear electrode, used for the semi-transparent top cell in Chapter 5, with a highly NIR transparent in-house sputtered IZO rear electrode, which further enhances the transmission of the semi-transparent top cell in the NIR wavelengths.

Aside from the optical benefits of IO:H substrates, we also demonstrate that IO:H/perovskite serves as a better interface compared to ITO/perovskite and FTO/perovskite interfaces, particularly for HTL-free PSCs with mixed Sn/Pb perovskite. X-ray photoelectron spectroscopy (XPS) exhibits formation of a lower amount of Sn^{4+} at this interface (IO:H/perovskite) during the growth of the perovskite, which can mitigate the oxidation of the mixed Sn/Pb perovskite thin film at this interface resulting in structurally more stable perovskite thin films.

Future work can be dedicated to replacing the IZO rear with an IO:H rear electrode that has even lower absorption in the NIR region and is expected to potentially increase the transmittance of the semi-transparent top PSC. Nevertheless, depositing highly crystalline IO:H requires a post-deposition annealing treatment at $\approx 200 \text{ }^\circ\text{C}$, which is a challenge as perovskite thin films tend to degrade at this temperature. Therefore, developing strategies to deposit high-quality IO:H rear electrode without compromising the quality of the IO:H as well as perovskite thin films are highly encouraged. However, improving other photovoltaic characteristics of the IO:H-based sub-cells, such as hysteresis and poor FF, can be another focus of the future studies.

Appendix

A. Appendix of Chapter 4

Pseudo-Voigt Profile

A pseudo-Voigt function is a linear contribution from both Gaussian and Lorentzian components. We define the following fitting equation - in Origin (version: 2018b 9.55) - for two bands:

$$f(x; A_1, X_{c1}, w_1, \mu_1, A_2, X_{c2}, w_2, \mu_2) =$$

$$A_1 \left[\mu_1 \frac{2}{\pi} \frac{w_1}{4(x - X_{c1})^2 + w_1^2} + (1 - \mu_1) \frac{\sqrt{4 \ln(2)}}{\sqrt{\pi} w_1} e^{-\frac{4 \ln(2)}{w_1^2} (x - X_{c1})^2} \right] +$$

$$A_2 \left[\mu_2 \frac{2}{\pi} \frac{w_2}{4(x - X_{c2})^2 + w_2^2} + (1 - \mu_2) \frac{\sqrt{4 \ln(2)}}{\sqrt{\pi} w_2} e^{-\frac{4 \ln(2)}{w_2^2} (x - X_{c2})^2} \right]$$

where x is energy in eV, A_1 and A_2 are the amplitudes, X_{c1} and X_{c2} are the center positions, and w_1 and w_2 are the FWHM of the two bands. $0 \leq \mu_1 \leq 1$ and $0 \leq \mu_2 \leq 1$ are the fractions of Lorentzian profiles in the function, such that if μ equals one the band is pure Lorentzian, and if it equals zero the band is pure Gaussian.

We carry out the fitting computation for the delayed PL spectra on days 1 and 10 (Figure. 4.14) using two-peak pseudo-Voigt profiles, wherein the peak positions, widths, and contributing factors are shared between fitting profiles used for day 1 and 10, whereas the area is allowed to change. Relative area (R. Area) under PL peaks extracted from the fitting analysis of the PL spectra on days 1 and 10 is listed in the following table:

Storage Time	R. Area(1.54 eV)	R. Area(1.62 eV)
Day 1	81641	41820
Day 10	15260	56353

B. Appendix of Chapter 5

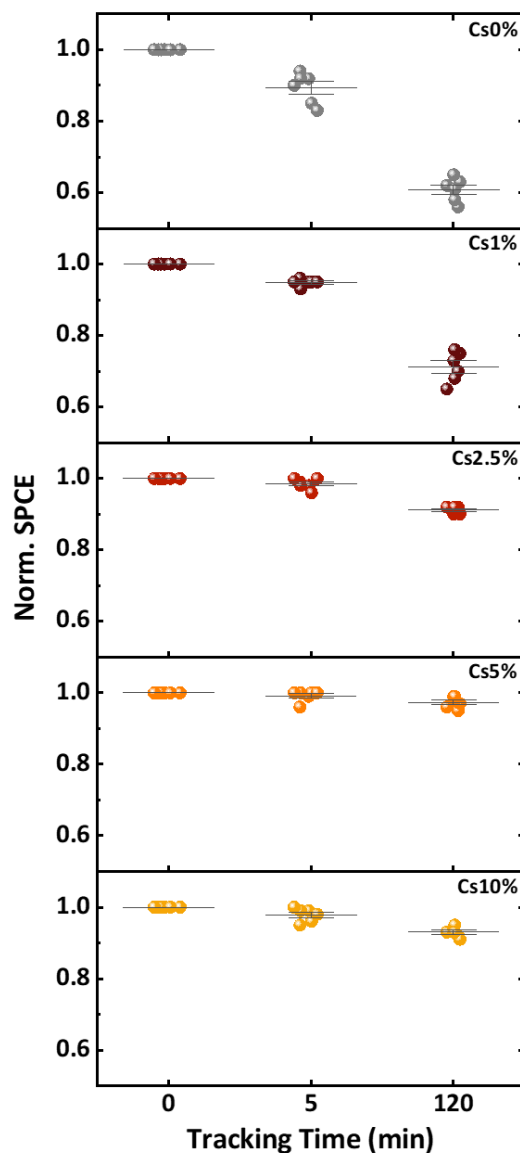


Figure B1. Stabilized power conversion (SPCE) from maximum power point (MPP) tracking measurements at 0 min (when the lamp is on), and after 5 and 120 min derived from narrow bandgap PSCs with different Cs concentrations varying from 0% to 10% (top to bottom), which were identically prepared in different batches. The initial values (at 0 min) are normalized to 1. Reproduced from [155] with permission of The Royal Society of Chemistry.

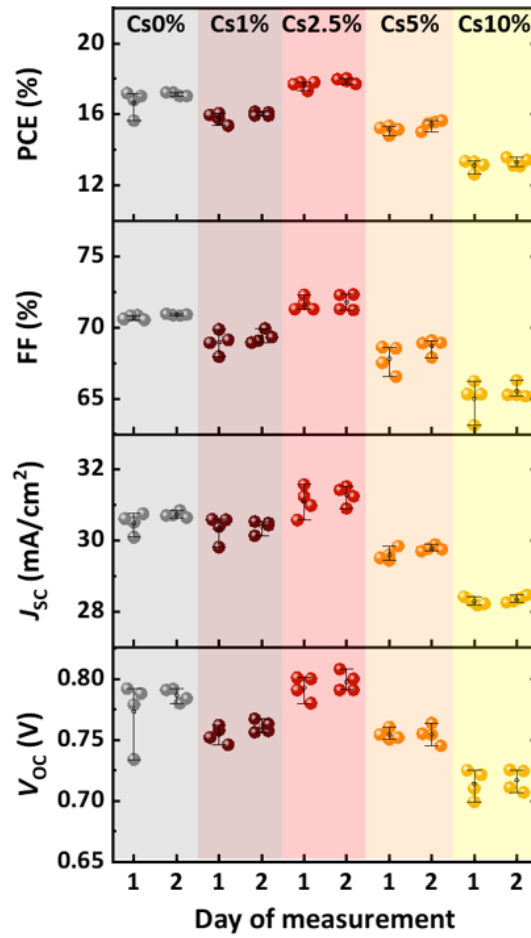


Figure B2. From top to bottom, power conversion efficiency (PCE), fill factor (FF), short-circuit current (J_{sc}), and open-circuit voltage (V_{oc}) of champion narrow-bandgap PSCs (from different batches) with different Cs concentrations measured on day 1 (day of device preparation) and day 2 (after one night of storage in a dark inert atmosphere). Reproduced from [155] with permission of The Royal Society of Chemistry.

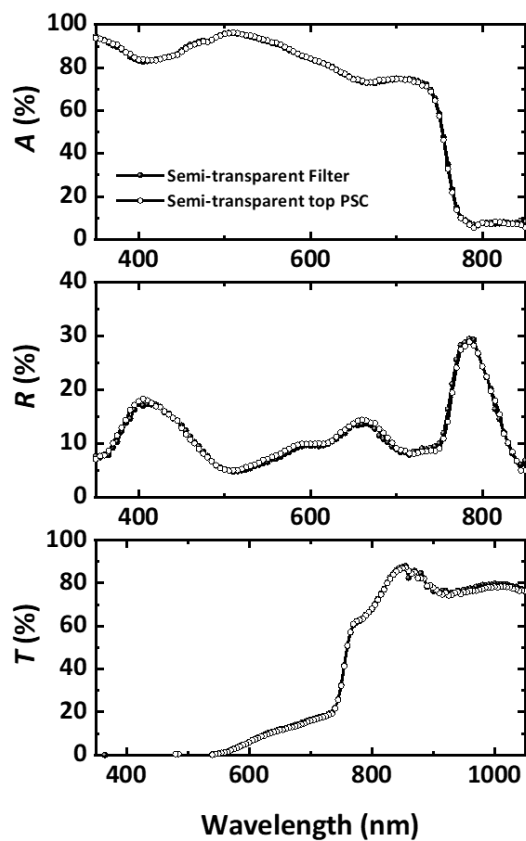


Figure B3. From top to bottom, absorbance (A), reflectance (R), and transmittance (T) spectra of a semi-transparent perovskite filter and a semi-transparent top PSC, composed of a double-cation $\text{Cs}_{0.17}\text{FA}_{0.83}\text{Pb}(\text{I}_{0.76}\text{Br}_{0.24})_3$ perovskite thin film with a bandgap of $E_g \approx 1.65$ eV. The relative difference in transmittance and reflectance on average (derived from three filters and three PSCs) is equal to $\pm 1.1\%$ and $\pm 0.1\%$, respectively (weighted to AM1.5G). Reproduced from [155] with permission of The Royal Society of Chemistry.

References

1. Newell, R. G., Raimi, D. & Aldana, G. Global Energy Outlook 2019: The Next Generation of Energy. *Resour. Futur.* 46 (2019).
2. Sato, Y. Energy consumption: an environmental problem. *IEEEJ Trans. Electr. Electron. Eng.* **2**, 12–16 (2007).
3. Heede, R. & Oreskes, N. Potential emissions of CO₂ and methane from proved reserves of fossil fuels: An alternative analysis. *Glob. Environ. Chang.* (2016). doi:10.1016/j.gloenvcha.2015.10.005
4. An IPCC Special Report. *Global warming of 1.5°C*. (2019). doi:10.1038/291285a0
5. Wang, J. & Chameides, B. Are Humans Responsible for Global Warming? *Environ. Def.* (2007).
6. UNFCCC. *PARIS AGREEMENT - Conference of the Parties COP 21. Adoption of the Paris Agreement. Proposal by the President*. (2015).
7. International Energy Agency (IEA). *Outlook for energy: a perspective to 2040*. (2019).
8. U.S. Energy Information Administration. *International Energy Outlook 2019 with projections to 2050*. (2019).
9. ISE, P. R. I. F. O. R. S. E. S. Photovoltaics Report. (2020).
10. Green, M. A. *et al.* Solar cell efficiency tables (Version 55). *Prog. Photovoltaics Res. Appl.* **28**, 3–15 (2020).
11. Wilson, G. M. *et al.* The 2020 photovoltaic technologies roadmap. *J. Phys. D. Appl. Phys.* **53**, 493001 (2020).
12. best-research-cell-efficiencies.20200925.pdf. *NREL* (2020).
13. Kojima, A., Teshima, K., Shirai, Y. & Miyasaka, T. Organometal Halide Perovskites as Visible-Light Sensitizers for Photovoltaic Cells. *J. Am. Chem. Soc.* **131**, 6050–6051 (2009).
14. Abzieher, T. *et al.* Electron-Beam-Evaporated Nickel Oxide Hole Transport Layers for Perovskite-Based Photovoltaics. *Adv. Energy Mater.* **9**, 1802995 (2019).
15. Cojocar, L. *et al.* Detailed Investigation of Evaporated Perovskite Absorbers with High Crystal Quality on Different Substrates. *ACS Appl. Mater. Interfaces* **10**, 26293–26302 (2018).
16. Howard, I. A. *et al.* Coated and Printed Perovskites for Photovoltaic Applications. *Adv. Mater.* **31**, 1806702 (2019).
17. Hwang, K. *et al.* Toward large scale roll-to-roll production of fully printed perovskite solar cells. *Adv. Mater.* **27**, 1241–1247 (2015).
18. Leijtens, T., Bush, K. A., Prasanna, R. & McGehee, M. D. Opportunities and

- challenges for tandem solar cells using metal halide perovskite semiconductors. *Nat. Energy* **3**, 828–838 (2018).
19. Correa-Baena, J.-P. *et al.* Promises and challenges of perovskite solar cells. *Science* **358**, 739–744 (2017).
 20. Wang, C., Song, Z., Li, C., Zhao, D. & Yan, Y. Low-Bandgap Mixed Tin-Lead Perovskites and Their Applications in All-Perovskite Tandem Solar Cells. *Adv. Funct. Mater.* **29**, 1808801 (2019).
 21. Tong, J. *et al.* Carrier lifetimes of $>1 \mu\text{s}$ in Sn-Pb perovskites enable efficient all-perovskite tandem solar cells. *Science* **364**, 475–479 (2019).
 22. Lin, R. *et al.* Monolithic all-perovskite tandem solar cells with 24.8% efficiency exploiting comproportionation to suppress Sn(II) oxidation in precursor ink. *Nat. Energy* **4**, 864–873 (2019).
 23. Yang, Z. *et al.* Enhancing electron diffusion length in narrow-bandgap perovskites for efficient monolithic perovskite tandem solar cells. *Nat. Commun.* **10**, 4498 (2019).
 24. Hörantner, M. T. & Snaith, H. J. Predicting and optimising the energy yield of perovskite-on-silicon tandem solar cells under real world conditions. *Energy Environ. Sci.* **10**, 1983–1993 (2017).
 25. Hörantner, M. T. *et al.* The Potential of Multijunction Perovskite Solar Cells. *ACS Energy Lett.* **2**, 2506–2513 (2017).
 26. Futscher, M. H. & Ehrler, B. Efficiency Limit of Perovskite/Si Tandem Solar Cells. *ACS Energy Lett.* **1**, 863–868 (2016).
 27. Gharibzadeh, S. *et al.* 2D/3D Heterostructure for Semitransparent Perovskite Solar Cells with Engineered Bandgap Enables Efficiencies Exceeding 25% in Four-Terminal Tandems with Silicon and CIGS. *Adv. Funct. Mater.* **30**, 1909919 (2020).
 28. Lehr, J. *et al.* Energy yield modelling of perovskite/silicon two-terminal tandem PV modules with flat and textured interfaces. *Sustain. Energy Fuels* **2**, 2754–2761 (2018).
 29. Jiang, T. *et al.* Realizing High Efficiency over 20% of Low-Bandgap Pb–Sn-Alloyed Perovskite Solar Cells by In Situ Reduction of Sn $4+$. *Sol. RRL* **4**, 1900467 (2020).
 30. Kapil, G. *et al.* Strain Relaxation and Light Management in Tin–Lead Perovskite Solar Cells to Achieve High Efficiencies. *ACS Energy Lett.* **4**, 1991–1998 (2019).
 31. Li, Z. *et al.* Stabilizing Perovskite Structures by Tuning Tolerance Factor: Formation of Formamidinium and Cesium Lead Iodide Solid-State Alloys. *Chem. Mater.* **28**, 284–292 (2016).
 32. Jaysankar, M. *et al.* Perovskite-silicon tandem solar modules with optimised light harvesting. *Energy Environ. Sci.* **11**, 1489–1498 (2018).
 33. Schultes, M. *et al.* Sputtered Transparent Electrodes (IO:H and IZO) with Low Parasitic Near-Infrared Absorption for Perovskite–Cu(In,Ga)Se₂ Tandem Solar Cells. *ACS Appl. Energy Mater.* **2**, 7823–7831 (2019).

34. Jacobs, D. A. *et al.* Light Management: A Key Concept in High-Efficiency Perovskite/Silicon Tandem Photovoltaics. *J. Phys. Chem. Lett.* **10**, 3159–3170 (2019).
35. Duong, T. *et al.* Semitransparent Perovskite Solar Cell With Sputtered Front and Rear Electrodes for a Four-Terminal Tandem. *IEEE J. Photovoltaics* **6**, 679–687 (2016).
36. Schultes, M. Four – Terminal Perovskite – CIGS Tandem Solar Cells with Improved Near – Infrared Response. (2019).
37. Brewer, S. H. & Franzen, S. Indium tin oxide plasma frequency dependence on sheet resistance and surface adlayers determined by reflectance FTIR spectroscopy. *J. Phys. Chem. B* **106**, 12986–12992 (2002).
38. Sathiaraj, T. S. Effect of annealing on the structural, optical and electrical properties of ITO films by RF sputtering under low vacuum level. *Microelectronics J.* **39**, 1444–1451 (2008).
39. Schulze, P. S. C. *et al.* 25.1% High-Efficiency Monolithic Perovskite Silicon Tandem Solar Cell with a High Bandgap Perovskite Absorber. *Sol. RRL* **4**, 2000152 (2020).
40. Aidarkhanov, D. *et al.* Passivation engineering for hysteresis-free mixed perovskite solar cells. *Sol. Energy Mater. Sol. Cells* **215**, 110648 (2020).
41. Roose, B. *et al.* Spontaneous crystal coalescence enables highly efficient perovskite solar cells. *Nano Energy* **39**, 24–29 (2017).
42. Fei, C. & Wang, H. Age-induced recrystallization in perovskite solar cells. *Org. Electron.* **68**, 143–150 (2019).
43. Ngo, T. T., Barea, E. M., Tena-Zaera, R. & Mora-Sero, I. Spray-Pyrolyzed ZnO as Electron Selective Contact for Long-Term Stable Planar CH₃NH₃PbI₃ Perovskite Solar Cells. *ACS Appl. Energy Mater.* **1**, 4057–4064 (2018).
44. Bi, C., Zheng, X., Chen, B., Wei, H. & Huang, J. Spontaneous Passivation of Hybrid Perovskite by Sodium Ions from Glass Substrates: Mysterious Enhancement of Device Efficiency Revealed. *ACS Energy Lett.* **2**, 1400–1406 (2017).
45. Prasanna, R. *et al.* Band Gap Tuning via Lattice Contraction and Octahedral Tilting in Perovskite Materials for Photovoltaics. *J. Am. Chem. Soc.* **139**, 11117–11124 (2017).
46. Jesper Jacobsson, T. *et al.* Exploration of the compositional space for mixed lead halogen perovskites for high efficiency solar cells. *Energy Environ. Sci.* **9**, 1706–1724 (2016).
47. De Wolf, S. *et al.* Organometallic halide perovskites: Sharp optical absorption edge and its relation to photovoltaic performance. *J. Phys. Chem. Lett.* **5**, 1035–1039 (2014).
48. Lin, Q., Armin, A., Nagiri, R. C. R., Burn, P. L. & Meredith, P. Electro-optics of perovskite solar cells. *Nat. Photonics* **9**, 106–112 (2015).
49. Miyata, A. *et al.* Direct measurement of the exciton binding energy and effective masses for charge carriers in organic–inorganic tri-halide perovskites. *Nat. Phys.* **11**,

- 582–587 (2015).
50. Stranks, S. D. *et al.* Electron-Hole Diffusion Lengths Exceeding 1 Micrometer in an Organometal Trihalide Perovskite Absorber. *Science* **342**, 341–344 (2013).
 51. Chen, Y. *et al.* Extended carrier lifetimes and diffusion in hybrid perovskites revealed by Hall effect and photoconductivity measurements. *Nat. Commun.* **7**, 12253 (2016).
 52. Wehrenfennig, C., Eperon, G. E., Johnston, M. B., Snaith, H. J. & Herz, L. M. High charge carrier mobilities and lifetimes in organolead trihalide perovskites. *Adv. Mater.* **26**, 1584–1589 (2014).
 53. Xiao, Z. & Yan, Y. Progress in Theoretical Study of Metal Halide Perovskite Solar Cell Materials. *Adv. Energy Mater.* **7**, 1701136 (2017).
 54. Li, C. *et al.* Formability of ABX₃ (X = F, Cl, Br, I) halide perovskites. *Acta Crystallogr. Sect. B Struct. Sci.* **64**, 702–707 (2008).
 55. Richard J. D. Tilley. *Perovskites Structure-Property Relationship*. Wiley (2016).
 56. Travis, W., Glover, E. N. K., Bronstein, H., Scanlon, D. O. & Palgrave, R. G. On the application of the tolerance factor to inorganic and hybrid halide perovskites: a revised system. *Chem. Sci.* **7**, 4548–4556 (2016).
 57. Weller, M. T., Weber, O. J., Henry, P. F., Di Pumpo, A. M. & Hansen, T. C. Complete structure and cation orientation in the perovskite photovoltaic methylammonium lead iodide between 100 and 352 K. *Chem. Commun.* **51**, 4180–4183 (2015).
 58. Eperon, G. E. *et al.* Inorganic caesium lead iodide perovskite solar cells. *J. Mater. Chem. A* **3**, 19688–19695 (2015).
 59. Lee, J.-W. *et al.* Formamidinium and Cesium Hybridization for Photo- and Moisture-Stable Perovskite Solar Cell. *Adv. Energy Mater.* **5**, 1501310 (2015).
 60. Saliba, M. *et al.* Cesium-containing triple cation perovskite solar cells: improved stability, reproducibility and high efficiency. *Energy Environ. Sci.* **9**, 1989–1997 (2016).
 61. Yin, W.-J., Shi, T. & Yan, Y. Unique Properties of Halide Perovskites as Possible Origins of the Superior Solar Cell Performance. *Adv. Mater.* **26**, 4653–4658 (2014).
 62. Meloni, S., Palermo, G., Ashari-Astani, N., Grätzel, M. & Rothlisberger, U. Valence and conduction band tuning in halide perovskites for solar cell applications. *J. Mater. Chem. A* **4**, 15997–16002 (2016).
 63. Milot, R. L., Eperon, G. E., Snaith, H. J., Johnston, M. B. & Herz, L. M. Temperature-Dependent Charge-Carrier Dynamics in CH₃NH₃PbI₃ Perovskite Thin Films. *Adv. Funct. Mater.* **25**, 6218–6227 (2015).
 64. Parrott, E. S. *et al.* Effect of Structural Phase Transition on Charge-Carrier Lifetimes and Defects in CH₃NH₃SnI₃ Perovskite. *J. Phys. Chem. Lett.* **7**, 1321–1326 (2016).
 65. Hao, F., Stoumpos, C. C., Chang, R. P. H. & Kanatzidis, M. G. Anomalous Band Gap Behavior in Mixed Sn and Pb Perovskites Enables Broadening of Absorption

- Spectrum in Solar Cells. *J. Am. Chem. Soc.* **136**, 8094–8099 (2014).
66. Im, J., Stoumpos, C. C., Jin, H., Freeman, A. J. & Kanatzidis, M. G. Antagonism between Spin-Orbit Coupling and Steric Effects Causes Anomalous Band Gap Evolution in the Perovskite Photovoltaic Materials $\text{CH}_3\text{NH}_3\text{Sn}_{1-x}\text{Pb}_x\text{I}_3$. *J. Phys. Chem. Lett.* **6**, 3503–3509 (2015).
67. Noh, J. H., Im, S. H., Heo, J. H., Mandal, T. N. & Seok, S. Il. Chemical management for colorful, efficient, and stable inorganic-organic hybrid nanostructured solar cells. *Nano Lett.* **13**, 1764–1769 (2013).
68. Juarez-Perez, E. J. *et al.* Photoinduced Giant Dielectric Constant in Lead Halide Perovskite Solar Cells. *J. Phys. Chem. Lett.* **5**, 2390–2394 (2014).
69. Ponceca, C. S. *et al.* Organometal Halide Perovskite Solar Cell Materials Rationalized: Ultrafast Charge Generation, High and Microsecond-Long Balanced Mobilities, and Slow Recombination. *J. Am. Chem. Soc.* **136**, 5189–5192 (2014).
70. Chen, J. & Park, N. Causes and Solutions of Recombination in Perovskite Solar Cells. *Adv. Mater.* **31**, 1803019 (2019).
71. Lloyd-Hughes, J. *et al.* Influence of surface passivation on ultrafast carrier dynamics and terahertz radiation generation in GaAs. *Appl. Phys. Lett.* **89**, 232102 (2006).
72. Shi, D. *et al.* Low trap-state density and long carrier diffusion in organolead trihalide perovskite single crystals. *Science* **347**, 519–522 (2015).
73. Xing, G. *et al.* Long-range balanced electron-and hole-transport lengths in organic-inorganic $\text{CH}_3\text{NH}_3\text{PbI}_3$. *Science* **342**, 344–347 (2013).
74. Chin, X. Y., Cortecchia, D., Yin, J., Bruno, A. & Soci, C. Lead iodide perovskite light-emitting field-effect transistor. *Nat. Commun.* **6**, 7383 (2015).
75. Shrestha, S. *et al.* Assessing Temperature Dependence of Drift Mobility in Methylammonium Lead Iodide Perovskite Single Crystals. *J. Phys. Chem. C* **122**, 5935–5939 (2018).
76. Giorgi, G., Fujisawa, J.-I., Segawa, H. & Yamashita, K. Small Photocarrier Effective Masses Featuring Ambipolar Transport in Methylammonium Lead Iodide Perovskite: A Density Functional Analysis. *J. Phys. Chem. Lett.* **4**, 4213–4216 (2013).
77. Brivio, F., Butler, K. T., Walsh, A. & van Schilfhaarde, M. Relativistic quasiparticle self-consistent electronic structure of hybrid halide perovskite photovoltaic absorbers. *Phys. Rev. B* **89**, 155204 (2014).
78. Correa Baena, J. P. *et al.* Highly efficient planar perovskite solar cells through band alignment engineering. *Energy Environ. Sci.* **8**, 2928–2934 (2015).
79. Belisle, R. A., Jain, P., Prasanna, R., Leijtens, T. & McGehee, M. D. Minimal Effect of the Hole-Transport Material Ionization Potential on the Open-Circuit Voltage of Perovskite Solar Cells. *ACS Energy Lett.* **1**, 556–560 (2016).
80. Ibrahim, A. Analysis of Electrical Characteristics of Photovoltaic Single Crystal Silicon Solar Cells at Outdoor Measurements. *Smart Grid Renew. Energy* **02**, 169–

- 175 (2011).
81. Snaith, H. J. *et al.* Anomalous Hysteresis in Perovskite Solar Cells. *J. Phys. Chem. Lett.* **5**, 1511–1515 (2014).
 82. Tress, W. Metal Halide Perovskites as Mixed Electronic–Ionic Conductors: Challenges and Opportunities—From Hysteresis to Memristivity. *J. Phys. Chem. Lett.* **8**, 3106–3114 (2017).
 83. Tress, W. *et al.* Understanding the rate-dependent J–V hysteresis, slow time component, and aging in CH₃NH₃PbI₃ perovskite solar cells: the role of a compensated electric field. *Energy Environ. Sci.* **8**, 995–1004 (2015).
 84. Ding, C. *et al.* Effect of the conduction band offset on interfacial recombination behavior of the planar perovskite solar cells. *Nano Energy* **53**, 17–26 (2018).
 85. Shockley, W. & Queisser, H. J. Detailed Balance Limit of Efficiency of p–n Junction Solar Cells. *J. Appl. Phys.* **32**, 510–519 (1961).
 86. Hossain, M. I. *et al.* Perovskite/Silicon Tandem Solar Cells: From Detailed Balance Limit Calculations to Photon Management. *Nano-Micro Lett.* **11**, 58 (2019).
 87. (NREL), N. R. E. L. Best Research Efficiency. [Http://www.Nrel.Gov/Ncpv/Images/Efficiency_Chart.Jpg](http://www.nrel.gov/npcv/images/efficiency_chart.jpg) (2016).
 88. Vos, A. De. Detailed balance limit of the efficiency of tandem solar cells. *J. Phys. D. Appl. Phys.* **13**, 839–846 (1980).
 89. Kapil, G. *et al.* Highly Efficient 17.6% Tin–Lead Mixed Perovskite Solar Cells Realized through Spike Structure. *Nano Lett.* **18**, 3600–3607 (2018).
 90. Dinnebier, R. E. & Billinge, S. J. L. *Powder Diffraction*. (Royal Society of Chemistry, 2008). doi:10.1039/9781847558237
 91. Caroli, C., Lederer-Rozenblatt, D., Roulet, B. & Saint-James, D. Inelastic Effects in Photoemission: Microscopic Formulation and Qualitative Discussion. *Phys. Rev. B* **8**, 4552–4569 (1973).
 92. Seah, M. P. & Dench, W. A. Quantitative electron spectroscopy of surfaces: A standard data base for electron inelastic mean free paths in solids. *Surf. Interface Anal.* **1**, 2–11 (1979).
 93. Wagner, C. D. & Muilenberg, G. E. *Handbook of X-ray photoelectron spectroscopy*. (Perkin-Elmer, 1979).
 94. Tanuma, S., Shinotsuka, H., Powell, C. J. & Penn, D. R. Calculation of electron inelastic mean free paths. *J. Surf. Anal.* **21**, 165–176 (1994).
 95. Tress, W. *et al.* Interpretation and evolution of open-circuit voltage, recombination, ideality factor and subgap defect states during reversible light-soaking and irreversible degradation of perovskite solar cells. *Energy Environ. Sci.* **11**, 151–165 (2018).
 96. Caprioglio, P. *et al.* On the Origin of the Ideality Factor in Perovskite Solar Cells.

- Adv. Energy Mater.* **10**, 2000502 (2020).
97. Moghadamzadeh, S. *et al.* Spontaneous enhancement of the stable power conversion efficiency in perovskite solar cells. *J. Mater. Chem. A* **8**, 670–682 (2020).
 98. Ito, N. *et al.* Mixed Sn-Ge Perovskite for Enhanced Perovskite Solar Cell Performance in Air. *J. Phys. Chem. Lett.* **9**, 1682–1688 (2018).
 99. Correa-Baena, J.-P. *et al.* Identifying and suppressing interfacial recombination to achieve high open-circuit voltage in perovskite solar cells. *Energy Environ. Sci.* **10**, 1207–1212 (2017).
 100. *Organic-Inorganic Halide Perovskite Photovoltaics*. *Organic-Inorganic Halide Perovskite Photovoltaics* (Springer International Publishing, 2016). doi:10.1007/978-3-319-35114-8
 101. Hu, Y. *et al.* Understanding the Role of Cesium and Rubidium Additives in Perovskite Solar Cells: Trap States, Charge Transport, and Recombination. *Adv. Energy Mater.* **8**, 1703057 (2018).
 102. Hu, Y., Aygüler, M. F., Petrus, M. L., Bein, T. & Docampo, P. Impact of Rubidium and Cesium Cations on the Moisture Stability of Multiple-Cation Mixed-Halide Perovskites. *ACS Energy Lett.* **2**, 2212–2218 (2017).
 103. Saliba, M. *et al.* M. Saliba et al.- Incorporation of rubidium cations into perovskite solar cells improves photovoltaic performance (2016 Science). **5557**, (2016).
 104. Climent-Pascual, E. *et al.* Influence of the substrate on the bulk properties of hybrid lead halide perovskite films. *J. Mater. Chem. A* **4**, 18153–18163 (2016).
 105. De Bastiani, M., D’Innocenzo, V., Stranks, S. D., Snaith, H. J. & Petrozza, A. Role of the crystallization substrate on the photoluminescence properties of organolead mixed halides perovskites. *APL Mater.* **2**, (2014).
 106. Miller, E. M. *et al.* Substrate-controlled band positions in CH₃NH₃PbI₃ perovskite films. *Phys. Chem. Chem. Phys.* **16**, 22122–22130 (2014).
 107. Cho, A. N. & Park, N. G. Impact of Interfacial Layers in Perovskite Solar Cells. *ChemSusChem* **10**, 3687–3704 (2017).
 108. Saliba, M. *et al.* Cesium-containing triple cation perovskite solar cells: improved stability, reproducibility and high efficiency. *Energy Environ. Sci.* **9**, 1989–1997 (2016).
 109. Duong, T. *et al.* Rubidium Multication Perovskite with Optimized Bandgap for Perovskite-Silicon Tandem with over 26% Efficiency. *Adv. Energy Mater.* **7**, 1700228 (2017).
 110. Yang, W. S. *et al.* Iodide management in formamidinium-lead-halide-based perovskite layers for efficient solar cells. *Science* **356**, 1376–1379 (2017).
 111. Saliba, M. *et al.* Incorporation of rubidium cations into perovskite solar cells improves photovoltaic performance. *Science* **354**, 206–209 (2016).

112. Wojciechowski, K. *et al.* Heterojunction Modification for Highly Efficient Organic–Inorganic Perovskite Solar Cells. *ACS Nano* **8**, 12701–12709 (2014).
113. Cai, F. *et al.* Eliminated hysteresis and stabilized power output over 20% in planar heterojunction perovskite solar cells by compositional and surface modifications to the low-temperature-processed TiO₂ layer. *J. Mater. Chem. A* **5**, 9402–9411 (2017).
114. Li, Y. *et al.* Multifunctional Fullerene Derivative for Interface Engineering in Perovskite Solar Cells. *J. Am. Chem. Soc.* **137**, 15540–15547 (2015).
115. Tiwana, P., Docampo, P., Johnston, M. B., Snaith, H. J. & Herz, L. M. Electron Mobility and Injection Dynamics in Mesoporous ZnO, SnO₂, and TiO₂ Films Used in Dye-Sensitized Solar Cells. *ACS Nano* **5**, 5158–5166 (2011).
116. Jiang, Q. *et al.* Enhanced electron extraction using SnO₂ for high-efficiency planar-structure HC(NH₂)₂PbI₃-based perovskite solar cells. *Nat. Energy* **2**, 16177 (2017).
117. Jiang, Q., Zhang, X. & You, J. SnO₂: A Wonderful Electron Transport Layer for Perovskite Solar Cells. *Small* **14**, 1801154 (2018).
118. Farooq, A. *et al.* Spectral Dependence of Degradation under Ultraviolet Light in Perovskite Solar Cells. *ACS Appl. Mater. Interfaces* **10**, 21985–21990 (2018).
119. Singh, T. & Miyasaka, T. Stabilizing the Efficiency Beyond 20% with a Mixed Cation Perovskite Solar Cell Fabricated in Ambient Air under Controlled Humidity. *Adv. Energy Mater.* **8**, 1700677 (2018).
120. Li, Z. *et al.* Extrinsic ion migration in perovskite solar cells. *Energy Environ. Sci.* **10**, 1234–1242 (2017).
121. Bastos, J. P. *et al.* Light-Induced Degradation of Perovskite Solar Cells: The Influence of 4-Tert-Butyl Pyridine and Gold. *Adv. Energy Mater.* **8**, 1800554 (2018).
122. Castro-Méndez, A. F., Hidalgo, J. & Correa-Baena, J. P. The Role of Grain Boundaries in Perovskite Solar Cells. *Adv. Energy Mater.* **9**, 1–10 (2019).
123. Lee, J.-W. *et al.* The role of grain boundaries in perovskite solar cells. *Mater. Today Energy* **7**, 149–160 (2018).
124. Kim, H. Do, Ohkita, H., Benten, H. & Ito, S. Photovoltaic Performance of Perovskite Solar Cells with Different Grain Sizes. *Adv. Mater.* **28**, 917–922 (2016).
125. Ren, X. *et al.* Modulating crystal grain size and optoelectronic properties of perovskite films for solar cells by reaction temperature. *Nanoscale* **8**, 3816–3822 (2016).
126. Chen, B. *et al.* Grain Engineering for Perovskite/Silicon Monolithic Tandem Solar Cells with Efficiency of 25.4%. *Joule* **3**, 177–190 (2019).
127. Cai, F. *et al.* Ionic Additive Engineering Toward High-Efficiency Perovskite Solar Cells with Reduced Grain Boundaries and Trap Density. *Adv. Funct. Mater.* **28**, 1801985 (2018).
128. Rahman, S. I. *et al.* Grain Boundary Defect Passivation of Triple Cation Mixed Halide Perovskite with Hydrazine-Based Aromatic Iodide for Efficiency Improvement. *ACS*

- Appl. Mater. Interfaces* **12**, 41312–41322 (2020).
129. Son, D.-Y. *et al.* Self-formed grain boundary healing layer for highly efficient CH₃NH₃PbI₃ perovskite solar cells. *Nat. Energy* **1**, 16081 (2016).
 130. Chen, Q. *et al.* Controllable Self-Induced Passivation of Hybrid Lead Iodide Perovskites toward High Performance Solar Cells. *Nano Lett.* **14**, 4158–4163 (2014).
 131. Long, R., Liu, J. & Prezhdov, O. V. Unravelling the Effects of Grain Boundary and Chemical Doping on Electron–Hole Recombination in CH₃NH₃PbI₃ Perovskite by Time-Domain Atomistic Simulation. *J. Am. Chem. Soc.* **138**, 3884–3890 (2016).
 132. Sheng, R. *et al.* Photoluminescence characterisations of a dynamic aging process of organic-inorganic CH₃NH₃PbBr₃ perovskite. *Nanoscale* **8**, 1926–31 (2016).
 133. Jacobsson, T. J., Schwan, L. J., Ottosson, M., Hagfeldt, A. & Edvinsson, T. Determination of Thermal Expansion Coefficients and Locating the Temperature-Induced Phase Transition in Methylammonium Lead Perovskites Using X-ray Diffraction. *Inorg. Chem.* **54**, 10678–10685 (2015).
 134. Thirumoorthi, M. & Thomas Joseph Prakash, J. Structure, optical and electrical properties of indium tin oxide ultra thin films prepared by jet nebulizer spray pyrolysis technique. *J. Asian Ceram. Soc.* **4**, 124–132 (2016).
 135. Ryu, S. Y. *et al.* Effects of the Wrinkle Structure and Flat Structure Formed during Static Low-Temperature Annealing of ZnO on the Performance of Inverted Polymer Solar Cells. *J. Phys. Chem. C* **121**, 9191–9201 (2017).
 136. Jouane, Y. *et al.* Room temperature ZnO growth by rf magnetron sputtering on top of photoactive P3HT: PCBM for organic solar cells. *J. Mater. Chem.* **21**, 1953–1958 (2011).
 137. Moloney, E. G., Yeddu, V. & Saidaminov, M. I. Strain Engineering in Halide Perovskites. *ACS Mater. Lett.* **2**, 1495–1508 (2020).
 138. Bush, K. A. *et al.* Controlling Thin-Film Stress and Wrinkling during Perovskite Film Formation. *ACS Energy Lett.* **3**, 1225–1232 (2018).
 139. Zhao, J. *et al.* Strained hybrid perovskite thin films and their impact on the intrinsic stability of perovskite solar cells. *Sci. Adv.* **3**, eaao5616 (2017).
 140. Xue, D.-J. *et al.* Regulating strain in perovskite thin films through charge-transport layers. *Nat. Commun.* **11**, 1514 (2020).
 141. Jones, T. W. *et al.* Lattice strain causes non-radiative losses in halide perovskites. *Energy Environ. Sci.* **12**, 596–606 (2019).
 142. Sha, W. E. I. *et al.* Quantifying Efficiency Loss of Perovskite Solar Cells by a Modified Detailed Balance Model. *Adv. Energy Mater.* **8**, 1701586 (2018).
 143. Wetzelaer, G. J. A. H. *et al.* Trap-Assisted Non-Radiative Recombination in Organic-Inorganic Perovskite Solar Cells. *Adv. Mater.* **27**, 1837–1841 (2015).
 144. Correa-Baena, J. P. *et al.* Identifying and suppressing interfacial recombination to

- achieve high open-circuit voltage in perovskite solar cells. *Energy Environ. Sci.* **10**, 1207–1212 (2017).
145. Ran, C., Xu, J., Gao, W., Huang, C. & Dou, S. Defects in metal triiodide perovskite materials towards high-performance solar cells: origin, impact, characterization, and engineering. *Chem. Soc. Rev.* **47**, 4581–4610 (2018).
146. Xing, G. *et al.* Low-temperature solution-processed wavelength-tunable perovskites for lasing. *Nat. Mater.* **13**, 476–480 (2014).
147. Zhu, C. *et al.* Strain engineering in perovskite solar cells and its impacts on carrier dynamics. *Nat. Commun.* **10**, 815 (2019).
148. Wang, J. T. W. *et al.* Efficient perovskite solar cells by metal ion doping. *Energy Environ. Sci.* **9**, 2892–2901 (2016).
149. Mooney, J. & Kambhampati, P. Get the Basics Right: Jacobian Conversion of Wavelength and Energy Scales for Quantitative Analysis of Emission Spectra. *J. Phys. Chem. Lett.* **4**, 3316–3318 (2013).
150. Doherty, T. A. S. *et al.* Performance-limiting nanoscale trap clusters at grain junctions in halide perovskites. *Nature* **580**, 360–366 (2020).
151. Calado, P. *et al.* Identifying Dominant Recombination Mechanisms in Perovskite Solar Cells by Measuring the Transient Ideality Factor. *Phys. Rev. Appl.* **11**, 1 (2019).
152. Correa-Baena, J. P. *et al.* Changes from Bulk to Surface Recombination Mechanisms between Pristine and Cycled Perovskite Solar Cells. *ACS Energy Lett.* **2**, 681–688 (2017).
153. Gordillo, G., Otálora, C. A. & Reinoso, M. A. Trap center study in hybrid organic-inorganic perovskite using thermally stimulated current (TSC) analysis. *J. Appl. Phys.* **122**, 075304 (2017).
154. Baumann, A. *et al.* Identification of Trap States in Perovskite Solar Cells. *J. Phys. Chem. Lett.* **6**, 2350–2354 (2015).
155. Moghadamzadeh, S. *et al.* Triple-cation low-bandgap perovskite thin-films for high-efficiency four-terminal all-perovskite tandem solar cells. *J. Mater. Chem. A* **8**, 24608–24619 (2020).
156. Zhang, X. *et al.* Tuning Bandgap of Mixed-Halide Perovskite for Improved Photovoltaic Performance Under Monochromatic-Light Illumination. *Phys. status solidi* **216**, 1800727 (2019).
157. Hörantner, M. T. *et al.* The Potential of Multijunction Perovskite Solar Cells. *ACS Energy Lett.* **2**, 2506–2513 (2017).
158. Zhao, B. *et al.* High Open-Circuit Voltages in Tin-Rich Low-Bandgap Perovskite-Based Planar Heterojunction Photovoltaics. *Adv. Mater.* **29**, 1604744 (2017).
159. Liao, W. *et al.* Fabrication of Efficient Low-Bandgap Perovskite Solar Cells by Combining Formamidinium Tin Iodide with Methylammonium Lead Iodide. *J. Am. Chem. Soc.* **138**, 12360–12363 (2016).

160. Parrott, E. S. *et al.* Interplay of Structural and Optoelectronic Properties in Formamidinium Mixed Tin-Lead Triiodide Perovskites. *Adv. Funct. Mater.* **28**, 1802803 (2018).
161. Eperon, G. E. *et al.* Perovskite-perovskite tandem photovoltaics with optimized band gaps. *Science*. **354**, 861–865 (2016).
162. Leijtens, T., Prasanna, R., Gold-Parker, A., Toney, M. F. & McGehee, M. D. Mechanism of Tin Oxidation and Stabilization by Lead Substitution in Tin Halide Perovskites. *ACS Energy Lett.* **2**, 2159–2165 (2017).
163. Shi, Z. *et al.* Lead-Free Organic-Inorganic Hybrid Perovskites for Photovoltaic Applications: Recent Advances and Perspectives. *Adv. Mater.* **29**, 1605005 (2017).
164. Juarez-Perez, E. J. *et al.* Photodecomposition and thermal decomposition in methylammonium halide lead perovskites and inferred design principles to increase photovoltaic device stability. *J. Mater. Chem. A* **6**, 9604–9612 (2018).
165. Nie, W. *et al.* Light-activated photocurrent degradation and self-healing in perovskite solar cells. *Nat. Commun.* **7**, 11574 (2016).
166. Juarez-Perez, E. J., Ono, L. K. & Qi, Y. Thermal degradation of formamidinium based lead halide perovskites into: Sym-triazine and hydrogen cyanide observed by coupled thermogravimetry-mass spectrometry analysis. *J. Mater. Chem. A* **7**, 16912–16919 (2019).
167. Arabpour Roghabadi, F. *et al.* Stability progress of perovskite solar cells dependent on the crystalline structure: From 3D ABX₃ to 2D Ruddlesden–Popper perovskite absorbers. *J. Mater. Chem. A* **7**, 5898–5933 (2019).
168. Stoumpos, C. C., Malliakas, C. D. & Kanatzidis, M. G. Semiconducting Tin and Lead Iodide Perovskites with Organic Cations: Phase Transitions, High Mobilities, and Near-Infrared Photoluminescent Properties. *Inorg. Chem.* **52**, 9019–9038 (2013).
169. Wei, M. *et al.* Combining Efficiency and Stability in Mixed Tin–Lead Perovskite Solar Cells by Capping Grains with an Ultrathin 2D Layer. *Adv. Mater.* **32**, 1907058 (2020).
170. Chen, Z. *et al.* Stable Sn/Pb-Based Perovskite Solar Cells with a Coherent 2D/3D Interface. *iScience* **9**, 337–346 (2018).
171. Ruggeri, E. *et al.* Controlling the Growth Kinetics and Optoelectronic Properties of 2D/3D Lead–Tin Perovskite Heterojunctions. *Adv. Mater.* **31**, 1905247 (2019).
172. Marshall, K. P., Walker, M., Walton, R. I. & Hatton, R. A. Enhanced stability and efficiency in hole-transport-layer-free CsSnI₃ perovskite photovoltaics. *Nat. Energy* **1**, 16178 (2016).
173. Kumar, M. H. *et al.* Lead-Free Halide Perovskite Solar Cells with High Photocurrents Realized Through Vacancy Modulation. *Adv. Mater.* **26**, 7122–7127 (2014).
174. Koh, T. M. *et al.* Formamidinium tin-based perovskite with low E_g for photovoltaic applications. *J. Mater. Chem. A* **3**, 14996–15000 (2015).

175. Gupta, S., Cahen, D. & Hodes, G. How SnF₂ Impacts the Material Properties of Lead-Free Tin Perovskites. *J. Phys. Chem. C* **122**, 13926–13936 (2018).
176. Jung, M. C., Raga, S. R. & Qi, Y. Properties and solar cell applications of Pb-free perovskite films formed by vapor deposition. *RSC Adv.* **6**, 2819–2825 (2016).
177. Tsai, C.-M. *et al.* Role of Tin Chloride in Tin-Rich Mixed-Halide Perovskites Applied as Mesoscopic Solar Cells with a Carbon Counter Electrode. *ACS Energy Lett.* **1**, 1086–1093 (2016).
178. Xu, X. *et al.* Ascorbic acid as an effective antioxidant additive to enhance the efficiency and stability of Pb/Sn-based binary perovskite solar cells. *Nano Energy* **34**, 392–398 (2017).
179. Tai, Q. *et al.* Antioxidant Grain Passivation for Air-Stable Tin-Based Perovskite Solar Cells. *Angew. Chemie - Int. Ed.* **58**, 806–810 (2019).
180. Liu, X. *et al.* Improved efficiency and stability of Pb–Sn binary perovskite solar cells by Cs substitution. *J. Mater. Chem. A* **4**, 17939–17945 (2016).
181. Leijtens, T. *et al.* Tin–lead halide perovskites with improved thermal and air stability for efficient all-perovskite tandem solar cells. *Sustain. Energy Fuels* **2**, 2450–2459 (2018).
182. Anaya, M. *et al.* Optical analysis of CH₃NH₃Sn:XPb_{1-x}I₃ absorbers: A roadmap for perovskite-on-perovskite tandem solar cells. *J. Mater. Chem. A* **4**, 11214–11221 (2016).
183. Zhu, H. L. *et al.* Controllable Crystallization of CH₃NH₃Sn_{0.25}Pb_{0.75}I₃ Perovskites for Hysteresis-Free Solar Cells with Efficiency Reaching 15.2%. *Adv. Funct. Mater.* **27**, 1605469 (2017).
184. Abdollahi Nejad, B. *et al.* Vacuum-Assisted Growth of Low-Bandgap Thin Films (FA_{0.8}MA_{0.2}Sn_{0.5}Pb_{0.5}I₃) for All-Perovskite Tandem Solar Cells. *Adv. Energy Mater.* **10**, 1902583 (2020).
185. Chen, W. *et al.* Conjugated Polymer–Assisted Grain Boundary Passivation for Efficient Inverted Planar Perovskite Solar Cells. *Adv. Funct. Mater.* **29**, 1808855 (2019).
186. Tavakoli, M. M. *et al.* Synergistic Crystal and Interface Engineering for Efficient and Stable Perovskite Photovoltaics. *Adv. Energy Mater.* **9**, 1802646 (2019).
187. Schoonman, J. Organic–inorganic lead halide perovskite solar cell materials: A possible stability problem. *Chem. Phys. Lett.* **619**, 193–195 (2015).
188. Liu, F. *et al.* Is Excess PbI₂ Beneficial for Perovskite Solar Cell Performance? *Adv. Energy Mater.* **6**, 1502206 (2016).
189. Fassel, P. *et al.* Fractional deviations in precursor stoichiometry dictate the properties, performance and stability of perovskite photovoltaic devices. *Energy Environ. Sci.* **11**, 3380–3391 (2018).
190. Lee, Y. H. *et al.* Unraveling the Reasons for Efficiency Loss in Perovskite Solar Cells.

- Adv. Funct. Mater.* **25**, 3925–3933 (2015).
191. Jacobsson, T. J. *et al.* Unreacted PbI₂ as a Double-Edged Sword for Enhancing the Performance of Perovskite Solar Cells. *J. Am. Chem. Soc.* **138**, 10331–10343 (2016).
 192. Duong, T. *et al.* High Efficiency Perovskite-Silicon Tandem Solar Cells: Effect of Surface Coating versus Bulk Incorporation of 2D Perovskite. *Adv. Energy Mater.* **10**, 1903553 (2020).
 193. Xiao, C. *et al.* Mechanisms of Electron-Beam-Induced Damage in Perovskite Thin Films Revealed by Cathodoluminescence Spectroscopy. *J. Phys. Chem. C* **119**, 26904–26911 (2015).
 194. Duong, T. *et al.* Light and Electrically Induced Phase Segregation and Its Impact on the Stability of Quadruple Cation High Bandgap Perovskite Solar Cells. *ACS Appl. Mater. Interfaces* **9**, 26859–26866 (2017).
 195. Duong, T. *et al.* Structural engineering using rubidium iodide as a dopant under excess lead iodide conditions for high efficiency and stable perovskites. *Nano Energy* **30**, 330–340 (2016).
 196. Jacob, K. T., Raj, S. & Rannesh, L. Vegard's law: a fundamental relation or an approximation? *Int. J. Mater. Res.* **98**, 776–779 (2007).
 197. Gao, X. & Daw, M. S. Investigation of band inversion in (Pb,Sn)Te alloys using ab initio calculations. *Phys. Rev. B* **77**, 033103 (2008).
 198. Dimmock, J. O., Melngailis, I. & Strauss, A. J. Band Structure and Laser Action in PbxSn(1-x)Te. *Phys. Rev. Lett.* **16**, 1193–1196 (1966).
 199. Zhao, D. *et al.* Low-bandgap mixed tin–lead iodide perovskite absorbers with long carrier lifetimes for all-perovskite tandem solar cells. *Nat. Energy* **2**, 17018 (2017).
 200. Niemann, R. G. *et al.* Cs + incorporation into CH₃NH₃PbI₃ perovskite: substitution limit and stability enhancement. *J. Mater. Chem. A* **4**, 17819–17827 (2016).
 201. Brivio, F., Caetano, C. & Walsh, A. Thermodynamic Origin of Photoinstability in the CH₃NH₃Pb(I_{1-x}Br_x)₃ Hybrid Halide Perovskite Alloy. *J. Phys. Chem. Lett.* **7**, 1083–1087 (2016).
 202. Han, Q. *et al.* High-performance perovskite/Cu(In,Ga)Se₂ monolithic tandem solar cells. *Science* **361**, 904–908 (2018).
 203. Manzoor, S. *et al.* Improved light management in planar silicon and perovskite solar cells using PDMS scattering layer. *Sol. Energy Mater. Sol. Cells* **173**, 59–65 (2017).
 204. Dottermusch, S. *et al.* Micro-cone textures for improved light in-coupling and retroreflection-inspired light trapping at the front surface of solar modules. *Prog. Photovoltaics Res. Appl.* **27**, 3133 (2019).
 205. Schmager, R. *et al.* Texture of the Viola Flower for Light Harvesting in Photovoltaics. *ACS Photonics* **4**, 2687–2692 (2017).

206. Langenhorst, M. *et al.* Liquid Glass for Photovoltaics: Multifunctional Front Cover Glass for Solar Modules. *ACS Appl. Mater. Interfaces* **11**, 35015–35022 (2019).
207. Lee, S. J. *et al.* Reducing Carrier Density in Formamidinium Tin Perovskites and Its Beneficial Effects on Stability and Efficiency of Perovskite Solar Cells. *ACS Energy Lett.* **3**, 46–53 (2018).
208. Diao, E. W. G., Jokar, E. & Rameez, M. Strategies to improve performance and stability for tin-based perovskite solar cells. *ACS Energy Lett.* **4**, 1930–1937 (2019).
209. Ratcliff, E. L. *et al.* Evidence for near-Surface NiOOH Species in Solution-Processed NiO x Selective Interlayer Materials: Impact on Energetics and the Performance of Polymer Bulk Heterojunction Photovoltaics. *Chem. Mater.* **23**, 4988–5000 (2011).
210. Prasanna, R. *et al.* Design of low bandgap tin–lead halide perovskite solar cells to achieve thermal, atmospheric and operational stability. *Nat. Energy* **4**, 939–947 (2019).
211. Werner, J. *et al.* Improving Low-Bandgap Tin–Lead Perovskite Solar Cells via Contact Engineering and Gas Quench Processing. *ACS Energy Lett.* **5**, 1215–1223 (2020).
212. Bi, C. *et al.* Non-wetting surface-driven high-aspect-ratio crystalline grain growth for efficient hybrid perovskite solar cells. *Nat. Commun.* **6**, 7747 (2015).
213. Liu, X. *et al.* 20.7% Highly Reproducible Inverted Planar Perovskite Solar Cells With Enhanced Fill Factor and Eliminated Hysteresis. *Energy Environ. Sci.* **12**, 1622–1633 (2019).
214. Petrović, M. *et al.* Limitations of a polymer-based hole transporting layer for application in planar inverted perovskite solar cells. *Nanoscale Adv.* **1**, 3107–3118 (2019).
215. Khadka, D. B., Shirai, Y., Yanagida, M., Ryan, J. W. & Miyano, K. Exploring the effects of interfacial carrier transport layers on device performance and optoelectronic properties of planar perovskite solar cells. *J. Mater. Chem. C* **5**, 8819–8827 (2017).
216. Jäger, T. *et al.* Hydrogenated indium oxide window layers for high-efficiency Cu(In,Ga)Se₂ solar cells. *J. Appl. Phys.* **117**, 205301 (2015).
217. Koida, T., Fujiwara, H. & Kondo, M. Hydrogen-doped In₂O₃ as High-mobility Transparent Conductive Oxide. *Jpn. J. Appl. Phys.* **46**, L685–L687 (2007).
218. Jiang, Y. *et al.* High-Mobility In₂O₃:H Electrodes for Four-Terminal Perovskite/CuInSe₂ Tandem Solar Cells. *ACS Nano* **14**, 7502–7512 (2020).
219. Kuang, Y. *et al.* Towards the implementation of atomic layer deposited In₂O₃:H in silicon heterojunction solar cells. *Sol. Energy Mater. Sol. Cells* **163**, 43–50 (2017).
220. Dawood, Y. Z., Mohammed, M. S. & Al-Hamdani, A. H. Characterization and optimization of In₂O₃ thin films for application in heterojunction silicon solar cells. *Juornal Mater. Sci. Eng. A* **2**, 352–356 (2012).
221. Jäger, T. *et al.* Improved open-circuit voltage in Cu(In,Ga)Se₂ solar cells with high

- work function transparent electrodes. *J. Appl. Phys.* **117**, 225303 (2015).
222. Fu, F. *et al.* Low-temperature-processed efficient semi-transparent planar perovskite solar cells for bifacial and tandem applications. *Nat. Commun.* **6**, 8932 (2015).
223. Zhang, D. *et al.* Combination of Advanced Optical Modelling with Electrical Simulation for Performance Evaluation of Practical 4-terminal Perovskite/c-Si Tandem Modules. *Energy Procedia* **92**, 669–677 (2016).
224. Löper, P. *et al.* Complex Refractive Index Spectra of CH₃NH₃PbI₃ Perovskite Thin Films Determined by Spectroscopic Ellipsometry and Spectrophotometry. *J. Phys. Chem. Lett.* **6**, 66–71 (2015).
225. Ball, J. M. *et al.* Optical properties and limiting photocurrent of thin-film perovskite solar cells. *Energy Environ. Sci.* **8**, 602–609 (2015).
226. Climent-Pascual, E. *et al.* Influence of the substrate on the bulk properties of hybrid lead halide perovskite films. *J. Mater. Chem. A* **4**, 18153–18163 (2016).
227. Haider, S. Z., Anwar, H., Jamil, Y. & Shahid, M. A comparative study of interface engineering with different hole transport materials for high-performance perovskite solar cells. *J. Phys. Chem. Solids* **136**, 109147 (2020).
228. Jeong, J. *et al.* Energy level alignment and hole injection property of poly(9-vinylcarbazole)/indium tin oxide interface. *Chem. Phys. Lett.* **706**, 317–322 (2018).
229. Weinhardt, L., Hauschild, D. & Heske, C. Surface and Interface Properties in Thin-Film Solar Cells: Using Soft X-rays and Electrons to Unravel the Electronic and Chemical Structure. *Adv. Mater.* **31**, 1806660 (2019).
230. Hauschild, D. *et al.* Impact of a RbF Postdeposition Treatment on the Electronic Structure of the CdS/Cu(In,Ga)Se₂ Heterojunction in High-Efficiency Thin-Film Solar Cells. *ACS Energy Lett.* **2**, 2383–2387 (2017).
231. Duncan, D. A. *et al.* A New Look at the Electronic Structure of Transparent Conductive Oxides-A Case Study of the Interface between Zinc Magnesium Oxide and Cadmium Telluride. *Adv. Mater. Interfaces* **3**, 1600418 (2016).
232. Kraut, E. A., Grant, R. W., Waldrop, J. R. & Kowalczyk, S. P. Precise Determination of the Valence-Band Edge in X-Ray Photoemission Spectra: Application to Measurement of Semiconductor Interface Potentials. *Phys. Rev. Lett.* **44**, 1620–1623 (1980).
233. Quases-Imfp-Tpp2M - Quases. Available at: <http://www.quases.com/products/quases-imfp-tpp2m/>.
234. Konstantakou, M. & Stergiopoulos, T. A critical review on tin halide perovskite solar cells. *J. Mater. Chem. A* **5**, 11518–11549 (2017).
235. Chen, B., Yang, M., Priya, S. & Zhu, K. Origin of J-V Hysteresis in Perovskite Solar Cells. *Journal of Physical Chemistry Letters* **7**, 905–917 (2016).
236. Schmidt, H. *et al.* Efficient semitransparent inverted organic solar cells with indium tin oxide top electrode. *Appl. Phys. Lett.* **94**, 243302 (2009).

List of Publications and Conference Contributions

Peer-reviewed publications (first author)

S. Moghadamzadeh, I. M. Hossain, M. Jakoby, B. Abdollahi Nejand, D. Rueda-Delgado, J. A. Schwenzler, S. Gharibzadeh, T. Abzieher, M. R. Khan, A. A. Haghighirad, I. A. Howard, B. S. Richards, U. Lemmer and U. W. Paetzold, Spontaneous enhancement of the stable power conversion efficiency in perovskite solar cells. *J. Mater. Chem. A* **8**, 670–682 (2019).

S. Moghadamzadeh, I. M. Hossain, T. Duong, S. Gharibzadeh, T. Abzieher, Huyen Pham, H. Hung, P. Fassel, U. Lemmer, B. Adollahi Nejand and U. W. Paetzold, Triple-cation low-bandgap perovskite thin-films for high-efficiency four-terminal all-perovskite tandem solar cells. *J. Mater. Chem. A* **8**, 24608–24619 (2020).

S. Moghadamzadeh, I. M. Hoassain, M. Loy, D. B. Ritzer, H. Hu, D. Hauschild, A. Mertens, J-P. Becker, E. Ahlswede, L. Weinhardt, U. Lemmer, B. Abdollahi Nejand and Ulrich W. Paetzold, Hole-Transport-Layer-Free Tin/Lead Perovskite Solar Cells for Four-Terminal All-Perovskite Tandem Solar Cells. (Submitted and under review)

Peer-reviewed publications (co-author)

Y. J. Donie, D. Theobald, **S. Moghadamzadeh**, A. Mertens, I. M. Hossain, U. W. Paetzold, U. Lemmer and G. Gomard, Planarized and Compact Light Scattering Layers Based on Disordered Titania Nanopillars for Light Extraction in Organic Light Emitting Diodes, *Adv. Opt. Mater.* **2001610**, 2001610 (2020).

I. M. Hossain, Y. J. Donie, R. Schmager, M. S Abdelkhalik, M. Rienäcker, T. F. Wietler, R. Peibst, A. Karabanov, J. Schwenzler, **S. Moghadamzadeh**, U. Lemmer, B. S. Richards, G. Gomard, U. W. Paetzold, Nanostructured front electrodes for perovskite/c-Si tandem photovoltaics. *Optics express* **28** (6), 8878-8897 (2020).

J. A. Schwenzler, L. Rakocevic, T. Abzieher, D. Rueda-Delgado, **S. Moghadamzadeh**, S. Gharibzadeh, I. M. Hossain, R. Gehlhaar, B. S Richards, U. Lemmer, U. W. Paetzold, Toward Stable Perovskite Solar Cell Architectures: Robustness Against Temperature Variations of Real-World Conditions. *IEEE Journal of Photovoltaics* **10** (3), 777-784 (2020).

B. Abdollahi Nejand, I. M. Hossain, M. Jakoby, **S. Moghadamzadeh**, T. Abzieher, S. Gharibzadeh, J. A. Schwenzler, P. Nazari, F. Schackmar, D. Hauschild, L. Weinhardt, U. Lemmer, B. S. Richards, I. A. Howard, U. W. Paetzold, Vacuum-Assisted Growth of Low-Bandgap Thin Films (FA_{0.8}MA_{0.2}Sn_{0.5}Pb_{0.5}I₃) for All-Perovskite Tandem Solar Cells. *Advanced Energy Materials* **10** (5), 1902583 (2020).

T. Abzieher, J. A. Schwenzler, **S. Moghadamzadeh**, F. Sutterlüti, I. M. Hossain, M. Pfau, E. Lotter, M. Hetterich, B. S. Richards, U. Lemmer, M. Powalla, U. W. Paetzold, Efficient All-Evaporated *pin*-Perovskite Solar Cells: A Promising Approach Toward Industrial Large-Scale Fabrication. *IEEE Journal of Photovoltaics* **9** (5), 1249-1257 (2019).

S. Gharibzadeh, B. Abdollahi Nejand, M. Jakoby, T. Abzieher, D. Hauschild, **S. Moghadamzadeh**, J. A. Schwenzler, P. Brenner, R. Schmager, A. A. Haghighirad, L. Weinhardt, U. Lemmer, B. S. Richards, I. A. Howard, U. W. Paetzold, Record Open-Circuit Voltage Wide-Bandgap Perovskite Solar Cells Utilizing 2D/3D Perovskite Heterostructure. *Advanced Energy Materials* **9** (21), 1803699 (2019).

T. Abzieher, **S. Moghadamzadeh**, F. Schackmar, H. Eggers, F. Sutterlütli, A. Farooq, D. Kojda, K. Habicht, R. Schmager, A. Mertens, R. Azmi, L. Klohr, J. A. Schwenzler, M. Hetterich, U. Lemmer, B. S. Richards, M. Powalla, U. W. Paetzold, Electron-beam-evaporated nickel oxide hole transport layers for perovskite-based photovoltaics. *Advanced Energy Materials* **9** (12), 1802995 (2019).

I. M. Hossain, D. Hudry, F. Mathies, T. Abzieher, **S. Moghadamzadeh**, D. Rueda-Delgado, F. Schackmar, M. Bruns, R. Andriessen, T. Aernouts, F. Di Giacomo, U. Lemmer, B. S. Richards, U. W. Paetzold, A. Hadipour, Scalable Processing of Low-Temperature TiO₂ Nanoparticles for High-Efficiency Perovskite Solar Cells. *ACS Applied Energy Materials* **2** (1), 47-58 (2018).

A. Farooq, I. M. Hossain, **S. Moghadamzadeh**, J. A. Schwenzler, T. Abzieher, B. S. Richards, E. Klampaftis, U. W. Paetzold, Spectral dependence of degradation under ultraviolet light in perovskite solar cells. *ACS applied materials & interfaces* **10** (26), 21985-21990 (2018).

J. A. Schwenzler, L. Rakocevic, R. Gehlhaar, T. Abzieher, S. Gharibzadeh, **S. Moghadamzadeh**, A. Quintilla, B. S. Richards, U. Lemmer, U. W. Paetzold, Temperature variation-induced performance decline of perovskite solar cells. *ACS applied materials & interfaces* **10** (19), 16390-16399 (2018).

H. Hu, **S. Moghadamzadeh**, R. Azmi, M. Kaiser, J. C. Fischer, Y. Li, Q. Jin, I. M. Hossain, U. Lemmer, B. S. Richards, U. W. Paetzold, B. A. Nejand, Fullerene-Passivated Sn-Pb Mixed Perovskites Enable Efficient Four-Terminal All-Perovskite Tandem Solar Cells, *Submitted*.

Conference contributions

S. Moghadamzadeh, I. M. Hossain, D. Rueda-Delgado, S. Gharibzadeh, J. A. Schwenzler, T. Abzieher, B. S. Richards, U. Lemmer, U. W. Paetzold, Enhancement of Stabilized Power Conversion Efficiency in Triple-Cation Perovskite Solar Cells. 18th International Conference on Hybrid and Organic Photovoltaics (HOPV), Benidorm, Spain (2018).

S. Moghadamzadeh, I. M. Hossain, B. Abdollahi Nejand, M. Jakoby, D. Rueda-Delgado, S. Gharibzadeh, J. A. Schwenzler, T. Abzieher, I. A. Howard, A. A. Haghighirad, B. S. Richards, U. Lemmer, U. W. Paetzold, Spontaneous Enhancement of Power Conversion Efficiency in Multi-Cation Perovskite Solar Cells. Oral talk, International Conference in Advanced Materials (EMRS), Nice, France (2019).

- **S. Moghadamzadeh**, S. Gharibzadeh, M. Jakoby, M. Rahman Khan, A. A. Haghighirad, I. A. Howard, B. S. Richards, U. Lemmer, U. W. Paetzold, Spontaneous Enhancement of the

Power Output in in Surface-Passivated Triple-Cation Perovskite Solar Cells. 47th IEEE Photovoltaic Specialists Conference (PVSC), Calgary, Canada, AB, 1217-1219 (2020), doi: 10.1109/PVSC45281.2020.9300632

Acknowledgements

I would like to take this opportunity to express my deepest appreciation to all the people who contributed to this work one way or another.

I am deeply grateful to DAAD (Deutscher Akademischer Austauschdienst/German academic exchange service) for supporting me in perusing a wonderful experience of my life, doing a Ph.D.

I would like to extend my deep gratitude to Prof. Dr. Uli Lemmer for supervising this thesis. I am truly grateful for the precious time discussing my topic with an expert with invaluable insight into the field. He has been always supportive and never lost his confidence in my work. I would also like to extend my sincere thanks to Dr. Ulrich W. Paetzold who immensely contributed to the discussions of the results of this work. I truly appreciate the time he invested in proofreading and engaging in the scientific discussions of my work. I would like to express my special appreciation to Dr. Bahram Abdollahi Nejad for his invaluable contribution to this work, as well as his experience, motivation, and abundant support in challenging situations. I would also like to sincerely thank Prof. Dr. Jan Philipp Hofmann for spending the time and effort to act as the second referee.

I'd like to share my special appreciation with my very first colleagues I started this journey with from the scratch, Iteaz M. Hossain and Tobias Abzieher. Their help and support in challenging moments cannot be overestimated. Special thanks go to Paul Fassel who was always open to spending some time on fruitful and productive scientific discussions. I wish to extend my deep gratitude to all my colleagues who I had some of my best time shared with and received help and motivation from during the last four years; Yidenekachew Donie, Andres Rösch, Philipp Brenner, Diana Rueda-Delgado, Jonas A. Schwenzer, Amjad Farooq, Adrian Mertens, Raphael Schmager, Malte Langenhorst, Jonathan Lehr, Dominik Theobald, Henning Mescher, Simon Ternes, Fabian Schackmar, David Benedikt Ritzer, Helge Eggers, Isabel Allegro, Roja Singh, Julie Roger, Thomas Feeney, Fabrizio Gota, Felix Laufer, Ahmed Farag, Marco A. R. Preciado, Guillaume Gomard, Christian Kayser, Felix Geislhöringer, my student Robert Pfender-Siedle and all other former and current group members. I am grateful to my Iranian friends, Saba, Bahram, Pariya, Shahab, Amir, and Mahsa who were always supportive and caring.

I sincerely acknowledge the scientific collaboration and effort that I received from Dr. Amir. A. Haghghirad, Dr. Ian Howard, Marius Jakoby, Dr. Motiur Rahman Khan, Dr. Dirk Hauschild, Dr. Lothar Weinhardt, Dr. Michael Hetterich, and Prof. Dr. Bryce S. Richards.

I gratefully acknowledge the external collaboration partners, Dr. Erik Ahlswede, Dr. Moritz Loy, and Dr. Jan-Philipp Becker from ZSW as well as Dr. The Duong and Huyen Pham from ANU.

I also wish to thank Karlsruhe School of Optics and Photonics (KSOP) for providing a graduate program and for the great organization of many scientific and social events.

Acknowledgements

Last but not least, I would like to express my deepest gratitude to my beloved husband, Ali, who has always been there for me and never lost his faith in me. This milestone would have never been possible without the unconditional love and support from him and my dear family; my beloved parents and siblings. I am forever indebted to my dear parents who have always encouraged me to fight for my goals. I also wish to deeply thank my dearly loved in-law family and my friends back home.

این تجربه گران بها بدون وجود و حمایت صمیمانه خانواده ام هرگز امکان پذیر نبود.

And, I wanna thank me for not giving up on me.